



universität
wien

DISSERTATION/DOCTORAL THESIS

Titel der Disseration / Title of the Doctoral Thesis

Electron transport through redox-active transition metal complexes

verfasst von / submitted by
Mag. Georg Kastlunger

angestrebter akademischer Grad / in partial fulfilment of the requirements
for the degree of
Doktor der Naturwissenschaften (Dr. rer. nat.)

Wien/Vienna, 2016

Studienkennzahl lt. Studienblatt /degree programme
code as it appears on the student record sheet:

A 796 605 419

Dissertationsgebiet lt. Studienblatt /field of study
as it appears on the student record sheet:

Chemie

Betreut von /Supervisor:

Dipl. Ing. Dr. Robert Stadler Priv. Doz.

fürn Michi

Acknowledgements

I would like to thank

My supervisor Robert Stadler for giving me the possibility to work in his group, as well as his massive support and the numerous discussions we had during the whole time of my work on this thesis.

Florian Schwarz and Emanuel Lörtscher for performing the break junction measurements and for giving me the opportunity of a scientific visit in their lab in the course of our fruitful collaboration.

Venkatesan Koushik, Franziska Lissel and Heinz Berke for synthesising the compounds, which have been the basis for both the theoretical and experimental studies.

Elvar Ö. Jónsson and Pawel Zawadzki for their aid in implementing and using some of the computational techniques applied in the thesis.

The Austrian Science Fund (FWF), the Austrian Academy of Sciences (ÖAW), the Austrian Chemical Society (GÖCH), the Springer Science+Business Media and the Provinz Bozen for their funding, which made the work on the thesis possible in the first place.

My parents Robert and Martha and my siblings Ilse, Peter and Barbara for making all of this possible and for their support over all these years.

My friends Pü, Leo, Fabian, Heiko, Däni, Seppi, David, Greitl, Jemus, Sartoscht, Claudia (to mention a few) for the great time outside of science.

Last but not least I would like to thank my partner Irene for her love and patience.

This doctoral thesis is based on the following publications, which are included in their published form:

Georg Kastlunger and Robert Stadler

Charge localization on a redox-active single-molecule junction and its influence on coherent electron transport

Physical Review B **88**, 035418 (2013)

Florian Schwarz, Georg Kastlunger, Franziska Lissel, Heike Riel, Koushik Venkatesan, Heinz Berke, Robert Stadler, and Emanuel Lörtscher

High-Conductive Organometallic Molecular Wires with Delocalized Electron Systems Strongly Coupled to Metal Electrodes

Nano Letters, **14**, 5932-5940 (2014)

Georg Kastlunger and Robert Stadler

Density functional theory based calculations of the transfer integral in a redox-active single-molecule junction

Physical Review B **89**, 115412 (2014)

Georg Kastlunger and Robert Stadler

Density functional theory based direct comparison of coherent tunneling and electron hopping in redox-active single-molecule junctions

Physical Review B **91**, 125410 (2015)

Florian Schwarz, Georg Kastlunger, Franziska Lissel, Carolina Egler-Lucas, Sergey N. Semenov, Koushik Venkatesan, Heinz Berke, Robert Stadler and Emanuel Lörtscher

Field-induced conductance switching by charge-state alternation in organometallic single-molecule junctions

Nature Nanotechnology, Published online: 16 November 2015

(DOI: 10.1038/NNANO.2015.255)

Abstract

The thesis deals with the theoretical description of electron transport through transition metal complexes in the emerging field of single molecule electronics, where the main focus was on an analysis of the structural and environmental parameters, which are responsible for measured currents in experimental setups. The theory behind two experimental routes has been addressed explicitly, namely electrochemical scanning tunnelling microscope (STM) and mechanically controlled break-junctions (MCBJ) in ultra high vacuum.

For the theoretical description of an electrochemical STM this thesis focuses on electron transport through a Ru-complex with pyridyl anchor groups, where a special emphasis is put on the influence of the solvent and the redox state of the compound. Both possible transport regimes, namely coherent transport and two-step electron hopping, are addressed, where schemes for the simulation of a charged compound in the junction environment have been developed and the influence of a change in the redox state on the conductance was studied.

While the coherent tunnelling conductance is described on the basis of the well known Landauer-Büttiker formalism, the description of an electron hopping process had to be elaborated within the semi-classical Marcus-Hush theory, where all relevant quantities have been calculated within density functional theory (DFT). Three different approaches for the calculation of the transfer integral, all of them known from quantum chemistry, have been thoroughly tested and adapted in order to be applicable for a molecular compound trapped between two Au surfaces.

For the interpretation of the break junction experiments of our close collaborators at IBM Zürich a dinuclear Fe unit, $\{\text{Fe}\}-\text{C}_4-\{\text{Fe}\}$, with an extensive charge-delocalisation over the entire organometallic backbone with

five different end groups was studied. In this work a special emphasis was set on their suitability as molecular wires, based on their electronic coupling to the electrodes, energy level alignment and conductance decay with the molecular length.

As a second part of this collaboration, the influence of the atom type of the metal centre and its respective interactions with the ligands in mononuclear Fe-, Mo- and Ru-complexes coupled to Au electrodes via thiol groups has been investigated systematically. Although voltage-induced hysteresis was detected experimentally for all compounds an irreversible switching of the conductance was only found for the Mo-complex. These results could be theoretically explained by a two channel model combining coherent electron transport and electron hopping, where the underlying mechanism could be identified as a charging of the molecule in the junction made possible by the presence of a localised electronic state on the transition metal centre.

Zusammenfassung

Thema der Dissertation ist die theoretische Beschreibung des Elektronentransports durch Übergangsmetallkomplexe im Bereich der Einzelmolekülelektronik. Der Hauptfokus lag dabei auf einer Analyse der molekularen und experimentellen Einflüsse, welche für die gemessenen Ströme in Versuchsaufbauten verantwortlich sind. Theoretische Basis dafür bildete die Dichtefunktionaltheorie.

Zwei experimentellen Methoden, das elektrochemische Rastertunnelmikroskop (STM) und mechanisch gesteuerte Bruchkontakte (MCBJ) im Ultrahochvakuum wurden in dieser theoretischen Arbeit explizit adressiert.

Die Beschreibung des elektrochemischen STM konzentrierte sich auf den Elektronentransport durch einen Ru-Komplex mit Pyridyl-Ankergruppen, wobei ein Schwerpunkt auf den Einfluss des Lösungsmittels und den Redoxzustand der Verbindung gelegt wurde. Dabei wurden die beiden möglichen Transportregime, nämlich kohärentes Tunneln und zweistufiges “electron hopping” beschrieben. In diesem Zusammenhang wurden Methoden für die Simulation einer geladenen Verbindung gekoppelt an zwei Metallelektroden entwickelt.

Für die Beschreibung von “electron hopping” in einem Einzelmolekülkontakt wurde eine Methodik auf der Basis der semi-klassischen Marcus-Hush Theorie entwickelt, wobei alle relevanten Parameter mittels DFT berechnet wurden. Drei quantenchemische Ansätze für die Berechnung des Transferintegrals wurden dabei ausgiebig getestet und für die Anwendung auf eine Molekülverbindung zwischen zwei Goldoberflächen angepasst.

Für die Interpretation von Bruchkontaktexperimenten, welche von unseren Kollegen bei IBM Zürich durchgeführt wurden, wurden dinukleare Fe-Komplexe mit einer Delokalisierung des π -Systems über die gesamte metallorganische Brücke auf ihre Eignung als molekulare Drähte untersucht. Das

Hauptaugenmerk lag dabei auf dem Einfluss der molekularen Ankergruppen, wobei Komplexe mit fünf verschiedenen Endgruppen in Bezug auf ihre elektronische Kopplung an die Elektroden, Energieniveau- Anpassung und ihre Leitfähigkeitsabnahme mit der Moleküllänge studiert wurden.

Schliesslich wurde der Einfluss der Atomsorte des Metallzentrums in mononuklearen Fe-, Mo- und Ru-Komplexen systematisch untersucht. In den Experimenten in Zürich konnte für alle Verbindungen Hysterese detektiert werden. Ein irreversibles Umschalten der Leitfähigkeit der Nano-Kontakte konnte jedoch nur für den Mo-Komplex erzielt werden. Diese Ergebnisse konnten theoretisch durch eine Kombination von kohärentem Elektronentransport und "electron hopping" erklärt werden, wobei der zugrunde liegende Mechanismus als eine Aufladung des Moleküls identifiziert wurde, welche durch einen lokalisierten elektronischen Zustand am Übergangsmetallzentrum ermöglicht wird.

Contents

1	Introduction	1
2	Density functional theory	5
2.1	History of DFT	6
2.2	Schrödinger's equation	7
2.3	Hohenberg-Kohn theorems	8
2.4	Computational implementation of DFT	9
2.4.1	Kohn-Sham equations	9
2.4.2	Calculating the exchange-correlation energy	11
2.4.3	Exchange and correlation functionals	11
2.4.4	The projector augmented wave method (PAW)	13
2.4.5	Localised basis sets in GPAW	16
2.5	The Delta self consistent field method	17
3	Phase coherent electron transport	21
3.1	Phenomenological introduction	22
3.2	Electron transport through a single level	23
3.3	The Landauer Büttiker formalism	26
3.4	Conductance calculations for real systems	28
3.4.1	DFT based electron transport	29
3.4.2	The Transport Hamiltonian	29
3.4.3	Calculation of the lead self energies	32
3.4.4	k -point dependence	33
4	Energy level alignment and electronic coupling	35
4.1	Phenomenological introduction	36
4.2	Induced projected density of states	37
4.3	Mechanisms for the energy level alignment	38
4.3.1	Pauli repulsion	38
4.3.2	Partial filling of molecular eigenstates	40
4.4	Charge transfer and Fermi Level alignment in DFT	41
4.4.1	Subdiagonalisation of the molecular subspace	42

4.4.2	Vacuum level alignment	42
5	Charge localisation within DFT (Paper I)	45
5.1	Motivation	46
5.2	The Self Interaction Error (SIE)	46
5.3	Charge localisation via solvation shells	47
5.4	Charge localisation via Δ SCF	48
5.5	Outline of results and discussion of Paper I	50
6	Anchor group variation in molecular wires (Paper II)	53
6.1	Motivation	54
6.2	Energy level alignment	55
6.2.1	Excursion: The Scissor operator	58
6.3	Difference in couplings	59
6.4	Outline of results and discussion of Paper II	61
7	Incoherent electron transport	63
7.1	History of Marcus theory	64
7.2	Classical Marcus theory	65
7.2.1	Outer sphere reactions	65
7.2.2	Atomistic description of inner spheres	67
7.2.3	The preexponential factor	68
7.3	Electron hopping at metal surfaces	69
7.3.1	Adaptation of the transfer rate	69
8	Coherent conductance based on the Transfer integral (Paper III)	73
8.1	Motivation	74
8.2	Calculation methods	74
8.2.1	The energy gap approach	74
8.2.2	The expansion coefficient method	75
8.2.3	The effective coupling scheme	77
8.3	Transfer integral on a tight binding level	78
8.4	Application within DFT	80
8.4.1	Implementation on a single particle level	81
8.4.2	Implementation based on a many body level	82
8.5	Transfer integral in a single molecule junction	83
8.6	Relationship between Transfer integral and tunnelling conductance	85
8.7	Outline of results and discussion of Paper III	86
9	Electron hopping in single molecule junctions (Paper IV)	89
9.1	Motivation	90
9.2	Calculation schemes for the key parameters of Marcus theory	90

9.2.1	Driving force	90
9.2.2	Reorganisation energy	91
9.2.3	Transfer integral	95
9.3	Incoherent single molecule conductance	96
9.3.1	Influence of an electrochemical gate	97
9.4	Outline of Results and Discussion of Paper IV	98
10	Redox switching in single molecule junctions (Paper V)	101
10.1	Motivation	102
10.2	Electronic ground states calculated within DFT	102
10.2.1	Predictions from Ligand Field Theory	103
10.2.2	DFT results	104
10.3	The redox hysteresis model	105
10.3.1	Model setup	105
10.3.2	The transition rate	106
10.3.3	Hysteresis in a two-channel model	106
10.4	Description of hysteresis and switching with parameters obtained from DFT	110
10.5	Outline of results and discussion of Paper V	110
10.5.1	Experimental results	110
10.5.2	Theoretical results	111
	Bibliography	114
11	Paper I	125
12	Paper II	137
13	Paper III	149
14	Paper IV	161
15	Paper V	171
	Curriculum vitae	181

The evolution of information technology in the past sixty years had a tremendous impact on society and technology. This started with the invention of the transistor in 1948¹ paving the ground for future electronic devices. Gordon Moore, a co-founder of Intel, described the trend in the number of devices per integrated circuit in 1965 as an increase, where this number doubles over a period of approximately eighteen months.² This trend could be satisfied up to the present days. Modern manufacturing techniques, such as photolithography,³ however, soon will reach their limits in terms of miniaturisation, which would lead to an end of an increase of devices per chip at this rate, unless new techniques and materials could be applied. Single molecule electronics (SME) would be a promising successor for such top-down manufacturing methods, where it is envisioned, that single, or small ensembles of molecules could be applied as active or passive building blocks in electronic circuits.

The idea of employing a single molecule as an electronic component was first conceived by Arie Aviram and Mark Ratner in 1970.⁴ In their theoretical paper they laid the foundation of SME by proposing a molecule consisting of tetrathiafulvalene (TTF) and tetracyanoquinodimethane (TCNQ) groups, as donor and acceptor respectively, as agents inducing rectification in electronic devices. Based on this theoretical proposition, the first experimental observation of rectification based on a small ensemble of molecules was achieved in 1988 by Aviram et. al.⁵ In their measurements they applied a scanning tunnelling microscope (STM) with a Pt tip for performing an I/V scan of a monolayer of the asymmetric molecule hemiquinone on Au(111).

1. Introduction

Although a rectification in this measurement setup already results from the difference in tip and substrate material and geometry a distinct difference in the measured currents could be observed when comparing the bare Au surface and the substrate with the adsorbed monolayer. This experiment can be seen as the starting point for future research in the field of SME.

Besides current rectification, a variety of possible applications for molecular components in electronic circuits could be identified in the past decades. Single molecules were proposed to function as both passive (diodes,wires)⁶⁻¹⁴ and active (transistors,switches)¹⁵⁻³¹ devices in electronic components, where their most significant benefit is that the intrinsic functionality can be provided reliably by means of chemical synthesis.

Single molecule switching mechanisms are based on either conformational changes triggered by photons¹⁵⁻¹⁸ or bias,¹⁹⁻²⁴ spin crossover²⁵⁻²⁷ or a redox reaction, which is performed via the introduction of oxidating or reducing agents²⁸ or an electrochemical setup.²⁹⁻³¹ Historically, very prominent molecular systems exhibiting such a reversible switching behaviour were rotaxane molecules, consisting of single molecular compounds surrounded by crown ether based rings, studied by Collier et. al.^{32,33} The basic mechanism of the switching in their work was described as a change of the ring position triggered by the oxidation when a bias of at least 0.7V is applied. A back-reduction could then be performed through a voltage pulse of -2V. Since for the reading process only a bias of 0.1V is needed, stable ON and OFF states which can be switched into each other manually could be created.

An application of inorganic transition metal complexes as single molecule switches was first investigated in the group of Jens Ulstrup.³⁴⁻³⁷ In these studies the focus was put on complexes containing Os and Co metal centres, which were adsorbed on Au(111) and Pt(111) surfaces via pyridyl and thiol anchor groups respectively and the respective I/V behaviour was scanned by applying an electrochemical STM and in situ scanning tunnelling spectroscopy (STS). For measurements performed at constant source-drain bias, it could proven that the measured current is strongly dependent on the applied overpotential, therefore making the redox switching potential of the three compounds within the junction accessible. An electron transfer kinetics model was derived for the explanation of the trends found in these measurements, which is known as the Kuznetsov-Ulstrup model,³⁵⁻³⁸ and describes the electron transport in such junctions as a two step process of

subsequent resonant tunnelling aided by the vibrational relaxation of the molecular orbitals.

This thesis tries to move further in this direction by investigating the potential of transition metal complexes on the basis of density functional theory (DFT). For this purpose the electrochemical properties of a $\text{Ru}(\text{PPh}_2)_4(\text{C}_2\text{H}_4)_2$ -bis(pyridylacetylide) (in the following referred to as the Ru-complex) are studied. In contrast to the compounds of Ulstrup et. al.'s work the Ru-complex in this thesis includes two pyridine anchor groups allowing for symmetric adsorption on both substrate and tip. This structural difference opens the possibility for direct coherent tunnelling through the compound. In this context the influence of a change in the redox state of the Ru-complex on the molecular conductance was studied by elaborating a scheme, which allows to simulate a charged complex in the junction environment.

An experimental study on similar Ru-compounds has been performed by Kim et. al. on the basis of I/V measurements with a CP-AFM and cross-wires for junctions of monolayers of molecules with the same molecular backbone but cyano anchors¹⁰ on Au(111) substrates. A special emphasis in this work has been set on the dependence of the measured current on the length of the molecular species, where compounds containing 1,2 and 3 $\text{Ru}(\text{PPh}_2)_4(\text{C}_2\text{H}_4)_2$ blocks were studied. Based on their results Kim et. al. could show that the complex containing three Ru-centres (Ru3) exhibits strong temperature dependence in its I/V properties, while the shorter compounds do not. Therefore the authors proposed a temperature mediated two step electron hopping process to be responsible for the measured conductance of Ru3. Motivated by these experimental findings the transition from the coherent tunnelling regime to two step electron hopping in the Ru-complex was studied, where an application of Marcus theory in single molecule junctions based on DFT was derived.

The application of transition metal complexes as molecular wires was investigated in a close collaboration with our experimental partners at IBM Zürich and the University of Zürich. The important characteristics for molecular wires, namely (nearly) linear dependence of the current on the applied bias, can, in principle, be achieved by low injection barriers, arising from a close alignment of molecular orbitals with the Fermi energy of the electrodes and a high degree of electronic coupling between the molecule and the leads. Oligo(phenylene ethynylene)s (OPEs) with carbon termi-

nated anchor groups have recently been studied and proposed as the most promising class of molecules to be used as molecular wires.^{6,7} Transition metal complexes containing two metal centres connected by proper ligands have been shown, however, to exhibit a delocalised π -system over the entire molecular backbone,³⁹ with the additional benefit, that the metal centre d-states favor a close level alignment of the molecular eigenstates with the Fermi energy of the leads. In this context complexes with a $[\text{FeC}_4\text{Fe}]$ backbone have been studied regarding their suitability as molecular wires with a special emphasis on the anchor groups connected to the leads.

Migliore and Nitzan have recently proposed an explanation for hysteresis in single molecule I/V measurements based on the interplay of coherent tunnelling, defining the conductance, and electron hopping causing a time-delay or hysteresis in the I/V curves.^{40,41} The most important ingredient of this model is a localised state on the compound exhibiting a low degree of electronic coupling to the electrodes. Based on this model hysteresis effects found in mechanical break junction experiments performed by our collaborators in Zürich was analysed. In this work three transition metal complexes with a Fe, Ru and Mo-centre, respectively, have been studied regarding their electronic groundstate and switching properties, where an application of Migliore and Nitzan’s 2-channel scheme within the framework of DFT has been elaborated.

Structure of this thesis

Chapter 2 introduces density functional theory and its practical implementations.

Chapter 3 deals with the theoretical framework for the description of phase coherent electron transport in single molecule junctions.

Chapter 4 gives an overview of the mechanisms responsible for the energy level alignment and level broadening in single molecule junctions, as well as theoretical methods within DFT used for its evaluation.

Chapter 7 introduces the basic concepts of Marcus theory, which was the framework of our choice for the description of electron hopping.

Chapters 5, 6, 8, 9 and 10 give an overview of the papers included in this thesis, where the motivation for these studies, a detailed description of the theoretical methods applied, as well as a summary of the results are given.

Density functional theory

For the study of the electronic structure of atoms, molecules and condensed systems a quantum mechanical description is needed. Such a treatment requires the determination of the electronic eigenvalue spectrum from the application of the Hamilton operator in Schrödinger's equation. An exact solution of this problem is in general not known due to the correlation in the electronic interaction making approximate approaches necessary. Throughout this thesis density functional theory (DFT) has been applied for the solution of the electronic structure problem, whose basic concepts and practical aspects are presented in this section.

The chapter starts with a short outline of the history of DFT, followed by an introduction of Schrödinger's equation. Then the basic theorems of DFT and the practical scheme on the basis of the Kohn Sham equations, as well as the approximations applied for the exchange and correlation energies are described. Finally the projector augmented wave (PAW) method for the implementation of DFT used in this thesis is introduced, where also the application of a localised basis set and the Δ -Self consistent field method are outlined.

2.1 History of DFT

The basic concepts of density functional theory originate from a famous paper by Hohenberg and Kohn (HK) published in 1964.⁴² The fundamental hypothesis of their work was, that all ground state properties of an inhomogeneous electron gas in an external potential - in particular its ground state total energy - are uniquely defined by the ground state electron density. Following their proposition all ground state characteristics of a condensed matter system composed of N electrons, can be expressed by this electron density, which is a function dependent on one set of space coordinates and spin only. This is in contrast to other theories, which were exclusively used up to this point, where the basic quantity was the many body wave function, which is dependent on $4 \times N$ variables, namely the sets of space and a spin coordinates for each of the N electrons. This reasoning was not entirely new, since Thomas⁴³ and Fermi⁴⁴ (TF) proposed a similar concept already in 1927, although leaving out any description of many body electron interactions in their formalism. The basic assumption of TF was, that the kinetic energy is a functional of the electron density of non-interacting electrons in a homogeneous electron gas. In 1930 Paul Dirac added the exchange and correlation term to this theorem by formulating the local density approximation.⁴⁵ It has been shown, however, that the Thomas-Fermi-Dirac theory, which is based on a homogeneous electron gas model, was not accurate enough for useful predictions of properties in real systems in contrast to DFT.

HK's formulation alone, however, is not practicable for actual calculations because it does not provide a recipe for constructing the ground state electron density. One year after HK published their theory, Kohn and Sham⁴⁶ proposed a solution for this problem by including auxiliary single particle wavefunctions, so-called Kohn-Sham orbitals. The crucial idea of their framework is that the manybody problem can be projected onto a system of single particles, where the interaction between them enters through their common Hamiltonian. The Kohn-Sham equations are the basis of every practical DFT calculation up to the modern days.

2.2 Schrödinger's equation

In general, the Schrödinger equation in its stationary (non-relativistic) representation is an eigenvalue equation of the form

$$\hat{H}\Psi(\{\mathbf{r}_i\}, \{\mathbf{R}_\alpha\}) = E\Psi(\{\mathbf{r}_i\}, \{\mathbf{R}_\alpha\}) \quad (2.1)$$

with $\Psi(\{\mathbf{r}_i\}, \{\mathbf{R}_\alpha\})$ as the wave function of the system, which is dependent on the electronic coordinates $\mathbf{r}_i, i = 1, N$ (also including the spin degree of freedom) and the coordinates of the nuclei in the system $\mathbf{R}_\alpha, \alpha = 1, N_\alpha$. By applying the Born-Oppenheimer approximation the electronic and nuclear motion can be separated and equation (2.1) changes to

$$\hat{H}_{el}(\{\mathbf{r}_i\}, \{\mathbf{R}_\alpha\})\Psi_{el}(\{\mathbf{r}_i\}) = E_{el}\Psi_{el}(\{\mathbf{r}_i\}, \{\mathbf{R}_\alpha\}) \quad (2.2)$$

with the Hamilton operator,

$$\hat{H}_{el} = -\frac{\hbar}{2m_e} \sum_i \nabla_i^2 + \sum_i V_{ext}(\mathbf{r}) + \frac{1}{2} \sum_{i \neq j} \frac{e^2}{|\mathbf{r}_i - \mathbf{r}_j|}, \quad (2.3)$$

which is composed of the kinetic energy, the electron-nuclei Coulomb energy or external potential,

$$V_{ext}(\mathbf{r}) = - \sum_\alpha \frac{Z_\alpha}{r_{i\alpha}} \quad (2.4)$$

and the electron-electron interaction.

Following these definitions the total electronic energy is implicitly dependent on the spatial distribution of the nuclei in the system. Therefore the ground state energy $E_{el,0}$ refers always to the lowest energy for a specific distribution of atoms. In order to calculate the total energy of a system the Coulomb energy between the nuclei has to be added, leading to

$$E_0(\{\mathbf{R}_\alpha\}) = E_{el,0}(\{\mathbf{R}_\alpha\}) + \sum_{\alpha < \beta} \frac{Z_\alpha Z_\beta}{R_{\alpha\beta}} \quad (2.5)$$

as the ground state total energy of the given geometry.

2.3 Hohenberg-Kohn theorems

In principle the HK formalism is a description of an exact theory for many-body systems, with the electron density $n(\mathbf{r})$ as its basic quantity, which in this context is defined as

$$n(\mathbf{r}) = \int \dots \int d^3r_2 \dots d^3r_N |\Psi_{el}(\mathbf{r}_1, \dots, \mathbf{r}_N)|^2 \quad (2.6)$$

and has to obey the relation

$$\int n(\mathbf{r}) d^3r = N_{el}, \quad (2.7)$$

where N_{el} is the number of electrons in the system.

Two theorems form the pillars on which HK theory is based⁴² and are usually referred to as Hohenberg-Kohn-theorems:

- **Theorem I:** The external potential $V_{ext}(\mathbf{r})$ of a system is determined uniquely -except for a constant- by the ground state density $n_0(\mathbf{r})$. As a consequence, the respective Hamiltonian is fully defined -except for a constant energy shift- and with the Hamiltonian also the many-body wavefunction for the ground state is known.
- **Theorem II:** The ground state total energy $E[n]$ of a system with a particular $V_{ext}(\mathbf{r})$ is the global minimum of this functional with respect to $n(\mathbf{r}) = n_0$.

By making use of these two theorems the electronic energy-functional can be defined as a sum of the kinetic energy operator, the external potential (see equation (2.4)) and the so called exchange correlation functional E_{xc} . As a consequence the energy functional takes the form

$$\begin{aligned} E[n] &= T[n] + E_{xc} + \int d^3r n(\mathbf{r}) V_{ext}(\mathbf{r}) \\ &\equiv F_{HK}[n] + \int d^3r n(\mathbf{r}) V_{ext}(\mathbf{r}) \end{aligned} \quad (2.8)$$

with

$$F_{HK}[n] = T[n] + E_{xc} \quad (2.9)$$

as an universal functional $F_{HK}[n]$ including the kinetic energy and the exchange-correlation potential, where the latter will be further described in section 2.4.2. This functional is called universal for the electronic system, because of its sole dependency on the electronic density $n(\mathbf{r})$.

A minimisation of the energy functional with respect to $n(\mathbf{r})$ can now be performed, where the total charge has to be conserved in the integration of the density according to relation (2.7). By using the chemical potential μ as a Lagrange parameter one can formulate

$$\mu = \frac{\delta E[n]}{\delta n(\mathbf{r})} = V_{ext}(\mathbf{r}) + \frac{\delta F_{HK}[n]}{\delta n(\mathbf{r})}. \quad (2.10)$$

This formulation, although elegant, is still not sufficient for practical calculations. In the following section the crucial step towards a practical application of DFT namely the introduction of the Kohn-Sham equations is carried out.

2.4 Computational implementation of DFT

2.4.1 Kohn-Sham equations

As mentioned in the outline of this chapter Kohn and Sham (KS) expanded DFT in the year 1965 by reintroducing orbitals, i.e. projecting the interacting manybody system onto a independent-particle system, where these so called KS orbitals have to match the requirement to build up the real ground state density by summing up their individual contributions. Every modern DFT code solves the so called KS equations,

$$\hat{H}_{KS}\phi_i = \epsilon_i\phi_i \quad (2.11)$$

The Hamiltonian \hat{H}_{KS} in this definition is a sum of the single particle kinetic energy term T_S and the effective potential $v_{eff}(\mathbf{r})$, which are both acting on all individual electrons at the point \mathbf{r} (Note from now on atomic units will be used):

$$\hat{H}_{KS} = -\frac{1}{2} \nabla_i^2 + v_{eff}(\mathbf{r}) \quad (2.12)$$

$$= -\frac{1}{2} \nabla_i^2 + \int d\mathbf{r}' \frac{n(\mathbf{r}')}{|\mathbf{r} - \mathbf{r}'|} + v_{xc}(\mathbf{r}) + V_{ext}(\mathbf{r}). \quad (2.13)$$

2. Density functional theory

From this single electron formulation the kinetic energy term and the classical Coulomb interaction energy can be defined in analogy to Hartree-Fock theory:

$$T_s = -\frac{1}{2} \sum_{i=1}^N \langle \phi_i | \nabla^2 | \phi_i \rangle = -\frac{1}{2} \sum_{i=1}^N \int d^3r |\nabla \phi_i(\mathbf{r})|^2 \quad (2.14)$$

$$E_{Hartree}[n] = \frac{1}{2} \int d^3r \int d^3r' \frac{n(\mathbf{r})n(\mathbf{r}')}{|\mathbf{r} - \mathbf{r}'|} \quad (2.15)$$

with the electron density defined in HK theory:

$$n(\mathbf{r}) = \sum_i |\phi_i(\mathbf{r}, \sigma)|^2 \quad (2.16)$$

Applying these definition the electronic ground state energy $E_{KS,0}$ can now be rewritten in the Kohn-Sham approach as

$$E_{KS,0} = \sum_i^N \epsilon_i - E_{Hartree}[n] + E_{xc}[n] - \int \frac{\delta E_{xc}[n]}{\delta n(\mathbf{r})} n(\mathbf{r}) d\mathbf{r}, \quad (2.17)$$

where the double counting of the Hartree energy is corrected and the single particle exchange-correlation energy is cancelled. The many body interactions are captured in the exchange correlation energy $E_{xc}[n]$ in equation (2.17). One can interpret this term as the universal functional

$$E_{xc}[n] = F_{HK}[n] - (T_s[n] + E_{Hartree}[n]) \quad (2.18)$$

or

$$E_{xc}[n] = \langle \hat{T} \rangle - T_s[n] + \langle \hat{V}_{ee} \rangle - E_{Hartree}[n] \quad (2.19)$$

Analogous to HK theory the total ground state energy of a given system is calculated as a sum of the ground state electronic energy $E_{KS,0}$ and the nuclei-nuclei repulsion term.

$$E_0 = E_{KS,0} + E_{NN} \quad (2.20)$$

The ground state structure of the system can now be identified by a minimisation of the total energy term, with respect to the ion positions, and the volume and shape of the simulation cell.

2.4.2 Calculating the exchange-correlation energy

A crucial issue when solving the Kohn Sham equations is the approximation used for the exchange correlation functional $E_{xc}[n]$. If one would know this functional the exact ground state of a given system could be calculated solving the KS equations, but in praxis a few common approximation techniques have to be employed.

Due to the extraction of the one particle kinetic energy and the long range Hartree energy from the exchange-correlation functional, only local contributions enter $E_{xc}[n]$ in equation 2.19. This means it must be possible to also define the exchange-correlation energy by local or nearly local approximations and the functional can be rewritten as

$$E_{xc}[n] = \int d\mathbf{r} n(\mathbf{r}) v_{xc}([n], \mathbf{r}) \quad (2.21)$$

where $v_{xc}([n], \mathbf{r})$ is the respective single particle exchange-correlation potential term at any point \mathbf{r} , which only depends on the electronic density $n(\mathbf{r})$ around \mathbf{r} . For the sake of simplicity the spin densities are included in the $v_{xc}([n], \mathbf{r})$ in (2.21).

2.4.3 Exchange and correlation functionals

In principle the derivation of the KS equations given in the last section is complete. All complications related to the electronic manybody problem, i.e. exchange and correlation, are contained in the energy functional $E_{xc}[n^\uparrow, n^\downarrow]$ and its functional derivative $V_{xc}[n^\uparrow, n^\downarrow]$, where the spin-polarised notation has been used. In general these functionals are not known for realistic systems. Therefore approximations have to be introduced for their computation, whose quality determine the precision of a DFT calculation, which might have different consequences depending on the nature of the system and calculated quantity. The success of DFT shows that the common approximations are useful for the large range of problems, but improving on them is still a vivid field in the development of modern DFT based techniques.

Local spin density approximation

In order to arrive at an approximation for $E_{xc}[n^\uparrow, n^\downarrow]$ the exchange-correlation functional is often derived from expressions for the homogeneous electron gas. The most prominent example is the so called local spin density approximation (LSDA) where the densities n^\uparrow, n^\downarrow are calculated locally and $E_{xc}[n^\uparrow, n^\downarrow]$ is determined by applying the functional, which would be exact for the homogeneous electron gas, and which has the form

$$E_{xc}^{LSDA}[n^\uparrow, n^\downarrow] = \int d^3r n(\mathbf{r}) v_{xc}^{hom}(n^\uparrow(\mathbf{r}), n^\downarrow(\mathbf{r})). \quad (2.22)$$

In this expression $E_{xc}[n^\uparrow, n^\downarrow]$ is defined as an integral over exchange-correlation potentials per electron v_{xc}^{hom} as determined in a homogeneous electron gas, which can be further separated into two parts, namely, v_x^{hom} and v_c^{hom} describing the exchange (x) and correlation (c) contributions respectively. While v_x^{hom} can be determined analytically for any given value of the density, numerical parametrisations have to be performed for the correlation functional v_c^{hom} .

The striking advantage of the application of LSDA in any DFT code is its simplicity and remarkable efficiency. Even though using formulations for E_{xc} derived from the homogeneous electron gas might seem crude at first glance, this strategy has proven to work astonishingly well for a large number of systems. The accuracy provided by LSDA, however, decreases when the system under study deviates strongly from homogeneity. This occurs when localised states such as d-states of transition metals or surface states play an important role in the calculation, where binding energies are overestimated by the LSDA.

Generalised gradient approximation

The suggestion of an inclusion of the gradient of the density was already made by Kohn and Sham in their famous paper.⁴⁶ Herman et. al.⁴⁷ adopted this idea and expanded the LSDA by also including the second term in a Taylor expansion of $E_{xc}^{LSDA}[n^\uparrow, n^\downarrow]$ with respect to the electron density:

$$E_{xc}^{GGA}[n^\uparrow, n^\downarrow] = \int d^3r n(\mathbf{r}) \epsilon_{xc}(n^\uparrow, n^\downarrow, |\nabla n^\uparrow|, |\nabla n^\downarrow|) \quad (2.23)$$

The introduction of the density gradient, however, is not straightfor-

ward and therefore a variety of parametrisations exist in modern literature, where throughout this thesis the functional of Perdew, Burke and Ernzerhof (PBE)⁴⁸ has been applied.

The gradient term within the GGA corrects for the overbinding errors of LSDA, where for the famous example of the ground state of Fe LSDA wrongly predicts iron to be most stable in a nonmagnetic fcc-structure. In contrast GGA correctly predicts a ferromagnetic ground state with a bcc structure, which is also consistent with experimental findings. A better performance of GGA, however, is not found for every system where e.g. for heavy atoms such as the 5d-transition metals, an application of GGA leads to an overestimation of lattice spacings of about the same magnitude as LSDA is underestimating them.

2.4.4 The projector augmented wave method (PAW)

All DFT-calculations presented in this thesis were performed by applying the projector augmented wave method (PAW) implemented in the GPAW code^{49,50}.

The PAW formalism, first introduced by Blöchl,⁵¹ is a frozen-core method, where all-electron (AE) wavefunctions are reconstructed from pseudo (PS) wavefunctions after self-consistency of the electron density and the potential in the Hamiltonian have been achieved. It therefore resembles pseudopotential methods, while still addressing some of their shortcomings by preserving the nodal structure of orbitals, potential and density near the atomic cores.

The transformation operator T

The basic assumption of the PAW method is that the wavefunctions of a system can be divided into core states $\phi_i^{a,core}$ on the atoms a , whose shape is fixed to that of the isolated atoms and computationally less demanding smooth valence pseudo (PS) wavefunctions $\tilde{\Psi}_n(\mathbf{r})$, where the relation between them and the all electron (AE) wavefunctions $\Psi_n(\mathbf{r})$ is given by a linear transformation of the form

$$\Psi_n(\mathbf{r}) = T\tilde{\Psi}_n(\mathbf{r}), \quad (2.24)$$

with,

2. Density functional theory

$$T = (1 + \sum_a \sum_i (|\phi_i^a(\mathbf{r})\rangle - |\tilde{\phi}_i^a(\mathbf{r})\rangle)\langle\tilde{p}_i^a|). \quad (2.25)$$

T is composed of the identity plus contributions centred at each atom, which differ with the atom type and where $\phi_i^a(\mathbf{r})$ and $\tilde{\phi}_i^a(\mathbf{r})$ denote the AE and the smooth PS wavefunctions, which are returned to be equal outside atoms-centred augmentation spheres with a certain radius r_c^a and differ only at $r < r_c^a$. Additionally to the partial waves $\tilde{\phi}_i^a(\mathbf{r})$ so called projector functions $\tilde{p}_i^a(\mathbf{r})$ localised inside the augmentation sphere have to be chosen, allowing that every pseudo wave function $\tilde{\Psi}_n(\mathbf{r})$ can now be expressed in terms of $\tilde{\phi}_i^a(\mathbf{r})$ and $\tilde{p}_i^a(\mathbf{r})$.

In a practical calculation $\Psi_n(\mathbf{r})$ is never part of the self-consistent cycle, but it is derived at its end in order to obtain observables, which are dependent on the nodal structure of the core electronic states.

The Electron Density $n(\mathbf{r})$

In order to calculate the electron density with the PAW method in a first step the PS density outside the augmentation spheres can be calculated as

$$\tilde{n}(\mathbf{r}) = \sum_n f_n |\tilde{\Psi}_n(\mathbf{r})|^2 + \sum_a \tilde{n}_c^a(\mathbf{r}), \quad (2.26)$$

with f_n being the occupation numbers ranging from 0 to 2 for each Bloch band n , and $\tilde{n}_c^a(\mathbf{r})$ as a smooth atom centred core density, which has no physical meaning and will be removed in the end. The second step consists of correcting $\tilde{n}(\mathbf{r})$ by adding atom-centred density parts for the contribution of the core electrons:

From the atomic density matrix, consisting of

$$D_{i_1, i_2}^a = \sum_n \langle \tilde{\Psi}_n | \tilde{p}_{i_1}^a \rangle f_n \langle \tilde{p}_{i_2}^a | \tilde{\Psi}_n \rangle, \quad (2.27)$$

one can define the atom centred expansions of the AE and the PS densities as

$$n^a(\mathbf{r}) = \sum_{i_1, i_2} D_{i_1, i_2}^a \phi_{i_1}^a(\mathbf{r}) \phi_{i_2}^a(\mathbf{r}) + n_c^a(\mathbf{r}) \quad (2.28)$$

and

$$\tilde{n}^a(\mathbf{r}) = \sum_{i_1, i_2} D_{i_1, i_2}^a \tilde{\phi}_{i_1}^a(\mathbf{r}) \tilde{\phi}_{i_2}^a(\mathbf{r}) + \tilde{n}_c^a(\mathbf{r}), \quad (2.29)$$

respectively and finally the AE density as

$$n(\mathbf{r}) = \tilde{n}(\mathbf{r}) + \sum_a (n^a(\mathbf{r}) - \tilde{n}^a(\mathbf{r})). \quad (2.30)$$

The Total Energy E

Like for the wavefunctions and the electron density also the contributions to the total energy E are divided in those arising inside and outside the augmentation spheres, respectively,

$$E = \tilde{E} + \sum_a \Delta E^a \quad (2.31)$$

$$\begin{aligned} &= \tilde{E}_{kin} + \tilde{E}_{Hartree} + \tilde{E}_{xc} + \tilde{E}_{zero} \\ &+ \sum_a (\Delta E_{kin}^a + \Delta E_{Hartree}^a + \Delta E_{xc}^a + \Delta E_{zero}^a) \end{aligned} \quad (2.32)$$

where the first line of equation 2.32 contains the pseudo (valence) contributions and the sum in the second line those attributed to the core electrons at each atom a .

While the pseudo energy contributions can be calculated from the KS equations according section 2.4.1 by just replacing the AE quantities by their PS counterparts, the core related energies are calculated from expressions containing the differences between AE and PS densities.

Additionally a so called zero energy, defined as

$$\tilde{E}_{zero} = \int d^3r \tilde{n}(\mathbf{r}) \sum_a \bar{v}^a(\mathbf{r}) \quad (2.33)$$

$$\Delta E_{zero}^a = - \int d^3r \tilde{n}^a(\mathbf{r}) \sum_a \bar{v}^a(\mathbf{r}) \quad (2.34)$$

is added, which does not have a physical meaning, but does account for the incompleteness of partial waves and projectors by adding an arbitrary potential $\bar{v}^a(\mathbf{r})$ near the atomic cores, whose contribution to the total energy is set to be zero outside the augmentation sphere.^{49,50,52}

2.4.5 Localised basis sets in GPAW

A description of electron transport based on Non Equilibrium Greens functions (NEGF) needs a localised basis in order to distinguish between the leads and the scattering region in the transport Hamiltonian, as will be further illustrated in chapter 3. Common basis sets for this purpose are either linear combinations of atomic orbitals (LCAO) or starting from plane wave (PW) descriptions, with conversion into localised Wannier functions after convergence of the self consistent cycle.^{53,54} In the present thesis an LCAO basis was chosen for reasons of practicality. On one hand a LCAO basis set is computationally less demanding than a PW description and the Hamiltonian obtained from the DFT calculation can be imported into the NEGF routine without the need of any post-processing. On the other hand the accuracy provided by both basis sets is almost identical for electron transport calculations with gold leads and organic molecules in the scattering region, as shown by Strange et al.⁵⁵

The basic principles of the PAW formulation in GPAW, as outlined in section 2.4.4, also support the usage of a LCAO basis set.⁵⁶ As for every realisation of a LCAO basis the wave functions of the system are defined as a linear combination of well defined localised basis functions $|\Phi_\mu\rangle$, following

$$|\tilde{\Psi}_n\rangle = \sum_{\mu} c_{\mu n} |\Phi_\mu\rangle \quad (2.35)$$

where the coefficients $c_{\mu n}$ act as the variational parameters in order to minimise the total energy and $|\Phi_\mu\rangle$ in GPAW follow the definition by Sankey and Niklewski.⁵⁷ In a next step the density matrix, with

$$\rho_{\mu\nu} = \sum_n c_{\mu n} f_n c_{\nu n}^* \quad (2.36)$$

as its elements, can be defined, which can be used for the definition of the pseudo electron density

$$\tilde{n}(\mathbf{r}) = \sum_{\mu\nu} \Phi_\mu^*(\mathbf{r}) \Phi_\nu(\mathbf{r}) \rho_{\mu\nu} + \sum_a \tilde{n}_c^a(\mathbf{r}). \quad (2.37)$$

The elements of the Hamiltonian in matrix form used in an LCAO description can be defined by

$$H_{\mu\nu} = T_{\mu\nu} + V_{\mu\nu} + \sum_{aij} P_{i\mu}^{a*} \Delta H_{ij}^a P_{iv}^a, \quad (2.38)$$

where

$$T_{\mu\nu} = \langle \Phi_\mu | -\frac{1}{2} \nabla^2 | \Phi_\nu \rangle, \quad V_{\mu\nu} = \int \Phi_\mu^*(\mathbf{r}) \tilde{v}(\mathbf{r}) \Phi_\nu(\mathbf{r}) \quad (2.39)$$

and $P_{i\mu}^{a*} \Delta H_{ij}^a P_{iv}^a$ are the atomic contributions inside the augmentation spheres, with $P_{i\mu/v}^a = \langle \tilde{p}_i^a | \Phi_{\mu/v} \rangle$.

Finally the generalised eigenvalue problem can be written as

$$\sum_v H_{\mu\nu} c_{\nu n} = \sum_v S_{\mu\nu} c_{\nu n} \epsilon_n, \quad (2.40)$$

where

$$S_{\mu\nu} = \langle \Phi_\mu | \Phi_\nu \rangle + P_{i\mu}^{a*} \Delta S_{ij}^a P_{iv}^a \quad (2.41)$$

is the overlap matrix defined as the sum of the overlap in the basis functions and the contributions near the atomic cores. Equation 2.40 is solved for the coefficients $c_{\mu n}$ and the energies ϵ_n self-consistently in order to calculate the ground state energy of a given system.

2.5 The Delta self consistent field method

$\Delta\text{SCF}^{58,59}$ is a method similar to constrained DFT, which allows to define the occupation of particular electronic states of an atom, molecule, molecular fragment or solid as a constrained to the self consistent cycle. While constrained DFT makes use of a spatially defined potential to shift the electrons, generalised ΔSCF defines the state of interest $|\alpha\rangle$ by a linear combination of the other Kohn-Sham states in the system

$$|\alpha\rangle = \sum_n c_n |\Psi_n\rangle. \quad (2.42)$$

From this definition the contribution to the pseudo electron density can be written as

$$\Delta \tilde{n}_\alpha(\mathbf{r}) = \sum_{m,n} c_m^* c_n \tilde{\Psi}_m^*(\mathbf{r}) \tilde{\Psi}_n(\mathbf{r}). \quad (2.43)$$

2. Density functional theory

The electron, which is constrained to occupy $|\alpha\rangle$ is taken from the Fermi Level, and the total number of electrons in the system is reduced accordingly by one in order to ensure charge neutrality. Finally the single particle energy of $|\alpha\rangle$ is given as

$$\langle\alpha|\hat{H}|\alpha\rangle = \sum_{m,n} c_m^* c_n \langle\Psi_m|\hat{H}|\Psi_n\rangle = \sum_n |c_n|^2 \epsilon_n \quad (2.44)$$

Since the electronic structure is relaxed self consistently also the expansion coefficients of the defined orbital change in each iteration step.

In practical calculations with Δ SCF two possible methods on the basis of the PAW formalism can be applied:⁵⁰

- The All Electron method:

In this scheme the shape of the constrained orbital is defined starting from a gas phase calculation of the subsystem of interest. In a next step the gas phase orbital, corresponding to the state, which should be occupied or emptied in the whole system, is expanded as a linear combination of the Kohn Sham states of the whole system, following

$$c_n = \langle\Psi_n|\Psi_\alpha\rangle = \langle\tilde{\Psi}_n|\tilde{\Psi}_\alpha\rangle + \sum_{a,i,j} \langle\tilde{\Psi}_n|\tilde{p}_i^a\rangle \Delta S_{i,j}^a \langle\tilde{p}_j^a|\tilde{\Psi}_\alpha\rangle. \quad (2.45)$$

- The Pseudo-wavefunction method:

This method defines the constrained orbital by the use of the atomic orbitals, which leads to the possibility to define an orbital freely, by just regarding the quantum numbers (and therefore symmetry) and the involved atoms. The orbital is defined by specifying the basis functions which should build up the desired state. The next step is the same as in the AE routine, which means, that the state is expanded as a linear combination of the Kohn Sham states in the whole system.

Both methods have their advantages and drawbacks. The AEOrbitals scheme needs a gas phase calculation of the subsystem. As a consequence possible polarisation effects arising from the interaction of the subsystem with the rest of the atoms are not taken into account.

The Molecularorbitals scheme lacks accuracy if $|\alpha\rangle$ differs strongly from the atomic basis. This is a result of the approximative scheme used within

this method, where the overlap of the KS orbitals of the system with the atomic basis functions is calculated as

$$\langle \Psi_n | \Phi_i^a \rangle \approx \langle \tilde{\Psi}_n | \tilde{p}_i^a \rangle, \quad (2.46)$$

which neglects the overlap between atomic sites.

In this thesis both methods have been employed. The Pseudo-wavefunction method has been applied for constraining an additional electron on the Cl^- counterion, as it was done in Paper I,III and V in order to calculate the transmission functions of the charged molecule in a junction environment. In such a case the scheme is justified, since the constrained orbital is localised on a single atomic site only. For the manybody implementations of the calculation methods for the Transfer integral in Paper III, which will be presented in section 8.4, the AEOrbitals scheme has been applied, since the diabatic and adiabatic states, which are constrained regarding their occupancy, consist of KS orbitals delocalised over more than one atom.

Phase coherent electron transport

Progress in semiconductor research in the 1980s made it possible to create electronic components, which are so small in size that quantum effects could be investigated in electron transport experiments. Typical systems for such investigations were quantum dots⁶⁰ and quantum point contacts,⁶¹ which could be theoretically described as a two-dimensional electron gas and experimentally manipulated by gate electrodes. Since the size of such semiconductor structures is around $1\text{ }\mu\text{m}$, they are usually referred to as mesoscopic systems, meaning that they consist of a limited number of atoms, where the rules of classical physics gradually change to those of quantum mechanics in dependence on cross-section and length of homogeneous wires. In the last decade of the past century a profound theoretical description of such systems has been elaborated by Landauer.⁶²

In the following sections an approach elaborated by Landauer for metallic wires in the tunnelling regime will be used as a basis for a quantum mechanical description of electron transport. Starting from a single level tight binding formalism the most important quantities for this Ansatz will be introduced, followed by a generalisation to real systems, with a methodology on an *ab initio* level making use of Greens' function techniques. Finally practical schemes and algorithms will be described, which were applied for the calculations performed in this thesis.

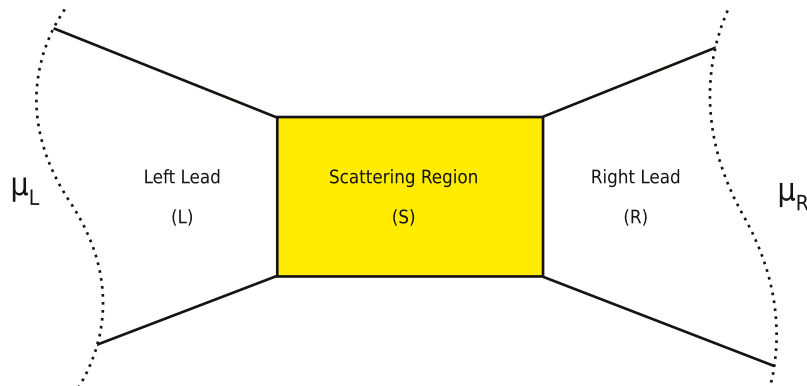


Figure 3.1: Schematic representation of a system in a description of electron transport through a scattering region (S) connected to thermal baths via a left (L) and a right (R) lead

3.1 Phenomenological introduction

Before starting with a detailed mathematical description of electron transport, let us ask the question: What is the underlying mechanism for the electron flow from one lead to the other in a molecular junction system? Let us therefore consider a sole infinitely large electrode. In equilibrium this bulk system has a well defined chemical potential μ_L (the index L marks the metal as the left electrode in order to be consistent with following sections), which is constant in time and does not experience any perturbation. If we now couple a scattering region S to a surface of this lead a Fermi Level equilibration, well known from thermodynamics, of the two sub-systems happens. This is achieved by a charge flow between the two parts of the system until the two chemical potentials match. Adding a second electrode, with μ_R , on the other side of the scattering region creates a total system consisting of three parts, as shown in figure 3.1, and just as in the two part system the electrons will flow until all three parts are balanced regarding their chemical potential. As a consequence of this scenario a system in equilibrium is created with a sole chemical potential, where no current flows by itself.

Now let's take this model further and add thermal baths, which will keep $\mu_{L/R}$ constant on a determined value. If as a first example we set the $\mu_L = \mu_R$, the system is in equilibrium and no net current can be measured. If we now change μ_L and μ_R into opposite directions, as it would happen for an applied voltage, the system will constantly try to equilibrate μ_L, μ_S and

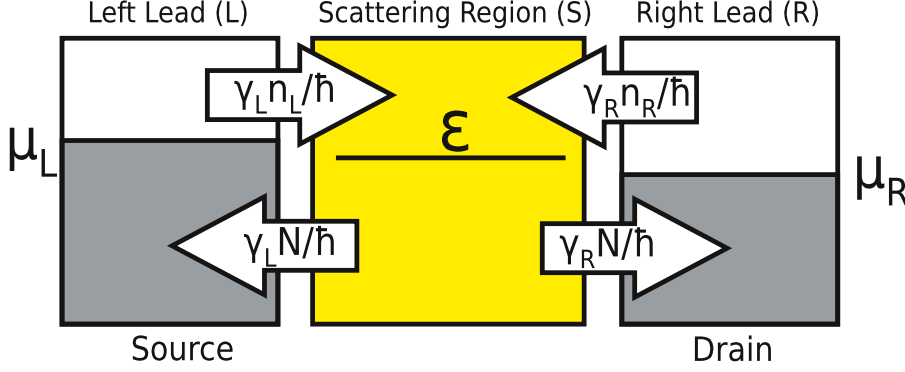


Figure 3.2: Schematic picture of the flux of electrons in a single level picture derived from rate equations.

μ_R by pumping electrons into S from the side with higher chemical potential and withdrawing electrons at the side with lower μ . Since we do not allow $\mu_{L/R}$ to change, due to our applied thermal baths, a steady-state current is created, which can be measured.⁶³

3.2 Electron transport through a single level

In order to derive the Landauer-Büttiker formula for the conductance it makes sense to start from a simple example, namely a single electronic level between two ideal electron reservoirs. As a starting point for that the net flux from and into the two electrodes is defined as

$$I_L(\epsilon) = (-q) \frac{\gamma_L}{\hbar} n_L(\epsilon) + q \frac{\gamma_L}{\hbar} N(\epsilon), \quad (3.1)$$

$$I_R(\epsilon) = (-q) \frac{\gamma_R}{\hbar} n_R(\epsilon) + q \frac{\gamma_R}{\hbar} N(\epsilon), \quad (3.2)$$

where the first term in both equations describes the flow of electrons from the respective electrode into the molecule and the second term describes the flow in the opposite direction, as illustrated in figure 3.2. In this equation $-q$ is the charge of an electron and $\frac{\gamma}{\hbar}$ is the rate constant. It is apparent from equations 3.1 and 3.2 that the flux is proportional to the difference of occupation of the molecular eigenstate $N(\epsilon)$ and the occupation in the lead represented by the Fermi Dirac distributions $n_{L/R}(\epsilon)$. For a steady state situation no net flux is present and $I_L + I_R = 0$. By solving the equations 3.1

3. Phase coherent electron transport

and 3.2 for $N(\epsilon)$ one can simply derive

$$N(\epsilon) = \frac{\gamma_L n_L(\epsilon) + \gamma_R n_R(\epsilon)}{\gamma_L + \gamma_R}. \quad (3.3)$$

and obtain the steady state current

$$I = I_1 = -I_2 = \frac{2q}{\hbar} \frac{\gamma_L \gamma_R}{\gamma_R + \gamma_L} [n_L(\epsilon) - n_R(\epsilon)], \quad (3.4)$$

where a factor of two is added to account for the different spins.

Equation 3.4 does already provide a lot of insight. The two most important findings from this equation are the facts that no current flows, when the Fermi levels coincide or ϵ is outside the gap between μ_L and μ_R .

Now the level broadening of the molecular level D_ϵ is introduced, which is a consequence of its coupling to the continuous density of states of the leads. Commonly the broadening function used for this purpose is a Lorentzian distribution centred at ϵ of the form

$$D_\epsilon(E) = \frac{\gamma/2\pi}{(E - \epsilon)^2 + (\gamma/2)^2}, \quad (3.5)$$

with $\gamma = \gamma_L + \gamma_R$. Considering the broadening of the molecular level equation 3.4 changes to

$$I = \frac{2q}{\hbar} \int_{-\infty}^{\infty} D_\epsilon(E) \frac{\gamma_L \gamma_R}{\gamma_R + \gamma_L} [n_L(\epsilon) - n_R(\epsilon)] dE, \quad (3.6)$$

with an integration over the energy space in order to account for the full molecular level. Assuming low temperatures, where $n_L(\epsilon) - n_R(\epsilon)$ is 1 in the energy range between μ_L and μ_R and 0 everywhere else, equation 3.6 can be simplified to

$$I = \frac{2q}{\hbar} \int_{\mu_2}^{\mu_1} D_\epsilon(E) \frac{\gamma_L \gamma_R}{\gamma_R + \gamma_L} dE = \frac{2q}{\hbar} \int_{\mu_2}^{\mu_1} T(E) dE. \quad (3.7)$$

In equation 3.7 the transmission function $T(E)$ has been introduced defined by

$$T(E) = 2\pi D_\epsilon(E) \frac{\gamma_L \gamma_R}{\gamma_R + \gamma_L} = \frac{\gamma_L \gamma_R}{(E - \epsilon)^2 + (\gamma_L + \gamma_R)^2/4}. \quad (3.8)$$

The electron occupation of the single level $N(\epsilon)$, given in equation 3.3, now results from an integration over the energy space. For that the energy

3.2. Electron transport through a single level

dependent electron density within the scattering region is introduced

$$n_\epsilon(E) = D_\epsilon(E) \frac{\gamma_L n_L(E - \mu_L) + \gamma_R n_R(E - \mu_R)}{\gamma_L + \gamma_R}, \quad (3.9)$$

where the electron occupation of the single level is determined by

$$N = \int_{-\infty}^{\infty} dE n_\epsilon(E). \quad (3.10)$$

As an interesting side effect of this derivation one can now also determine the maximum of conductance a single channel can provide, namely the conductance quantum G_0 . For that purpose equation 3.7 is rewritten at an infinitesimal small applied voltage, where it can be assumed that $T(E)$ is constant for potentials between μ_L and μ_R :

$$I = \frac{q}{h} [\mu_L - \mu_R] T = \frac{2q}{h} [\mu_L - \mu_R] \frac{\gamma_L \gamma_R}{(\mu - \epsilon)^2 + ((\gamma_L + \gamma_R)/2)^2} \quad (3.11)$$

In order to find the maximum in conductance from this formula $\mu = (\mu_L + \mu_R)/2$ is set equal to ϵ , creating a situation, where the molecular level lies in the middle of the window created by the two chemical potentials. Then the conductance is calculated applying Ohms law applying the substitution $\mu_1 - \mu_2 = qV$, with V as the applied bias, as

$$G \equiv \frac{I}{V} = \frac{2q^2}{h} \frac{4\gamma_L \gamma_R}{(\gamma_L + \gamma_R)^2}. \quad (3.12)$$

This equation maximises, when $\gamma_L = \gamma_R$ resulting in a value of $G_0 = \frac{2q^2}{h} \approx 77.5 \mu S$.

In order to build a bridge to a theoretical description of real systems the notation is now changed slightly by introducing the Green's function

$$G(E) = \frac{1}{E - \epsilon + (i\gamma/2)}. \quad (3.13)$$

As a consequence to this change in notation the quantities defined in equation 3.5 and 3.9 now become:

$$2\pi D_\epsilon(E) = G(E) \gamma G^*(E) = i(G - G^*) \quad (3.14)$$

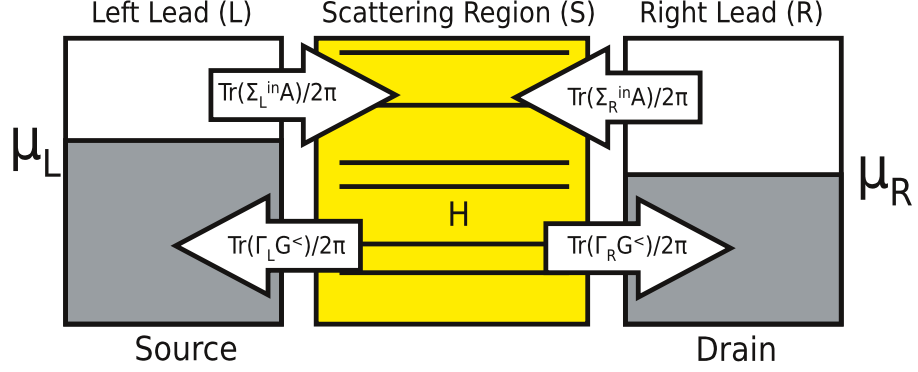


Figure 3.3: Schematic picture of the flux of electrons into and from a scattering region in a matrix representation.

$$2\pi n_\epsilon(E) = G(E)(\gamma_L n_L + \gamma_R n_R)G^*(E) \quad (3.15)$$

Additionally, one can now introduce the so called in-scattering function $\gamma_{L/R}^{in} = \gamma_{L/R} n_{L/R}$, which is responsible for the contact resistance for the transition from an electrode into the device and the out-scattering function $\gamma_{L/R}^{out} = \gamma_{L/R}(1 - n_{L/R})$, characterising the transition from the device to the electrodes. Applying these new definitions equation 3.6 can now be rewritten in the form

$$I_{L/R} = \frac{2q}{h} \int_{-\infty}^{\infty} dE \gamma_{L/R}^{in} D_\epsilon(E) - \gamma_{L/R} n(E), \quad (3.16)$$

with $\gamma_{L/R} = \gamma_{L/R}^{in} + \gamma_{L/R}^{out}$ and $\frac{2q}{h} \int_{-\infty}^{\infty} dE \gamma_{L/R}^{in} D_\epsilon(E)$ and $-\frac{2q}{h} \int_{-\infty}^{\infty} dE \gamma_{L/R} n(E)$ in this equation describing the in- and outflow of electrons, respectively.

3.3 The Landauer Büttiker formalism

In this section the picture introduced so far will be expanded in order to arrive at a description of a realistic system and to derive the Landauer-Büttiker formula. The generalisation is straightforward by substituting the scalar quantities introduced in the last section by matrices.⁶³

$\epsilon \implies$	\mathbf{H}	<i>Hamiltonian</i>
$\gamma_{L/R} \implies$	$\mathbf{\Gamma}_{L/R}$	<i>Broadening matrix/coupling</i>
$2\pi D(E) \implies$	$\mathbf{A}(E)$	<i>Spectral function</i>
$2\pi n(E) \implies$	$-i\mathbf{G}^<(E)$	<i>Lesser Green's function (Correlation function)</i>
$\gamma_{L/R}^{in} \implies$	$-i\mathbf{\Sigma}^<(E)$	<i>Lesser self energy</i>
$\gamma_{L/R}^{out} \implies$	$i\mathbf{\Sigma}^>(E)$	<i>Greater self energy</i>

After performing this transformation the definitions introduced for the single level model have to be rewritten, starting from the most crucial quantity, namely the current. The definition of $I_{L/R}$ in the matrix formulation keeps its basic form as an integration over energy space as shown in equation 3.16, but with the inflow of electrons changed into $-i\mathbf{\Sigma}^<(E)\mathbf{A}(E)$ and the outflow into $-i\mathbf{\Gamma}_{L/R}\mathbf{G}^<(E)$:

$$I_{L/R} = \frac{2qi}{h} \int_{-\infty}^{\infty} dE \text{Tr}(\mathbf{\Gamma}_{L/R}\mathbf{G}^<(E)) - \text{Tr}(\mathbf{\Sigma}_{L/R}^<(E)\mathbf{A}(E)). \quad (3.17)$$

After transformation of the definition of the broadening function $D_{\epsilon}(E)$ given in equation 3.14 into the spectral function,

$$\mathbf{A}(E) = \mathbf{G}(E)\mathbf{\Gamma}_R\mathbf{G}^{\dagger}(E) + \mathbf{G}(E)\mathbf{\Gamma}_L\mathbf{G}^{\dagger}(E) \quad (3.18)$$

and the definition of the electron density given in equation 3.15 into the lesser Green's function, leading to the Keldish equations,⁶⁴

$$\begin{aligned} \mathbf{G}^<(E) &= i\mathbf{G}(E)[n_L(E)\mathbf{\Gamma}_L + n_R(E)\mathbf{\Gamma}_R]\mathbf{G}^{\dagger}(E) \\ &= \mathbf{G}(E)\mathbf{\Sigma}^<(E)\mathbf{G}^{\dagger}(E), \end{aligned} \quad (3.19)$$

the current at the left electrode can be reformulated as

$$\begin{aligned}
I_L &= \frac{2q}{h} \int_{-\infty}^{\infty} dE \operatorname{Tr}(-\mathbf{\Gamma}_L \mathbf{G}(E)(n_L(E)\mathbf{\Gamma}_L + n_R(E)\mathbf{\Gamma}_R)\mathbf{G}^\dagger(E) \\
&\quad - i\mathbf{\Sigma}_L^<(E)(\mathbf{G}(E)\mathbf{\Gamma}_R\mathbf{G}^\dagger(E)) + \mathbf{G}(E)\mathbf{\Gamma}_L\mathbf{G}^\dagger(E))) \\
&= \frac{2q}{h} \int_{-\infty}^{\infty} dE (n_L(E) - n_R(E)) \operatorname{Tr}(\mathbf{\Gamma}_L \mathbf{G}(E)\mathbf{\Gamma}_R \mathbf{G}^\dagger(E)), \quad (3.20)
\end{aligned}$$

where the substitution $-i\mathbf{\Sigma}_L^< = \mathbf{\Gamma}_L n_L(E)$ was applied according to equation 3.19. The total current through the device for a steady state (replacing equation 3.4) can now be written as

$$I = I_L = -I_R = \frac{2q}{h} \int_{-\infty}^{\infty} dE \operatorname{Tr}(\mathbf{\Gamma}_L \mathbf{G}(E)\mathbf{\Gamma}_R \mathbf{G}^\dagger(E))(n_L - n_R) \quad (3.21)$$

$$= \frac{2q}{h} \int_{-\infty}^{\infty} dE T(E)(n_L - n_R). \quad (3.22)$$

This derivation finally leads to the definition of the transmission function $T(E) = \operatorname{Tr}(\mathbf{\Gamma}_L \mathbf{G}(E)\mathbf{\Gamma}_R \mathbf{G}^\dagger(E))$ within the Landauer-Büttiker formalism.^{65,66} These results were originally obtained from a time dependent Ansatz by Meir and Wingreen,⁶⁷ where a different road was followed starting from the fully interacting many body Hamiltonian including all interactions.

3.4 Conductance calculations for real systems

In this section a combination of the general transport formalism, introduced in section 3.3, with the Kohn Sham single electron description within DFT will be elaborated in order to achieve a description of phase-coherent electron transport on an *ab initio* level. A wide range of numerical methods have been proposed for this purpose, where all of them are based on the Landauer-Büttiker setup. Two different schemes are commonly used for the computation, where the first directly calculates the scattering wave function^{68,69} and the second applies a single particle Green's function theory,^{55,70-73} which was also the method of choice for the codes used in the present thesis. Independent from the applied method for the transport setup one can choose between different levels of approximation for the electronic structure ranging from tight binding models⁷⁴ to full DFT calculations.^{75,76}

3.4.1 DFT based electron transport

The basic assumption in the formalism of Landauer and Büttiker is that in the phase coherent regime electrons are quasi particles, which do not interact and have a life time longer than the time needed to travel through the scattering region. As a consequence the Hamiltonian of the system can be approximated as a single-particle matrix derived from a Kohn Sham formulation of DFT. It should be noted at this point that the Kohn Sham Hamiltonian leads to the correct electron density with a good approximation of V_{xc} , but does not lead to a quantitatively correct current,⁷⁷ due to the lack of many body interactions. In order to achieve a higher level of accuracy one might have to employ time dependent DFT⁷⁸ or expand the NEGF formalism within many body perturbation theory as it is the case in GW models.^{79–81} Both of these pathways are, however, only practicable for small molecular systems and have proven to be unsuitable for the large junctions investigated in this thesis. Therefore Hamiltonians on a Kohn-Sham level have been used exclusively assuming that their accuracy is sufficient for a correct description of the studied phenomena.

The division of the junction into the left and right leads and the scattering region requires a localised basis set for the NEGF-DFT formalism to be applicable. This can be achieved for instance by constructing Wannier functions from a plane wave basis⁵⁴ or by using wavelets.⁸² In the present thesis the calculations have been performed with a LCAO basis set, as introduced in section 2.4.5, which is already atom centred by definition making it ideal for an application within NEGF-DFT.

3.4.2 The Transport Hamiltonian

Within a localised basis set the Hamiltonian of the full system, consisting of the electrodes L and R and the scattering region S can be divided into its three parts. The Schrödinger equation of the whole problem now takes the form

$$\begin{pmatrix} H_L & \tau_{LS} & 0 \\ \tau_{LS}^\dagger & H_S & \tau_{RS}^\dagger \\ 0 & \tau_{RS} & H_R \end{pmatrix} \begin{pmatrix} |\Psi_L\rangle \\ |\Psi_S\rangle \\ |\Psi_R\rangle \end{pmatrix} = E \begin{pmatrix} |\Psi_L\rangle \\ |\Psi_S\rangle \\ |\Psi_R\rangle \end{pmatrix}, \quad (3.23)$$

where the non-diagonal elements $\tau_{\alpha,\beta}$ are the couplings between the scat-

3. Phase coherent electron transport

tering region and the leads and therefore define the probability of an incoming wave to be transmitted or reflected. The interaction between the two leads is set to zero, because, as will be described later on, some surface layers of the electrodes are included in the scattering region.

Here the Green's function is defined as

$$(E - \mathbf{H}) \mathbf{G}(E) = \mathbf{I}, \quad (3.24)$$

with \mathbf{I} being the identity matrix. For the sake of simplicity corrections for a non-orthogonal basis, which would include the overlap matrix \mathbf{S} , and the imaginary part are not included in equation 3.24. Such a (more general) definition would change equation 3.24 into $((E + i\nu)\mathbf{S} - \mathbf{H})\mathbf{G}(E) = \mathbf{I}$, with ν being an infinitesimal number. We will, however, come to this generalisation later in this section.

Due to its non-interacting single particle definition equation 3.24 can also be converted to the matrix equation

$$\begin{pmatrix} E - H_L & -\tau_{LS} & 0 \\ -\tau_{LS}^\dagger & E - H_S & -\tau_{RS}^\dagger \\ 0 & -\tau_{RS} & -H_R \end{pmatrix} \begin{pmatrix} G_L & G_{LS} & G_{LR} \\ G_{SL} & G_S & G_{SR} \\ G_{RL} & G_{RS} & G_R \end{pmatrix} = \begin{pmatrix} I & 0 & 0 \\ 0 & I & 0 \\ 0 & 0 & I \end{pmatrix}. \quad (3.25)$$

From this system of equations one can easily derive the Green's function of the scattering region \mathbf{G}_S (also referred to as the retarded Greens function \mathbf{G}_S^r) by retrieving the three equations involving the second column of the Green's function matrix and solving it for \mathbf{G}_S :

$$\begin{aligned}
 (E - H_L)G_{LS} - \tau_{LS}G_S &= 0 \\
 -\tau_{LS}^\dagger G_{LS} + (E - H_S)G_S - \tau_{RS}^\dagger G_{RS} &= I \\
 (E - H_R)G_{RS} - \tau_{RS}G_S &= 0
 \end{aligned}$$

$$\begin{aligned}
 \Rightarrow G_{LS} &= g_L \tau_{LS} G_S & \text{with} & \quad g_L = (E - H_L)^{-1} \\
 \Rightarrow G_{RS} &= g_R \tau_{RS} G_S & \text{with} & \quad g_R = (E - H_R)^{-1}
 \end{aligned}$$

$$\begin{aligned}
 \Rightarrow -\tau_{LS}^\dagger g_L \tau_{LS} G_S + (E - H_S)G_S - \tau_{RS}^\dagger g_R \tau_{RS} G_S &= I \\
 \Rightarrow G_S &= (E - H_S - \Sigma_L - \Sigma_R)^{-1},
 \end{aligned} \tag{3.26}$$

where $\Sigma_{L/R} = \tau_{L/R}^\dagger g_{L/R} \tau_{L/R}$ are the (retarded) lead self energies, which can be interpreted as the effect of the leads on the isolated scattering region Hamiltonian upon contact creation.

Let us now define the three most important quantities, which will be needed in the following, in a general way:

$$\mathbf{G}_S = ((E - i\nu)\mathbf{S}_S - \mathbf{H}_S - \Sigma_L(E) - \Sigma_R(E))^{-1}, \tag{3.27}$$

$$\Sigma_\alpha(E) = ((E - i\nu)\mathbf{S}_{\alpha S} - \tau_{\alpha S})g_\alpha^0(E)((E - i\nu)\mathbf{S}_{\alpha S}^\dagger - \tau_{\alpha S}^\dagger), \tag{3.28}$$

$$\mathbf{g}_\alpha^0(E) = ((E - i\nu)\mathbf{S}_\alpha - \mathbf{H}_\alpha)^{-1} \tag{3.29}$$

where $\alpha \in \{L, R\}$. From these three definitions Xue, Datta and Ratner⁸³ showed that the conductance formula derived in section 3.3 is valid for non-orthogonal basis sets as they are used, when ultra-soft pseudo potentials are applied in the DFT calculations.

Starting from these three equations the calculation of the transmission function $T(E) = \text{Tr}(\Gamma_L \mathbf{G}_S(E) \Gamma_R \mathbf{G}_S^\dagger(E))$ is straightforward by applying the definition of $\Gamma_{L/R}$ as the anti Hermitian of the lead self energies $\Sigma_\alpha(E)$

$$\Gamma_\alpha(E) = i(\Sigma_\alpha - \Sigma_\alpha^\dagger). \tag{3.30}$$

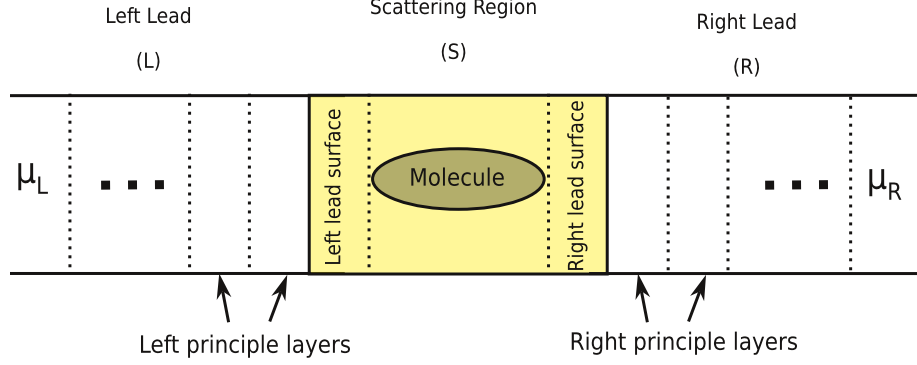


Figure 3.4: Schematic representation of the splitting in the transport Hamiltonian. The whole system is divided into three parts, namely left lead (L), right lead (R) and the scattering region (S), as already shown in figure 3.1. When it comes to a practical calculation the leads are divided in so called principle layers in order to be able to deal with the infinite size. To justify such a treatment of the lead Hamiltonians the scattering region has to contain a few electrode layers in order to achieve a bulk potential at the border to the leads.

3.4.3 Calculation of the lead self energies

Since the definition of the self energy in equation 3.28 contains the Green's function of the unperturbed or in other words uncoupled infinitely large electrode $g_{\alpha}^0(E)$, a special scheme has to be applied in order for it to represent the correct potential for semi-infinite leads in the transport direction. Due to their periodicity both lead Hamiltonians \mathbf{H}_{α} can be divided into regions in the transport direction, whose size is chosen in order to guarantee that only neighbouring sub-matrices interact (see figure 3.4). Such a division of the (in principle) infinitely large lead Hamiltonian is justified if the periodicity of the lead potential is preserved inside of the boundaries of the scattering region. For obtaining a system, where this condition is fulfilled, one usually defines the scattering region as a molecule with a few layers of the electrodes attached (also called the "extended molecule"), as depicted in figure 3.5. The electrode layers included in the scattering region now contain screening effects and all perturbations arising from the presence of the surfaces or molecule and the potential in the electrode surfaces reaches its bulk potential. This is due to the periodicity of the DFT calculations for

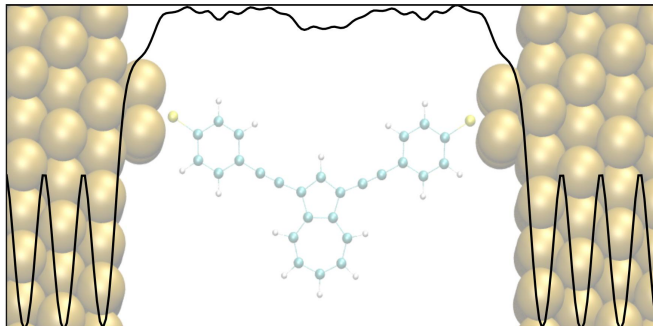


Figure 3.5: Typical setup of a scattering region in a NEGF-DFT transport calculation, where the electron potential in transport direction is drawn on top of the structure in order to show its rapid decay into the bulk potential after a few surface layers.

the scattering region also in the transport direction, its boundaries, visible in figure 3.5, touch the ones of neighbouring cells and therefore become bulk like.

The elegance of this approach is the replacement of the infinitely large electrodes by principle layers, which is possible because the scattering region only interacts with the first principle layer attached to it on both sides. Therefore the size of the Hamiltonian in equation 3.29 is drastically reduced and the calculation of the self energy becomes practicable.

3.4.4 k-point dependence

This section is dedicated to the treatment of periodic boundary conditions (pbc) in the space directions perpendicular to the transport direction. While the boundaries in the transport direction are defined by a matching of the potential in the extended molecule with the potentials of the principle layers of the leads, the dimensions of all electrode layers are infinite with regard to the transverse directions. In principle one also simulates an array of molecules by the introduction of periodic boundary conditions in the transverse direction, where the density and interaction of the molecules is dependent on the unit cell size in the DFT calculation of the scattering region, which might be inappropriate for a description of the single molecule conductance. One usually solves this issue by increasing the size of the unit cell in the transverse directions in order to avoid any interaction of the molecule with its images in neighbouring cells.

3. Phase coherent electron transport

Since the simulation cells for all three regions are periodic for the two lattice vectors perpendicular to the transport direction and the bulk electrodes require pbc in order to extend their electronic bands in \mathbf{k} -space the total transmission function can be decomposed into contributions arising a set of single k_{\perp} -points in the corresponding part of the Brillouin zone. The total transmission function can then be calculated as an integral over this two dimensional Brillouin zone

$$T(E) = \int d\mathbf{k}_{\perp} \frac{T(\mathbf{k}_{\perp}, E)}{A_{BZ}}, \quad (3.31)$$

where A_{BZ} is its area. In practice this integration is approximated by a sum $T(E) \approx \sum w_{\mathbf{k}_{\perp}} T(\mathbf{k}_{\perp})$, where $w_{\mathbf{k}_{\perp}}$ are weighting factors, whose sum is normalised to one.

Energy level alignment and electronic coupling

This chapter focuses on energy level alignment (ELA) and the electron coupling at the metal-molecule interface, which are the two main parameters determining the conductance of a molecule in a junction. The energetic ordering of the molecular eigenstates relative to the metal work function is one of the main topics in the investigation of adsorbed organic molecules on metal substrates for self assembled monolayers (SAM) as well as single molecule junctions. The main issue in these studies is the change of the electron affinity (EA) and ionisation potential (IP) of an adsorbed organic compound with respect to the molecule in vacuum, since this defines charge injection barriers and onset voltages in STM and mechanical break-junction experiments.

In order to arrive at a picture of energy level alignment and electron coupling this chapter is organised in the following way: After a short phenomenological introduction the concept of level broadening due to the adsorption of a molecule at a metal surface is presented, followed by an outline of the reasons for the shift in the energy of the molecular eigenstates with respect to the vacuum and electrode Fermi level. Finally tools for the evaluation and analysis of ELA within DFT are presented.

4.1 Phenomenological introduction

In order to motivate a physical picture of a molecule aligned in a single molecule junction environment, the starting point of this chapter consists of some phenomenological remarks similar to those in chapter 3. For this purpose it makes sense to start from the bare metal surface and a molecule situated at an infinite distance. In such a situation the metal electrode has a well defined Fermi level E_F (or chemical potential μ) and an undisturbed work function Φ_0 , which is defined as the energy needed to extract an electron from the surface into the vacuum. The molecule on the other hand is characterised by discrete electronic eigenstates, as depicted in panel a of Figure 4.1. When the molecule now approaches the surface different effects occur, which will be the main topic of the following sections. In this introduction, however, the focus is on the aspect that the molecular eigenstates start to broaden, as schematically shown in panel (b) of Figure 4.1. This broadening of the MOs transforms the discrete eigenvalue spectrum of a free molecule into a finite DOS, which is usually referred to as a projected density of states (pDOS), since it is a projection of the full DOS of the junction system onto the molecular subspace. The creation of a pDOS now also implies that one can define a Fermi Level of the molecule $E_{F,mol}$ (also called charge neutrality level CNL). Since a system in equilibrium can only have a single Fermi Level, the $E_{F,L}$ (L marks the metal as the left electrode) and $E_{F,mol}$ have to equilibrate.⁸⁴ This can happen either by charge reorganisation at the metal-molecule interface or by a partial emptying or filling of the molecular HOMO or LUMO, respectively, resulting in an alignment of the broadened eigenstates of the molecule with respect to μ_L . Different mechanisms have been proposed for the energy level alignment, which will be compared in the following section.

It has to be noted, that in addition to a shift of the molecular eigenenergies with respect to the vacuum level alignment of the free molecule also the HOMO-LUMO gap is reduced as a consequence of surface polarisation,^{85–87} an effect commonly referred to as screening. This effect, however, is not captured correctly in single particle descriptions based on DFT and would rather demand for many body corrections as they are included in e.g. GW approximations.^{88–90} There is, however, some degree of error-compensation with the underestimation of the HOMO-LUMO gap for the free molecule,

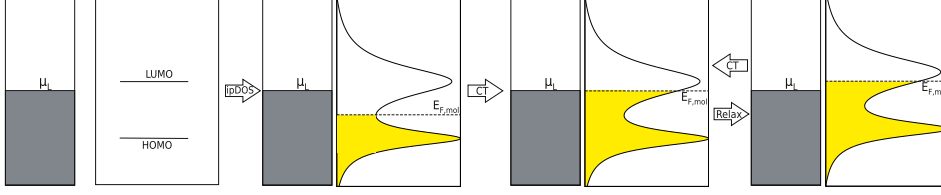


Figure 4.1: Schematic representation of the level broadening and energy level alignment upon adsorption of a molecule (right rectangle in each panel) onto a metal surface (left rectangle in each panel), where four situation are depicted, namely metal and molecule at infinite distance (a), level broadening upon contact (b) and energy level equilibration in combination with charge transfer (c and d). The yellow colour in panel b,c and d represents an occupation of the broadened molecular eigenstates

which is why this issue is not central to the results presented in this thesis.

4.2 Induced projected density of states

As already mentioned in chapter 3 the adsorption or coupling of a molecule on a metal surface leads to a broadening of the molecular eigenlevels. The degree of broadening is related to the wavefunction overlap with the metallic DOS of the electrodes and is directly proportional to the square of the non-diagonal matrix elements in the transport Hamiltonian defined in equation 3.23. In the Landauer-Büttiker formalism the coupling enters via the broadening matrix $\mathbf{\Gamma}$, defined as the imaginary part of the lead self energy $\mathbf{\Sigma}$, as shown in equation 3.30. Having determined the degree of broadening related to the electronic coupling of all eigenstates in the scattering region and the leads one can now determine a density of states of the molecular subspace by combining the $\mathbf{\Gamma}$ with the energetic position of the molecular levels. This is exactly what is done in the spectral function $\mathbf{A}(E)$ as it is defined in equation 3.18. The diagonal elements A_{ii} of the spectral function represent the contribution of the specific basis function i to the total DOS and as a consequence the projected density of states on the molecule can be defined as⁹¹

$$pDOS(E) = Tr(\mathbf{A}_{mol})(E), \quad (4.1)$$

with \mathbf{A}_{mol} being a sub-matrix of \mathbf{A} , containing only the molecular sub-

space.

This definition of a pDOS now allows for the determination of a well defined Fermi energy of the molecular subspace $E_{F,mol}$ (also referred to as the charge neutrality level (CNL)⁹² in the organic electronics and the organic semiconductor community), by integration up the number of electrons in the molecule:

$$\int_{-\infty}^{E_{F,mol}} dE \text{ pDOS}(E) = N \quad (4.2)$$

For a system to equilibrate the Fermi level of the metal electrodes and the molecule coupled to it, a partial charge transfer has to occur, where the mechanisms suitable for its description are highly dependent on the nature of the adsorption. Two typical examples for such mechanisms will be presented in the following.

4.3 Mechanisms for the energy level alignment

In this section the most representative models for the explanation and quantitative description of energy level alignment (ELA) are presented. Some of these models come from the organic electronics community, where organic bulk materials are adsorbed onto a metal substrate rather than single molecules, which suggests that some of them are not applicable for the description of ELA in single molecule electronics. The understanding of organic electronics, however, has matured more than the rather new field of single molecule electronics and therefore its elaborated models are also a useful starting point for the understanding of ELA in single molecule electronics.

4.3.1 Pauli repulsion

At a bare metal surface electrons spill out into vacuum thereby creating an intrinsic surface dipole. This fact was already discussed by Lang and Kohn in 1970, who applied a jellium model for the metal electronic density within a LDA approximation in DFT.⁹³ This surface dipole is strongly dependent on the nature of the metal substrate and is one of the main contributors to its work function Φ_0 . When a closed shell molecule is now adsorbed onto the metal surface, the electrons of the metal, which reach out into

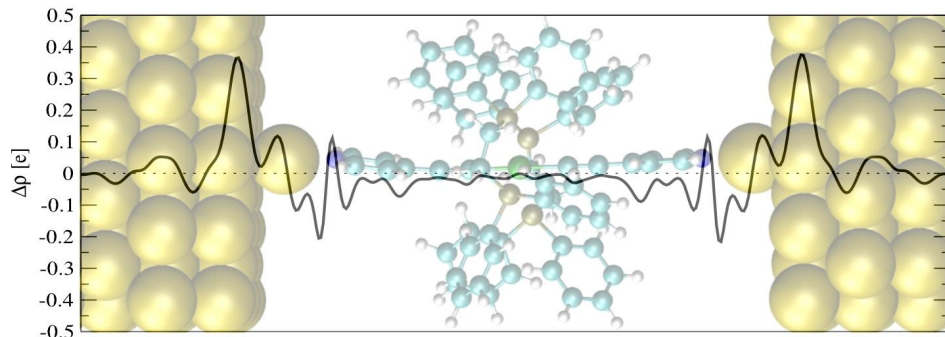


Figure 4.2: Electron density change defined as the difference between the coupled metal-molecule system and the two isolated systems, as derived from the Ru-complex, which was the system under study in Paper I. While the electron density changes only marginally in the centre of the molecule, the part near the interface shows the characteristic features of Pauli repulsion.

vacuum are pushed back into the bulk. The physical reason for this so called "pillow effect" is Pauli repulsion arising from an overlap of the electronic wave functions of an adsorbed closed shell molecule with those of the metal surface.⁹⁴ Due to the orthogonality constraint for all Kohn-Sham orbitals in the system, the metal electron wave functions, which spill out into the vacuum, are now distorted⁹⁵ in order to avoid this overlap, thereby raising their kinetic energy.⁹⁶ As a result the metal Fermi Level rises in energy (or in other words Φ is reduced), which in a schematic picture such as Figure 4.1 is displayed as part of the equilibration process.

While Bertel⁹⁶ and Bagus⁹⁴ established this explanation of energy level alignment through Pauli repulsion only for noble gas elements physisorbed on a metal surface, Stadler and Jacobsen have shown that this mechanism is also valid for the adsorption of Bipyridine on a Au(111) surface.⁹⁷ In their paper they interpreted the electron depletion at the interface between molecule and metal as a propagation of the electrons formerly resident on the lone pair of the nitrogen atom onto the area close to the metal surface, which results in a partial positive charge on the molecule. This loss of electrons near the surface leads to a decrease of the molecular eigenstate energies with respect to the metal Fermi energy, as a consequence of electron-electron repulsion at the molecule/metal interface. As a result of ELA for this system the conductance of Bipyridine is determined mainly by the tails attributed

to the molecular LUMO.

The change of the electron density distribution Δn upon adsorption, as it was found for the $\text{Ru}(\text{PPh}_2)_4(\text{C}_2\text{H}_4)_2\text{bis}(\text{pyridylacetylide})$ complex, which was the system under study in paper I, III and IV, is shown in Figure 4.2. This change is characteristic for Pauli repulsion, where the main effect of adsorption is an increase of electrons at the metal surface and a reduction of electrons at the molecular anchor. On the other hand no relevant change in the electron density distributions happens in the central part of the molecule, which indicates that the molecular eigenstates are not filled or emptied even though a net charge of -0.43 electrons on the molecule has been determined via a Bader partial charge distribution analysis.^{98,99} This finding for pyridil anchors is in perfect agreement with the results of Stadler and Jacobsen for the Bipyridine molecule.

4.3.2 Partial filling of molecular eigenstates

As the second of the two mechanisms for ELA, presented in this thesis, charge transfer from the metal to the molecule and vice versa via partial filling or emptying of MOs is considered, which implies a direct exchange of electrons/holes from the metal bands near the electrode Fermi energy and the frontier orbitals of the adsorbed compound. In order for giving such partial occupations a physically correct meaning an overlap of the molecular eigenstates and the electronic bands of the metal surface is necessary, because it allows for a hybridisation of the two. Through this hybridisation electronic eigenstates of the full junction system are created, which depending on their spatial distribution across the whole scattering region virtually remove/add electrons from/into the molecular HOMO/LUMO, which can be redefined by diagonalising the molecular subspace of the transport Hamiltonian even for the coupled system. The main factor redefining the direction of this partial electron exchange is the difference in electronegativity of the two subsystems, which is related to the respective energetic position of $E_{F,mol}$ and $E_{F,L}$, as it has been shown by Leung et. al.¹⁰⁰ For clarity the focus will now be on the case, where $E_{F,mol}$ is lower than $E_{F,L}$ in order to elaborate the final alignment of the broadened molecular level and the metal DOS by a self consistent line of thought. In such a situation a partial negative charge flows from the electrode onto the pDOS of the adsorbed molecule raising $E_{F,mol}$ according to equation 4.2. $E_{F,L}=\mu_L$ on the other hand remains

nearly constant due to the high number of degenerate electronic states near $E_{F,L}$ in the metal and the electron flux continues until both are energetically equal. The energetic position of the molecular eigenstates, however, is strongly dependent on the number of electrons in the system and therefore also the peaks in the pDOS start to shift, when a charge is introduced. In our example this shift leads to an additional increase of $E_{F,mol}$, because of an increase in electron-electron repulsion. Consequently $E_{F,mol}$ and μ_L have to be equilibrated again by a flow of electrons back into the metal and so on. These two processes, namely charge transfer and energetic relaxation due to the new electrons on the subsystem, now alternate self consistently until a converged Fermi level alignment has been reached. I want to stress again, that this kind of self consistent cycle was only a thought experiment, while in DFT calculations self-consistency is between the Kohn-Sham and Poisson equations, where the two processes outlined above are described implicitly and simultaneously.

4.4 Charge transfer and Fermi Level alignment in DFT

The relationship between charge transfer and the alignment of the molecular eigenstates with the metal Fermi level can be analysed within DFT. Since both mechanisms introduced in the last sections are involving a partial transfer of electrons from or onto the molecular subspace, the possibility to put a non-integer number of electrons on a unit cell in DFT can be used for the analysis.

One way to quantify the charge transfer following the adsorption of a molecule on a surface is by considering the energetic shift of the lowest lying molecular orbital of the molecule (MO1). Since in most cases the eigenenergy of MO1 lies far below the metallic band no hybridisation with the lead states can be expected.⁹⁷ As a consequence, the only shift MO1 experiences is due to the change in the electrostatic potential created by a partial increase/decrease of the electronic charge on the molecular subspace. In order to determine the eigenenergy of MO1 in a unit cell consisting of metal electrodes and the molecule, a subdiagonalisation of the molecular subspace in the transport Hamiltonian has to be performed. As another ingredient for this approach the alignment of the molecular eigenstates with

the metal Fermi level based calculations for the two isolated subsystems is required as will be explained in detail below.

4.4.1 Subdiagonalisation of the molecular subspace

For redefining MO energies in a junction environment the Hamiltonian matrix \mathbf{H} with matrix elements obtained from DFT calculations, is diagonalised with respect to the basis functions centred on the molecule only, which results in a diagonal sub-matrix \mathbf{H}_{sub} . \mathbf{H} is then transformed unitarily by

$$\mathbf{H}_{trans} = \langle \mathbf{c} | \mathbf{H} | \mathbf{c} \rangle \quad (4.3)$$

with the transformation matrix \mathbf{c} , being an identity matrix of the same dimensions as \mathbf{H} , with the subspace, corresponding to the molecular basis, formed by the normalised eigenfunctions of \mathbf{H}_{sub} .

As a result of this procedure, which is often referred to as the molecular projected self consistent Hamiltonian (MPSH) method, the part in the transport Hamiltonian describing the molecular subspace changes its basis vectors from a LCAO into a MO representation. The energies of the molecular orbitals can now be directly related to the Fermi energy of the unit cell, which is mainly determined by the DOS resulting from the metallic bands. Importantly, the electronic coupling i.e. the non-diagonal elements in the transport Hamiltonian undergo the same transformation as the eigenenergies, which makes a direct quantification of the coupling of the molecular MOs to the basis functions on the electrodes possible.^{101,102} This provides another important analysis tool, which will be made use of in subsequent chapters of this thesis.

4.4.2 Vacuum level alignment

In order to be able to align the molecular eigenenergies and the Fermi level of the metallic electrodes it has to be ensured that both are given relative to the same reference energy. Since the reference energy in modern DFT codes can be defined in various ways, e.g. as the average potential within the unit cell or the average of the potential at the border of the unit cell, it is crucial to replace this reference by one, which is independent of how the unit cell is constructed in detail. The following scheme shows a method, which can be

applied for the direct comparison of the MO energies and the metal's Fermi level:

1. Calculation of the molecular eigenenergies with respect to the vacuum potential: This step consists of a DFT calculation of the isolated molecule in a unit cell, which is large in size in order to ensure the Coulomb term in the Hamiltonian due to the molecule has decayed sufficiently at the border of the unit cell. The molecular eigenenergies relative to the vacuum energy are then determined as

$$\epsilon_{i,vac} = \epsilon_{i,DFT} - eV_{vac}, \quad (4.4)$$

where $\epsilon_{i,DFT}$ and V_{vac} represent the eigenenergies of the molecular levels and the potential far away from the molecule with respect to the arbitrary reference energy in a DFT calculation.

2. Calculation of the metal Fermi energy relative to the vacuum potential: In this step a DFT calculation of the metal electrodes without the molecule in between is performed. The vacuum potential can then be determined as the potential in the gap between the two surfaces, where usually a value in the middle of the vacuum region is taken. The Fermi level can now be determined relative to this vacuum level in the same way as for the molecular levels in step 1 (equation 4.4) shown in equation 4.4, namely by forming the difference:

$$\mu_{L,vac} = \mu_{L,DFT} - eV_{vac}, \quad (4.5)$$

3. Establishing a direct relation between the molecular eigenenergies and the metal's Fermi level: As a last step both energetic quantities are related to each other resulting in an alignment of the molecular MO eigenenergies relative to the metal Fermi level:

$$\epsilon_{i,\mu_L} = \epsilon_{i,vac} - \mu_{vac} \quad (4.6)$$

This scheme can be used in two ways: Having determined the energy of the MO1 relative to the metal Fermi level one can now compare it with its energy in the composite system determined via a subdiagonalisation of the

4. Energy level alignment and electronic coupling

molecular subspace. In most cases the energies do not correspond, which is due to the charge transfer between the subsystems. By the introduction of partial charges in the unit cell within DFT it is now possible to determine the shift of the MO1 with an introduced charge, thereby quantifying the partial charge transfer in the composite system.⁷³

The second way of using this analysis tool is to reproduce the energy level alignment via this procedure, when the amount of charge transfer is known, hence predicting the energetic peak position in the transmission function and relating them to molecular eigenstates. This procedure starts with a determination of the electron transfer within e.g. a Bader charge analysis⁹⁸ or a Mulliken charge analysis.¹⁰³ By introducing the determined partial charge in the calculation of the isolated molecule and subsequently comparing the molecular eigenenergies to the metal Fermi level one can predict the MO energies and the energies of the peaks in the transmission function. It has, however, to be noted that such a procedure does only work reliably for junction systems, where the molecule is only physisorbed to the metal surface. For open shell and therefore strongly coupled compounds the adsorption process requires also the breaking of covalent bonds within the molecule such as the S-H bond for thiol anchors. As a consequence the MO-spectrum of the free molecule cannot be directly compared to the adsorbed system due to the discrepancy between the closed shell molecule in vacuum and the biradical structure forming covalent bonds to the metal surface upon adsorption.

Charge localisation within DFT (Paper I)

This section is an outline of Paper I, where the applied methods and the reasoning behind them are presented. The main purpose of Paper I was to simulate a charged molecule inside a single molecule junction geometry within DFT. In experiments such a situation can be created by applying an electrochemical gate via a reference electrode embedded in a solvent, which adds a potential to the measured system.^{35,104–106} Since the potential difference between the source and drain electrodes in such an electrochemical cell is kept fixed only the molecular eigenstates shift in energy, which results in a change in energy level alignment and can, also lead to a change in the redox state of the measured compound, which then carries a charge.^{31,106,107} This charging of the molecule results in a large change of its conductance, an effect which is useful for the application of single molecule junctions as memory and logic elements in future computer architectures.^{108,109}

This chapter is organised in the following way: First the requirement for new methods within DFT for the simulation of an electrochemical gate is motivated. Then the problem of the self interaction error within DFT is addressed, which makes special schemes for the localisation of a charge necessary. These methods are then outlined in the remaining sections. Finally a short summary of the results in Paper I are given.

5.1 Motivation

In principle an electrochemical gate could be simulated by introducing a spatially constraint potential in the unit cell of the DFT calculation, as it was done in various studies of junctions in the Coulomb blockade regime.^{110,111} In this regime the electronic coupling between the metal surfaces and the adsorbed compound is very small and in some cases the distance between the conjugate molecular states and the metallic electrodes is among a few Å. For the coherent tunnelling regime, however, the molecular eigenstates overlap and hybridise significantly with the surface states of the leads. As a consequence a step-like potential in the unit cell, would introduce artefacts, because the discontinuities of its derivative would not be in regions with negligible electron density. Therefore a conceptually different strategy for introducing electrochemical gating in the coherent tunnelling regime was pursued in Paper I, where different methods for simulating a charged compound, namely an oxidized $\text{Ru}(\text{PPh}_2)_4(\text{C}_2\text{H}_4)_2\text{bis}(\text{pyridylacetylyde})$ complex, in a single molecule junction within DFT had to be elaborated. In Paper I, and also in Papers III, IV and V, we decided to use a chemically intuitive way to create charged species in a junction, namely the introduction of a counterion in the unit cell, which due to its high electronegativity extracts an electron from the compound. This method, however, brought its own difficulties, where the main issue to deal with was the self interaction error present in DFT, which makes the correct description of localised states notoriously hard.

5.2 The Self Interaction Error (SIE)

The Self interaction Error (SIE) is an artefact arising from the mean field description of the Hartree potential in DFT. Since E_{Hartree} , defined in equation 2.15, includes the full electron densities and their Coulomb interaction, each electron experiences a spurious interaction with itself.¹¹² As a consequence binding energies, on-site Coulomb energies and the exchange splitting of d- and f- states are underestimated, while the hybridisation of d- and p-states is overestimated.^{113,114} This artefact was first observed by Fermi and Amaldi in 1934, who proposed a first self interaction correction.¹¹⁵ Hartree Fock theory (HF), being a mean field theory as well, does also face the SIE

in its Hartree term. The exact exchange energy contained in the energy function of HF, however, corrects for it completely. Due to the approximative nature of the exchange-correlation functionals for the DFT calculations performed in this thesis the self interaction does not vanish and has to be accounted for, especially when dealing with localised MO's such as its most well-studied example, the dissociation of H_2^+ ,¹¹⁶ or the isolated p-orbitals of a Cl counterion as we use it in Paper I.

While various self interaction corrected exchange-correlation functionals have been proposed in recent literature^{113,117–120} for the localisation of an electron on an anion in the unit cell in Paper I we followed two alternative paths, namely a correction of the SIE by exploiting solvation energies and the ΔSCF method, as introduced in section 2.5.

5.3 Charge localisation via solvation shells

In their study on the quantification and reduction of the SIE, Lundberg and Siegbahn have shown that solvent effects work against delocalisation because the solvation energy E_{solv} is higher for integer charges than for delocalised partial charge distributions.¹¹⁴ It can be formulated as

$$E_{\text{solv}} = -\frac{\epsilon - 1}{2\epsilon} \cdot \frac{Q^2}{R}, \quad (5.1)$$

where ϵ is the dielectric constant of the solvent in a continuum model, Q is the charge on molecular fragments and R is the distance between these fragments. According to this formula integer charges increase the stabilisation arising from E_{solv} as it was shown for the dissociation of $\text{C}_6\text{H}_{14}^+$ in Reference.¹¹⁴

Jónsson et. al.¹²¹ have been the first to introduce a solvated counterion in a DFT based description of the charging of a molecule adsorbed on a metal surface in order to simulate a redox reaction in an attempt to mimic an electrochemical STM experiment. In their paper they could show, that a small number of solvent molecules already increases the localisation of negative charge on the counterion notably.

Following this work one road we chose in Paper I was the simulation of an oxidised molecule in a junction environment, where the charge on the counterion was screened by a solvation shell. For this purpose we started

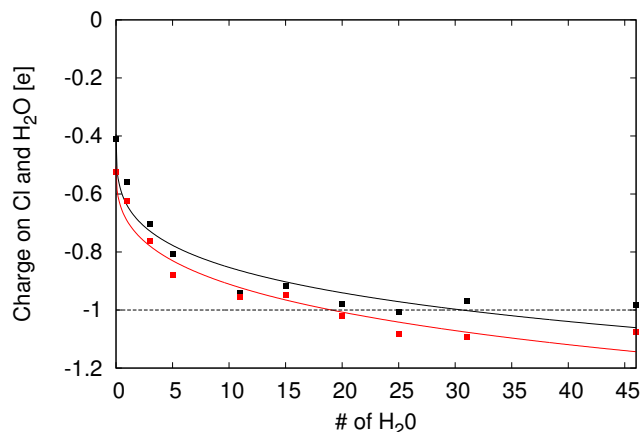


Figure 5.1: DFT calculations of the dependence of the counterion charge on the number of solvent molecules added in the unit cell. Calculations performed for the Ru-complex in the gas phase are shown in black, while the results in a junction environment are depicted in red. The charge was determined via a Bader charge analysis, where on the ordinate the charge on Cl and its first solvation shell is shown.

with a Ru-complex structure with an optimised geometry and a Cl counterion in 7 Å distance from the metal centre. Then we added H₂O molecules gradually, relaxing their nuclear coordinates in every addition step with the constraint that the Ru-Cl distance was kept fixed. Figure 5.1 shows how the charge on the counterion and its surrounding water molecules increases with the number of added solvent molecules. While a few water molecule already have a high influence on the charge localisation and therefore the charging of the molecule the amount of negative partial charge on Cl increases slowly with each shell leading to convergence around 30 water molecules for the system in vacuum and 20 for the system in a junction environment.

5.4 Charge localisation via Δ SCF

The second route we followed in Paper I, was the localisation of an electron on the Cl-anion via the Δ SCF method^{58,59} introduced in section 2.5. This is very appealing, since by directly defining the occupation of AOs no additional means are needed in order to achieve an integer charged counterion, which saves a lot of computational effort compared to the localisation via solvation shells, which have to be relaxed in every step as described in the

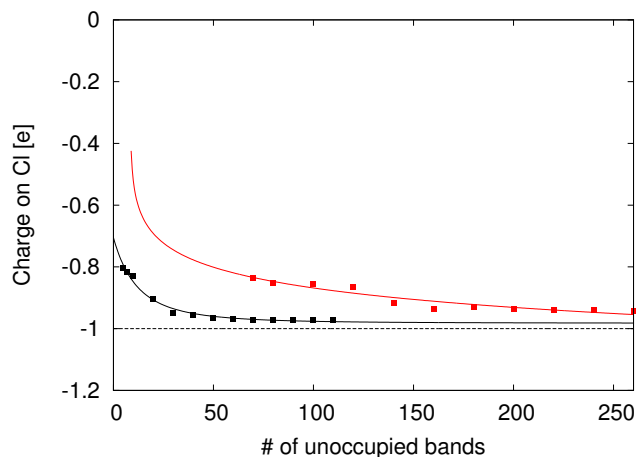


Figure 5.2: Dependence of the partial charge on the counterion on the number of unoccupied electron bands in the DFT calculation. Calculations performed for the Ru-complex in the gas phase are shown in black, while the results in a junction environment are depicted in red.

last section.

An usual Δ SCF calculation for achieving an oxidised molecule requires a unit cell, where the properly geometry optimised molecule is contained along with the counter ion situated at a reasonable distance, where hybridisation of compound and chlorine orbitals is not possible. In the Δ SCF framework we use in Paper I all three 3p-orbitals of Cl are constraint to be occupied. This high number of electron constraints is necessary due to the degeneracy of the 3p-states and constraining only one of the three orbitals would result in a partial dissoccupation of the other two.

The main technical issue, which arises from the formalism of Δ SCF is that in order to be able to create the orbital, which one would like to constrain, an appropriate number of unoccupied MO's have to be included in the DFT ground state calculation. This is especially the case, when a metal surface is included in the unit cell, because a high number of electronic bands have to be accounted for, although they contribute only small fractions to the constraint state. The dependence of the partial charge on the Cl anion on the number of unoccupied electronic states included in the calculation is shown in figure 5.2. While for a gas phase calculation only a low number of unoccupied bands is needed in order to achieve a reasonable counter-charge on Cl, the calculation in a junction environment already needs 70

unoccupied orbitals for convergence and does only constrain 0.84 electrons onto the anion in this case (for comparison the charge on the Cl without the Δ SCF scheme is 0.42e). In both vacuum and junction environment, however, the amount of charge constraint converges with an increase in the bands included in the calculation following only asymptotically. Hence performing a calculation, where the charge is constraint via Δ SCF one has to deal with the trade off between having an ideal charge transfer onto the counterion and reducing the computational effort. In Paper I we settled for 250 unoccupied bands for the junction system, which resulted in a sufficient amount of counter-charge, namely 0.97e for the compound in vacuum and 0.94e for the junction system.

5.5 Outline of results and discussion of Paper I

In an electrochemical STM setup the electrochemical potential shifts the molecular eigenstates with respect to the two Fermi levels of the electrodes, which are equal for zero bias calculations. This is the effect on the transmission function we wanted to simulate by charging the Ru-complex. In order to put a positive charge on a molecule in an experimental junction setup a gate potential has to be applied, which shifts the occupied eigenstates of the molecule towards the chemical potential of the electrodes, where in principle, in order for a subsystem to exhibit a singly occupied state (SOMO), the energy of the MO has to be exactly the same as the Fermi level of the total system. Figure 2 of Paper I shows, that the goal of shifting the HOMO peak in the transmission function towards the E_F has been achieved nicely and an increase in the zero bias conductance has been found. This increase in conductance is due to the Fermi energy’s climbing up the peak related to the molecular HOMO, when the corresponding eigenenergy is shifted by the applied gate. The HOMO peak, however, is not pinned to the Fermi level of the system as it would be expected to be for a system with a SOMO. In order to understand this aspect one has to consider, that even though the coupling of a molecule with pyridine anchor groups is small compared to chemisorped compounds, as they were studied in Paper II, hybridisation between the molecule and the electrodes still plays a role, which delocalises the introduced charge between the molecular subspace and the electrodes. As a consequence a partial positive charge is also introduced in the surface

states of the leads.

In order to understand the ELA and to investigate its physical nature we also examined the neutral and charged system in terms of electronegativity theory,^{122–124} where the main focus was on the charge transfer ΔN between the Au electrodes and the Ru-complex. Therefore we studied ΔN in dependence on the size of the metallic slab the molecule is adsorbed on starting from a single Au atom on both terminals of the complex up to the slabs for the large metal surface we also used in the simulation with periodic boundary conditions.

For single Au atom electrodes a large fraction of a positive charge, introduced as an external parameter in the cluster setup, is situated on the molecule. An increase in slab size, however, leads to a nearly complete absorption of the electron hole in the high number of metal bands near E_f and none of the additional charge can be found on the molecule. The charging via a counterion on the other side localises a substantial amount of the positive partial charge on the molecular subspace, which makes a calculation of the conductance of a charged species in a junction environment possible.

For further details, I would like to refer the reader to Paper I included in this thesis.

Anchor group variation in molecular wires (Paper II)

The main topic of Paper II was the investigation of the influence of terminal groups of dinuclear Fe-compounds¹²⁵ on the conductance in a single molecule junction. For this purpose the -CN,-NCS,-NCSe,-CC- and -CCCC- anchored molecules were systematically studied both on a theoretical level and via mechanically controlled break junction experiments (MCBJ) performed by our collaborators at IBM Zurich. Apart from potential candidates for active electronic building blocks such as switches^{16, 19, 20, 31, 106} (as also studied in Paper V), in single molecule electronics passive elements such as molecular wires are required.⁶⁻⁹ Two main parameters determine if a molecule is suitable as a molecular wire, namely its conductance which should be high both at infinitely small and high bias voltages and its ideally quite moderate decrease with the length of the compound.⁹⁻¹⁴

This chapter is organised in the following way: First our motivation for Paper II is given, followed by an analysis of both the energy level alignment and the electronic coupling strength of the different molecular wires under study. Then it will be concluded with a short outline of our results in Paper II and a comparison with the experimental results of our coworkers.

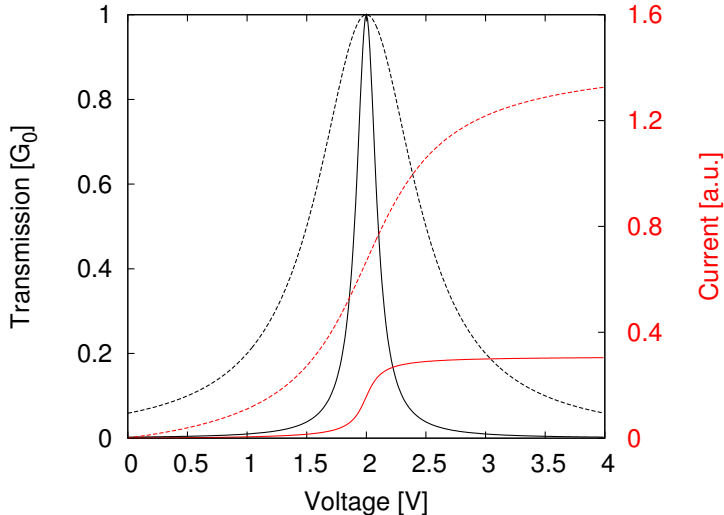


Figure 6.1: Examples for the relation between I/V characteristics and the width of the MO peaks in the transmission function, with the single MO transmission functions (black) defined according to equation 3.8, with $\gamma_L = \gamma_R$ set to 0.1 eV (solid line) and 0.5 eV (dotted line) and $\epsilon=2$ eV. The current for these two values of $\gamma_{L(R)}$ calculated via equation 6.4 is shown in red.

6.1 Motivation

Due to its dependence on the transmission function in single molecule junctions the electronic conductance is not independent of the source drain voltage, as it is the case in macroscopic systems, because of Ohm's law.⁷¹ In other words, this means that the measured current does not depend linearly on the applied bias, but can increase strongly when a MO peak is approached by the voltage and on the other hand can be nearly constant when no transmission channels are energetically near the bias window defined by the metal's chemical potential and the applied voltage. The amount of current increase when approaching a molecular eigenstate is dependent on the electronic coupling between the compound and the metal surface, which is related to the width of the corresponding peak created in the transmission function as illustrated in Figure 6.1. From that we conclude, that wide peaks in the transmission function are desirable for molecular wires due to the larger area below them and the higher current passing through the junction at a given voltage, accordingly.

The influence of the anchor groups on the conductance of a molecule is

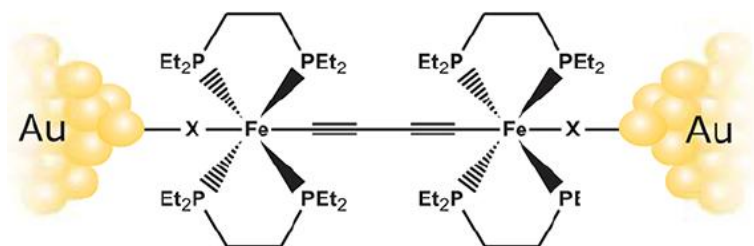


Figure 6.2: Molecular wire backbone structure of the dinuclear iron complexes studied in Paper II, where X denotes the anchor groups, which have been varied between -CN, -NCS, -NCSe, -CC- and -CCCC-.

twofold. On one side these groups are responsible for the electronic coupling strength between the metal electrodes and the central part of the compound and therefore determine the degree of hybridisation and peak broadening of the molecular eigenstates. Secondly, there is also an influence on the energy level alignment as was already explained in section 4.3. In Paper II we studied both physisorbed and chemisorbed molecules, where both Pauli repulsion and charge reorganisation decided about the final alignment of the molecular eigenstates.

6.2 Energy level alignment

While one might intuitively assume that the differences in the conductances of the studied molecules in Paper II arise mainly from the differences in electronic coupling between the compounds and the electrode's surface states, the ELA has to be discussed too, since it also has a part in defining the conductance.¹²⁶ The studied $X(PP)_2FeC_4Fe(PP)_2X$ ($PP = Et_2PCH_2CH_2PEt_2$) molecular wires, shown in figure 6.2, with the different anchoring schemes are good examples for the two mechanisms of ELA described in section 4.3. While the -CN, -NCS, and -NCSe terminated molecules are closed shell systems, which do only physisorb on the surface, the carbon terminated compounds represent an example of chemisorption including strong hybridisation.

The eigenenergies of the complexes in vacuum relative to the metal work function before the adsorption processes are shown in the left panel of figure 6.3. All five compounds exhibit frontier orbitals, which are located above the metal Fermi energy by 1.4-1.7 eV, with the sequence $\epsilon_{HOMO,-CC-} >$

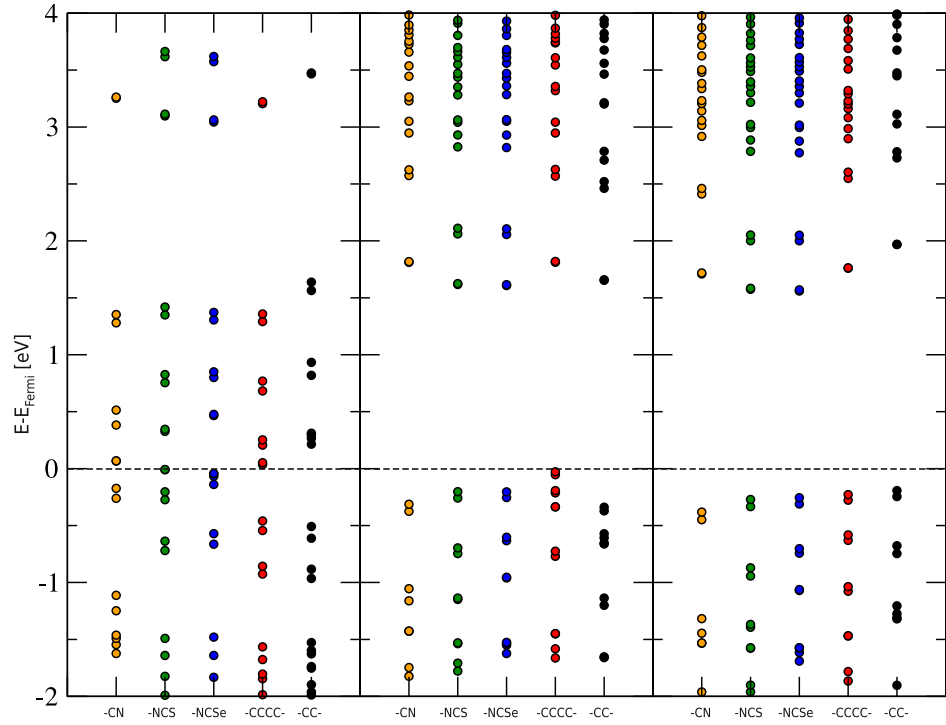


Figure 6.3: Molecular eigenvalues relative to the electrode's Fermi level. Left panel: MOs of uncharged compounds in the gas phase, Middle panel: MO energies of the compounds in the gas phase with partial charges as determined from calculations in the junction environment calculated in gas phase, Right panel: MO energies of the studied complexes in the junction environment determined by a subdiagonalisation of the molecular subspace in the transport Hamiltonian.

	-CN	-NCS	-NCSe	-CC-	-CCCC-
Charge on compound [e]	0.46	0.38	0.43	0.41	0.23

Table 6.1: Partial charges on the adsorbed dinuclear Fe-complexes studied in Paper II, calculated via a Bader analysis⁹⁸

$\epsilon_{HOMO,NCS} > \epsilon_{HOMO,NCSe} \approx \epsilon_{HOMO,CN} > \epsilon_{HOMO,-CCCC-}$. Therefore an electron transfer from the molecular subspace onto the electrodes can be expected in order for the chemical potentials of the two subsystems to equilibrate. This was also the result gotten from performing a Bader charge analysis⁹⁸ of the adsorbed species as shown in Table 6.1.

Introducing the determined partial charges into the DFT unit cells for the gas phase calculations and relating it to the electrodes' Fermi energy, following the procedure described in section 4.4.2, the respective MO energy spectrum of the five compounds in the junction could be reproduced, as shown in the middle panel of figure 6.3. The procedure worked astonishingly well for the three weakly coupled compounds. For the two carbon terminated compounds, however, the energy level alignment resulting from this technique could only approximately recreate the situation in the junction. The reason for that lies in the high degree of hybridisation of the molecular eigenstates and the metallic surface states making a distinction of the molecular subspace and the electrodes on the basis of the electron density difficult for the Bader analysis.

In the junction environment, the energetic ordering of the frontier orbitals, shown in the right panel of figure 6.3, changes. While the -CC-anchor still exhibits the highest ϵ_{HOMO} , with respect to the metal Fermi level, the HOMO of -CCCC- formerly being the lowest in energy now comes second, followed by $\epsilon_{HOMO,NCSe}$, $\epsilon_{HOMO,NCS}$ and finally $\epsilon_{HOMO,CN}$. This new order can be attributed to the respective differences in the mechanisms behind the energy level alignment. The carbon anchors mainly lose their electrons due to a charge reorganization between the molecule and the electrodes' surface states, while the three closed shell compounds additionally show the characteristic behaviour of Pauli repulsion, as it was described in section 4.3.1. As a result the occupied orbitals of these compounds are pushed further away from the metal Fermi level as it is common for adsorptions including Pauli repulsion.⁹⁷

6.2.1 Excursion: The Scissor operator

One of the main problems for a direct comparison of conductances computed from single particle DFT and determined experimentally is a systematic discrepancy in absolute values. While important parameters unknown from the experiment, such as contact geometry, bonding sites and the electrode surface's detailed atomic structure, are possible reasons for the quantitative disagreement with the calculations, where all these structural details are idealised by assuming high symmetry as a starting point for energy minimisation, a possible reason in terms of the theoretical methodology is the gap problem within DFT, which also has an impact on calculated transmission functions. In order to address this issue in Paper II we applied a so called scissor operator (SO) approach,^{89,90,127} which expands the single particle HOMO-LUMO gap, by correcting it with the many body contributions contained in calculated total energies.

Such a correction starts from the ionisation potential I_0 determined in a gas phase calculation, which can be calculated based on DFT total energies, as

$$I_0 = E_{q=+1} - E_{q=0} \quad (6.1)$$

In a simplest approximation the eigenenergy of the molecular orbitals in the transport Hamiltonian can be corrected as

$$\epsilon_{i,SO} = \epsilon_i \mp \Sigma_0 \quad (6.2)$$

with

$$\Sigma_0 = -(\epsilon_{HOMO} + I_0), \quad (6.3)$$

where Σ_0 is added or subtracted to the frontier orbitals in such a way that the molecular HOMO-LUMO gap is increased by pushing the unoccupied states energetically up and the occupied states down.

As a second part of the correction an image charge contribution is added, which accounts for the polarisation of the molecular subsystem by the metal electrodes^{127,128} (which will be further discussed in section 9.2.2). Combining these two corrections the molecular HOMO-LUMO gap is increased, shifting the frontier orbitals further away from the electrodes Fermi level

	-CN	-NCS	-NCSe	-CC-	-CCCC-
Γ [eV]	$2.1 \cdot 10^{-3}$	$2.0 \cdot 10^{-3}$	$2.1 \cdot 10^{-3}$	$1.1 \cdot 10^2$	$9.2 \cdot 10^{-3}$

Table 6.2: Electronic coupling Γ determined from the width of the peak in the single level transmission function shown in figure 6.4 by applying equation 3.8.

and therefore the molecular conductance is scaled down thereby achieving a more quantitatively comparable result. One, however has to be aware, that such a correction can only be applied for weakly coupled systems such as the closed shell compounds in Paper II, because the approximation of taking the gas phase HOMO-LUMO gap as a reference cannot be applied for strongly hybridised metal molecule systems.

6.3 Difference in couplings

Although the differences in ELA, discussed in the previous section are quantitatively important, the electronic coupling of the molecular frontier orbitals with the metal surface bands is responsible for most of the structure dependence of the conductances found in Paper II. While the -CN,-NCS and -NCSe anchored compounds exhibit comparatively narrow peaks in the transmission function, the carbon terminated complexes show wider peaks with a higher transmission at the metal Fermi level.

Figure 6.4 shows single level transmission functions calculated only from the molecular HOMO's contribution to the junction's conductance. The apparent ordering in peak width is $\Gamma_{-CC-} \approx \Gamma_{-CCCC-} > \Gamma_{-NCSe} \approx \Gamma_{-NCS} \approx \Gamma_{-CN}$. Applying equation 3.8 one can now determine values for the peak width of the five compounds representing a measure for the electronic coupling, which are listed in table 6.2.

The differences in electronic coupling and therefore peak width can be rationalised as follows: While the main difference arises from the type of adsorption, namely chemisorption for the -CC- and -CCCC- compounds and physisorption for the -CN,-NCS and -NCSe terminated molecules, slighter differences such as the difference between -CC- and -CCCC- arise from a difference in molecular length. While both compounds, in principle, have the ability to bond covalently to the metal surface, the molecular HOMO of the -CCCC- molecule is delocalised over a wider area due to the overall

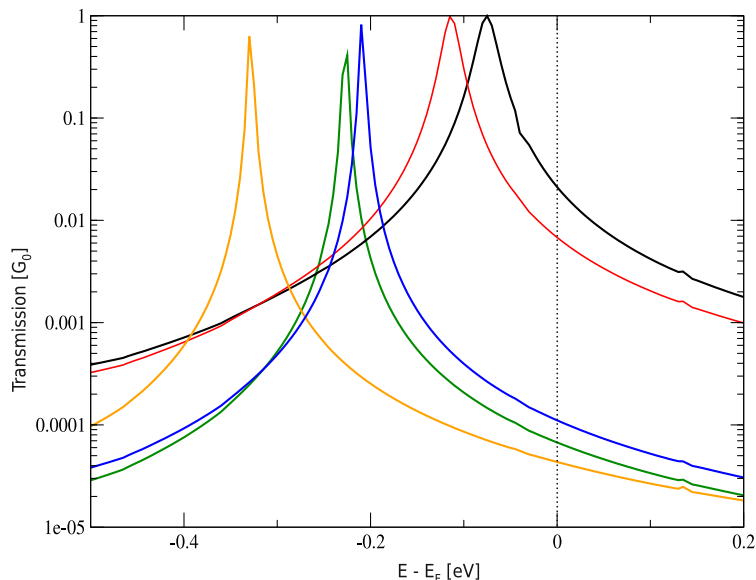


Figure 6.4: Tight binding transmission functions of the molecules studied in Paper II, where only the molecular HOMO has been regarded for the compounds transmission.

higher length of the compound and therefore has a lower amplitude on the C-atom directly connected to the Au-electrodes. This results in a lower wavefunction overlap and therefore also in a lower electronic coupling and peak width when compared to the -CC- terminated compound.

Regarding the slight difference in conductance between the selenium and sulphur anchors the length dependence argument does not hold. In this case no argument, that would explain, why the electronic coupling of -NCSe might be higher than for -NCS anchors, is apparent. The two terminal atoms are isoelectronic, therefore the number of valence electrons cannot be responsible for the observed difference in conductance. While a vast number of experimental studies on sulphur (mainly thiol) terminated molecules have been performed,^{129–134} the data on selenium anchors is more limited,^{135–138} even for chemisorbed species. It was, however shown, that the bonding of benzeneselenol monolayers on Au(111) is stronger than for corresponding thiophenol,¹³⁹ consistent with STM-results on terthiophene molecules.¹³⁵ On the other side Samant et. al. have shown that the chemisorption of docosanethiol on Au(111) is stronger than that of docosaneselenol.¹⁴⁰ According to our transmission functions shown in figure 6.4 (as well as figure 4

of Paper II) and regarding the findings in the experimental studies it can be concluded, that the difference in conductance found for the -NCS and -NCSe anchored molecules does arise from the difference in energy level alignment rather than in electronic coupling, which is consistent with the finding of Patrone et. al.,¹³⁷ who arrived to a similar result on the basis of ultra-violet photoelectron spectroscopy (UPS) of adsorbed S and Se terminated oligothiophenes on gold.

Finally, the conductance of the -CN terminated molecule comes last in the studied series of compounds. The same argument as given in the previous paragraph also holds for this complex. While the electronic coupling of the molecular HOMO is nearly identical to the values for -NCS and -NCSe, as shown in table 6.2, its different energy level alignment leads to a lower zero bias conductance.

6.4 Outline of results and discussion of Paper II

As already stated in the previous sections, the zero bias conductance order we calculated is $G_{CC-} > G_{CCCC-} > G_{NCSe} > G_{NCS} > G_{CN}$ (exact numbers can be found in figure 5 of Paper II). This was in good qualitative agreement with the experimentally determined order from break junction measurements performed under ultra high vacuum, although the computed values are systematically higher. This overestimation is around two orders of magnitude for -NCS and -NCSe terminated compounds and around one order of magnitude for the two chemisorbed species. Such an overestimation is common in single particle GF-DFT calculations for the conductances¹²⁷ and as mentioned at least partially due to DFT’s gap problem. In order to account for the underestimation of the HOMO-LUMO gap we also performed corrections in the transport Hamiltonian based on a scissor operator (SO), introduced in section 6.2.1. Although decreasing the determined zero bias conductance for the physisorbed compounds, a quantitative agreement could not be achieved for the conductances, which, however, is not expected from such a crude ad-hoc correction. A better agreement would be achieved by applying methods going beyond DFT such as the GW approximation.^{79,80,88}

All the compounds studied in Paper II exhibit inversion symmetry, which means there is no dipole moment in the transport direction. As a consequence, the frontier orbitals of the compounds are shifted with respect to

the electrodes' Fermi energy only by a second order Stark effect when a bias is applied. Hence, instead of accounting for the bias dependence of the transmission function explicitly the current was determined in a linear response regime with symmetric coupling to the two electrodes, which is defined as an integration over the zero bias transmission function

$$I(V) = G_0 \int_{-\infty}^{\infty} T(E = V)(n_L - n_R)dV = G_0 \int_{-V/2}^{V/2} T(E = V)dV. \quad (6.4)$$

The IV-curves determined by applying this scheme are shown in figure 4c of Paper II. An excellent correspondence regarding the onset voltages between theory and experiment could be achieved, showing no relevant onset voltages for the carbon terminated wires, while the -CN,-NCS and -NCSe terminated molecules exhibit no meaningful current for up to 0.25-0.5 V. This conduction gap in the experimental dI/dV curves is directly related to both level alignment and electronic coupling of the frontier MOs as derived from the theoretical findings in the investigation.

For a more detailed analysis of experimental data and comparison with the theoretical results, as well as a study on the length dependence for comparing the studied complexes with other proposals for molecular wires, I would like to refer the reader to Paper II, which is included in this thesis.

Incoherent electron transport

One of the main objectives of this thesis was to establish a theoretical description of sequential electron hopping in an electrochemical STM junction environment based on parameters obtained from DFT calculations. In this chapter the fundamental framework of Marcus theory is presented, which is the formalism employed for this purpose.

While the description of coherent electron transport in single molecule junctions is already well established, a treatment of incoherent sequential electron hopping in the literature is still mostly limited to molecular electron donor-acceptor systems or adsorbed molecules on a single surface as they were first proposed in a series of articles by Rudolph Marcus.¹⁴¹ An adaptation of the formalism for electron hopping based on Marcus' earlier work for single molecule junctions has been addressed by e.g. Ulstrup and Kuznetsov^{142, 143} and has been further developed by Nitzan and co-workers recently.¹⁴⁴ Both groups, however, did not address the determination of the key parameters in a junction environment from DFT calculations, but rather used model systems, such as spheres between two metallic electrodes.

This chapter is organised as follows: First a short overview of the history of Marcus theory and its original formalism is given. Then an adaptation of the definition of the key parameters for electron hopping in order to describe redox reactions at metallic electrodes is provided in order to build a bridge to the work performed in Paper IV and V.

7.1 History of Marcus theory

In 1956 Rudolph A. Marcus published an article, where he proposed a formalism for the explicit calculation of the rates of electron transfer reactions,¹⁴⁵ which in its initial formulation considered only reactions between two iron cations, namely Fe^{2+} and Fe^{3+} . In such a so called outer sphere electron transfer reaction no internal structural changes during the process are required and the surrounding solvent was described by a homogeneous medium characterised only by its dielectric constant. In subsequent publications Marcus and Hush extended this formalism in order to include the effect of the distance between the reactants and a relaxation of the surrounding solvent, where the donor and acceptor are surrounded by solvation shells^{141, 146} up to the point where electron transfer reactions at electrodes have been described.¹⁴⁷

The striking novelty of Marcus' outer sphere theory compared to other reaction theories such as Eyring's transition state theory, was that no adiabatic transition state, defined as an activated complex of donor and acceptor is required, but the reaction is driven by the thermally induced reorganisation of the surroundings of the weakly coupled reactants, while the theory still assumes an Arrhenius form for the transfer rates. Along this line of thought the key quantities responsible for electron hopping are simply the reorganisation energy λ of the surrounding medium, which describes the energetics of the solvent related to its adaptation to the dislocation of a transferred charge, the overall driving force of the reaction ΔG^0 , that is the reaction free enthalpy, and the transfer integral H_{AB} , which is the electronic coupling between the initial and final state of the reaction.

R.A. Marcus was honoured with the Nobel Prize in Chemistry in 1992 for this theory, because it provides a formalism for the description of a high number of chemical and biological processes, where electron transfer reactions play a crucial role. The most famous and counter-intuitive consequence of Marcus theory is the so called "Marcus inverted region", where a reduction of the electron transfer rates with increasing exothermic character of a reaction is predicted, which was also experimentally verified in 1984 by Miller et al.¹⁴⁸

7.2 Classical Marcus theory

7.2.1 Outer sphere reactions

In an outer sphere reaction there are no vibrational degrees of freedom for the reacting species, leaving only the reorganisation (or polarisation when formulated for a dielectric continuum) of the solvent driving the reaction. Therefore the Gibbs energy of the system only has contribution from the electronic energies of the reactants ϵ_1 and ϵ_2 , the solvation Gibbs energy G_{solv} and a Coulomb interaction term, $e_1 e_2 / \epsilon_s R$ between donor and acceptor, with e_i being their respective charges, ϵ_s the dielectric constant of the solvent and R their distance. While ϵ_1, ϵ_2 and the Coulomb interaction are straightforward to evaluate in terms of ab initio calculations, where partial charges can be obtained from a Mulliken¹⁰³ or Bader⁹⁸ analysis and single particle energies can be attributed to MO's of the reactants, the calculation of the solvation energy from the related change of the dielectric polarisation function requires more demanding calculation schemes such as molecular dynamics (MD) and QM/MM simulations. Marcus' original work¹⁴⁵ did not aim at an explicit description of the solvent and he simply applied Born's model,¹⁴⁹ where the reactants or inner shells are treated as spheres with a radius a and a charge e_i , and the surrounding solvent is described as a dielectric continuum. In such a treatment the Gibbs energy of solvation takes the simple form¹⁵⁰

$$G_{solv} = -\frac{e^2}{2a} \left(1 - \frac{1}{\epsilon_s}\right). \quad (7.1)$$

Combining all the contributions named above, the Gibbs free energies of both the reactants and the products can be defined as

$$G_K = \epsilon_{1,K} + \epsilon_{2,K} - \frac{e_{1,K}^2}{2a_{1,K}} \left(1 - \frac{1}{\epsilon_s}\right) - \frac{e_{2,K}^2}{2a_{2,K}} \left(1 - \frac{1}{\epsilon_s}\right) + \frac{e_{1,K} e_{2,K}}{\epsilon_s R} \quad (7.2)$$

with $K \in \{r, p\}$ denoting the reactant or the product state (Note that the distance R between the reactants is constant on this level of theory).

In a next step a reaction coordinate q is introduced, where one can interpret q as the shortest path from the reactant state to the product state on the Potential energy surface, which is spanned by considering all vibrational

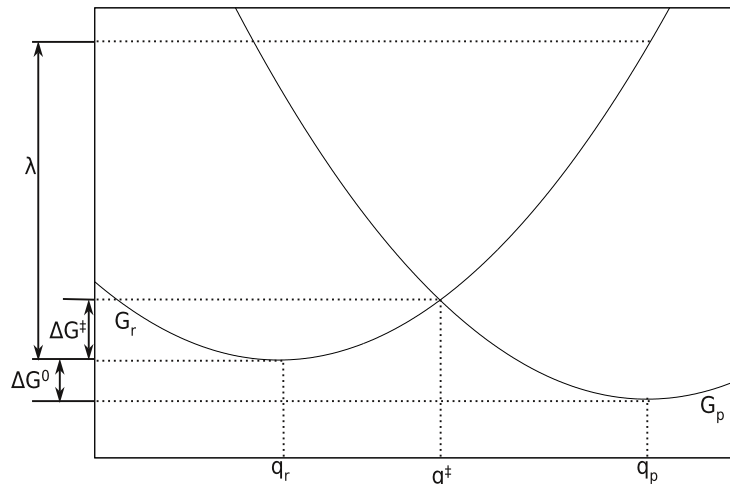


Figure 7.1: Schematic representation of the two Marcus parabolas and their intersection in the fully non-adiabatic regime, showing also the basic quantities of the classical Marcus theory formalism.

and translational degrees of freedom. On this reaction pathway q_r and q_p represent the geometry of the reactant and product state in their respective equilibrium configurations considering both the reacting species and the solvent, while q^\ddagger denotes the nuclear configurations at the intersection point of the two Gibbs free energy parabolas, which is defined by the condition

$$G_r(q^\ddagger) = G_p(q^\ddagger). \quad (7.3)$$

The challenge now is to calculate the change in G_K at any point q between q_r and q_p . From thermodynamics it is known that this change can be calculated from the reversible work carried out from q to q_K , but one has to find an appropriate path. Marcus solved this problem by proposing a thought experiment, where he first charges the reactants to a hypothetical charge e_0 , quantifying the work required for that, and then discharges the system again, but only allowing the electronic (high frequency) polarisation of the solvent to adapt, while the static contributions remain in the charged state. Following these two steps, he was able to define the Gibbs energy change from the equilibrium to the non-equilibrium system as

$$\Delta G_{solv,K} = \left[\frac{(e_{1,K} - e_{0,1,K})^2}{2a_{1,K}} + \frac{(e_{2,K} - e_{0,2,K})^2}{2a_{2,K}} + \frac{(e_{1,K} - e_{0,1,K})(e_{2,K} - e_{0,2,K})}{R} \right] \left(\frac{1}{\epsilon_{op}} - \frac{1}{\epsilon_s} \right), \quad (7.4)$$

with ϵ_{op} being the optical (high frequency) dielectric constant. The Gibbs energies at the intersection point can now be written as

$$G_K(q^\ddagger) = G_K(q_K) + \Delta G_{solv,K} \quad (7.5)$$

and from the definition of the Gibbs free energy of the reaction ΔG^0 and equation 7.3 follows

$$\Delta G^0 = G_p(q_p) - G_r(q_r) = \Delta G_{solv,r} - \Delta G_{solv,p}. \quad (7.6)$$

By minimising $\Delta G_{solv,r}$ while imposing the condition given in equation 7.3 via Lagrangian multipliers, Marcus could derive an expression for the Gibbs Free energy of activation:

$$\Delta G_{solv}^\ddagger = \Delta G^\ddagger = \frac{\lambda_{out}}{4} \left(1 + \frac{\Delta G^0}{\lambda_{out}} \right)^2 = \frac{(\lambda_{out} + \Delta G^0)^2}{4\lambda_{out}} \quad (7.7)$$

where

$$\lambda_{out} = \Delta e^2 \left(\frac{1}{2a_1} + \frac{1}{2a_2} - \frac{1}{R} \right) \left(\frac{1}{\epsilon_{op}} - \frac{1}{\epsilon_s} \right) \quad (7.8)$$

is the so called (outer shell) reorganisation energy of the solvent in its description as a dielectric continuum.

With this definition for the Gibbs free energy of activation the exponential part of the reaction rate is now be obtained with the Arrhenius type form:

$$k_{ET} = A \cdot e^{-\frac{\Delta G^\ddagger}{k_b T}} = A \cdot e^{-\frac{(\lambda + \Delta G^0)^2}{4\lambda k_b T}}. \quad (7.9)$$

7.2.2 Atomistic description of inner spheres

In a more microscopic picture, i.e. when the spheres used for the reactants in the original theory are replaced by atomistically described systems leads

7. Incoherent electron transport

to further development of Marcus' transfer rates, by including the change in reactant's geometries during the process of electron hopping. When developing his theory from hard spheres representing ionic atoms in a solvent ($\text{Fe}^{2+}/\text{Fe}^{3+}$), as described in the previous section, Marcus in a first step also included their first solvation shell. With more than a single ion for each reactant vibrational degrees of freedom, as well as changes in the reactant's size and geometry now become important, while the constraint that at the transition point, in contrast to the respective equilibrium configurations, the geometry and Gibbs free energy of the reactant and product state have to be identical (see equation 7.3) remains valid.

For the definition of ΔG^\ddagger one now has to change ΔG^0 and λ accordingly: For ΔG^0 as the energy difference between the reactant and product equilibrium states regarding both charge and geometry, the change is trivial since it only leads to a minor change of the terms in G_K (see equation 7.2) and in the electronic energies. λ on the other side, which is responsible for the slope of the Gibbs free energy parabolas, an adaptation is required in order to account explicitly for the vibrational degrees of freedom or the relaxation of the reactant geometries to those of the product state.

In a paper published in 1965 Marcus established a formalism for the calculation of the inner sphere reorganisation energy with its dependency on the vibration modes of the reactants given as^{147,151}

$$\lambda_{in} = \sum_j \frac{f_j^r f_j^p}{f_j^r + f_j^p} (\Delta q_j)^2, \quad (7.10)$$

where f_j^K are the force constants of the j th normal modes and Δq_j represents the change of the reaction coordinate relative to the equilibrium structure. The total reorganisation energy now adds up to

$$\lambda = \lambda_{in} + \lambda_{out} \quad (7.11)$$

7.2.3 The preexponential factor

The preexponential factor in equation 7.9 corresponds to the frequency of electron jumps when the system is at the transition point. In Marcus theory it is defined according to Fermi's golden rule^{147,152,153}

$$k_{ET} = \frac{2\pi}{\hbar} |\langle p|H|r \rangle|^2 FC, \quad (7.12)$$

where $|\langle p|H|r \rangle|$ defines a coupling element of the perturbed Hamiltonian between the reactant (r) and product (p) state and FC is the Franck Condon factor describing the probability of the system to arrive at the transition point, where FC in a Marcus theory notation takes the form

$$FC = \frac{1}{\sqrt{4\pi\lambda k_b T}} e^{-\frac{(\lambda + \Delta G_0)^2}{4\lambda k_b T}} \quad (7.13)$$

With this preexponential factor an extension of classical Marcus theory into a quantum mechanical description is taking place, where now the electronic interaction or coupling between the initial and final state at the transition point determines the frequency of the electron transfer reaction. Combining the classical part of k given in equation 7.9 with this transition coefficient leads to the final form of the transition rate

$$k_{ET} = \frac{2\pi}{\hbar} H_{rp}^2 \frac{1}{\sqrt{4\lambda k_b T}} \cdot e^{-\frac{(\lambda + \Delta G^\ddagger)^2}{4\lambda k_b T}}, \quad (7.14)$$

where in this equation H_{rp} is the transfer integral between the reactant and product state. In the picture of figure 7.1, H_{rp} changes the nature of the crossing point of the two diabatic parabolas at q^\ddagger into an adiabatic reaction pathway with a saddle point at q^\ddagger , where ΔG^\ddagger is lowered according to H_{rp} .

The calculation of H_{rp} within DFT for single-molecule junctions was the main topic of Paper III of this thesis.

7.3 Electron hopping at metal surfaces

7.3.1 Adaptation of the transfer rate

When describing electron transfer reactions for an atom or molecule adsorbed at an electrode surface, it is crucial to account for the large number of electronic bands near the metal's Fermi level. Therefore, k_{ET} has to be changed by describing the various possible electron donor/acceptor states replacing the picture of the two intersecting parabolas with multiples of them, as indicated in figure 7.2. Each of the parabolas describes one electronic state of the resulting manifold, where the probability of finding it in one

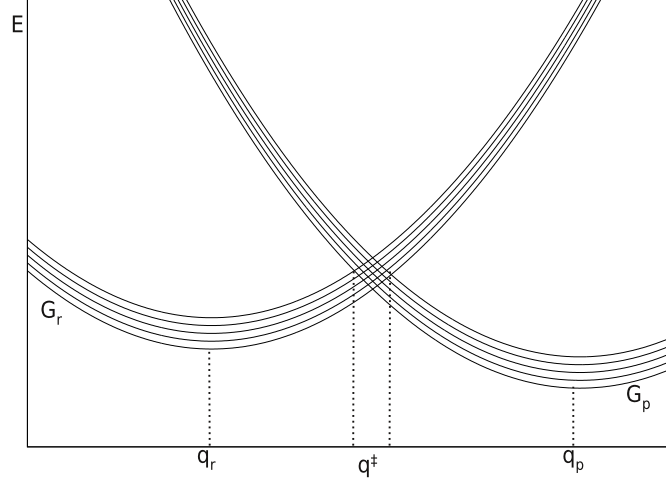


Figure 7.2: Schematic representation of the Gibbs free energy surfaces and their intersections for electron transfer reaction between a metal electrode and an adsorbed molecule.

of them is defined by the Fermi Dirac distribution of the electrode. As a consequence the Gauss-like expression in equation 7.14 has to be modified into an error function, accounting for the high number of metal bands which can participate in the reaction.^{144,154,155} For a reduction and an oxidation reaction, the transfer rate can then be expressed as

$$k_{red} = \frac{2\pi}{\hbar} \frac{1}{\sqrt{4\lambda k_b T}} \cdot \int_{-\infty}^{\infty} H_{DA}^2(\epsilon) e^{-\frac{(\lambda - \Delta G^0 + \epsilon)^2}{4\lambda k_b T}} f(\epsilon) d\epsilon, \quad (7.15)$$

and

$$k_{ox} = \frac{2\pi}{\hbar} \frac{1}{\sqrt{4\lambda k_b T}} \cdot \int_{-\infty}^{\infty} H_{mk}^2(\epsilon) e^{-\frac{(\lambda + \Delta G^0 + \epsilon)^2}{4\lambda k_b T}} [1 - f(\epsilon)] d\epsilon, \quad (7.16)$$

respectively, with the Fermi-Dirac distribution of the electrode

$$f(\epsilon) = \frac{1}{e^{\epsilon - E_{Fermi}/k_b T} + 1} \quad (7.17)$$

taking into account the thermal broadening of the Fermi levels of the leads at finite temperatures. $f(\epsilon)$ is the same in both equations 7.15 and

7.16 because in the oxidation reaction only the unoccupied states of the left lead can provide a positive charge (hole) and only the occupied states of the right lead can absorb it for the reduction reaction.

The electronic coupling H_{mk} between the molecular eigenstate m and the metallic band i , is energy dependent because of the difference in overlap of the molecular eigenstate participating in the electron transfer reaction, with the various electronic bands of the electrode, so that^{144, 156}

$$H_{mk}(\epsilon)^2 = \sum_k |H_{mk}|^2 \delta(\epsilon - \epsilon_k). \quad (7.18)$$

Coherent conductance based on the Transfer integral (Paper III)

The aim of Paper III was to establish a formalism for the calculation of the transfer integral H_{DA} suitable for a single molecule junction setup. For this purpose three methods known from quantum chemistry, namely the energy gap approach,¹⁵⁷ Migliore's scheme using the molecular expansion coefficients,¹⁵⁸ and Larsson's formula^{159–161} have been tested and adapted to describe the transfer integral for a molecule trapped between two metallic surfaces. The testing and comparison was performed on the level of a tight binding Hamiltonian, as well as for molecular benchmark systems. Additionally, an extension of the techniques for the description of their \mathbf{k} -space dependence for a metallic DOS, has been introduced. Finally the zero bias conductance for coherent tunnelling was determined in terms of H_{DA} and compared with the results of Paper I.

This chapter is organised in the following way: After a short motivation for Paper III, the three calculation schemes are presented as they were derived and applied in recent literature. In the following sections the approaches are applied with a tight binding Hamiltonian and for exemplary molecular systems with a description within DFT. Finally, their application in a junction system is addressed and a scheme for the determination of conductance in the coherent tunnelling regime in terms of H_{DA} is presented.

8.1 Motivation

Paper III was meant as a first approach towards the description of incoherent electron transport in single molecule junctions by addressing the explicit calculation of one of the three key parameters of Marcus theory, namely the transfer integral H_{DA} . Numerous calculation schemes for H_{DA} are known for inter- and intramolecular charge transport in the quantum chemical literature.^{157–170} For the description of electron hopping reactions in single molecule junctions, however, these schemes often are not applicable due to their reliance on accurate methods for treating excited states or have to be adapted in order to account for \mathbf{k} -space dispersion. Additionally, in order to describe coherent and incoherent electron transport on the same level of theory, as it is necessary for the comparison of the two regimes in Paper IV, schemes have to be checked for their suitability in this context. Therefore we chose three known approaches from quantum chemistry and adapted them in order to be applicable for single molecule junction systems. In order to be able to benchmark the three methods with NEGF-DFT calculations the zero bias conductance for coherent tunnelling was determined from H_{DA} , where the two metallic surfaces play the roles of the donor and acceptor states, while the compound’s MOs contribute as bridging channels mediating between the two.

By applying the schemes in that way we were able to compare the zero bias conductance with the results of Paper I, and could determine the specific contributions of frontier orbitals to it.

8.2 Calculation methods

8.2.1 The energy gap approach

The energy gap approach, which is based on Koopman’s theorem, is a widely used method for the calculation of the transfer integral in quantum chemistry.^{157,165–167} Its basic idea is to exploit the fact, that at the transition point ($q=0$ in figure 7.1) the splitting of the two diabatic Gibbs energy parabolas into two adiabatic curves is directly proportional to the electronic coupling between the donor and acceptor states. Hence, the transfer integral can be calculated from the relation

$$\Delta E_{\alpha,\beta,q=0} = 2H_{DA}. \quad (8.1)$$

This expression follows directly from the diagonalisation of the 2-state Hamiltonian matrix

$$\mathbf{H}^{2st} = \begin{pmatrix} \epsilon_D & H_{DA} \\ H_{DA} & \epsilon_A \end{pmatrix}, \quad (8.2)$$

where ϵ_D and ϵ_A refer to the onsite energies of the diabatic donor and acceptor states, respectively, and H_{DA} is the electronic coupling between them. By solving the eigenvalue problem for \mathbf{H}^{2st} it can be shown easily, that the energy splitting of the resulting two adiabatic states α and β is given by

$$\Delta E_{\alpha,\beta} = \sqrt{(\epsilon_D - \epsilon_A)^2 + 4H_{DA}^2}. \quad (8.3)$$

At the transition point ($\epsilon_D = \epsilon_A$) H_{DA} is defining the adiabatic splitting completely, as already stated in equation 8.1, and therefore the transfer integral can be determined from the difference of the adiabatic eigenenergies alone.

In order to define H_{DA}^{gap} (the superscript denotes the applied method) at $q \neq q^\ddagger$ equation 8.3 has to be applied. In such a case, however, an orthonormal basis has to be used for A and D, or otherwise of a Löwdin transformation¹⁷¹ has to be performed.¹⁵⁷

While, in rigorous terms, the energy gap method is only correct in a 2-state approximation, the scheme can still be used in a good approximation, when states bridging donor and acceptor are included. The requirements for that are that the adiabatic eigenenergies are selected correctly and that the coupling to the bridge states is small, as it was shown for a 3-state tight binding Hamiltonian in Paper III.

8.2.2 The expansion coefficient method

In contrast to the energy gap approach, which relies directly on the adiabatic states of the D-A system, the expansion coefficient method is based on their relation to the expansion coefficients a, b defining them in linear combinations of the diabatic donor and acceptor states

$$\begin{aligned} |\Psi_\alpha\rangle &= a|\Phi_D\rangle + b|\Phi_A\rangle \\ |\Psi_\beta\rangle &= a|\Phi_D\rangle - b|\Phi_A\rangle \end{aligned} \quad (8.4)$$

where in a 2-state model the condition $a^2 + b^2 = 1$ has to be fulfilled.

This method has been developed comparatively recently by Migliore et al.^{158,168,172} and has not yet been used by other authors that frequently.^{173,174} In his paper¹⁷² Migliore derived, that the coefficients a and b in equation 8.4 can be written as

$$a = \langle \Psi_D | \Psi_\alpha \rangle \cong e^{i\theta} \sqrt{\frac{1}{2} \left(1 - \frac{\epsilon_D - \epsilon_A}{\Delta E_{\alpha,\beta}} \right)} \quad (8.5)$$

and

$$b = \langle \Psi_A | \Psi_\alpha \rangle \cong s e^{i\theta} \sqrt{\frac{1}{2} \left(1 + \frac{\epsilon_D - \epsilon_A}{\Delta E_{\alpha,\beta}} \right)}, \quad (8.6)$$

where $e^{i\theta}$ is a phase factor and $s = \text{sgn}(H_{DA})$. Combining equation 8.3 with equation 8.5 or 8.6 it follows, that

$$|H_{DA}| \cong \left| \frac{a(\epsilon_D - \epsilon_A)}{2a^2 - 1} \right| \sqrt{1 - a^2} \quad (8.7)$$

and

$$|H_{DA}| \cong \left| \frac{b(\epsilon_D - \epsilon_A)}{2b^2 - 1} \right| \sqrt{1 - b^2}, \quad (8.8)$$

which by using the 2-state model condition $a^2 + b^2 = 1$ finally leads to the definition¹⁷²

$$|H_{DA}^{coeff}| \cong \left| \frac{ab}{a^2 - b^2} (\epsilon_1 - \epsilon_2) \right|. \quad (8.9)$$

for an orthogonal basis.

For atomistic descriptions, especially within a PAW framework, the used basis set is not orthonormal by definition. Therefore an orthogonalisation via the inclusion of the overlap matrix elements between donor and acceptor ($S_{DA} = \langle \Psi_D | \Psi_A \rangle$) becomes necessary and the final definition of H_{DA}^{coeff} is then given by

$$H_{DA}^{coeff} = \left| \frac{ab}{a^2 - b^2} (\epsilon_D - \epsilon_A) \left(1 + \frac{a^2 + b^2}{2ab} S_{DA} \right) \frac{1}{1 - S_{DA}^2} \right|, \quad (8.10)$$

as it was applied for all DFT calculations of transfer integrals in Paper III.

Although this formalism was derived for a 2-state system, the effect of bridging states between donor and acceptor can be accounted for. In such a case equation 8.4 changes into

$$|\Psi_\alpha\rangle = a|\Phi_D\rangle + b|\Phi_A\rangle + c|\Phi_B\rangle, \quad (8.11)$$

with Φ_B containing all the bridge states mediating between A and D. The corresponding Hamiltonian takes the form

$$\mathbf{H}^{3st} = \begin{pmatrix} \epsilon_D & V_{DB} & V_{DA} \\ V_{DB} & \epsilon_B & V_{BA} \\ V_{DA} & V_{BA} & \epsilon_A \end{pmatrix}, \quad (8.12)$$

where for the sake of simplicity an orthonormal basis is assumed. By solving the secular equation $HC = ESC$ for this three state model one can now derive, that H_{DA} in such a system can be calculated as¹⁷²

$$H_{DA} = H_{DA}^{2st} + \left(\left[\frac{\text{sgn}(a)c}{|a| + |b|} \right] - \left[\frac{\text{sgn}(a)c}{|a| + |b|} \right]_{q=0} \right) V_{DB}, \quad (8.13)$$

where it was assumed that $V_{DB}=V_{BA}$. From that one can see that the influence of c onto H_{DA} is that of a perturbation term, which increases in size with the distance of the reaction coordinate q to the transition point. Since in Paper III we were only interested in the electronic coupling at (or in the vicinity of) the transition point, the definition from the 2-state model Hamiltonian has proven to be a good approximation for the calculation of H_{DA} .

8.2.3 The effective coupling scheme

The basic idea of the effective coupling scheme is that, the coupling of a donor (D) and an acceptor (A) H_{DA} connected by bridge states (B) can be substituted by an effective coupling H_{DA}^{eff} between D and A.^{159–161} The

simplest model system for the determination of H_{DA}^{eff} is a 3-state tight binding Hamiltonian as shown in equation 8.12. By applying perturbation schemes^{159, 175} the D-B-A system can now be substituted by a two-state effective Hamiltonian of the form

$$\mathbf{H}^{eff}(\mathbf{E}) = \begin{pmatrix} \epsilon_D^{eff} & H_{DA}^{eff} \\ H_{DA}^{eff} & \epsilon_A^{eff} \end{pmatrix} = \begin{pmatrix} \epsilon_D & V_{DA} \\ V_{DA} & \epsilon_A \end{pmatrix} + \begin{pmatrix} V_{DB} \\ V_{BA} \end{pmatrix} \frac{1}{E - \epsilon_B} \begin{pmatrix} V_{DB} & V_{BA} \end{pmatrix}. \quad (8.14)$$

Solving equation 8.14 for H_{DA}^{eff} leads to the definition

$$H_{DA}^{eff}(E) = V_{DA} - \frac{V_{BA}V_{DB}}{\epsilon_B - E}, \quad (8.15)$$

which in a good approximation can be expressed as

$$H_{DA}^{eff} \approx V_{DA} - \frac{V_{BA}V_{DB}}{\epsilon_B - \frac{\epsilon_D + \epsilon_A}{2}}. \quad (8.16)$$

Moving from a 3-state system to a case containing N bridge states, the reduction of the corresponding Hamiltonian now has the size $(N+2) \times (N+2)$ and the reduction leading to \mathbf{H}^{eff} can not be performed in a single step, as it was done in equation 8.14. By a step wise reduction the Hamiltonian following the shown procedure and assuming the bridge states to be orthogonal, however, one arrives at the definition

$$H_{DA}^{eff} \approx V_{DA} - \sum_{i=1}^N \frac{V_{iA}V_{Di}}{\epsilon_i - \frac{\epsilon_D + \epsilon_A}{2}}, \quad (8.17)$$

where the bridge states influence the effective coupling as independent additive terms in a series.

8.3 Transfer integral on a tight binding level

As a first test of the three calculation schemes for H_{DA} presented above for a system, where donor and acceptor are connected via a single bridging state, it is convenient to start with a simple tight binding Hamiltonian, where the relevant quantities are just replaced by typical numbers and the diabatic states are assumed to be orthogonal. For that purpose the three state Hamiltonian introduced in equation 8.12 is applied and its elements

are set to $\epsilon_A = \epsilon_D=0, \epsilon_B=1, V_{DA}=-0.01, V_{DB}=V_{BA}=-0.1$.

Solving the eigenvalue problem for \mathbf{H}^{3st} leads to the adiabatic states

$$\begin{aligned}\Psi_\alpha &= 0.7005\Phi_D + 0.1361\Phi_B + 0.7005\Phi_A, \\ \Psi_\beta &= 0.7071\Phi_D - 0.7071\Phi_A, \\ \Psi_\gamma &= 0.0962\Phi_D + 0.9907\Phi_B + 0.0962\Phi_A,\end{aligned}\tag{8.18}$$

with their respective eigenvalues $\epsilon_\alpha = -0.0294$, $\epsilon_\beta = 0.01$ and $\epsilon_\gamma = 1.0194$.

For applying the energy gap formalism for the calculation of H_{DA} , it is now important to select the appropriate two eigenstates of the system, which form the relevant energy gap. In this case the selection is fairly easy since Ψ_γ does exhibit an almost complete localisation on the bridging state. As a consequence H_{DA}^{gap} can easily be calculated as

$$H_{DA}^{gap} = \frac{\epsilon_\beta - \epsilon_\alpha}{2}\tag{8.19}$$

resulting in a value of 0.0197. The rather small deviation from the correct transfer integral (including the effect of the bridge orbital) of 0.02 for this TB Hamiltonian arises from the fact that a three state model has been applied and as a consequence Φ_B also contributes to Ψ_α . One can account for this deviation by transforming \mathbf{H}^{3st} into an effective 2-state Hamiltonian, according to the definition in the effective coupling scheme shown in equation 8.14. For this particular example the effective Hamiltonian takes the form

$$\mathbf{H}^{eff} = \begin{pmatrix} -0.01 & -0.02 \\ -0.02 & -0.01 \end{pmatrix}.\tag{8.20}$$

A Diagonalisation of \mathbf{H}^{eff} now leads to the effective states

$$\Psi_\alpha^{eff} = 0.7071\Phi_D + 0.7071\Phi_A, \Psi_\beta^{eff} = 0.7071\Phi_D - 0.7071\Phi_A,$$

with their respective eigenvalues $\epsilon_\alpha^{eff} = -0.03$ and $\epsilon_\beta^{eff} = 0.01$, which leads to $H_{DA}^{gap,eff}=0.02$.

The usage of the effective coupling technique in this TB study is rather straightforward. By making use of equation 8.16 one arrives at a value of

0.02, which is not surprising since the method is almost identical to the scheme for $H_{DA}^{gap,eff}$, with the only difference lying in the fact that H_{DA}^{eff} is calculated explicitly, while in the corrected energy gap method it is implicitly contained in the adiabatic eigenvalues.

When applying Migliore's expansion coefficient method the system has to be slightly moved away from the transition point in its reaction coordinate, due to the divergence of the method for $a = b$. Therefore the parameters used in the TB Hamiltonian are changed slightly by shifting the energies of donor and acceptor with respect to each other. In the following $\epsilon_D = -\epsilon_A = -0.01$ is used. Solving the eigenvalue problem for this new Hamiltonian $\mathbf{H}_{q \neq q^\dagger}$ leads to the following eigenstates and energies:

$$\begin{aligned}\Psi_\alpha &= 0.8448\Phi_D + 0.1321\Phi_B + 0.5185\Phi_A, \quad \text{with} \quad \epsilon_\alpha = -0.0318 \\ \Psi_\beta &= -0.5265\Phi_D + 0.0327\Phi_B + 0.8495\Phi_A \quad \text{with} \quad \epsilon_\beta = 0.0123 \\ \Psi_\gamma &= -0.0953\Phi_D + 0.9907\Phi_B - 0.0972\Phi_A, \quad \text{with} \quad \epsilon_\gamma = 1.0194\end{aligned}$$

By applying equation 8.9 one can now calculate H_{DA}^{coeff} to be 0.0197, which is within an acceptable accuracy compared with the results from the other two methods.

8.4 Application within DFT

A physical meaningful calculation of the transfer integral from DFT has to account for the single particle character of the Kohn Sham eigenstates, where the presented methods can be used in two ways: The first is a direct application of the Hamiltonian resulting from the self consistent cycle, where typical DFT problems such as the HOMO-LUMO gap underestimation are directly affecting the results. The second way is to calculate H_{DA} from total energies resulting from DFT, which in principle is more correct, but creates the necessity for all three methods, to be applied on this level of theory. For the application within this level of accuracy in Paper III, the energy gap method and expansion coefficient method have been combined with a Δ SCF based procedure for the calculation of the systems total energies. The effective coupling method does not have a variation, which could be used on a many body level, since it makes direct use of the matrix elements in the

Kohn Sham Hamiltonian.

8.4.1 Implementation on a single particle level

The single particle Hamiltonian (\mathbf{H}^{KS}) based application of the three schemes is rather straightforward and follows the same procedures described in section 8.2. However, it has to be accounted for that contrarily to the atomic orbitals in a simple TB-model the donor and acceptor states in DFT calculations consist of more than a single basis function, and are rather hybridised fragment orbitals of the whole system. Therefore, in a first step \mathbf{H}^{KS} needs to be transformed so that suitable donor, acceptor and bridge states form its basis vectors, explicitly. This can be done by subsequent subdiagonalisations for the full system as described in section 4.4.1. After such a procedure the eigenfunctions of \mathbf{H}_{trans}^{KS} explicitly reflects the donor-bridge-acceptor setup and the three described schemes can be applied in the following way:

Energy gap method

The application of the energy gap approach consists of solving the eigenvalue problem for \mathbf{H}_{trans}^{KS} and a subsequent identification of the two created adiabatic states and their respective energies, in order to apply equation 8.3 for the calculation of H_{DA} . This identification is achieved by sorting states formed by hybridisation according to their amplitudes on the donor and acceptor, determined via

$$a = \langle \Phi_D | \Psi_\alpha \rangle, b = \langle \Psi_\alpha | \Phi_A \rangle, \quad (8.21)$$

with α denoting the respective selected adiabatic state.

From the eigenenergies of the two selected adiabatic states, which represent the bonding and antibonding hybrid of D and A linked by the bridge states, the adiabatic energy splitting can be determined.

Expansion coefficient method

Similar to the calculation of H_{DA}^{gap} , the expansion coefficient scheme starts with solving the eigenvalue problem for \mathbf{H}_{trans}^{KS} and a subsequent identification of the bonding and antibonding states attributed to the donor and acceptor. In a second step one of the two adiabatic states is chosen for the

determination of the expansion coefficients a and b via equation 8.21. Finally, H_{DA} is calculated from equation 8.10, with ϵ_A and ϵ_D being the onsite energies of the donor and acceptor states in \mathbf{H}_{trans}^{KS} , respectively.

Effective coupling method

The application of the effective coupling method directly uses the matrix elements of \mathbf{H}_{trans}^{KS} , where the H_{DA} can be calculated directly from equation 8.17, with V_{Di} and V_{iA} being the non-diagonal matrix elements $\langle \Psi_D | \mathbf{H}_{trans}^{KS} | \Psi_i \rangle$ and $\langle \Psi_i | \mathbf{H}_{trans}^{KS} | \Psi_A \rangle$ and ϵ_i the onsite energy of the respective bridge state i , obtained from respective diagonal elements of \mathbf{H}_{trans}^{KS} .

8.4.2 Implementation based on a many body level

For a many body implementation of the schemes it is crucial that all the energies used in the formalism are total energies resulting from DFT calculations. In order to be able to calculate these energies the Δ SCF scheme introduced in section 2.5 has been applied, since it is the ideal tool for manipulating the occupation of diabatic as well as adiabatic states of the system. Many body applications for both the energy gap method and the expansion coefficient scheme have been developed, where the Δ SCF procedure has to be applied differently in each of them as described in detail in the following paragraphs.

Energy gap method

The crucial part of a many body application of the energy gap scheme is the identification of the bonding and antibonding adiabatic states, resulting from a hybridisation of the diabatic donor and acceptor states. The corresponding $\Delta E_{\alpha\beta}$ is the difference in total energy of the integer charged molecule with the excess electron (hole) residing in the bonding and the antibonding MO, respectively. For forming these two many body states the Δ SCF routine can be applied, where it can be defined explicitly from which MO the transferred electron is taken out and the total energies of the respective many body states can be evaluated accordingly, where the transfer integral is then obtained from equation 8.1.

Expansion coefficient method

For the determination of H_{DA} via the expansion coefficient method, three DFT total energy calculations are needed. These consist of a DFT-calculation of the system at the transition point q^\ddagger for the definition of the adiabatic state, and two calculations, where the electron(hole) resides in one of the diabatic states, respectively. This is required because one needs the total energies for these three systems, as well as the expansion coefficients of both the adiabatic and the diabatic states in terms of the applied basis functions in order to apply equation 8.9. In order to determine the total energy of the two diabatic states the Δ SCF method is applied, where the excess electron(hole) is constraint to one of the two diabatic eigenstates, respectively. The expansion coefficients are again calculated, via equation 8.21, but in contrast to the single particle Hamiltonian based scheme the Ψ_α , Φ_D and Φ_A as well as the total energies are determined from three different DFT calculations.

8.5 Transfer integral in a single molecule junction

For the situation, where the transfer integral is calculated for two metal surfaces bridged by a molecule, it has to be accounted for the fact that not only a single donor and acceptor state are involved in the electron transport but rather all the metallic bands contributing to the respective densities of states of the two metal surfaces. For this purpose the picture developed in the last section has to be extended again in order to account for the resulting higher number of possible donor and acceptor states.

In Paper III we were mainly interested in the zero bias conductance within the coherent tunnelling regime arising from $H_{DA}(E_F)$, in order to be able to compare with the results from Paper I as a benchmark. Hence the first task was to identify the surface states, which give a non-zero contribution to the DOS at the Fermi energy. This can be done by first performing three subsequent subdiagonalisation runs, as described in section 4.4.1 in order to create \mathbf{H}_{trans}^{sp} , whose basis vectors consist of donor (left metal surface), bridge (molecule) and acceptor (right metal surface) fragment orbitals. In a next step the contribution of each metallic eigenstate (ρ) to the total DOS at E_F is determined by broadening the states with a Gaussian function

$$\rho_{i(j)}(E_F) = \frac{e^{-\left(\frac{\epsilon_{i(j)} - E_F}{\sqrt{k_b T}}\right)^2}}{\sqrt{\pi k_b T}}, \quad (8.22)$$

where the subscripts i and j refer to the two metallic surfaces respectively and T denotes the electronic temperature, which in Paper III has been chosen to be room temperature.

The relevant metallic bands are used as the donor and acceptor states and the transfer integral between each of the donor (Ψ_{D_i})-acceptor (Ψ_{A_j}) pairs can now be calculated applying the three schemes in a single particle description described in the previous sections. In order to deal with the high number of donor and acceptor states, the transfer integrals for each pairing is then calculated explicitly on sub-matrices $\mathbf{H}_{trans, D_i, A_j}^{sp}$, with the size $(N+2) \times (N+2)$, containing only the selected donor and acceptor state but the whole range of N bridging states between them. As a result every pairing of D_i and A_j has its own transfer integral $H_{D_i A_j}$, where the contribution of all bridge states is included. In a final step the total transfer integral between the two metallic surfaces is calculated by weighting $H_{D_i A_j}$ with the contribution of D_i and A_j to the total DOS at the Fermi energy:

$$H_{DA, \mathbf{k}}(E_F) = \frac{\sum_{i,j=1}^N H_{D_i A_j, \mathbf{k}}(E_F) (\rho(E_F)_{i, \mathbf{k}} + \rho(E_F)_{j, \mathbf{k}})}{\sum_{i,j=1}^N \rho_{i, \mathbf{k}}(E_F) + \rho_{j, \mathbf{k}}(E_F)}. \quad (8.23)$$

The subscript \mathbf{k} in equation 8.23 refers to the \mathbf{k} -point dependency of $H_{DA, \mathbf{k}}(E_F)$, which arises because the donor and acceptor states are metallic bands. In order to include their band dispersion in the calculation of H_{DA} a \mathbf{k} -space integration is performed, following the definition by Gosavi and Marcus¹⁷⁶ and substituting the integral over the wave vectors \mathbf{k} by a discretised sums over the weighted contributions for each pairing:

$$H_{DA}(E_F) = \frac{\sum_{\mathbf{k}} H_{DA, \mathbf{k}}(E_F) \sum_{i,j=1}^N \rho_{i, \mathbf{k}}(E_F) + \rho_{j, \mathbf{k}}(E_F)}{\sum_{\mathbf{k}} \sum_{i,j=1}^N \rho_{i, \mathbf{k}}(E_F) + \rho_{j, \mathbf{k}}(E_F)} \quad (8.24)$$

8.6 Relationship between Transfer integral and tunnelling conductance

The relation between H_{DA} and the conductance in the coherent tunnelling regime used in Paper III is based on a formulation by Abraham Nitzan.¹⁷⁷⁻¹⁷⁹ In his papers he developed this relationship for a system consisting of a donor and an acceptor, connected by a bridge, which is segmented into a chain of N states, and where the whole system is adsorbed on metallic leads. Therefore in his model the transfer integral for the electron hopping reaction takes the form

$$H_{DA}(E) = V_{D1}V_{NA}G_{1N}(E), \quad (8.25)$$

where V_{D1} and V_{NA} are the coupling matrix elements between the donor state and the first state in the bridge, and between the last bridge state and the acceptor state. The part inside the bridging chain is described by the non-diagonal element $G_{1N}(E)$ of the bridge's Green's function.

Accordingly one can also define a conductance based on the Landauer's formula⁶⁵ in the weak coupling regime or by applying Fermi's golden rule, which has the form

$$g(E) = G_0 |G_{DA}(E)|^2 \Gamma_D^L(E) \Gamma_A^R(E), \quad (8.26)$$

and where G_0 is the conductance quantum, and $\Gamma_{A/D}^{L/R}(E)$ are the broadening matrix elements related to the coupling of the donor and acceptor to the metallic leads (see section 3.3). In the specific case of Paper III this directly corresponds to the imaginary part of the lead self energies $\Sigma_{L/R}$ arising from the system setup, which consists of lead (L), scattering region (S) and right lead (R), following the picture shown in figure 3.4. G_{DA} is a matrix element of the scattering region's Green's function related to the donor-acceptor interaction, where the molecular bridge states have been accounted for by a projection onto the molecular subspace.¹⁷⁷

By using the correspondence between equations 8.25 and 8.26 the relation between $G_{DA}(E)$ and H_{DA} can now be formulated as^{177,179}

$$G_{DA}(E) = \frac{V_{D1}V_{NA}G_{1N}(E)}{(E - E_D - \Sigma_D(E))(E - E_A - \Sigma_A(E))} \quad (8.27)$$

$$= \frac{H_{DA}(E)}{(E - E_D - \Sigma_D(E))(E - E_A - \Sigma_A(E))}. \quad (8.28)$$

Finally, by combining equation 8.26 and 8.28, the conductance for coherent tunnelling can be expressed as a function of the transfer integral:

$$g(E) = G_0 \frac{|H_{DA}(E)|^2 \Gamma_D(E) \Gamma_A(E)}{((E - E_D)^2 + (\Gamma_D(E)/2)^2)((E - E_A)^2 + (\Gamma_A(E)/2)^2)}. \quad (8.29)$$

In Paper III we were only interested in the conductance at zero bias and could therefore simplify equation 8.29 by setting $E=E_D=E_A=E_F$. Additionally, we also assumed $\Gamma_A(E)$ and $\Gamma_D(E)$ to be equal due to the symmetry of the scattering region in the transport direction and chose a value of 0.5eV within a wide band approximation for it, which is reasonable for the coupling strength between gold layers in a bulk structure.⁷² With these simplifications equation 8.29 becomes the simple relation

$$g(E_F) \approx 64G_0 |H_{DA}(E_F)|^2, \quad (8.30)$$

which for a comparison of the results from Paper III and I, was used in order to transform the conductance obtained from NEGF-DFT into a transfer integral $H_{DA}^G(E_F)$.

8.7 Outline of results and discussion of Paper III

In Paper III the presented methods for the calculation of H_{DA} have been applied to four different systems with step wise increase in complexity combined with benchmarking at every level. The first example shown is the application on a tight binding Hamiltonian as it was also used in section 8.3 in order to present the methods as well as their strengths and weaknesses decoupled from any higher level ab initio issues. The next system was an ethylene dimer as it was studied by Valeev et.al¹⁵⁷ in order to benchmark the approaches to real systems, but without any molecular bridge between donor and acceptor. In order to introduce bridge states within a rather simple ex-

ample, the next system we investigated was a tetrathiafulvalene-diquinone anion (Q-TTF-Q⁻) as it was also studied by Wu and van Voorhis.¹⁶⁹ Finally, the schemes were applied for a single molecule junction setup, where the results from the transfer integral calculations for the conductance in coherent tunnelling were compared with those obtained from NEGF-DFT in Paper I.

When applying the three calculation methods for the junction system of Paper I we used three different setups, namely a molecule between two Au pyramids and the periodic junction with both only the Γ -point and a set of 8 transversal \mathbf{k} -points in the irreducible Brillouin zone. The latter two cases were then directly compared with the values of the transfer integral calculated from the NEGF-DFT zero bias conductance and using equation 8.30, where an excellent agreement could be achieved between NEGF-DFT and the three quantum chemical schemes for the calculation of H_{DA} .

As an additional benefit the contribution from the frontier orbitals of the molecular bridge could be explicitly evaluated from the effective coupling method, where it could be nicely shown that in the neutral state of the studied molecule the main contributor to the zero bias conductance is the molecular LUMO, with the influence of the HOMO and HOMO-1 being negligible. In the charged molecule, which we created by using the Δ SCF based method, described in section 5.4, on the other hand the conductance is mainly determined by the molecular HOMO-1. The HOMO's contribution is only minor in both cases, which is due to its rather high degree of localisation on the molecular centre and its resulting low coupling to both metallic surfaces.

Electron hopping in single molecule junctions (Paper IV)

The topic of Paper IV was a study of electron hopping as a mechanism for electron transport in a single molecule junction and a quantitative comparison with coherent tunnelling for the interpretation of the measured current in STM or MCBJ experiments. Various factors determine, which of the two processes is dominant for the conductance of a compound, where in our work we focused on a transition between the coherent tunnelling regime and incoherent electron hopping in dependence on the length of molecular wires with a varying number of $\text{Ru}(\text{PPh}_2)_4(\text{C}_2\text{H}_4)_2$ monomers trapped between two metal electrodes via pyridyl anchor groups and the effect of an electrochemically applied gate voltage.

The chapter starts with a short introductory section, where the motivation for the paper is given, followed by a description of the methods used for the calculation of the quantities needed within Marcus theory for the definition of a two step hopping conductance in a single molecule junction environment, namely the driving force ΔG^0 , the reorganisation energy λ and the transfer integral H_{Au-Mol} . Then an adequate expression for the transfer rates for such a scenario will be derived. Finally an outline of the results of Paper IV and a short discussion of them is given.

9.1 Motivation

The main goal of the paper was a direct comparison of both transfer regimes in dependence on the molecular length and the influence of a gate potential. While coherent tunnelling is mostly described within Landauer theory, as it was presented in chapter 3 and where its treatment is well established in the community, a complete description of electron hopping as an electron transport regime in single molecule electronics on the basis of atomistic methods has not been achieved before. Therefore one task for the work presented in Paper IV was the development of calculation schemes for the main quantities in Marcus theory, namely the transfer integral H_{DA} , the reorganisation energy λ and the driving force ΔG^0 of the reaction. In order to be able to directly compare the two respective conductance values for coherent tunnelling and electron hopping it also had to be ensured, that both theories are treated on the same level of approximation, where Landauer theory is usually applied on a single particle level within DFT. Therefore we also adapted our description of electron hopping in such a way that this single particle description is matched in order to make a quantitative comparison reasonable. The starting point of this comparison was the Ru-complex also studied in Paper I and III.

9.2 Calculation schemes for the key parameters of Marcus theory

9.2.1 Driving force

The driving force ΔG^0 within Marcus theory is generally defined as the difference of the minima of the Marcus parabolas, which corresponds to the ground state energy of the initial and final state of the reaction in their respective equilibrium geometries. According to this definition one could, in principle, calculate ΔG_0 in a single molecule junction setup by comparing the ionisation potential of the compound in its neutral and charged state and relate it to the work function of the metal electrodes in both states. Such a procedure, however, would not include screening effects during the adsorption process, which lead to a shift of the molecular eigenstate energies relative to the Fermi level of the metal μ and a possible change in the HOMO-

LUMO gap size. Therefore, we decided to apply a method which includes these effects directly and is also consistent with our description of coherent tunnelling.

Since the first of the two subsequent redox reactions in the transport through the junction we studied is an oxidation of the molecular compound, we defined the driving force of the reaction as the energy needed to take out an electron from the molecular HOMO,

$$E_{ox,mol} = \epsilon_{HOMO} - E_{vac} \quad (9.1)$$

and to then add it to the electrode's Fermi level E_F . Combining the two energetic contributions leads to the simple expression

$$\Delta G^0 = \epsilon_{HOMO} - \mu. \quad (9.2)$$

Such a definition is valid on a single particle level, where the relaxation of the other molecular eigenstates as a consequence of the missing electron is not included, and the respective change in the Fermi level of the metal is on the other side negligible due to the high number of electronic bands in the relevant energy range near E_F .

Another interpretation of this definition is that ΔG^0 corresponds to the change in the electrode's Fermi level via an applied bias or the change of the HOMO's eigenenergy via an applied gate potential needed for achieving resonance between the molecular state and the metallic Fermi level. Such a definition is adequate for the comparison we wanted to make in our paper and also allows for a straightforward implementation of an electrochemical gate within a rigid-band approximation, in which the effect of a gate is simply described by a rigid shift of the molecular eigenvalues with respect to E_F .

9.2.2 Reorganisation energy

In a single molecule junction setup an additional contribution has to be added to the definition of the reorganisation energy given in section 7.2, namely the image contribution arising from the screening of the charge due to the presence of the metallic surfaces,^{142,143,147} which can be simply added to λ_{tot} :

$$\lambda_{tot} = \lambda_{in} + \lambda_{solv} + \lambda_{image}. \quad (9.3)$$

The calculation of λ_{in} is straightforward, since it is the energy, which is required to relax the nuclei from the systems equilibrium state, namely the uncharged molecule in the junction setup, to its oxidised state, i.e. the positively charged compound between the surfaces or vice versa. Because during the reaction no structural rearrangement of the infinitely large metal electrodes can be expected, only changes in the molecular geometry change have to be considered. Therefore, $\lambda_{in,if}$ for the molecular oxidation reaction can be calculated as the total energy difference of the neutral (initial) molecule in the equilibrium structure of the charged (final) state $E_0(q_f)$ and its relaxed (initial) geometry $E_0(q_i)$. For the second reaction, which is a reduction of the charged molecular compound, $\lambda_{in,fi}$ is defined accordingly, namely as the difference of the total energies of the charged system in the nuclear arrangement of the neutral system $E_{+1}(q_i)$ and its own equilibrium geometry $E_{+1}(q_f)$. According to Marcus theory the curvature of both Gibbs energy parabolas should be identical (see figure 7.1). In practical calculations, however, the respective values can differ slightly,¹⁸⁰ and that is why we calculated the inner part of the reorganisation energy as

$$\lambda_{in} = \frac{\lambda_{in,if} + \lambda_{in,fi}}{2} = \frac{E_0(q_f) - E_0(q_i) + E_{+1}(q_i) - E_{+1}(q_f)}{2}. \quad (9.4)$$

For the computation of λ_{solv} we employed a solvent continuum model based on the generalised Born approximation,¹⁴⁹ where the main ingredients for the calculation of the solute-solvent electrostatic polarisation (G_{pol}) are the so called atomic Born radii α_i , which were calculated via an analytical method established by Qui et.al.¹⁸¹ The derivation of this method starts with the calculation of the atomic contribution to the polarisation energy, which assumes a unit charge on the atoms of the solute and a high dielectric constant of the surrounding medium

$$G'_{pol,i} = \frac{1}{R_{vdW,i} + \phi + P_1} + \sum_j^{1,2} \frac{P_2 V_j}{r_{ij}^4} + \sum_j^{1,3} \frac{P_3 V_j}{r_{ij}^4} + \sum_j^{1,\geq 4} \frac{P_4 V_j CCF}{r_{ij}^4}, \quad (9.5)$$

9.2. Calculation schemes for the key parameters of Marcus theory

with $R_{vdW,i}$ being the van der Waals radius of atom i (as taken from the definition of the OPLS force field¹⁸² in our work), ϕ the dielectric offset, P_1 - P_4 empirical scaling factors as derived by Xie and Haijan,¹⁸³ and CCF the close contact function for nonbonding interactions, which is defined as

$$CCF = 1.0 \quad \text{if} \quad \left(\frac{r_{ij}}{R_{vdw,i} + R_{vdW,j}} \right)^2 > \frac{1}{P_5} \quad (9.6)$$

and otherwise

$$CCF = \left[\frac{1}{2} \left[1.0 - \cos \left[\left(\frac{r_{ij}}{R_{vdW,i} + R_{vdW,j}} \right)^2 P_5 \pi \right] \right] \right]^2 \quad (9.7)$$

with P_5 as an empirical cutoff parameter.

The atomic volumes V_j used in equation 9.5 are defined as the spherical atomic volumes obtained from the respective van der Waals radii minus the part of this volume with overlap to neighbouring atoms, resulting in

$$V_j = \frac{4}{3}\pi R_{vdW,j}^3 - \sum_k \frac{1}{3}\pi h_{jk}^2 (3R_{vdW,j} - h_{jk}) \quad (9.8)$$

where h_{jk} is the deviation of the vector from the centre to the outer border of atom j from $R_{vdW,j}$ due to the intersection with other atoms k ,

$$h_{jk} = R_{vdW,j} \left(1 + \frac{R_{vdW,k}^2 - R_{vdW,j}^2 - r_{jk}^2}{2R_{vdW,j}r_{jk}} \right). \quad (9.9)$$

The atomic Born radius of atom i with a charge of $1e$ can now be calculated by

$$\alpha_i = \frac{1}{G'_{pol,i}}. \quad (9.10)$$

It has to be noted, that in both equation 9.5 and 9.10 the coulomb constant has been set to one, since it cancels out.

With this definition of the atomic Born radii the outer shell reorganisation energy $\lambda_{solv,GB}$ can now be calculated as the difference of the electronic polarisation Gibbs Free energy ΔG_{pol} between the neutral system and the oxidised one:

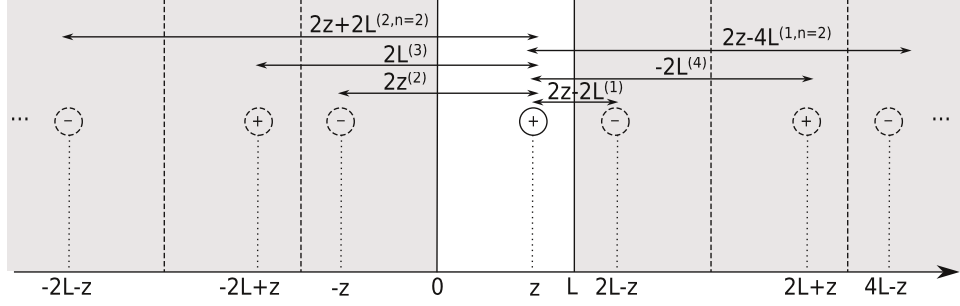


Figure 9.1: Schematic representation of the image charges created by a positive charge between the two parallel planes at a distance L , where their respective positions and distances to the original charge are shown explicitly. The corresponding terms in the sum of equation 9.14 are shown in brackets at the corresponding distances.

$$\lambda_{solv,GB} = \Delta G_{pol} = \frac{1}{8\pi\epsilon_0} \left(\frac{1}{\epsilon_\infty} - \frac{1}{\epsilon_s} \right) \sum_i \sum_j \frac{\Delta q_i \Delta q_j}{f_{GB}}, \quad (9.11)$$

with¹⁸⁴

$$f_{GB} = \sqrt{r_{ij}^2 + \alpha_{ij}^2} e^{-\frac{r_{ij}^2}{2\alpha_{ij}^2}} \quad (9.12)$$

and

$$\alpha_{ij} = \sqrt{\alpha_i \alpha_j}. \quad (9.13)$$

where ϵ_∞ and ϵ_s are the optical and static permittivities of the solvent, respectively, and $\Delta q_{i(j)}$ are partial charge differences for each atom between the neutral and the oxidised compounds in vacuum, which were obtained from a Mulliken charge analysis within DFT.¹⁰³

The last contribution to λ_{tot} in equation 9.3, namely λ_{image} was calculated from an image charge model consisting of an infinite sum of Coulomb interactions between the partially charged molecule caused by an infinite number of mirror images to the charge due to the 2-electrode setup^{127,128} (see figure 9.1):

$$\lambda_{image} = -\frac{1}{2}\left(\frac{1}{\epsilon_{\infty}} - \frac{1}{\epsilon_s}\right) \sum_{i,j}^N \Delta q_i \Delta q_j \times \quad (9.14)$$

$$\sum_{n=1}^{\infty} \left[\frac{1}{\sqrt{(z_i + z_j - 2nL)^2 + R_{ij}^2}} + \frac{1}{\sqrt{(z_i + z_j + 2(n-1)L)^2 + R_{ij}^2}} \right. \\ \left. - \frac{1}{\sqrt{(z_i - z_j + 2nL)^2 + R_{ij}^2}} - \frac{1}{\sqrt{(z_i - z_j - 2nL)^2 + R_{ij}^2}} \right],$$

where $R_{ij}^2 = (x_i - x_j)^2 + (y_i - y_j)^2$ and $x_{i,j}, y_{i,j}, z_{i,j}$ are the positions of the atoms of the molecule, with the z coordinate being the transport direction.

9.2.3 Transfer integral

The determination of the transfer integral H_{DA} was also the main topic of Paper III, where we have shown that the conductance for coherent tunnelling, which is usually determined from Landauer theory can also be calculated via a formalism based on the transfer integral. For a two-step electron hopping reaction, however, the required transfer integral is a different one, where one is only interested in the direct coupling between one electrode and the molecule for each of the two reactions.

In Paper III we have shown, that the transfer integral is in principle both energy and k -point dependent, because it is related to the density of states in the metallic electrode. In order to make the comparison between our coherent and incoherent transport results as consistent as possible, a simplified scheme compared with the definitions in Paper III on the basis of Landauer theory was applied as it was already deduced and used in a publication by Stadler and Marcussen.⁷² This scheme exploits the fact that the width of a peak in a single MO transmission function calculated in Landauer theory is directly related to H_{DA} on a single particle level. Accordingly, for a given molecular orbital MOX H_{DA} can be computed by a numerical fit of a Lorentzian function of the form

$$T_{MOX}(E) = \frac{4H_{DA,MOX}^2}{4H_{DA,MOX}^2 + (E - \epsilon_{MOX})^2}. \quad (9.15)$$

9.3 Incoherent single molecule conductance

For a direct comparison of the conductance for a particular compound from coherent tunnelling and electron hopping, an appropriate definition of it for both regimes is necessary. In our work we limited the descriptions to the case of an infinitesimally small source-drain voltage in order to exclude finite bias effects. Within Landauer theory this zero bias conductance G_{coh} is defined as a product of the conductance quantum G_0 and the value of the dimensionless transmission function $T(E) = Tr(G_d \Gamma_L G_d^\dagger \Gamma_R)$, where G_d is the Green's function of the device and $\Gamma_{L/R}$ is the imaginary part of the lead self energies, as it was described in chapter 3.

The calculation of the conductance in Marcus theory, on the other side, is based on two consecutive hopping reactions, i.e. an electron (hole) jump onto and a subsequent jump from the molecule onto the other electrode. In Paper IV the first reaction consists of an oxidation of the molecule, which creates a positively charged compound followed by a reduction on the second metal surface, thereby creating the measured current by two consecutive jumps. In each of the two reactions only the transfer integral of one of the two metallic electrodes is involved, while the second electrode only contributes to ΔG_0 and λ . Therefore the reaction rates describing the electron jump at one of the two electrodes can be calculated according to equations 7.15 and 7.16, where the key parameters have to be determined with respect to the full junction system, as discussed in section 9.2.

In order to calculate the conductance one has to evaluate the reaction rates for both hopping steps and combine them according to kinetic theory. Migliore et al. have shown that the zero bias conductance based on incoherent two-step hopping can be calculated as¹⁴⁴

$$G_{hop,0V} = \frac{e^2}{k_b T} \frac{k_{ox,L} k_{red,R}}{k_{ox,L} + k_{red,L} + k_{ox,R} + k_{red,L}}. \quad (9.16)$$

where the direction of the electron transport has been chosen to be from the left (L) to the right (R) electrode.

For the case studied in our work the junction is symmetric regarding the electrodes and molecular structure in the transport direction, therefore resulting in identical electrode band structures and transfer integrals $H_{Au,Mol}$ on both sides. As a consequence, also the reaction rates are symmetric, that

is $k_{ox,L} = k_{ox,R}$ and $k_{red,L} = k_{red,R}$, and the conductance in equation 9.16 can be simplified to

$$G_{hop} = \frac{e^2}{2k_b T} \frac{k_{ox} k_{red}}{k_{ox} + k_{red}}. \quad (9.17)$$

9.3.1 Influence of an electrochemical gate

One of the main advantages of an electrochemical cell in an experimental setup is that a gate potential can be applied in a single molecule junction without a third electrode on the nanoscale.^{35,36,185} An overpotential η introduced via a third electrode, being part of the macroscopic setup of the electrochemical cell, however, can still be applied, which changes the conductance by shifting the molecular eigenstates' energies relative to the electrode's Fermi level, thus moving them into the bias window scanned in the experiments (for a more detailed description see the introduction of chapter 5). In a single particle description such a shift is achieved by a direct change of ΔG^0 , as it was first shown by Ulstrup et al.,¹⁴² which redefines the transfer rates into

$$k_{red,\eta} = \frac{2\pi}{\hbar} \frac{1}{\sqrt{4\lambda k_b T}} \cdot \int_{-\infty}^{\infty} H_{DA}^2(\epsilon) e^{-\frac{(\lambda - \Delta G_{\eta}^0 + \epsilon)^2}{4\lambda k_b T}} f(\epsilon) d\epsilon, \quad (9.18)$$

and

$$k_{ox,\eta} = \frac{2\pi}{\hbar} \frac{1}{\sqrt{4\lambda k_b T}} \cdot \int_{-\infty}^{\infty} H_{DA}^2(\epsilon) e^{-\frac{(\lambda + \Delta G_{\eta}^0 + \epsilon)^2}{4\lambda k_b T}} [1 - f(\epsilon)] d\epsilon, \quad (9.19)$$

with $\Delta G_{\eta}^0 = \Delta G^0 + e\eta$.

Figure 9.2 shows how the applied overvoltage influences the reaction rates in the junction as well as the resulting conductance for a two step hopping reaction. As expected from equations 9.18 and 9.19, the transfer rates shown in the left panel take the form of error functions. These error functions cross at $-\Delta G^0$ and their inflection point is shifted by $\mp\lambda$ with respect to $-\Delta G^0$. The mirroring of the two error functions arises from the Fermi-Dirac distributions, which determine whether the occupied or unoccupied metal bands participate in the reaction. Relating this functional behaviour

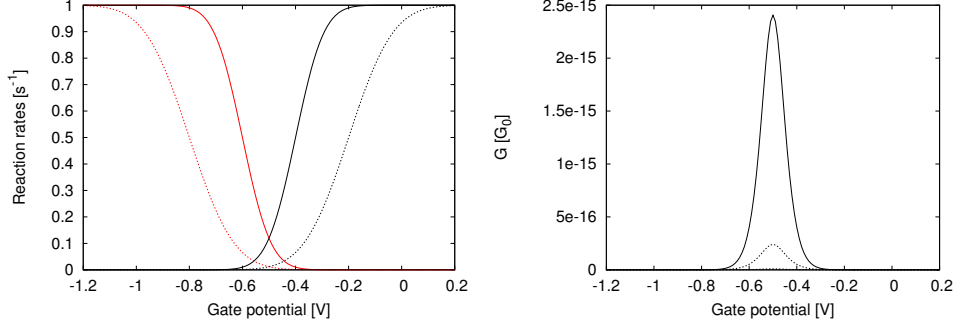


Figure 9.2: Gate dependence of the reaction rates, defined in equations 9.18 and 9.19 (left panel), and the conductance according to equation 9.17 (right panel) shown at two different values for λ , where the solid lines correspond to a calculation with $\lambda=0.1\text{eV}$ and the dotted lines represent $\lambda=0.3\text{ eV}$. ΔG^0 has been set to 0.5eV and the electrodes have been approximated by a wide band limit in both panels. In the left panel k_{ox} and k_{red} , shown in red and black respectively, are normalised by setting $\frac{2\pi}{\hbar}H_{DA}^2=1$.

to the two-step hopping conductance reveals a maximum in the conductance, when $e\eta$ cancels ΔG^0 completely, i.e. for $\Delta G_\eta^0 = 0$. The absolute value of the conductance in the right panel of figure 9.2 at this resonance gate potential on the other side depends on the value of the reorganisation energy, which is responsible for the outward shift of $k_{ox,\eta}$ and $k_{red,\eta}$ with respect to $-\Delta G^0$. The influence of the electronic coupling was neglected in figure 9.2 by setting the super exchange rate $\frac{2\pi}{\hbar}H_{DA}^2$ to one. In a practical system, however this preexponential factor scales the reaction rates and changes their maximum to $\frac{2\pi}{\hbar}H_{DA}^2$. This scaling is directly projected onto the conductance accordingly.

9.4 Outline of Results and Discussion of Paper IV

The most striking finding in Paper IV is that, while the conductance in the coherent tunnelling regime exhibited an exponential decay of conductance as expected, we found that the conductance resulting from electron hopping does even rise with the length of the molecular wire for small lengths. The reason for this initial increase is that the reduction of the molecular HOMO-LUMO gap with the number of contained atoms results in a decrease of ΔG_0 and therefore an increase in the exponential function in $k_{ox/red}$. In addition, the reorganisation energy is also lower for higher molecular lengths,

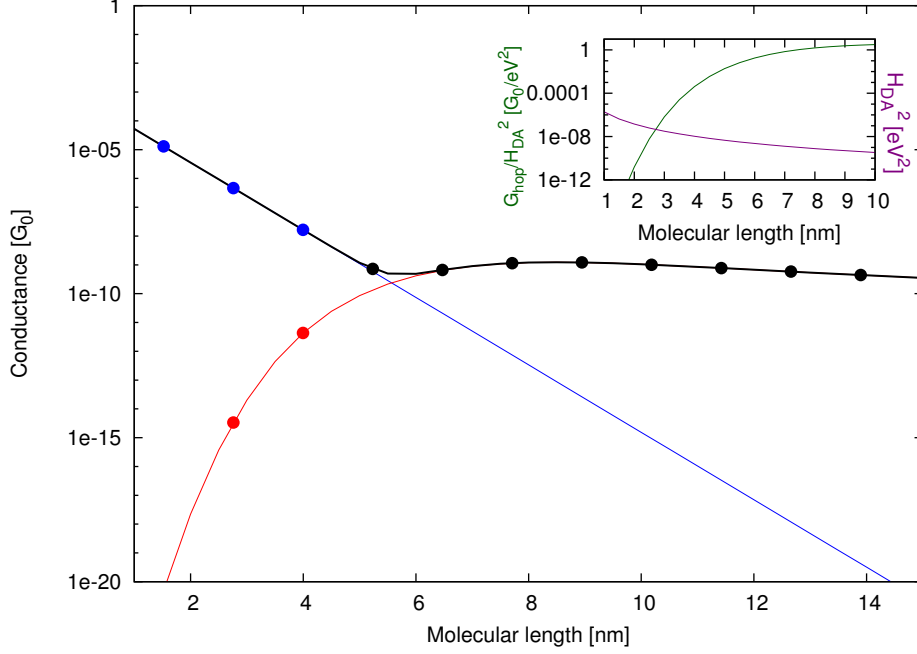


Figure 9.3: Molecular length dependence of the single molecule conductance from coherent tunnelling G_{coh} (shown in blue) and two step electron hopping G_{hop} (marked in red). The conductance, which would be accessible to experiments for such molecular wires, being $G_{coh} + G_{hop}$, is represented by the black line. The coloured dots on each line refer to the values directly calculated from DFT for up to three Ru-centres, while the values for higher molecular lengths, marked with black dots, have been determined via extrapolation of the key parameters in Marcus theory and assuming exponential decay for G_{coh} . The respective evolution of the transfer integral H_{DA}^2 (purple line) and the remaining factor G_{hop}/H_{DA}^2 (green line), which is exclusively defined by ΔG^0 and λ are shown in the inset.

which can be attributed to the added charge being delocalised over a wider area. The electronic coupling, however, decreases rapidly with the molecular length, which dominates the behaviour of G_{hop} at large molecular wire lengths.

We further extrapolated our results in order to determine, where the two conductance values corresponding to electron hopping and coherent tunnelling, respectively, cross. The result of this extrapolation is shown in Figure 9.3. We could determine that the molecular length corresponding to the crossing point is at 5.76 nm, which is in good agreement with other transition lengths for similar molecular wires found in the literature.^{186–189}

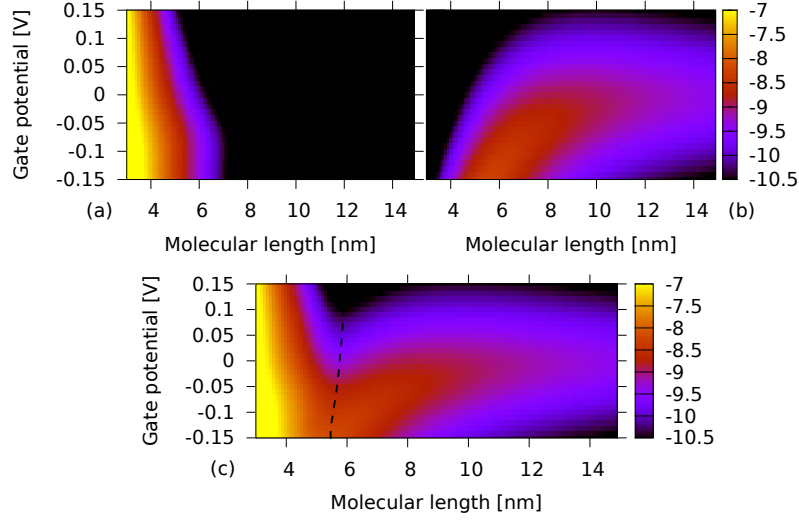


Figure 9.4: Extension of the length dependence shown in figure 9.3 into a second dimension with an applied gate potential as an additional coordinate, where the contour plots contain G_{coh} (a), G_{hop} (b) and $G_{coh}+G_{hop}$ (c). The numbers given in the colour code on the side of the panels refer to a logarithmic scale and should be understood as powers of ten. The black dashed line in panel (c) represents the crossover point between G_{coh} and G_{hop} .

Finally we examined the gate dependence of this conductance crossing point. The result is shown in Figure 9.4. We found that the change in the critical molecular length is minor when an electrochemical gate voltage is introduced into the junction. The reason for that is that both coherent tunnelling and electron hopping depend on the energetic position of the molecular HOMO with respect to the metal's Fermi level. Therefore a shift of the eigenstates arising from a gate potential influences both conductances in the same direction, but slightly favouring electron hopping at negative gate potentials (a HOMO shift towards E_F) due to the faster decay of the Gaussian tails compared with the typical Lorentzian form in coherent tunnelling. As a consequence a slight almost linear shift of the critical length towards shorter molecular lengths has been found. For a more detailed discussion of the results, which have been shortly summarised in this section, I refer to Paper IV included in the thesis.

Redox switching in single molecule junctions (Paper V)

The aim of Paper V was the identification and characterisation of the mechanism behind hysteresis features observed in the current-voltage curves in break junction experiments performed by our collaborators at IBM Zürich. The molecular compounds within the junctions under study for this task were three transition metal complexes differing in the species of the central metal atom (see figure 10.1).

While all three compounds exhibited hysteresis features in the I/V-measurements, only the Mo-complex has shown an abrupt switching in the conductance, which could be preserved even when the bias was turned back to low values. We elaborated a model which explains these hysteresis effects as well as the abrupt switching of the conductance with electron hopping reactions between two redox states with different coherent tunnelling conductances. In order to enable this kind of hysteresis a molecular eigenstate, only weakly coupled to the electrodes has to be present on the molecule in the junction. This MO does not (or only marginally) contribute to the conductance, but is crucial for the electron hopping reactions, which are responsible for the switching.

This chapter is organised in the following way: First calculations for the ground state of the three molecules are presented, where our reasoning leading to the selection of the model is also explained. Then the applied formalism is introduced and our choices for its different parameters are motivated and discussed. Finally, an outline of the results of Paper V including a comparison with the experiments of our partners is given.

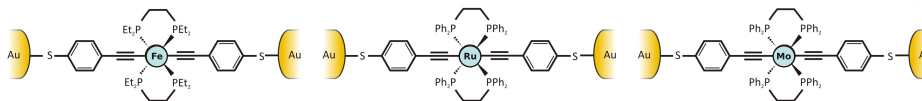


Figure 10.1: Chemical structures of the three compounds studied in Paper V, namely *trans* - $(SC_6H_4C \equiv C)_2M(1,2 - bis(diphenylphosphino)ethane)_2$ ($M = Mo, Ru$) and *trans* - $(SC_6H_4C \equiv C)_2M(1,2 - bis(diethylphosphino)ethane)_2$ ($M = Fe$), where the junction configuration is shown.

10.1 Motivation

Encouraged by the appearance of hysteresis in some of the experiments performed in Paper II, Paper V is the result of an application of similar transition metal complexes as single molecule switches. For this purpose the molecular structure has been simplified by substituting the dinuclear iron compounds, with complexes containing only one metal atom, which was varied to be Fe, Ru or Mo, respectively. Performing MCBJ based I/V sweeps on the three compounds revealed, that all of them exhibit hysteresis, but only the Mo-complex has the ability to switch into a 1000 times higher conducting state irreversibly.

From a theory perspective it was now a challenge to identify the switching mechanism responsible for these experimental findings. From differences in the electronic structure for the three compounds an explanation could be proposed combining coherent tunnelling and electron hopping, whose implementation within DFT has not been achieved before to our best knowledge.

10.2 Electronic ground states calculated within DFT

One of our main findings in Paper V was that the nature of the electronic ground state of the Mo-complex compared with the Fe/Ru-compounds, as illustrated in figure 10.1, is crucial for explaining its unique ability to exhibit irreversible switching behaviour. In this section the electronic structure details defining the MO eigenvalues and occupations for the three molecules in vacuum and in the junction environment are provided. For this purpose both predictions from Ligand Field Theory (LFT)¹⁹⁰ as well as DFT electronic structure calculations are presented and compared.

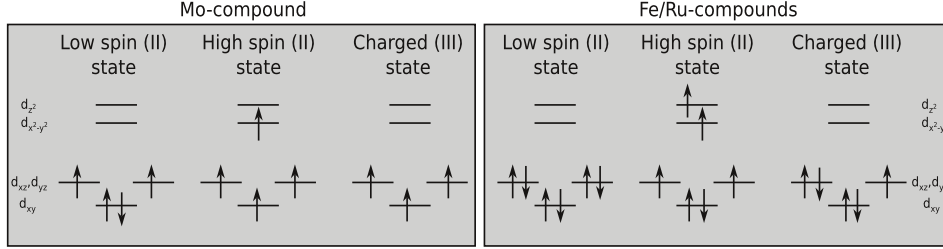


Figure 10.2: Energetic ordering and electron occupations of the d-orbitals in an octahedral ligand field according to Ligand Field Theory for the three studied compounds, where the symmetry of the respective d-states is denoted explicitly.

10.2.1 Predictions from Ligand Field Theory

As a starting point for our investigation of the ground state of transition metal complexes we analysed the nuclear configurations of the three compounds with an emphasis on the symmetry of the ligand shells around the metal cores. The studied complexes consist of the transition metal, with four ligands, namely 1,2-bis(diphenylphosphino)ethane for the Mo- and Ru-compounds and 1,2-bis(diethylphosphino)ethane for the Fe-molecule, situated quadratically in a plane perpendicular to the transport direction. Additionally, two ligands in transport direction are bound covalently with shorter Me-C distances completing the overall octahedral ligand structure and allowing for a delocalisation of the molecular π -system from lead to lead. A prediction of the energetic MO ordering in such a geometry can be made via LFT including Jahn Teller distortion in transport (z) direction, where the corresponding relative ordering of MO eigenenergies is shown in figure 10.2. The model predicts a lower lying d_{xy} orbital, with respect to d_{xz} and d_{yz} , while the e_g orbitals, namely $d_{x^2-y^2}$ and d_{z^2} are situated higher in energy.

In the lowspin state, which has been determined to be the ground state of all three systems by DFT total energy calculations, the filling of the respective eigenstates with electrons leads to an occupation of the t_{2g} orbitals, with four and six electrons for MO(II) and Fe(II)/Ru(II) respectively. Hence, a singlet state is predicted to be the ground state for the iron and ruthenium compounds, while the Mo-complex exhibits a net spin moment of 1 and therefore has a paramagnetic triplet state as its most stable electronic configuration.

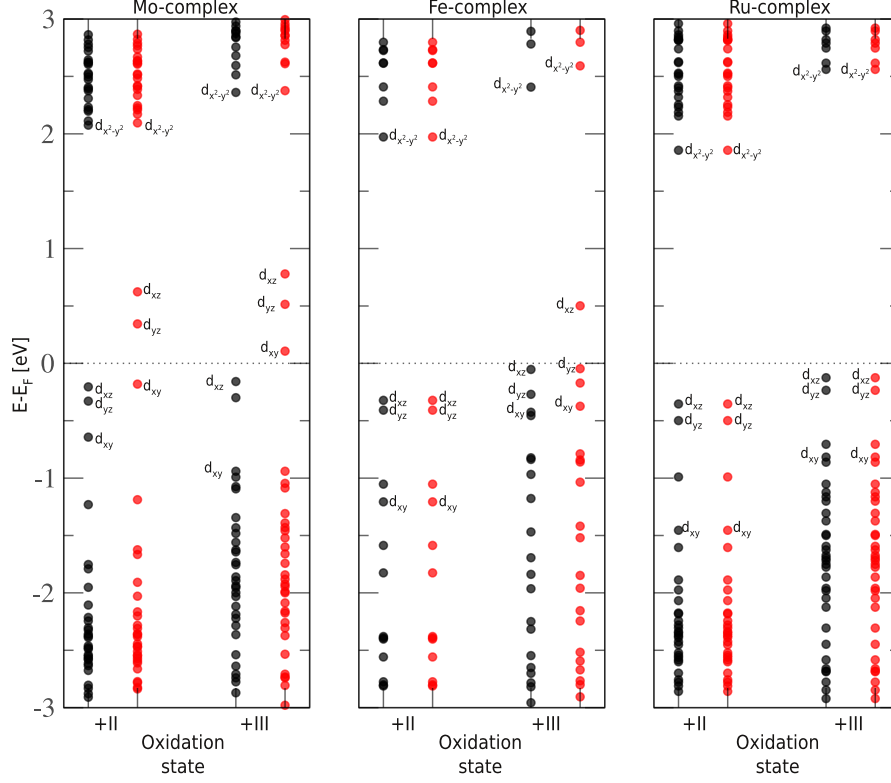


Figure 10.3: Molecular eigenvalues for the neutral and charged state of the three transition metal complexes as obtained from the junction setup by subdiagonalisation of the molecular subspace of the transport Hamiltonian with respect to the metal Fermi energy. The spin up and spin down eigenvalues have been marked by black and red circles, respectively

10.2.2 DFT results

The respective ground state MO spectra computed from DFT calculations in a junction environment with a subsequent subdiagonalisation of the molecular subspace of the transport Hamiltonian are shown in figure 10.3. These results are in perfect agreement with the predictions given in the last section exhibiting no spin splitting in the ground state of the Fe(II) and Ru(II) compounds, while in the Mo(II) complex only the lower lying d_{xy} -orbital is fully occupied as a result of the spin polarisation of the Kohn-Sham orbitals. Furthermore, the energy splitting between the spin up and spin down orbitals of the Mo(II)-complex changes the sequence, resulting in the d_{xy} orbital now becoming the molecular HOMO.

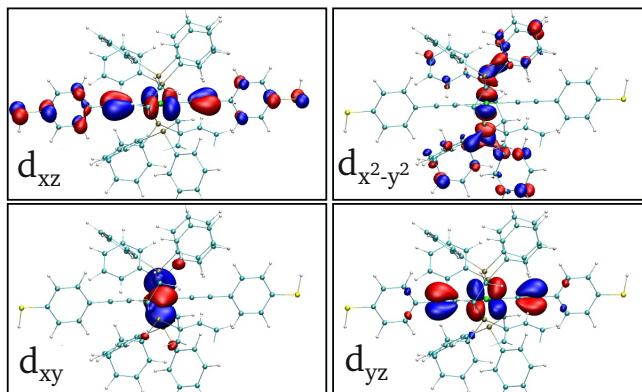


Figure 10.4: Spatial shape of the respective MOs containing contributions from the transition metal d-orbitals found in all three compounds, but with different energetical ordering.

The spatial distributions of the frontier orbitals, situated near the Fermi Level of the electrodes in a junction setup, are shown in Figure 10.4. It can be seen clearly that the d_{xz} and d_{yz} metal AOs hybridise with the C-ligands resulting in conjugated MOs, whose contribution to the phase coherent conductance is most likely decisive. On the other side, the $d_{x^2-y^2}$ and d_{xy} orbitals are not oriented along the transport direction, therefore not contributing to a conductance based on coherent tunnelling. Their very low (but still finite) coupling to the metallic bands, however, makes them still accessible for electron hopping reactions onto/from them, which could explain hysteresis or switching features in I/V measurements, if a so created charged state would exhibit a long enough lifetime.

10.3 The redox hysteresis model

10.3.1 Model setup

The model for the description of hysteresis features and switching events, which we applied in Paper V is based on the theoretical considerations of Migliore and Nitzan,⁴⁰ who identified a possible reason for hysteresis in the occurrence of two electron transfer reactions, which can happen simultaneously, but on different time scales. While the faster reaction in this so called two channel model is defining the measured conductance, the slower one is

the reason for an observed hysteresis or switching. Translating this framework into a single molecule junction setup the coherent electron transport is mainly responsible for the conductance, therefore being the "fast channel". The most reasonable mechanism for the switching in conductance for the molecules in figure 10.1 has been determined to be a change in the redox state via electron hopping onto a localised state on the molecule.

10.3.2 The transition rate

With a redox reaction as the source of the observed hysteresis features, the definition of the corresponding rates can be calculated as electron transfer rates according to Marcus theory. For their definition, the formalism established in Paper IV can be applied, but it has to be extended in order to account for measurements performed at finite bias:

$$R_{ox,L}(V) = \frac{2\pi}{\hbar} H_{X,L}^2 \frac{1}{\sqrt{4\pi\lambda k_b T}} \int e^{-\frac{(\lambda - \Delta G_X^0 + \epsilon + eV/2)^2}{4\lambda k_b T}} (1 - f(\epsilon)) d\epsilon \quad (10.1)$$

$$R_{red,L}(V) = \frac{2\pi}{\hbar} H_{X,L}^2 \frac{1}{\sqrt{4\pi\lambda k_b T}} \int e^{-\frac{(\lambda + \Delta G_X^0 + \epsilon + eV/2)^2}{4\lambda k_b T}} f(\epsilon) d\epsilon, \quad (10.2)$$

$$R_{ox,R}(V) = \frac{2\pi}{\hbar} H_{X,R}^2 \frac{1}{\sqrt{4\pi\lambda k_b T}} \int e^{-\frac{(\lambda - \Delta G_X^0 + \epsilon - eV/2)^2}{4\lambda k_b T}} (1 - f(\epsilon)) d\epsilon \quad (10.3)$$

$$R_{red,R}(V) = \frac{2\pi}{\hbar} H_{X,R}^2 \frac{1}{\sqrt{4\pi\lambda k_b T}} \int e^{-\frac{(\lambda + \Delta G_X^0 + \epsilon - eV/2)^2}{4\lambda k_b T}} f(\epsilon) d\epsilon. \quad (10.4)$$

The form of the driving force ΔG_X^0 and the transfer integrals $H_{X,K}$ follow the respective definitions given in section 9.2 with X denoting the MO involved in the reaction. The reorganisation energy λ , on the other side, has to be adapted to the experimental setup, where no solvent is present in the MCBJ measurements, which is simply achieved by excluding the solvent polarisation term leading to

$$\lambda_{tot} = \lambda_{in} + \lambda_{image}. \quad (10.5)$$

10.3.3 Hysteresis in a two-channel model

The simplest way to introduce our scheme for the description of redox-based switching is with a tight binding model system consisting of two MOs

in a junction setup, which in the following will be denoted as $|\alpha\rangle$ and $|\beta\rangle$. While $|\alpha\rangle$ exhibits a high degree of electron coupling to the electrodes therefore being the exclusively responsible for the conductance measured for the modelled junction, $|\beta\rangle$ is localised on the core of the molecule, therefore coupling only weakly to the electrodes and not contributing to coherent electron transport.

In the following ϵ_α denotes the energetic position of $|\alpha\rangle$ with respect to the Fermi level of the metal, which also defines the peak centre in the transmission function of the model system. The respective coupling values $H_{\alpha,K}$ characterise the width of this peak, leading to the following definition of the transmission function:

$$T(E) = G_0 \times \frac{4H_{\alpha,L}H_{\alpha,R}}{(H_{\alpha,L} + H_{\alpha,R})^2 + (\epsilon - \epsilon_\alpha)^2}. \quad (10.6)$$

Finally the corresponding I/V curve is defined by an integration over equation 10.6, where finite bias effects are not considered for this simple model system:

$$I = G_0 \times \int_{-\infty}^{\infty} T(E)(f(\epsilon, V/2) - f(\epsilon, -V/2))d\epsilon. \quad (10.7)$$

In this equation $f(\epsilon, \mp V/2) = 1/(e^{\frac{\epsilon \pm V/2}{k_b T}} + 1)$ are the Fermi-Dirac distributions for the metallic leads.

In order to describe hysteresis effects and switching, two different I/V curves are needed, one corresponding to the system before and one to that after the redox reaction has occurred. Within the present TB model these can be easily incorporated by a definition of two different eigenenergies $\epsilon_{\alpha,0}$ and $\epsilon_{\alpha,1}$, resulting in two different $T(E)$ and therefore changed I/V curves. In principle, also a modification of $H_{\alpha,K}$ due to the redox reaction could be included,¹⁴⁴ but for the sake of simplicity it is neglected within this model.

The corresponding I/V curves, describing the oxidised and reduced state of the molecule, respectively, serve as outer borders for the I/V curves appearing in measurements. As a next step the hopping reaction based on the weakly coupled MO ($|\beta\rangle$) has to be analysed regarding its time scale, in order to determine if and how often redox reactions happen within the time needed for the measurement of one current value in the experiment. Since only the net oxidation/reduction frequency is important for the de-

scription of a hysteresis effects in the measurement, the definition of the rates is simplified to $R_{ox} = R_{ox,L} + R_{ox,R}$ and $R_{red} = R_{red,L} + R_{red,R}$ in the following.

In contrast to the approach by Migliore and Nitzan of Ref.,⁴⁰ where the mean results of a certain number of bias sweeps was calculated in their equation 32, in our model as applied in Paper V the system was only allowed to reside in one of the oxidation states at any given point in time, which corresponds to the description of individual sweeps. Hence, the next step consists in the definition of a probability $P(V)$ for a redox state change for any given external voltage. For that purpose, two types of time intervals are defined, namely Δt , the experimental integration time used for obtaining the current for one point in the I/V-curves, and dt , which is a mere convergence parameter in our simulations, and which defines the time the system has for a single redox reaction. The definition of dt is important, since more than one redox reaction is possible within Δt and due to the integration of the number of electrons over this time interval only a mean current is measured. Introducing $dt \ll \Delta t$, according to

$$\Delta t = n dt \quad (10.8)$$

the time resolution inside a specific Δt window for the simulations is defined.

During Δt the applied voltage V is constant and as a consequence also $R_{ox/red}(V)$, resulting in $P(V)$ being defined by the simple product

$$P(V) = R_{ox}(V)dt \quad or \quad P(V) = R_{red}(V)dt \quad (10.9)$$

depending on the redox state of the compound at the beginning of each time interval dt .

At this point the stochastic nature of the approach becomes important. From its definition in equation 10.9 $P(V)$ could in principle have any values between 0 and infinity. Therefore, in order to define it as a proper probability with values between 0 and 1 one has to adjust dt accordingly, which does not qualitatively change the obtained results as will be shown in the next section.

In a next step $P(V)$ is compared with a random number x ranging from 0 to 1 in order to decide if a reaction takes place, allowing it only for $P(V)$

$> x$.

Finally, the current measured at each experimental bias point V within a time interval Δt can be obtained from our simulations by:

$$I(V)_{\Delta t} = \frac{1}{n} \sum_{i=1}^n I(V, s_i) \quad (10.10)$$

with

$$I(V, s_i) = (1 - s_i) \cdot I_{ox(red)}(V) + s_i \cdot I_{red(ox)}(V) \quad (10.11)$$

where $s_i \in \{0,1\}$ represents the redox state the system is in at the end of each dt window.

Influence of the values of dt and n

While at first glance the results of the formalism described in this section seem to depend on the choice of n and dt , it can be easily shown, that their influence is only that of a convergence parameter. For this purpose it is convenient to use a simple example, where dt is changed, while all other parameters in the model are kept constant:

For both examples in the following Δt will be kept fixed at 1s. During Δt also V is constant and therefore also R_{ox} and R_{red} , which are set to $1s^{-1}$. All in all, one would expect one hopping reaction to happen within Δt with this parameters, since $R_K \Delta t = 1$. Now instead we split the interval into 100 substeps, i.e. $n = 100, dt = 1/100s$. For this case $P(V) = 0.01$, which makes it probable (but not certain) that from 100 possible reactions only one electron jump and associated change of the redox state of the compound takes place. The precise moment within Δt , at which this reaction happens is completely dependent on the random number x and so is the final value of $I(V)_{\Delta t}$.

Modifying dt to $1/1000s$ and therefore also n to 1000, changes the value of $P(V)$ to $1/1000$ accordingly, which means that while the probability of an electron jump is ten times lower, there are also ten times more possibilities for it to occur. Hence, it is still most likely, that only one hopping reaction happens during Δt . The difference to the first parameter set is that now more intermediate values between I_{red} and I_{ox} are possible due to the higher time resolution, which identifies dt as a mere convergence parameter, which is still crucial for the quality of the number obtained from our simulations.

10.4 Description of hysteresis and switching with parameters obtained from DFT

When replacing the two-state TB model by a description based on DFT, the model needs to be modified. The most prominent difference is that the I/V curves for the neutral and charged state are not determined for chosen parameters anymore, but are based on the transmission functions of the two states, as obtained from NEGF-DFT calculations. Therefore, the outer borders in resulting I/V curves, defined by I_{ox}/V and I_{red}/V , are now directly related to the eigenvalue spectrum of the compounds with respect to the metal's chemical potential. In Paper V the corresponding I/V curves have been calculated from an integration over $T(E)$ calculated within Landauer theory, as described in chapter 3. This is straightforward for the neutral state and in order to determine the transmission function of the charged state, the charging scheme developed in Paper I has been applied.

In addition to the changes for the “fast channel” also the description of the slow channel needs to be modified for real systems. The key parameters for electron hopping now have to be determined based on the atomistic results, where in Paper V a single particle DFT description was chosen as it was also applied in Paper IV and the corresponding quantities were determined accordingly.

Finally, the sweeping parameters, namely $\Delta t, \Delta V, V_{max}$ and T , are determined from the experimental setup. This leaves only n or dt (related via equation 10.8) to be freely chosen in the simulation, where it has been shown earlier, that their only purpose is to function as convergence parameters in the simulation.

10.5 Outline of results and discussion of Paper V

10.5.1 Experimental results

For all three compounds hysteresis effects in the MCBJ measurements performed with UHV at 50K have been observed, where they differ in the sense that for the Fe-complex these effects were measured in 85% , for the Ru-complex in 80% and for the Mo-compound in 95% of the individual mea-

surements. In all three compounds hysteresis, denoted as type I switching in Paper V, occurs when forward and backward sweeping rate are chosen differently. This kind of hysteresis does not affect the conduction gap and exhibits a continuous transition between the I/V curves for the neutral and charged state.

For the Mo-complex, however, a second type of hysteresis was observed, which is characterised by an abrupt irreversible switching in conductance (denoted as type II switching) at higher voltages. These measured curves exhibit ON currents, which are 100 times lower than for the ones in the I/V curves described in the last paragraph and this behaviour is only found at the longest elongated junction shortly before the breaking point.

While for type I hysteresis ratios between ON and OFF states around 1.5 to 20 could be determined, the type II switching in the Mo-compound led to ratios between the currents for the two states of the molecular switch exceeding 1000.

10.5.2 Theoretical results

By applying the model described in the last sections, we were able to reproduce the key characteristics of the experimentally determined I/V-curves, namely hysteresis features for the Fe- and the Ru-complexes and both reversible and irreversible switching for the Mo-complex.

The differences in measurements for the three investigated compounds has been identified to arise from corresponding differences in the nature of the ground states of the molecules, where the Mo-complex was the only one of the three exhibiting spin polarisation. This results in a shift of the highly localised d_{xy} into the range which is accessible for an applied bias, and allows for redox reactions with a very low hopping rate possible.

For the other two compounds, the HOMO-1 exhibiting the d_{yz} orbital symmetry on the metal centre has been identified as the slow channel for the hopping reaction. Its electronic coupling to the electrodes, however, has been determined to be two orders of magnitude higher than the one for the d_{xy} orbital of the Mo-complex. Therefore, the redox reactions for Fe and Ru only cause a small delay in the response of the system to an applied voltage. In principle, such a delay does not result in hysteresis effects, for a constant sweeping rate, but pockets can be found in the I/V-curves when the forward and backward sweeping rate differ, as it was the case for the

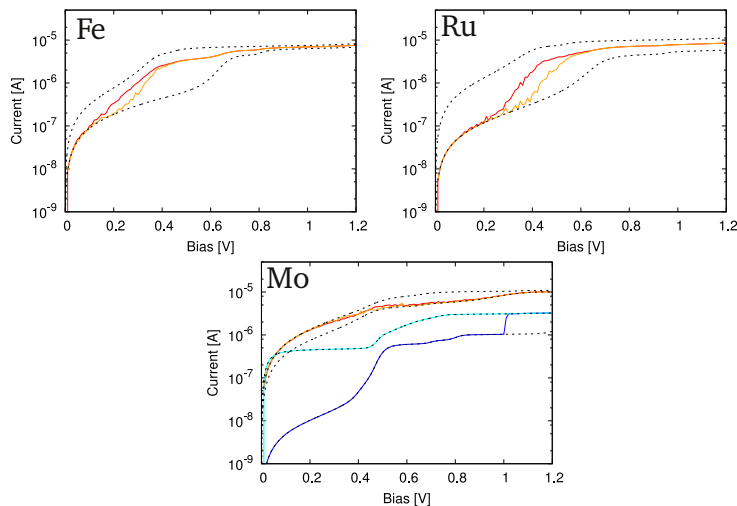


Figure 10.5: Calculated I/V curves using a combination of NEGF-DFT and the model described in section 10.3, where only the positive bias branch is shown since in the model system a complete symmetry regarding the bias direction is assumed as justified by the inversion symmetry of the molecules.

experiments carried out by our partners. Applying our model the formation of pockets in the I/V curves could be reproduced nicely, when the sweeping rates depended on the sweeping direction, as can be seen from the simulation results shown in figure 10.5.

The same kind of pocket formation was also found for the Mo-complex adsorbed in hollow position at equilibrium distance, as shown by the red/orange curves in the right panel of figure 10.5. In order to simulate a situation, where the system is stretched and near the rupture point, we also analysed the junction setup for an elongated S-Au distance, where we found that the electronic coupling is further reduced by an order of magnitude. Applying our hysteresis model to this junction system led to the appearance of type II switching in the simulation, as shown by the blue/cyan curves in the right panel of figure 10.5. Additionally the reduction in measured current could be reproduced by the simulations for such an elongated setup, which is a further consequence of the decrease in electronic coupling to the electrodes, but now directly affecting the phase coherent electron transport, i.e. the "fast channel".

It has to be noted, however, that in order to achieve a correspondence of experimental and theoretical result, we had to scale the electronic cou-

pling of the slow channel down by a factor of 100 for all three systems. We attributed this necessity to two causes, namely to the self interaction error within DFT, which tends to increase the spatial extension of localised orbitals, therefore increasing the through vacuum coupling and on the other hand the highly symmetric setup used in the simulations with two perfectly planar Au(111) surfaces, which is in distinct contrast with the much more disordered junction geometry expected for the MCBJ experiments.

Overall, the results from theory and experiment have shown an excellent qualitative agreement and further experimental details as well as further analysis can be found in Paper V included in this thesis.

Bibliography

- ¹ J. Bardeen and W. H. Brattain, "The Transistor, A Semi-Conductor Triode," *Phys. Rev.*, vol. 74, pp. 230–231, Jul 1948.
- ² G. Moore, "Cramming More Components Onto Integrated Circuits," *Proceedings of the IEEE*, vol. 86, pp. 82–85, Jan 1998.
- ³ "Device photolithography: Foreword," *Bell System Technical Journal, The*, vol. 49, pp. 1995–1996, Nov 1970.
- ⁴ A. Aviram and M. A. Ratner, "Molecular rectifiers," *Chemical Physics Letters*, vol. 29, no. 2, pp. 277 – 283, 1974.
- ⁵ A. Aviram, C. Joachim, and M. Pomerantz, "Evidence of switching and rectification by a single molecule effected with a scanning tunneling microscope," *Chemical Physics Letters*, vol. 146, no. 6, pp. 490 – 495, 1988.
- ⁶ W. Chen, J. R. Widawsky, H. Vázquez, S. T. Schneebeli, M. S. Hybertsen, R. Breslow, and L. Venkataraman, "Highly Conducting π -Conjugated Molecular Junctions Covalently Bonded to Gold Electrodes," *Journal of the American Chemical Society*, vol. 133, no. 43, pp. 17160–17163, 2011. PMID: 21939263.
- ⁷ W. Hong, H. Li, S.-X. Liu, Y. Fu, J. Li, V. Kaliginedi, S. Decurtins, and T. Wandlowski, "Trimethylsilyl-Terminated Oligo(phenylene ethynylene)s: An Approach to Single-Molecule Junctions with Covalent Au–C σ -Bonds," *Journal of the American Chemical Society*, vol. 134, no. 47, pp. 19425–19431, 2012. PMID: 23126569.
- ⁸ S. Stojkovic, C. Joachim, L. Grill, and F. Moresco, "The contact conductance on a molecular wire," *Chemical Physics Letters*, vol. 408, no. 1–3, pp. 134 – 138, 2005.
- ⁹ L. Lafferentz, F. Ample, H. Yu, S. Hecht, C. Joachim, and L. Grill, "Conductance of a Single Conjugated Polymer as a Continuous Function of Its Length," *Science*, vol. 323, no. 5918, pp. 1193–1197, 2009.
- ¹⁰ Kim, J. M. Beebe, C. Olivier, S. Rigaut, D. Touchard, J. G. Kushmerick, X.-Y. Zhu, and C. D. Frisbie, "Temperature and Length Dependence of Charge Transport in Redox-Active Molecular Wires Incorporating Ruthenium(II) Bis(σ -arylacetylide) Complexes," *The Journal of Physical Chemistry C*, vol. 111, no. 20, pp. 7521–7526, 2007.
- ¹¹ L. Luo, A. Benameur, P. Brignou, S. H. Choi, S. Rigaut, and C. D. Frisbie, "Length and Temperature Dependent Conduction of Ruthenium-Containing Redox-Active Molecular Wires," *The Journal of Physical Chemistry C*, vol. 115, no. 40, pp. 19955–19961, 2011.
- ¹² R. Yamada, H. Kumazawa, T. Noutoshi, S. Tanaka, and H. Tada, "Electrical Conductance of Oligothiophene Molecular Wires," *Nano Letters*, vol. 8, no. 4, pp. 1237–1240, 2008. PMID: 18311936.
- ¹³ Y. Karzazi, J. Cornil, and J. L. Brédas, "Resonant Tunneling Processes along Conjugated Molecular Wires: A Quantum-Chemical Description," *Adv. Funct. Mater.*, vol. 12, pp. 787–794, 2002.
- ¹⁴ C. Nacci, F. Ample, D. Blegier, S. Hecht, C. Joachim, and L. Grill, "Conductance of a single flexible molecular wire composed of alternating donor and acceptor units," *Nature Communications*, vol. 6, p. 7397, 2015.
- ¹⁵ M. Irie, "Diarylethenes for Memories and Switches," *Chemical Reviews*, vol. 100, no. 5, pp. 1685–1716, 2000. PMID: 11777416.
- ¹⁶ D. Dulić, S. J. van der Molen, T. Kudernac, H. T. Jonkman, J. J. D. de Jong, T. N. Bowden, J. van Esch, B. L. Feringa, and B. J. van Wees, "One-Way Optoelectronic Switching of Photochromic Molecules on Gold," *Phys. Rev. Lett.*, vol. 91, p. 207402, Nov 2003.
- ¹⁷ A. J. Kronemeijer, H. B. Akkerman, T. Kudernac, B. J. van Wees, B. L. Feringa, P. W. M. Blom, and B. de Boer, "Reversible Conductance Switching in Molecular Devices," *Advanced Materials*, vol. 20, no. 8, pp. 1467–1473, 2008.

BIBLIOGRAPHY

- ¹⁸ T. Sendler, K. Luka-Guth, M. Wieser, Lokamani, J. Wolf, M. Helm, S. Gemming, J. Kerbusch, E. Scheer, T. Huhn, and A. Erbe, "Light-Induced Switching of Tunable Single-Molecule Junctions," *Advanced Science*, vol. 2, no. 5, pp. n/a–n/a, 2015.
- ¹⁹ A. S. Blum, J. G. Kushmerick, D. P. Long, C. H. Patterson, J. C. Yang, J. Henderson, Y. Yao, J. M. Tour, R. Shashidhar, and B. R. Ratna, "Molecularly inherent voltage-controlled conductance switching," *Nature Materials*, vol. 4, p. 167, 2005.
- ²⁰ E. Lörtscher, J. Ciszek, J. Tour, and H. Riel, "Reversible and Controllable Switching of a Single-Molecule Junction," *Small*, vol. 2, no. 8-9, pp. 973–977, 2006.
- ²¹ J. Mielke, S. Selvanathan, M. Peters, J. Schwarz, S. Hecht, and L. Grill, "Molecules with multiple switching units on a Au(111) surface: self-organization and single-molecule manipulation," *Journal of Physics: Condensed Matter*, vol. 24, no. 39, p. 394013, 2012. Although switching could not be achieved in the adsorbed molecules, the methodology and systems are common for such a kind of switching mechanism.
- ²² M. Alemani, M. V. Peters, S. Hecht, K.-H. Rieder, F. Moresco, and L. Grill, "Electric Field-Induced Isomerization of Azobenzene by STM," *Journal of the American Chemical Society*, vol. 128, no. 45, pp. 14446–14447, 2006. PMID: 17090013.
- ²³ C. Dri, M. V. Peters, J. Schwarz, S. Hecht, and L. Grill, "Spatial periodicity in molecular switching," *Nature Nanotechnology*, vol. 3, pp. 649 – 653, 2008.
- ²⁴ F. Moresco, G. Meyer, K.-H. Rieder, H. Tang, A. Gourdon, and C. Joachim, "Conformational Changes of Single Molecules Induced by Scanning Tunneling Microscopy Manipulation: A Route to Molecular Switching," *Phys. Rev. Lett.*, vol. 86, pp. 672–675, Jan 2001.
- ²⁵ F. Prins, M. Monrabal-Capilla, E. A. Osorio, E. Coronado, and H. S. J. van der Zant, "Room-Temperature Electrical Addressing of a Bistable Spin-Crossover Molecular System," *Advanced Materials*, vol. 23, no. 13, pp. 1545–1549, 2011.
- ²⁶ S. Wagner, F. Kisslinger, S. Ballmann, F. Schramm, R. Chandrasekar, T. Bodenstein, O. Fuhr, D. Secker, K. Fink, M. Ruben, and H. B. Weber, "Switching of a coupled spin pair in a single-molecule junction," *Nature Nanotechnology*, vol. 8, pp. 575–579, 2013.
- ²⁷ N. Baadji and S. Sanvito, "Giant Resistance Change across the Phase Transition in Spin-Crossover Molecules," *Phys. Rev. Lett.*, vol. 108, p. 217201, May 2012.
- ²⁸ J. Liao, J. S. Agustsson, S. Wu, C. Schönenberger, M. Calame, Y. Leroux, M. Mayor, O. Jeannin, Y.-F. Ran, S.-X. Liu, and S. Decurtins, "Cyclic Conductance Switching in Networks of Redox-Active Molecular Junctions," *Nano Letters*, vol. 10, no. 3, pp. 759–764, 2010. PMID: 20121193.
- ²⁹ S. Tsoi, I. Griva, S. A. Trammell, A. S. Blum, J. M. Schnur, and N. Lebedev, "Electrochemically controlled conductance switching in a single molecule: Quinone-modified oligo(phenylene vinylene)," *ACS Nano*, vol. 2, no. 6, pp. 1289–1295, 2008.
- ³⁰ N. Darwish, I. Díez-Pérez, S. Guo, N. Tao, J. J. Gooding, and M. N. Paddon-Row, "Single molecular switches: Electrochemical gating of a single anthraquinone-based norbornylogous bridge molecule," *The Journal of Physical Chemistry C*, vol. 116, no. 39, pp. 21093–21097, 2012.
- ³¹ S. Guo, J. M. Artés, and I. Díez-Pérez, "Electrochemically-gated single-molecule electrical devices," *Electrochimica Acta*, vol. 110, pp. 741 – 753, 2013.
- ³² C. P. Collier, E. W. Wong, M. Belohradský, F. M. Raymo, J. F. Stoddart, P. J. Kuekes, R. S. Williams, and J. R. Heath, "Electronically configurable molecular-based logic gates," *Science*, vol. 285, no. 5426, pp. 391–394, 1999.
- ³³ C. P. Collier, G. Mattersteig, E. W. Wong, Y. Luo, K. Beverly, J. Sampaio, F. M. Raymo, J. F. Stoddart, and J. R. Heath, "A [2]Catenane-Based Solid State Electronically Reconfigurable Switch," *Science*, vol. 289, no. 5482, pp. 1172–1175, 2000.
- ³⁴ T. Albrecht, A. Guckian, J. Ulstrup, and J. Vos, "Transistor effects and in situ STM of redox molecules at room temperature," *Nanotechnology, IEEE Transactions on*, vol. 4, pp. 430–434, July 2005.
- ³⁵ T. Albrecht, A. Guckian, J. Ulstrup, and J. G. Vos, "Transistor-like Behavior of Transition Metal Complexes," *Nano Letters*, vol. 5, no. 7, pp. 1451–1455, 2005. PMID: 16178256.
- ³⁶ T. Albrecht, K. Moth-Poulsen, J. B. Christensen, A. Guckian, T. B. rnholm, J. G. Vos, and J. Ulstrup, "In situ scanning tunnelling spectroscopy of inorganic transition metal complexes," *Faraday Discuss.*, vol. 131, pp. 265–279, 2006.

BIBLIOGRAPHY

- ³⁷ T. Albrecht, A. Guckian, A. M. K. J. G. Vos, and J. Ulstrup, "Mechanism of Electrochemical Charge Transport in Individual Transition Metal Complexes," *Journal of the American Chemical Society*, vol. 128, no. 51, pp. 17132–17138, 2006. PMID: 17177467.
- ³⁸ I. V. Pobelov, Z. Li, and T. Wandlowski, "Electrolyte Gating in Redox-Active Tunneling Junctions-An Electrochemical STM Approach," *Journal of the American Chemical Society*, vol. 130, no. 47, pp. 16045–16054, 2008.
- ³⁹ F. Pevny, E. D. Piazza, L. Norel, M. Drescher, R. F. Winter, and S. Rigaut, "Fully Delocalized (Ethinyl)(vinyl)phenylene-Bridged Diruthenium Radical Complexes," *Organometallics*, vol. 29, no. 22, pp. 5912–5918, 2010.
- ⁴⁰ A. Migliore and A. Nitzan, "Irreversibility and Hysteresis in Redox Molecular Conduction Junctions," *Journal of the American Chemical Society*, vol. 135, no. 25, pp. 9420–9432, 2013. PMID: 23679824.
- ⁴¹ A. Migliore and A. Nitzan, "Nonlinear Charge Transport in Redox Molecular Junctions: A Marcus Perspective," *ACS Nano*, vol. 5, no. 8, pp. 6669–6685, 2011. PMID: 21721583.
- ⁴² P. Hohenberg and W. Kohn, "Inhomogeneous Electron Gas," *Phys. Rev.*, vol. 136, pp. B864–B871, Nov 1964.
- ⁴³ L. H. Thomas, "The calculation of atomic fields," *Mathematical Proceedings of the Cambridge Philosophical Society*, vol. 23, pp. 542–548, 1926.
- ⁴⁴ E. Fermi, "Un metodo statistico per la determinazione di alcune proprieta dell' atome," *Rend. Accad. Naz. Lincei*, vol. 6, pp. 602–607, 1927.
- ⁴⁵ P. Dirac, "Note on Exchange Phenomena in the Thomas Atom," *Mathematical Proceedings of the Cambridge Philosophical Society*, vol. 26, pp. 376–385, 1930.
- ⁴⁶ W. Kohn and L. J. Sham, "Self-Consistent Equations Including Exchange and Correlation Effects," *Phys. Rev.*, vol. 140, pp. A1133–A1138, Nov 1965.
- ⁴⁷ Herman, Frank, V. Dyke, J. P., Ortenburger, and I. B., "Improved Statistical Exchange Approximation for Inhomogeneous Many-Electron Systems," *Phys. Rev. Lett.*, vol. 22, pp. 807–811, Apr 1969.
- ⁴⁸ J. Perdew, K. Burke, and M. Ernzerdorf, "General gradient approximation made simple," *Phys. Rev. Lett.*, vol. 23, pp. 3865–3868, 1996.
- ⁴⁹ J. J. Mortensen, L. B. Hansen, and K. W. Jacobsen, "Real-space grid implementation of the projector augmented wave method," *Physical Review B*, vol. 71, p. 035109, 2005.
- ⁵⁰ J. Enkovaara, C. Rostgaard, J. J. Mortensen, J. Chen, M. Dulak, L. Ferrighi, J. Gavnholt, C. Glinsvad, V. Haikola, H. A. Hansen, H. H. Kristoffersen, M. Kuisma, A. H. Larsen, L. Lehtovaara, M. Ljungberg, O. Lopez-Acevedo, P. G. Moses, J. Ojanen, T. Olsen, V. Petzold, N. A. Romero, J. Stausholm-Møller, M. Strange, G. A. Tritsarlis, M. Vanin, M. Walter, B. Hammer, H. Häkkinen, G. K. H. Madsen, R. M. Nieminen, J. K. Nørskov, M. Puska, T. T. Rantala, J. Schiøtz, K. S. Thygesen, and K. W. Jacobsen, "Electronic structure calculations with GPAW: a real-space implementation of the projector augmented-wave method," *Journal of Physics: Condensed Matter*, vol. 22, no. 25, p. 253202, 2010.
- ⁵¹ P. E. Blöchl, "Projector augmented-wave method," *Phys. Rev. B*, vol. 50, pp. 17953–17979, Dec 1994.
- ⁵² A. Kiejna, G. Kresse, J. Rogal, A. De Sarkar, K. Reuter, and M. Scheffler, "Comparison of the full-potential and frozen-core approximation approaches to density-functional calculations of surfaces," *Phys. Rev. B*, vol. 73, p. 035404, Jan 2006.
- ⁵³ I. Souza, N. Marzari, and D. Vanderbilt, "Maximally localized Wannier functions for entangled energy bands," *Phys. Rev. B*, vol. 65, p. 035109, Dec 2001.
- ⁵⁴ K. Thygesen and K. Jacobsen, "Molecular transport calculations with Wannier functions," *Chemical Physics*, vol. 319, no. 1–3, pp. 111 – 125, 2005. Molecular Charge Transfer in Condensed Media - from Physics and Chemistry to Biology and Nanoengineering in honour of Alexander M. Kuznetsov on his 65th birthday.
- ⁵⁵ M. Strange, I. S. Kristensen, K. S. Thygesen, and K. W. Jacobsen, "Benchmark density functional theory calculations for nanoscale conductance," *The Journal of Chemical Physics*, vol. 128, no. 11, pp. –, 2008.
- ⁵⁶ A. H. Larsen, M. Vanin, J. J. Mortensen, K. S. Thygesen, and K. W. Jacobsen, "Localized atomic basis set in the projector augmented wave method," *Phys. Rev. B*, vol. 80, p. 195112, Nov 2009.

BIBLIOGRAPHY

- ⁵⁷ O. F. Sankey and D. J. Niklewski, “Ab initio multicenter tight-binding model for molecular-dynamics simulations and other applications in covalent systems,” *Phys. Rev. B*, vol. 40, pp. 3979–3995, Aug 1989.
- ⁵⁸ J. Gavnholt, T. Olsen, M. Engelund, and J. Schiøtz, “ Δ self-consistent field method to obtain potential energy surfaces of excited molecules on surfaces,” *Phys. Rev. B*, vol. 78, p. 075441, Aug 2008.
- ⁵⁹ R. O. Jones and O. Gunnarsson, “The density functional formalism, its applications and prospects,” *Rev. Mod. Phys.*, vol. 61, pp. 689–746, Jul 1989.
- ⁶⁰ R. C. Ashoori, “Electrons in artificial atoms,” *Nature*, vol. 379, pp. 413–419, 1996.
- ⁶¹ R. de Picciotto, H. Stormer, L. Pfeiffer, K. W. Baldwin, and K. West, “Four-terminal resistance of a ballistic quantum wire,” *Nature*, vol. 411, pp. 51–54, 2001.
- ⁶² M. Büttiker, Y. Imry, R. Landauer, and S. Pinhas, “Generalized many-channel conductance formula with application to small rings,” *Phys. Rev. B*, vol. 31, pp. 6207–6215, May 1985.
- ⁶³ S. Datta, “Electrical resistance: an atomistic view,” *Nanotechnology*, vol. 15, no. 7, p. S433, 2004.
- ⁶⁴ L. V. Keldish, “Diagram technique for non-equilibrium processes,” *Soviet Physics JETP-USSR*, vol. 20, p. 1018, 1965.
- ⁶⁵ R. Landauer, “Spatial Variation of Currents and Fields Due to Localized Scatterers in Metallic Conduction,” *IBM J. Res. Dev.*, vol. 1, p. 233, 1957.
- ⁶⁶ M. Büttiker, “Symmetry of electrical conduction,” *IBM J. Res. Dev.*, vol. 32, p. 317, 1988.
- ⁶⁷ Y. Meir and N. S. Wingreen, “Landauer formula for the current through an interacting electron region,” *Phys. Rev. Lett.*, vol. 68, pp. 2512–2515, Apr 1992.
- ⁶⁸ N. D. Lang, “Resistance of atomic wires,” *Phys. Rev. B*, vol. 52, pp. 5335–5342, Aug 1995.
- ⁶⁹ H. Joon Choi and J. Ihm, “Ab initio pseudopotential method for the calculation of conductance in quantum wires,” *Phys. Rev. B*, vol. 59, pp. 2267–2275, Jan 1999.
- ⁷⁰ M. Brandbyge, J.-L. Mozos, P. Ordejón, J. Taylor, and K. Stokbro, “Density-functional method for nonequilibrium electron transport,” *Phys. Rev. B*, vol. 65, p. 165401, Mar 2002.
- ⁷¹ S. Datta, *Electronic transport in mesoscopic systems*. Cambridge ; New York : Cambridge University Press, 1st paperback ed., 1995. Includes bibliographical references and index.
- ⁷² R. Stadler and T. Markussen, “Controlling the transmission line shape of molecular t-stubs and potential thermoelectric applications,” *The Journal of Chemical Physics*, vol. 135, no. 15, pp. –, 2011.
- ⁷³ R. Stadler, “Conformation dependence of charge transfer and level alignment in nitrobenzene junctions with pyridyl anchor groups,” *Phys. Rev. B*, vol. 81, p. 165429, Apr 2010.
- ⁷⁴ T. Markussen, R. Stadler, and K. S. Thygesen, “The Relation between Structure and Quantum Interference in Single Molecule Junctions,” *Nano Letters*, vol. 10, no. 10, pp. 4260–4265, 2010. PMID: 20879779.
- ⁷⁵ P. Tröster, P. Schmitteckert, and F. Evers, “Transport calculations based on density functional theory, Friedel’s sum rule, and the Kondo effect,” *Phys. Rev. B*, vol. 85, p. 115409, Mar 2012.
- ⁷⁶ L. Yan, E. J. Bautista, and J. M. Seminario, “Ab initio analysis of electron currents through benzene, naphthalene, and anthracene nanojunctions,” *Nanotechnology*, vol. 18, no. 48, p. 485701, 2007.
- ⁷⁷ G. C. Solomon, J. R. Reimers, and N. S. Hush, “Single molecule conductivity: The role of junction-orbital degeneracy in the artificially high currents predicted by ab initio approaches,” *The Journal of Chemical Physics*, vol. 121, no. 14, pp. 6615–6627, 2004.
- ⁷⁸ G. Stefanucci and C.-O. Almbladh, “Time-dependent quantum transport: An exact formulation based on TDDFT,” *EPL (Europhysics Letters)*, vol. 67, no. 1, p. 14, 2004.
- ⁷⁹ F. Aryasetiawan and O. Gunnarsson, “The GW method,” *Reports on Progress in Physics*, vol. 61, no. 3, p. 237, 1998.
- ⁸⁰ K. S. Thygesen, “Impact of Exchange-Correlation Effects on the IV Characteristics of a Molecular Junction,” *Phys. Rev. Lett.*, vol. 100, p. 166804, Apr 2008.

BIBLIOGRAPHY

- ⁸¹ J. Xia, B. Capozzi, S. Wei, M. Strange, A. Batra, J. R. Moreno, R. J. Amir, E. Amir, G. C. Solomon, L. Venkataraman, and L. M. Campos, "Breakdown of Interference Rules in Azulene, a Nonalternant Hydrocarbon," *Nano Letters*, vol. 14, no. 5, pp. 2941–2945, 2014. PMID: 24745894.
- ⁸² K. S. Thygesen, B. M. V., and K. W. Jacobsen, "Conductance calculations with a wavelet basis set," *Phys. Rev. B*, vol. 67, p. 115404, 2003.
- ⁸³ Y. Xue, S. Datta, and M. A. Ratner, "First-principles based matrix Green's function approach to molecular electronic devices: general formalism," *Chemical Physics*, vol. 281, no. 2–3, pp. 151 – 170, 2002.
- ⁸⁴ X. Crispin, V. M. Geskin, C. Bureau, R. Lazzaroni, W. Schmickler, and J. L. Brédas, "A density functional model for tuning the charge transfer between a transition metal electrode and a chemisorbed molecule via the electrode potential," *The Journal of Chemical Physics*, vol. 115, no. 22, pp. 10493–10499, 2001.
- ⁸⁵ J. M. Garcia-Lastra, C. Rostgaard, A. Rubio, and K. S. Thygesen, "Polarization-induced renormalization of molecular levels at metallic and semiconducting surfaces," *Phys. Rev. B*, vol. 80, p. 245427, Dec 2009.
- ⁸⁶ R. Hesper, L. H. Tjeng, and G. A. Sawatzky, "Strongly reduced band gap in a correlated insulator in close proximity to a metal," *EPL (Europhysics Letters)*, vol. 40, no. 2, p. 177, 1997.
- ⁸⁷ S. Y. Sayed, J. A. Fereiro, H. Yan, R. L. McCreery, and A. J. Bergren, "Charge transport in molecular electronic junctions: Compression of the molecular tunnel barrier in the strong coupling regime," *Proceedings of the National Academy of Sciences*, vol. 109, no. 29, pp. 11498–11503, 2012.
- ⁸⁸ K. S. Thygesen and A. Rubio, "Nonequilibrium GW approach to quantum transport in nano-scale contacts," *The Journal of Chemical Physics*, vol. 126, no. 9, pp. –, 2007.
- ⁸⁹ P. Darancet, J. R. Widawsky, H. J. Choi, L. Venkataraman, and J. B. Neaton, "Quantitative Current-Voltage Characteristics in Molecular Junctions from First Principles," *Nano Letters*, vol. 12, no. 12, pp. 6250–6254, 2012. PMID: 23167709.
- ⁹⁰ J. B. Neaton, M. S. Hybertsen, and S. G. Louie, "Renormalization of Molecular Electronic Levels at Metal-Molecule Interfaces," *Phys. Rev. Lett.*, vol. 97, p. 216405, Nov 2006.
- ⁹¹ C. Rostgaard, K. W. Jacobsen, and K. S. Thygesen, "Fully self-consistent GW calculations for molecules," *Phys. Rev. B*, vol. 81, p. 085103, Feb 2010.
- ⁹² H. Vázquez, W. Gao, F. Flores, and A. Kahn, "Energy level alignment at organic heterojunctions: Role of the charge neutrality level," *Phys. Rev. B*, vol. 71, p. 041306, Jan 2005.
- ⁹³ N. Lang and W. Kohn, "Theory of metal surfaces: charge density and surface energy," *Phys. Rev. B*, vol. 1, p. 4555, 1970.
- ⁹⁴ P. S. Bagus, V. Staemmler, and C. Wöll, "Exchangelike Effects for Closed-Shell Adsorbates: Interface Dipole and Work Function," *Phys. Rev. Lett.*, vol. 89, p. 096104, Aug 2002.
- ⁹⁵ I. G. Hill, A. Rajagopal, A. Kahn, and Y. Hu, "Molecular level alignment at organic semiconductor-metal interfaces," *Applied Physics Letters*, vol. 73, no. 5, pp. 662–664, 1998.
- ⁹⁶ E. Bertel, "The interaction of rare gases with transition metal surfaces," *Surface Science*, vol. 367, no. 2, pp. L61 – L65, 1996.
- ⁹⁷ R. Stadler and K. W. Jacobsen, "Fermi level alignment in molecular nanojunctions and its relation to charge transfer," *Phys. Rev. B*, vol. 74, p. 161405, Oct 2006.
- ⁹⁸ R. F. W. Bader, A. Larouche, C. Gatti, M. T. Carroll, P. J. MacDougall, and K. B. Wiberg, "Properties of atoms in molecules: Dipole moments and transferability of properties," *The Journal of Chemical Physics*, vol. 87, no. 2, pp. 1142–1152, 1987.
- ⁹⁹ A. Krawczuk-Pantula, D. Perez, K. Stadnicka, and P. Macchi, "Distributed atomic polarizabilities from electron density," *Trans. Am. Crystallogr. Assoc.*, vol. 42, pp. 1–25, 2011.
- ¹⁰⁰ T. C. Leung, C. L. Kao, W. S. Su, Y. J. Feng, and C. T. Chan, "Relationship between surface dipole, work function and charge transfer: Some exceptions to an established rule," *Phys. Rev. B*, vol. 68, p. 195408, Nov 2003.
- ¹⁰¹ L. hua Wang, Y. Sun, Z. zhen Zhang, B. jun Ding, and Y. Guo, "Molecular rectification modulated by alternating boron and nitrogen co-doping in a combined heterostructure of two zigzag-edged trigonal graphenes," *Physics Letters A*, vol. 378, no. 7–8, pp. 646 – 649, 2014.

BIBLIOGRAPHY

- ¹⁰² H. Liu, H. Wang, J. Zhao, and M. Kiguchi, "Molecular rectification in triangularly shaped graphene nanoribbons," *Journal of Computational Chemistry*, vol. 34, no. 5, pp. 360–365, 2013.
- ¹⁰³ R. S. Mulliken, "Electronic Population Analysis on LCAO–MO Molecular Wave Functions. I," *The Journal of Chemical Physics*, vol. 23, no. 10, pp. 1833–1840, 1955.
- ¹⁰⁴ W. Haiss, H. van Zalinge, S. J. Higgins, D. Bethell, H. Höbenreich, D. J. Schiffrin, and R. J. Nichols, "Redox State Dependence of Single Molecule Conductivity," *Journal of the American Chemical Society*, vol. 125, no. 50, pp. 15294–15295, 2003. PMID: 14664565.
- ¹⁰⁵ Xu, Xiao, X. Yang, L. Zang, and Tao, "Large Gate Modulation in the Current of a Room Temperature Single Molecule Transistor," *Journal of the American Chemical Society*, vol. 127, no. 8, pp. 2386–2387, 2005. PMID: 15724981.
- ¹⁰⁶ F. Chen, J. He, C. Nuckolls, T. Roberts, J. E. Klare, and S. Lindsay, "A Molecular Switch Based on Potential-Induced Changes of Oxidation State," *Nano Letters*, vol. 5, no. 3, pp. 503–506, 2005. PMID: 15755102.
- ¹⁰⁷ D. I. Gittins, D. Bethell, D. J. Schiffrin, and R. J. Nichols, "A nanometre-scale electronic switch consisting of a metal cluster and redox-addressable groups," *Nature*, vol. 408, pp. 67–69, 2000.
- ¹⁰⁸ N. J. Tao, "Electron transport in molecular junctions," *Nature Nanotechnology*, vol. 1, pp. 173–181, 2006.
- ¹⁰⁹ M. L. Perrin, E. Burzuri, and H. S. J. van der Zant, "Single-molecule transistors," *Chem. Soc. Rev.*, vol. 44, pp. 902–919, 2015.
- ¹¹⁰ R. Stadler, V. Geskin, and J. Cornil, "Screening effects in a density functional theory based description of molecular junctions in the Coulomb blockade regime," *Phys. Rev. B*, vol. 79, p. 113408, Mar 2009.
- ¹¹¹ S. Kubatkin, A. Danilov, M. Hjort, J. Cornil, J. Brédas, N. Stuhr-Hansen, P. Hedegard, and T. Bjørnholm, "Single-electron transistor of a single organic molecule with access to several redox states," *Nature*, vol. 425, pp. 698–701, 2003.
- ¹¹² J. P. Perdew and A. Zunger, "Self-interaction correction to density-functional approximations for many-electron systems," *Phys. Rev. B*, vol. 23, pp. 5048–5079, May 1981.
- ¹¹³ A. Filippetti and N. A. Spaldin, "Self-interaction-corrected pseudopotential scheme for magnetic and strongly-correlated systems," *Phys. Rev. B*, vol. 67, p. 125109, 2003.
- ¹¹⁴ M. Lundberg and P. E. M. Siegbahn, "Quantifying the effects of the self-interaction error in DFT: When do the delocalized states appear?," *J. Chem. Phys.*, vol. 122, p. 224103, 2005.
- ¹¹⁵ E. Fermi and E. Amaldi, "Le orbite 8s degli elementi," *Mem. Accad. d'Italia*, vol. 6, pp. 119–149, 1934.
- ¹¹⁶ A. Ruzsinszky, J. P. Perdew, G. I. Csonka, O. A. Vydrov, and G. E. Scuseria, "Density functionals that are one- and two- are not always many-electron self-interaction-free, as shown for H₂⁺, He₂⁺, LiH⁺, and Ne₂⁺," *The Journal of Chemical Physics*, vol. 126, no. 10, p. 104102, 2007.
- ¹¹⁷ M. R. Pederson, A. Ruzsinszky, and J. P. Perdew, "Communication: Self-interaction correction with unitary invariance in density functional theory," *The Journal of Chemical Physics*, vol. 140, no. 12, pp. –, 2014.
- ¹¹⁸ I. Tavernelli, "Self-interaction Corrected Density Functional Theory for the Study of Intramolecular Electron Transfer Dynamics in Radical Carbocations," *J. Phys. Chem. A*, vol. 111, pp. 13528–13536, 2007.
- ¹¹⁹ C. D. Pemmaraju, T. Archer, D. Sánchez-Portal, and S. Sanvito, "Atomic-orbital-based approximate self-interaction correction scheme for molecules and solids," *Phys. Rev. B*, vol. 75, p. 045101, Jan 2007.
- ¹²⁰ C. Toher and S. Sanvito, "Efficient Atomic Self-Interaction Correction Scheme for Nonequilibrium Quantum Transport," *Phys. Rev. Lett.*, vol. 99, p. 056801, Jul 2007.
- ¹²¹ E. O. Jónsson, K. S. Thygesen, J. Ulstrup, and K. W. Jacobsen, "Ab Initio Calculations of the Electronic Properties of Polypyridine Transition Metal Complexes and Their Adsorption on Metal Surfaces in the Presence of Solvent and Counterions," *The Journal of Physical Chemistry B*, vol. 115, no. 30, pp. 9410–9416, 2011.
- ¹²² R. G. Parr and R. G. Pearson, "Absolute hardness: companion parameter to absolute electronegativity," *Journal of the American Chemical Society*, vol. 105, no. 26, pp. 7512–7516, 1983.
- ¹²³ R. S. Mulliken, "A New Electroaffinity Scale; Together with Data on Valence States and on Valence Ionization Potentials and Electron Affinities," *The Journal of Chemical Physics*, vol. 2, no. 11, pp. 782–793, 1934.

BIBLIOGRAPHY

- ¹²⁴ J. Cioslowski and B. B. Stefanov, "Electron flow and electronegativity equalization in the process of bond formation," *The Journal of Chemical Physics*, vol. 99, no. 7, pp. 5151–5162, 1993.
- ¹²⁵ F. Lissel, F. Schwarz, O. Blacque, H. Riel, E. Lörtscher, K. Venkatesan, and H. Berke, "Organometallic Single-Molecule Electronics: Tuning Electron Transport through X(diphosphine)₂FeC₄Fe(diphosphine)₂X Building Blocks by Varying the Fe–X–Au Anchoring Scheme from Coordinative to Covalent," *Journal of the American Chemical Society*, vol. 136, no. 41, pp. 14560–14569, 2014. PMID: 25233357.
- ¹²⁶ L. A. Zotti, T. Kirchner, J.-C. Cuevas, F. Pauly, T. Huhn, E. Scheer, and A. Erbe, "Revealing the Role of Anchoring Groups in the Electrical Conduction Through Single-Molecule Junctions," *Small*, vol. 6, no. 14, pp. 1529–1535, 2010.
- ¹²⁷ D. J. Mowbray, G. Jones, and K. S. Thygesen, "Influence of functional groups on charge transport in molecular junctions," *J. Chem. Phys.*, vol. 128, p. 111103, 2008.
- ¹²⁸ T. Markussen, C. Jin, and K. S. Thygesen, "Quantitatively accurate calculations of conductance and thermopower of molecular junctions," *physica status solidi (b)*, vol. 250, no. 11, pp. 2394–2402, 2013.
- ¹²⁹ L. Strong and G. M. Whitesides, "Structures of Self-Assembled Monolayer Films of Organosulfur Compounds Adsorbed on Gold Single Crystals: Electron Diffraction Studies," *Langmuir*, vol. 4, pp. 546–558, 1988.
- ¹³⁰ M. A. Bryant and J. E. Pemberton, "Surface Raman Scattering of Self-Assembled Monolayers Formed from 1-Alkanethiols: Behavior of Films at Au and Comparison to Films at Ag," *J. Am. Chem. Soc.*, vol. 113, pp. 8284–8293, 1991.
- ¹³¹ D. M. Jaffey and R. J. Madix, "The reactivity of sulfur-containing molecules on noble metal surfaces: III. Ethanethiol on Au(110) and Ag(110)," *Surface Science*, vol. 311, no. 1–2, pp. 159 – 171, 1994.
- ¹³² S. Chenakin, B. Heinz, and H. Morgner, "Sputtering of hexadecanethiol monolayers self-assembled onto Ag(111)," *Surface Science*, vol. 397, no. 1–3, pp. 84 – 100, 1998.
- ¹³³ A. Danilov, S. Kubatkin, S. Kafanov, P. Hedegård, N. Stühr-Hansen, K. Moth-Poulsen, and T. Bjørnholm, "Electronic Transport in Single Molecule Junctions: Control of the Molecule-Electrode Coupling through Intramolecular Tunneling Barriers," *Nano Letters*, vol. 8, no. 1, pp. 1–5, 2008. PMID: 18085806.
- ¹³⁴ R. Cohen, K. Stokbro, J. M. L. Martin, and M. A. Ratner, "Charge Transport in Conjugated Aromatic Molecular Junctions: Molecular Conjugation and Molecule-Electrode Coupling," *The Journal of Physical Chemistry C*, vol. 111, no. 40, pp. 14893–14902, 2007.
- ¹³⁵ L. Patrone, S. Palacin, J. Bourgoin, J. Lagoute, T. Zambelli, and S. Gauthier, "Direct comparison of the electronic coupling efficiency of sulfur and selenium anchoring groups for molecules adsorbed onto gold electrodes," *Chemical Physics*, vol. 281, no. 2–3, pp. 325 – 332, 2002.
- ¹³⁶ L. Patrone, S. Palacin, and J. Bourgoin, "Direct comparison of the electronic coupling efficiency of sulfur and selenium alligator clips for molecules adsorbed onto gold electrodes," *Applied Surface Science*, vol. 212–213, pp. 446 – 451, 2003. 11th International Conference on Solid Films and Surfaces.
- ¹³⁷ L. Patrone, S. Palacin, J. Charlier, F. Armand, J. P. Bourgoin, H. Tang, and S. Gauthier, "Evidence of the Key Role of Metal-Molecule Bonding in Metal-Molecule-Metal Transport Experiments," *Phys. Rev. Lett.*, vol. 91, p. 096802, Aug 2003.
- ¹³⁸ S. Yasuda, S. Yoshida, J. Sasaki, Y. Okutsu, T. Nakamura, A. Taninaka, O. Takeuchi, and H. Shigekawa, "Bond Fluctuation of S/Se Anchoring Observed in Single-Molecule Conductance Measurements using the Point Contact Method with Scanning Tunneling Microscopy," *Journal of the American Chemical Society*, vol. 128, no. 24, pp. 7746–7747, 2006. PMID: 16771482.
- ¹³⁹ M. H. Dishner, J. C. Hemminger, and F. J. Feher, "Scanning Tunneling Microscopy Characterization of Organoselenium Monolayers on Au(111)," *Langmuir*, vol. 13, no. 18, pp. 4788–4790, 1997.
- ¹⁴⁰ M. G. Samant, C. A. Brown, and J. G. Gordon, "Formation of an ordered self-assembled monolayer of docosaneselenol on gold(111). Structure by surface x-ray diffraction," *Langmuir*, vol. 8, no. 6, pp. 1615–1618, 1992.
- ¹⁴¹ "See Rudolph Marcus' publication page at <http://chemistry.caltech.edu/faculty/marcus/pubsfull.html> and especially the publications between 1956 and 1970."
- ¹⁴² E. P. Friis, Y. I. Kharkats, A. M. Kuznetsov, and J. Ulstrup, "In Situ Scanning Tunneling Microscopy of a Redox Molecule as a Vibrationally Coherent Electronic Three-Level Process," *The Journal of Physical Chemistry A*, vol. 102, no. 40, pp. 7851–7859, 1998.

BIBLIOGRAPHY

- ¹⁴³ A. M. Kuznetsov and J. Ulstrup, "Mechanisms of in Situ Scanning Tunnelling Microscopy of Organized Redox Molecular Assemblies," *The Journal of Physical Chemistry A*, vol. 104, no. 49, pp. 11531–11540, 2000.
- ¹⁴⁴ A. Migliore, P. Schiff, and A. Nitzan, "On the relationship between molecular state and single electron pictures in simple electrochemical junctions," *Phys. Chem. Chem. Phys.*, vol. 14, pp. 13746–13753, 2012.
- ¹⁴⁵ R. A. Marcus, "On the Theory of Oxidation-Reduction Reactions Involving Electron Transfer. I," *The Journal of Chemical Physics*, vol. 24, no. 5, pp. 966–978, 1956.
- ¹⁴⁶ N. S. Hush, "Adiabatic theory of outer sphere electron-transfer reactions in solution," *Trans. Faraday Soc.*, vol. 57, pp. 557–580, 1961.
- ¹⁴⁷ R. A. Marcus, "On the Theory of Electron-Transfer Reactions. VI. Unified Treatment for Homogeneous and Electrode Reactions," *The Journal of Chemical Physics*, vol. 43, no. 2, pp. 679–701, 1965.
- ¹⁴⁸ J. R. Miller, L. T. Calcaterra, and G. L. Closs, "Intramolecular long-distance electron transfer in radical anions. The effects of free energy and solvent on the reaction rates," *Journal of the American Chemical Society*, vol. 106, no. 10, pp. 3047–3049, 1984.
- ¹⁴⁹ M. Born, "Volumen und Hydratationswärme der Ionen," *Zeitschrift für Physik*, vol. 1, no. 1, pp. 45–48, 1920.
- ¹⁵⁰ R. Marcus, "Tutorial on rate constants and reorganization energies," *Journal of Electroanalytical Chemistry*, vol. 483, no. 1–2, pp. 2 – 6, 2000.
- ¹⁵¹ R. Marcus and N. Sutin, "Electron transfers in chemistry and biology," *Biochimica et Biophysica Acta (BBA) - Reviews on Bioenergetics*, vol. 811, no. 3, pp. 265 – 322, 1985.
- ¹⁵² E. Fermi, *Nuclear Physics*. University of Chicago Press, 1950.
- ¹⁵³ P. A. M. Dirac, "The Quantum Theory of the Emission and Absorption of Radiation," *Proceedings of the Royal Society of London A: Mathematical, Physical and Engineering Sciences*, vol. 114, no. 767, pp. 243–265, 1927.
- ¹⁵⁴ C. E. D. Chidsey, "Free Energy and Temperature Dependence of Electron Transfer at the Metal-Electrolyte Interface," *Science*, vol. 251, no. 4996, pp. 919–922, 1991.
- ¹⁵⁵ A. Migliore and A. Nitzan, "On the evaluation of the Marcus–Hush–Chidsey integral," *Journal of Electroanalytical Chemistry*, vol. 671, pp. 99 – 101, 2012.
- ¹⁵⁶ S. Gosavi, Y. Q. Gao, and R. Marcus, "Temperature dependence of the electronic factor in the nonadiabatic electron transfer at metal and semiconductor electrodes," *Journal of Electroanalytical Chemistry*, vol. 500, no. 1–2, pp. 71 – 77, 2001.
- ¹⁵⁷ E. F. Valeev, V. Coropceanu, D. A. da Silva Filho, S. Salman, and J.-L. Brédas, "Effect of Electronic Polarization on Charge-Transport Parameters in Molecular Organic Semiconductors," *Journal of the American Chemical Society*, vol. 128, no. 30, pp. 9882–9886, 2006.
- ¹⁵⁸ A. Migliore, "Nonorthogonality Problem and Effective Electronic Coupling Calculation: Application to Charge Transfer in Π -Stacks Relevant to Biochemistry and Molecular Electronics," *Journal of Chemical Theory and Computation*, vol. 7, no. 6, pp. 1712–1725, 2011.
- ¹⁵⁹ S. Larsson, "Electron transfer in chemical and biological systems. Orbital rules for nonadiabatic transfer," *Journal of the American Chemical Society*, vol. 103, no. 14, pp. 4034–4040, 1981.
- ¹⁶⁰ A. A. Voityuk, "Charge-on-site scheme to estimate the electronic coupling in electron transfer systems," *Chemical Physics Letters*, vol. 451, no. 1–3, pp. 153 – 157, 2008.
- ¹⁶¹ A. A. Voityuk, "Electronic coupling for charge transfer in donor-bridge-acceptor systems. Performance of the two-state FCD model," *Phys. Chem. Chem. Phys.*, vol. 14, pp. 13789–13793, 2012.
- ¹⁶² R. S. Mulliken, "Molecular compounds and their spectra. ii," *Journal of the American Chemical Society*, vol. 74, no. 3, pp. 811–824, 1952.
- ¹⁶³ N. Hush, "Homogeneous and heterogeneous optical and thermal electron transfer," *Electrochimica Acta*, vol. 13, no. 5, pp. 1005 – 1023, 1968.
- ¹⁶⁴ C. Liang and M. D. Newton, "Ab initio studies of electron transfer. 2. pathway analysis for homologous organic spacers," *The Journal of Physical Chemistry*, vol. 97, no. 13, pp. 3199–3211, 1993.

BIBLIOGRAPHY

- ¹⁶⁵ M. Ottonelli, M. Piccardo, D. Duce, S. Thea, and G. Dellepiane, "Koopmans' Transfer Integral Calculation: A Comparison between the Hartree-Fock and the Density Functional Results," *Energy Procedia*, vol. 31, pp. 31 – 37, 2012. Proceedings of the Spring 2011 E-MRS Meeting, Symposium S: Organic Photovoltaics: Science and Technology.
- ¹⁶⁶ G. R. Hutchison, M. A. Ratner, and T. J. Marks, "Intermolecular Charge Transfer between Heterocyclic Oligomers. Effects of Heteroatom and Molecular Packing on Hopping Transport in Organic Semiconductors," *Journal of the American Chemical Society*, vol. 127, no. 48, pp. 16866–16881, 2005. PMID: 16316233.
- ¹⁶⁷ J. L. Bredas, J. P. Calbert, D. A. da Silva Filho, and J. Cornil, "Organic semiconductors: A theoretical characterization of the basic parameters governing charge transport," *Proceedings of the National Academy of Sciences*, vol. 99 (9), pp. 5804–5809, 2002.
- ¹⁶⁸ A. Migliore, P. H.-L. Sit, and M. L. Klein, "Evaluation of Electronic Coupling in Transition-Metal Systems Using DFT: Application to the Hexa-Aquo Ferric-Ferrous Redox Couple," *Journal of Chemical Theory and Computation*, vol. 5, no. 2, pp. 307–323, 2009.
- ¹⁶⁹ Q. Wu and T. V. Voorhis, "Extracting electron transfer coupling elements from constrained density functional theory," *The Journal of Chemical Physics*, vol. 125, no. 16, p. 164105, 2006.
- ¹⁷⁰ R. J. Cave and M. D. Newton, "Generalization of the mulliken-hush treatment for the calculation of electron transfer matrix elements," *Chemical Physics Letters*, vol. 249, no. 1–2, pp. 15 – 19, 1996.
- ¹⁷¹ P.-O. Löwdin, "On the Non-Orthogonality Problem Connected with the Use of Atomic Wave Functions in the Theory of Molecules and Crystals," *The Journal of Chemical Physics*, vol. 18, no. 3, pp. 365–375, 1950.
- ¹⁷² A. Migliore, S. Corni, R. Di Felice, and E. Molinari, "First-principles density-functional theory calculations of electron-transfer rates in azurin dimers," *The Journal of Chemical Physics*, vol. 124, no. 6, pp. –, 2006.
- ¹⁷³ A. Migliore, "Full-electron calculation of effective electronic couplings and excitation energies of charge transfer states: Application to hole transfer in DNA π -stacks," *The Journal of Chemical Physics*, vol. 131, no. 11, pp. –, 2009.
- ¹⁷⁴ A. Migliore, S. Corni, R. D. Felice, and E. Molinari, "Water-Mediated Electron Transfer between Protein Redox Centers," *The Journal of Physical Chemistry B*, vol. 111, no. 14, pp. 3774–3781, 2007. PMID: 17388538.
- ¹⁷⁵ S. S. Skourtis, D. N. Beratan, and J. N. Onuchic, "The two-state reduction for electron and hole transfer in bridge-mediated electron-transfer reactions," *Chemical Physics*, vol. 176, no. 2–3, pp. 501 – 520, 1993.
- ¹⁷⁶ S. Gosavi, , and R. A. Marcus, "Nonadiabatic Electron Transfer at Metal Surfaces," *The Journal of Physical Chemistry B*, vol. 104, no. 9, pp. 2067–2072, 2000.
- ¹⁷⁷ A. Nitzan, "A Relationship between Electron-Transfer Rates and Molecular Conduction," *The Journal of Physical Chemistry A*, vol. 105, no. 12, pp. 2677–2679, 2001.
- ¹⁷⁸ A. Nitzan, "Electron Transmission Through Molecules and Molecular Interfaces," *Annual Review of Physical Chemistry*, vol. 52, no. 1, pp. 681–750, 2001. PMID: 11326078.
- ¹⁷⁹ A. Nitzan, "The relationship between electron transfer rate and molecular conduction 2. The sequential hopping case," *Israel Journal of Chemistry*, vol. 42, no. 2-3, pp. 163–166, 2002.
- ¹⁸⁰ G. Pourtois, D. Beljonne, J. Cornil, M. A. Ratner, and J. L. Brédas, "Photoinduced Electron-Transfer Processes along Molecular Wires Based on Phenylenevinylene Oligomers: A Quantum-Chemical Insight," *Journal of the American Chemical Society*, vol. 124, no. 16, pp. 4436–4447, 2002. PMID: 11960473.
- ¹⁸¹ D. Qiu, P. S. Shenkin, F. P. Hollinger, and W. C. Still, "The GB/SA Continuum Model for Solvation. A Fast Analytical Method for the Calculation of Approximate Born Radii," *The Journal of Physical Chemistry A*, vol. 101, no. 16, pp. 3005–3014, 1997.
- ¹⁸² W. L. Jorgensen and J. Tirado-Rives, "The OPLS [optimized potentials for liquid simulations] potential functions for proteins, energy minimizations for crystals of cyclic peptides and crambin," *Journal of the American Chemical Society*, vol. 110, no. 6, pp. 1657–1666, 1988.
- ¹⁸³ L. Xie and H. Liu, "The treatment of solvation by a generalized Born model and a self-consistent charge-density functional theory-based tight-binding method," *Journal of Computational Chemistry*, vol. 23, no. 15, pp. 1404–1415, 2002.
- ¹⁸⁴ A. Onufriev, D. A. Case, and D. Bashford, "Effective Born radii in the generalized Born approximation: The importance of being perfect," *Journal of Computational Chemistry*, vol. 23, no. 14, pp. 1297–1304, 2002.

- ¹⁸⁵ C. Li, A. Mishchenko, Z. Li, I. Pobelov, T. Wandlowski, X. Q. Li, F. Würthner, A. Bagrets, and F. Evers, "Electrochemical gate-controlled electron transport of redox-active single perylene bisimide molecular junctions," *Journal of Physics: Condensed Matter*, vol. 20, no. 37, p. 374122, 2008.
- ¹⁸⁶ T. Hines, I. Diez-Perez, J. Hihath, H. Liu, Z.-S. Wang, J. Zhao, G. Zhou, K. Müllen, and N. Tao, "Transition from Tunneling to Hopping in Single Molecular Junctions by Measuring Length and Temperature Dependence," *Journal of the American Chemical Society*, vol. 132, no. 33, pp. 11658–11664, 2010. PMID: 20669945.
- ¹⁸⁷ X. Zhao, C. Huang, M. Gulcur, A. S. Batsanov, M. Baghernejad, W. Hong, M. R. Bryce, and T. Wandlowski, "Oligo(aryleneethynylene)s with Terminal Pyridyl Groups: Synthesis and Length Dependence of the Tunneling-to-Hopping Transition of Single-Molecule Conductances," *Chemistry of Materials*, vol. 25, no. 21, pp. 4340–4347, 2013.
- ¹⁸⁸ S. Ho Choi, B. Kim, and C. D. Frisbie, "Electrical Resistance of Long Conjugated Molecular Wires," *Science*, vol. 320, no. 5882, pp. 1482–1486, 2008.
- ¹⁸⁹ R. Yamada, H. Kumazawa, S. Tanaka, and H. Tada, "Electrical Resistance of Long Oligothiophene Molecules," *Applied Physics Express*, vol. 2, no. 2, p. 025002, 2009.
- ¹⁹⁰ C. E. Schäffer, C. Anthon, and J. Bendix, "Kohn-Sham DFT results projected on ligand-field models: Using DFT to supplement ligand-field descriptions and to supply ligand-field parameters," *Coordination Chemistry Reviews*, vol. 253, no. 5–6, pp. 575 – 593, 2009. Theory and Computing in Contemporary Coordination Chemistry.

PAPER I

Charge localization on a redox-active single-molecule
junction and its influence on coherent electron transport

Charge localization on a redox-active single-molecule junction and its influence on coherent electron transport

Georg Kastlunger and Robert Stadler*

Department of Physical Chemistry, University of Vienna, Sensengasse 8/7, A-1090 Vienna, Austria

(Received 13 March 2013; revised manuscript received 26 June 2013; published 11 July 2013)

To adjust the charging state of a molecular metal complex in the context of a density functional theory description of coherent electron transport through single-molecule junctions, we correct for self-interaction effects by fixing the charge on a counterion, which in our calculations mimics the effect of the gate in an electrochemical scanning tunneling microscope setup, with two competing methods, namely, the generalized Δ self consistent field (Δ SCF) technique and screening with solvation shells. One would expect a transmission peak to be pinned at the Fermi energy for a nominal charge of +1 on the molecule in the junction, but we find a more complex situation in this multicomponent system defined by the complex, the leads, the counterion, and the solvent. In particular the equilibrium charge transfer between the molecule and the leads plays an important role, which we investigate in relation to the total external charge in the context of electronegativity theory.

DOI: [10.1103/PhysRevB.88.035418](https://doi.org/10.1103/PhysRevB.88.035418)

PACS number(s): 73.63.Rt, 73.20.Hb, 73.40.Gk

I. INTRODUCTION

Most studies in the vibrant field of single-molecule electronics focus on the low bias current flow through rather small benchmark molecules anchored to metal leads in ultrahigh vacuum (UHV) at very low temperatures. Under those restrictions the underlying electron-transport problem is now straightforwardly accessible to a computational treatment with a nonequilibrium Green's function (NEGF) approach¹ in combination with a density functional theory (DFT)-based description of the electronic structure of the separate and combined components of the junction, namely, the leads and the scattering region.^{2–5} This method allows for an atomistic interpretation of associated UHV experiments on such benchmark systems in a mechanical break-junction or scanning tunneling microscope (STM) setup,^{6–9} thereby contributing to the fundamental understanding of the dependence of the electronic conductance of the junction on the details of its structure within the boundary conditions of a low-pressure and low-temperature regime.

For single-molecule junctions to be useful as molecular devices, however, their operability at room temperature is required, and the presence of a solvent allows for electrochemical gating, which makes it possible to avoid the potentially destructive effect of the rather high local electric fields, which otherwise would be needed for inducing a larger current.¹⁰ Experimentally, these ambient conditions can be achieved with an electrochemical STM,^{10–13} where the nanojunction is an integral part of an electrochemical cell and the investigated molecules usually have a redox-active center with an oxidation state which can be regulated via gating.¹⁰ Depending on the setup as well as the structural details of the system, two competing electron-transport mechanisms have to be considered for a theoretical description of such experiments, namely, electron hopping, which is a thermally induced multiple-step process, and coherent tunneling, which is the standard one-step phenomenon known from benchmark molecules without a redox-active center and relatively strongly coupled to metallic electrodes at temperatures close to 0 K. In both cases an atomistic description of the process under

electrochemical conditions provides a formidable challenge for a DFT-based theory. For the former, the difficulty lies in a simplified and compact but nevertheless sufficiently accurate description of the nuclear vibrations of the molecule and solvent which drive the electron flow. For the latter it becomes necessary to adjust the oxidation state of the redox-active center in the scattering region and therefore deal with the issue of charge localization in a multicomponent system, which is the topic we address in this paper.

The correct description of localized charges is notoriously hard to achieve within a DFT framework because the Coulomb and exchange parts of the interaction of an electron with itself do not cancel out exactly in a standard Kohn-Sham (KS) Hamiltonian and the corresponding self-interaction (SI) errors result in an artificial tendency towards delocalization.^{14–17} As has been shown recently, both for a continuum solvation model¹⁸ and for an explicit description of a periodic cell with its vacuum part filled with H₂O molecules,¹⁹ a polar solvent has a screening effect on the Coulomb potential which reduces SI errors and stabilizes localized charges within DFT. Another way to enforce localization is based on the generalized Δ self consistent field (Δ SCF) technique,^{20,21} where an arbitrary integer value between 0 and 2 for the occupation number of a particular crystal eigenstate or linear combination of crystal orbitals can be defined as a boundary condition to the self-consistency cycles determining the electronic structure of a given system.

In our paper we pursue both avenues for a study of the coherent electron transport through the Ru(PPh₂)₄(C₂H₄)₂ bis(pyridylacetylide) complex in Fig. 1, which we will often refer to as just the “Ru complex” in the following since it is the only system we investigate here and where for experiments in an aqueous solution with chlorine counterions the oxidation state of the redox-active ruthenium atom can be switched between +II and +III by varying the electrochemical potential of the cell corresponding to an overall charge of 0 and +1 on the molecular complex, respectively. We chose this particular system because it was used in previous conductance measurements^{22,23} as a monomer of chains, albeit with different anchor groups, where it was found that depending

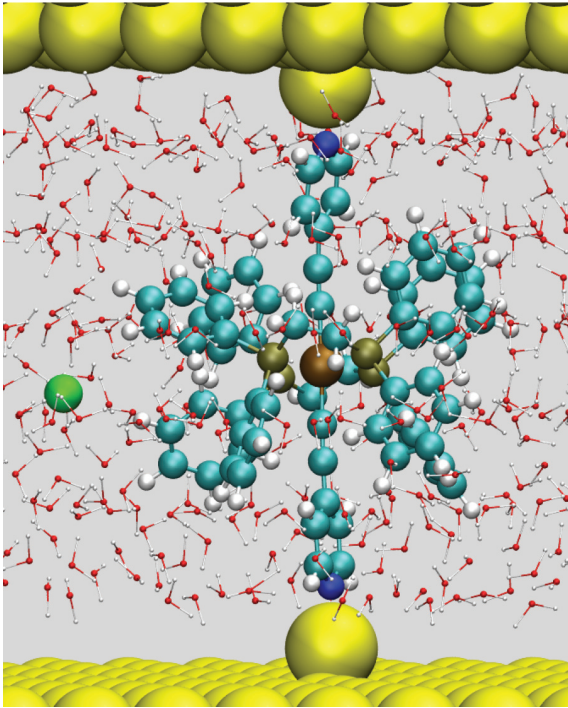


FIG. 1. (Color online) Geometry of the $\text{Ru(PPh}_2)_4(\text{C}_2\text{H}_4)_2$ bis(pyridylacetylide) complex studied throughout our paper bonded to adatoms on Au fcc (111) surfaces within an aqueous solvent and containing a Cl counterion.

on the chain length either coherent transport or electron hopping is observed.²² In addition spectroscopic and quantum chemical studies on similar Ru complexes^{24–28} suggest that this molecular species offers the possibility to easily link two carbon-rich chains to each other for the formation of reversible redox systems^{29–31} with distinct optical transition properties,^{32,33} thereby serving as a starting point for the investigation of chains with multiple redox-active centers.²⁷ In contrast to Ref. 22 we use pyridyl groups as anchors to the leads because they provide peaks in the transmission function which are narrow enough to assume that a charge on the complex has an impact on the conductance but broad enough to avoid the Coulomb blockade regime.^{34–36}

While reports of conductance calculations on redox-active complexes have been published before,^{37,38} our paper presents a DFT-based study of coherent electron transport through such a molecular complex which explicitly investigates the influence of the formal oxidation state of its central metal atom on the resulting transmission function. There have been previous studies on the impact the solvent has on smaller benchmark molecules without a redox center,^{39–42} where some of them^{40,42} have found a “chemical gating” effect, i.e., a shift in the transmission function induced by the surrounding molecules, which was explained by dipole fields. We do not consider configurational fluctuations of the solvent molecules in our paper, not only because of the high computational demands this would generate for our rather large junction but also because it would lead to fluctuations in the charge on the Ru complex, whereas the main aim in this work is to keep it fixed and to study its influence in a systematic way.

It has to be stressed that by this restriction we neglect an important solvent effect, which would modify electron transport due to the related electron-phonon coupling. While this effect is crucial for electron hopping, which is not the topic of this paper, we believe our omission to be justified in the context of coherent tunneling where the solvent’s main influence is of an electrostatic nature and the statistics for the positions of water nuclei should change the transmission function and conductance of the junction only to a small extent. The main electrostatic screening effect of the solvent in our calculations, namely, the localization of the charge on the counterion, can also be mimicked in a more technical way by fixing the charge on a Cl atom with the ΔSCF technique, and in this paper we compare the results of this approach with that of the explicit presence of the solvent.

This paper is organized as follows: In the next section we present transmission functions and conductances for the Ru complex at charging states of 0 and +1 (i.e., with the Ru atom in its formal oxidation states +II and +III, respectively), where in order to mimic the gate potential generating the +1 state in experiments, the countercharge is localized on a chlorine ion, and we assume that a Cl atom oxidizes the complex and is thereby reduced to an anion. We do not suggest that this redox process necessarily takes place in the actual STM experiments, but rather use it as a convenient tool to simulate the effect of electrochemical gating, namely, charging the Ru complex in the junction, in our calculations. The two ways of reducing SIE mentioned above, i.e., employing the generalized ΔSCF technique and introducing H_2O molecules explicitly as a solvent, are used to make sure that the Cl atom is indeed charged with a whole electron in our setup. In Sec. III we investigate the shift in projected molecular eigenvalues with both methods in terms of the distribution of partial charges throughout the junction, which is a multicomponent system in the sense that implementing the gate means not only that the charge on the Ru complex and counterion can vary but also that the gold leads and aqueous solvent can and do lose or gain fractions of electrons. For an analysis of this complex behavior in Sec. IV we start with cluster models within the simplified picture of electronegativity (EN) theory,⁴³ and from their direct comparison with our full calculations on the junctions represented by Fig. 1 we derive the nature of the driving forces, which define the charge-density distributions we observe. We conclude with a brief summary of our results.

II. ELECTRON-TRANSPORT CALCULATIONS FOR THE NEUTRAL AND CHARGED COMPLEXES

All calculations of transmission probabilities $T(E)$ in this paper were performed within a NEGF-DFT framework^{2–5} with the GPAW code,^{44,45} where the core electrons are described with the projector augmented wave (PAW) method and the basis set for the KS wave functions can be optionally chosen to be either a real-space grid or a linear combination of atomic orbitals (LCAO), and we opted for the latter on a double-zeta level with polarization functions (DZP) for all of our electron-transport and electronic-structure calculations. The sampling of the potential-energy term in the Hamiltonian is always done on a real-space grid when using GPAW, where we chose 0.18 Å for its spacing and a Perdew-Burke-Ernzerhof

(PBE)⁴⁶ parametrization for the exchange-correlation (XC) functional throughout this paper.

Within NEGF the transmission function $T(E)$ is defined by $T(E) = \text{Tr}(G_d \Gamma_L G_d^\dagger \Gamma_R)$, where $G_d = (E - H_d - \Sigma_L - \Sigma_R)^{-1}$ represents the Green's function of the device containing the self-energy matrices $\Sigma_{L/R}$ due to the left/right lead, $\Gamma_{L/R} = i(\Sigma_{L/R} - \Sigma_{L/R}^\dagger)$, and H_d is the Hamiltonian matrix for the device region, which contains not only the Ru complex but also three to four layers of the aligned Au surface on each side. Due to the rather large size of the central molecule (Fig. 1), we had to use gold slabs with a 6×6 unit cell in the surface plane in order to ensure that neighboring molecules do not interact. With the two Au adatoms directly coupling to the molecule (Fig. 1), the device region contains a total of 254 Au atoms in addition to the atoms of the complex itself and up to 64 H₂O molecules. As a consequence, H_d reached a size which was beyond our computational capabilities to handle efficiently for electron-transport calculations and therefore needed to be reduced.

Since it is known that the solvent does not contribute to the peak structure in $T(E)$,⁴² but instead adds a baseline conductance with a rather small energy dependence,⁴⁷ we cut out the lines and rows indexing H₂O basis functions in the matrix H_d , which we initially obtained from an electronic-structure calculation for the full device region. In a second effort towards memory reduction we cut out very high- and very low-lying MOs from H_d after subdiagonalizing it with respect to molecular basis functions,^{48,49} where we assumed that molecular eigenstates which are more than 5 eV apart from E_F would have no effect on the conductance or on the transmission function on the much smaller energy range on which we show them.

To ensure overall charge neutrality in the unit cell of our device region, which is a necessity for a charged junction when applying periodic boundary conditions for electronic-structure calculations, the countercharge to the positively charged Ru complex has to be an explicit part of the cell, and we represent it by a Cl counterion. There are two methods we exploit in this paper to overcome the SI problem, which leads to an artificial delocalization of otherwise localized charges in DFT: (i) We make explicit use of the findings of other groups^{18,19} that a polar solvent, H₂O in our case, stabilizes localized charges because the solvation enthalpy and therefore also the total energy of the system become more negative the more pointlike the charges on the solutes are distributed; (ii) we also employ the generalized Δ SCF technique,^{20,21,45} which has been previously used as a feature of GPAW to correctly describe excitation processes in molecules adsorbed on surfaces^{19,20} and of electron hopping between layers of oxides.^{50,51}

In practical terms the first scheme starts with the relaxation of the nuclear positions of the isolated Ru complex towards the convergence criterium of 0.02 eV/Å for the average force. Then we add the Cl counterion with a fixed Ru-Cl distance of 7 Å and embed the resulting system in a solvent shell of 46 molecules by making use of the graphical interface of the GHEMICAL code,⁵² which places H₂O molecules in the cell with a high degree of artificial translational symmetry. In a next step we relax the nuclei of the system now comprising the complex, the counterion, and the solvation shell in order to create a more natural distribution of water molecules, where

hydrogen bonds create a network structure, but we keep the Ru-Cl distance constant as a boundary condition for avoiding hybridization between the Ru complex and the chlorine ion, which is statistically unlikely in nature but might happen in our relatively small unit cell. During this relaxation process we regularly probe the charge distribution in the system. Once we achieve a one-electron charge on the Ru complex, i.e., a formal oxidation state of +III on the Ru atom, we stop the relaxation and align the whole system between two gold fcc (111) surfaces with adatoms, and the nitrogen of the pyridyl anchors at a distance of 2.12 Å to establish the direct electronic contact.³⁵ For this system we then calculate the transmission function as described above.

In our second approach based on the generalized Δ SCF method, we make use of its flexibility to define the spatial expansion of an orbital forced to contain an electron as an arbitrary linear combination of Bloch states.^{20,21} By extracting one electron from the system and inserting it into a predefined orbital in the beginning of every iteration step, the self-consistency cycle progresses as usual, but with the electron density of this particular orbital as a contribution to the external potential. In this way we can fix the electron occupation of the Cl counterion manually, which solves the self-interaction problem implicitly and makes this method ideal for charge localization as needed in the present work. When applying this technique, we chose the nuclear positions relaxed for the neutral complex aligned between the gold surfaces, where one counterion was added with one supplementary electron constrained to completely fill its p shell. This procedure also had the benign consequence that the calculation of $T(E)$ was reduced significantly in terms of computational demand because we do not need an explicit solvent here and therefore do not have to remove the respective states from the transport Hamiltonian.

Figure 2 shows the transmission function calculated for the neutral Ru complex and with a positive charge put on

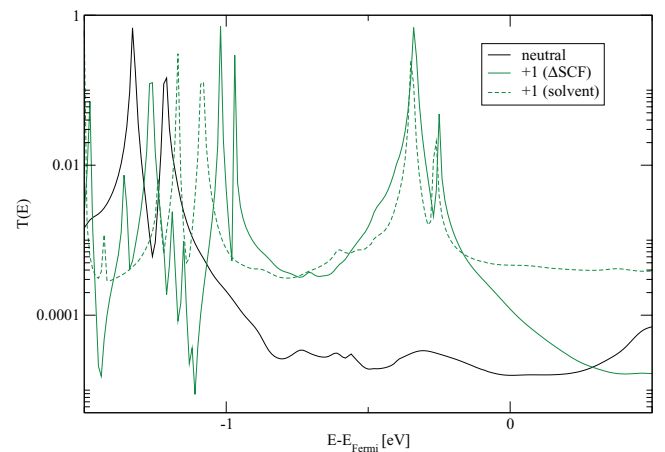


FIG. 2. (Color online) Transmission function of the neutral Ru complex (solid black line) and that with a charge of +1, which was adjusted with two different methods, i.e., (i) Δ SCF (solid green line) and (ii) solvent screening (dashed green line). In both methods a Cl atom was used as a counterion to extract an electron from the Ru complex. The k -point sampling was performed on a $4 \times 4 \times 1$ mesh for all three curves.

TABLE I. Conductance of the Ru complex corresponding to the curves in Fig. 1 as calculated by NEGF-DFT and with the conductance quantum G_0 as its unit.

	Neutral molecule	+1 (Δ SCF)	+1 (solvent)
$G (G_0)$	1.6×10^{-5}	1.2×10^{-4}	4.6×10^{-4}

the junction with the two methods described above. One would expect the charged complex corresponding to a Ru atom with an oxidation number of +III to have a higher conductance than the neutral one (oxidation number +III) due to a supposedly half-filled molecular orbital (MO) at the Fermi level. While no Fermi-level pinning can be observed in Fig. 2, the conductance of the +1 state is indeed distinctly higher than that of the neutral junction, as shown in Table I, but the respective numbers obtained from the two methods for applying the charge differ by a factor of 4.

The main reason for this disagreement is illustrated in Fig. 2, where we find that the incompleteness in decoupling the H_2O orbitals from the transport Hamiltonian, conceding that LCAO basis functions located on specific atoms also contribute to the description of their surrounding, creates a “transmission baseline” which fits the behavior previously investigated in theoretical studies of the conductance of water⁴⁷ and is absent in the Δ SCF calculations. In this line of argument, the difference of the transmission function and conductance for the +1 state calculated with Δ SCF and solvent screening is caused by the solvent retaining some presence in one of the transport Hamiltonians because electrons in the solvent are, to some extent, described by basis functions localized on the complex and therefore contribute to the transport.

III. CHARGE-DENSITY DISTRIBUTION AND ITS IMPACT ON THE PROJECTED MO EIGENENERGIES

In order to understand the peak structure in Fig. 2 in more detail we now study the electronic structure of the junction by investigating the electronic states of the device in terms of the molecular eigenenergies and their shape. Since the coupling of the Ru complex to the Au surface leads to a hybridization of the respective electronic states, it is necessary for the projection of molecular eigenvalues localized on the Ru complex from the Hamiltonian matrix to eliminate their coupling to the surface states in a subdiagonalization procedure.^{48,49} The MO-eigenvalue distributions obtained in this way are shown in Fig. 3. The MO eigenenergies are calculated by decoupling the basis functions localized on the molecule from that of the surface states with a subdiagonalization of the transport Hamiltonian for the neutral complex for panel C0.4 and for a complex with a charge of +1 applied by Δ SCF and the solvent screening method for panels C0.8 and C0.89, respectively. The energies in panels A0, A0.4, A0.8, and A0.89 result from vacuum-level alignment of separate calculations for the Ru complex and the Au slab, where the numbers in the panel labels refer to a positive charge of that size on the complex. For panel A(Cl)0.95 a chlorine atom is added to the Ru complex for the alignment. By inspecting the shape of the two relevant orbitals for coherent transport through the Ru complex in both charging states, namely, the highest occupied molecular orbital

(HOMO) and HOMO-1, which we show as insets in Fig. 3, we find that both MOs are characterized by a conjugated π system, which is delocalized over the whole bridge of the complex, and their respective energies match the double-peak structure in the transmission function in Fig. 2. While HOMO-1 in Fig. 3 has a high localization at the interface region, the HOMO does not, which explains the relative proportions of the widths of the two merged peaks in Fig. 2.

For very weak coupling between the leads and a molecule one would expect that charging the molecule to its +1 state would extract one electron from the complex’s HOMO, leading to a singly occupied MO (SOMO), which by definition is situated at the Fermi energy E_F . In the composite junction we investigate in this paper, however, where the degree of electronic coupling is intermediate and we can only obtain molecular orbitals by projecting them out of lead/complex hybrid states via a dehybridization procedure, the situation is less clear-cut, and in Fig. 3 we find the HOMO always below the junctions’ Fermi level, which is mostly defined by the leads due to their metallic character and the large number of gold atoms in the device region. The key to understanding the peak positions in the transmission function and the Fermi-level alignment of the corresponding MOs in such a scenario lies in understanding the zero-bias charge transfer, as has been demonstrated in Refs. 53–55 for bipyridine and other similarly small organic molecules. The present case, however, is more difficult because here we have to deal with a four-component system containing the Ru complex, the Cl ion, the solvent, and the leads, where for a detailed charge-density distribution analysis we use the Bader method for the definition of the

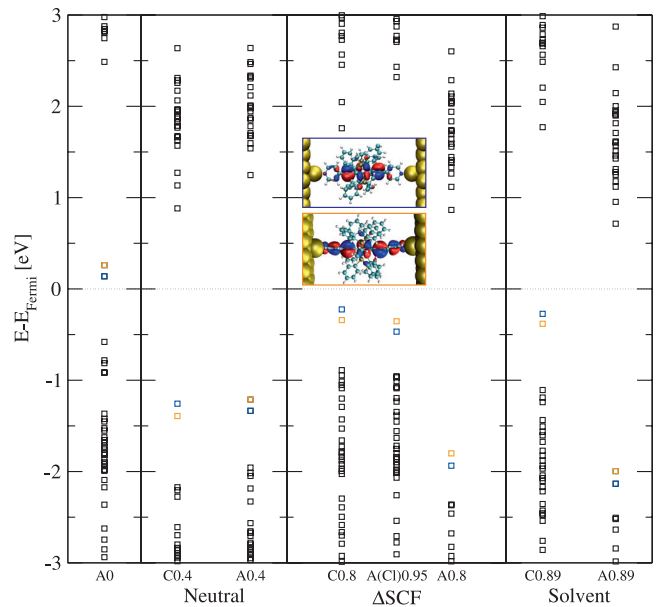


FIG. 3. (Color online) MO eigenvalue spectrum of the device region, where the spatial shapes of the HOMO and HOMO-1 are shown as insets, where the C panels are obtained from a subdiagonalization of the transport Hamiltonian and the A panels are obtained from a vacuum-level alignment of the isolated molecule and leads. The numbers in the panel descriptions refer to the charge on the complex; further technical details are described in the main text.

TABLE II. Distribution of the partial charges in the junction as calculated from a Bader analysis for the neutral complex and the complex with one positive charge applied by fixing the countercharge on a Cl ion with Δ SCF and solvent screening, respectively, where numbers from calculations without a Au slab are also shown in parentheses for comparison. All values are given in fractions of electrons.

	Au	H ₂ O	Cl	H ₂ O + Cl	Ru complex	Ru
Neutral complex	0.39				−0.43	−0.21
Δ SCF	−0.16		0.94	0.94 (0.97)	−0.80 (−0.97)	−0.25 (−0.35)
Solvent (1 Cl/46 H ₂ O)	−0.21	0.37 (0.28)	0.71 (0.70)	1.08 (0.98)	−0.90 (−0.98)	−0.24 (−0.33)

electronic charges belonging to particular nuclei^{56,57} in the following.

In Table II we present the charge distribution for both the neutral and charged junctions, where values from separate simulations for the Ru complex without Au leads but for the charged case including the counterion and solvent are given in parentheses for comparison, and they are also highlighted in Table III and compared with values calculated with the Becke three-parameter Lee-Yang-Parr (B3LYP) hybrid functional. In the absence of the Au surface the charge values on the Ru complex can be adjusted rather precisely with both applied charge localization methods with the only difference between them being that with solvent screening, 28% of the negative countercharge is found on the solvent and Δ SCF by definition puts a whole electron on the chlorine. We also illustrate in Table III that a small admixture of Hartree-Fock exchange, contained in the B3LYP functional with the aim of reducing SI effects, does not necessarily help us obtain the physically correct charge localization, as has been discussed by one of us in the context of electron coupling in a recent paper,¹⁷ and the functional is impractical for a treatment of the whole junction in terms of computational expediency.

While gold creates a new reference energy for the molecular eigenstates, it also plays the role of an electron donor or acceptor, meaning, that it can accept charge from both the complex and the counterion/solvent system. We also note in this context that for pyridyl anchors on gold surfaces Pauli repulsion leads to an electron depletion on the complex, which lowers its eigenstates energetically⁵³. This is exactly what we also find for the neutral complex in the composite junction here, where it loses electrons to the Au surface, and Fig. 4 shows that the charge transfer happens mostly at the interface, with the rest of the junction not contributing to it in a significant way, while for the charged junction the gold bulk absorbs some of the positive charge, as shown in Table II.

TABLE III. Partial charges on a Cl ion (and if applicable also on the solvent) sharing the same cell with the complex in the absence of the Au leads in units of fractions of an electron. Both the solvent screening method and Δ SCF generate the correct result of one electron, while B3LYP underestimates charge localization in the same way as PBE.

	Uncorrected		Solvent	Δ SCF
	B3LYP	PBE	PBE	PBE
Countercharge	0.41	0.42	0.98	0.97

Whether this latter charge absorption is due to SI artifacts in the calculations or is a realistic result for the investigated system is a delicate question. While we deal explicitly with the SI error for the charge localization on the chlorine counterion, the charge distribution between the Ru complex and the gold slab is not necessarily strongly localized anywhere. The Ru atom is embedded into the complex by rather strong covalent bonds with its carbon ligands, and as a consequence, it contains only a fraction of a positive charge in both the neutral and charged complexes (i.e., for its formal oxidation numbers +II and +III), regardless of whether the complex is attached to the surface or not, as can be seen from the values in Table II. Also the electronic coupling at the interface is of intermediate strength, as indicated by the rather broad peak shape in the transmission functions. This does not contradict the fact that the bonding between the pyridyl anchor group and gold atom is rather weak³⁵ because in the case of Pauli repulsion the coupling with filled MOs produces bonding and antibonding states.⁵³ So the charge distribution we find in Table II could be physically correct, although it is not what one would attribute to the system when writing down its redox equations. To investigate further the issue of whether the charge distribution in the junction is realistic, we employ electronegativity theory in the next section, where we reduce the complexity of the investigated four-component system by replacing the chlorine ion and solvent by an external charge for our analysis.

At this point we just use the partial charges computed with Bader's method and given in Table II to analyze the contributions defining the projected MO eigenenergies in Fig. 3 in the way established in Ref. 53. In panel A0 we align vacuum potentials between the isolated Au slab and the isolated Ru complex without any charging of the components,

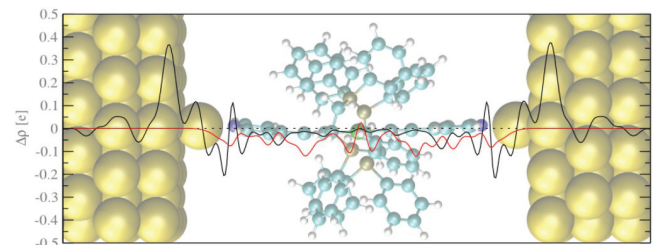


FIG. 4. (Color online) Charge-density difference between the coupled system and the isolated complex and gold slab (black curve) and between the isolated complex in its charged and neutral states (red curve), where pseudodensities in terms of the PAW formalism have been used for the densities in order to eliminate artificial peaks near the nuclei.

which results in the HOMO and HOMO-1 being energetically higher than the Fermi level of the gold leads. If we consider the changes in the respective vacuum potentials due to the negative charge on the Au slab (+0.39 electrons) and the positive one on the complex (−0.43 electrons), we arrive at the level positions given in panel A0.4 with the HOMO and HOMO-1 well below E_F , which almost exactly match the projections from the composite junctions, which are also shown in panel C0.4. This good agreement is somewhat surprising given that while the Pauli repulsion effect depletes electrons mainly from the pyridyl anchor groups of the Ru complex, a partial charge externally put on the isolated complex is distributed evenly because it is achieved by emptying the HOMO, as can be seen by comparing the black and red curves in Fig. 4. The situation becomes more complicated for charging state +1 of the junction, where there is an apparent mismatch between MO projections from the composite system (panels C0.8 and C0.89 for Δ SCF and solvent screening, respectively) and their analogs from the vacuum alignment of the separated Au slab and Ru complex (panels A0.8 and A0.89), where the partial charges from Table II have been applied externally.

Although it is natural that panels A0.8 and A0.89 exhibit lower eigenenergies of MOs than panel A0.4 due to the increased binding of electrons in more strongly positively charged molecules, the HOMO has to be close to E_F , i.e., within the range of the Fermi width, because it is partially emptied for charging state +1, which is indeed the case for the projections in panels C0.8 and C0.89. The solution to this conundrum can be found when considering the role of the counterion, which also influences the vacuum potential if now the Ru complex and the chlorine are considered to be one component in the alignment process, with the Au slab being the other one. This scenario is depicted in panel A(Cl)0.95, where we perform the level alignment starting from a calculation with a chlorine charged with an electron by Δ SCF and extracting the countercharge from the complex as the molecular component. Unfortunately, we can define our constraints within Δ SCF only for integer charges, but a hypothetical A(Cl)0.8 would result in slightly higher MO eigenenergies compared to panel A(Cl)0.95 and therefore be in perfect agreement with panel C0.8 in Fig. 3. The distinct rise in energies going from panel A0.8 to A(Cl)0.95 is intuitively clear because we are replacing the vacuum potential of a strongly positively charged component with that of a strongly polarized but overall neutral one. We note that in all cases HOMO and HOMO-1 switch their respective energetic positions, as indicated by the colors used in Fig. 3, which can be readily explained by their different localization patterns at the interface, which we referred to at the beginning of this section.

IV. INTERPRETATION OF THE CHARGE DISTRIBUTION IN TERMS OF ELECTRONEGATIVITY THEORY

In order to find explanations for the charge-density distributions described in the last section, we now analyze the junction in terms of electronegativity theory following the concepts of Parr and Pearson.⁴³ The key quantities in this approach are the electronegativity μ and the hardness ν , where the first is based

on Mulliken's definition of electronegativity,⁵⁸ i.e.,

$$\mu = \left(\frac{\partial E}{\partial N} \right)_q = \frac{I + A}{2}, \quad (1)$$

and the latter is defined as

$$\nu = \frac{1}{2} \left(\frac{\partial^2 E}{\partial N^2} \right)_q = \frac{I - A}{2}, \quad (2)$$

with I being the ionization potential, calculated as the total energy difference of the N and $N - 1$ systems, and A being the electron affinity, defined as $E(N + 1) - E(N)$.

When two different systems are brought into contact, the charge transfer from one to the other can be calculated as

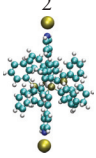
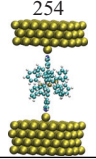
$$\Delta N = \frac{\mu_2 - \mu_1}{2(\nu_1 + \nu_2)}, \quad (3)$$

where both the electronegativities and hardnesses of the separate components have an impact on the amount of charge transfer between them.⁴³

The ionization potential I and the electron affinity A are commonly defined for the neutral state of the individual subsystems, but as shown by Balbas *et al.*,⁵⁹ their role of defining the electronegativity and hardness is also valid for ions, which allows us to describe also the charge distribution in the junction with a charging state of +1 in terms of EN theory. As discussed in the previous sections, we fixed the charges on the counterion and solvent manually, and therefore in this section we are mostly interested in understanding the charge distribution between the Au slab and the Ru complex. For this purpose we adjust their respective charging states by putting an external charge q on the subsystems in separate calculations without periodic boundary conditions, where the charge in the simulation cell can be defined by the total number of electrons without having to worry about electrostatic interactions with neighboring cells. The definitions of μ and ν in Eqs. (1) and (2) as functions of such an external charge q is unusual but not in contradiction to the basic assumptions of EN theory.

It requires, however, some statistics for taking into account the possible starting points for the charge transfer. In the case without external charge only one such initial electron configuration of the components has to be dealt with, i.e., a neutral gold slab and a neutral complex. Raising the external charge to $+1|e|$ allows for two different starting points for the charge transfer, namely, Ru complex⁺¹/Au⁰ and Ru complex⁰/Au⁺¹. In principle the calculation of ΔN for both should lead to identical predictions for the final charge distribution in the composite system with a total charge of +1, but imperfections in our DFT-based total-energy calculations such as SI errors and the approximative nature of the XC functional lead to deviations, as shown in Table IV. Averaging ΔN over all possible integer configurations should provide an improvement with regard to such errors. Hereby special emphasis has to be put on the reference point for ΔN , i.e., the subsystem with index 1 in Eq. (3). Since the Ru complex and the gold slab enter this equation at charged states, the calculated μ_i , ν_i , and ΔN also refer to these charged states. In order to obtain the change of electrons relative to the neutral subsystems the related integer charges have to be subtracted.

TABLE IV. (Color online) Illustration of the statistics in our EN theory predictions for charged states, which arises from the possibility of different initial charge configurations on the subsystems before they are brought into contact. The point of reference for ΔN is the Ru complex in its charging state 0.

Number of gold atoms	Starting charges		ΔN	$\overline{\Delta N}$
	Ru complex	Au cluster		
 2	+1	0	-0.69	-0.66
	0	+1	-0.64	
	+2	0	-1.28	-1.17
	+1	+1	-1.29	
	0	+2	-0.95	
 254	+1	0	-0.24	+0.29
	0	+1	-0.34	
	+2	0	-0.52	+0.51
	+1	+1	-0.50	
	0	+2	-0.50	

To understand the role of the size of the gold slab for the charge distribution we model the gold component in our EN theory analysis with clusters of different sizes, starting with the adatom and reaching the full gold surface used in the junction, as shown in Fig. 5, where we computed the electronegativities and hardnesses for charging states from 0 to +2 for each cluster size in a setup without periodic boundary conditions and calculated ΔN averaged over initial electron configurations as described above. Although only charging states 0 and +1 correspond to the experimentally relevant oxidation states for the Ru atom, +II and +III, respectively, we nevertheless go to higher positive charges in this study in order to investigate the distribution between lead surface and metal complex in more general and systematic terms. In Table IV we show the related statistical spread for the smallest and largest of our cluster sizes. Although we find that the deviations increase with both the external charge and the size of the Au cluster, their overall values are reasonably small, indicating that our predictions for ΔN from EN theory are not particularly limited in their accuracy by SIE or our choice of XC functional.

To build a bridge between the predictions for the charge distribution from EN theory and the actual ones we find in the periodic systems we use as device regions in the transport calculations, we also performed cluster calculations containing both subsystems. The charge distributions in the resulting cluster cells were analyzed according to Bader,^{56,57} where we imposed external charges for varying the charging state as we did for the subsystems for the EN predictions. The appeal of this intermediate step towards the periodic system calculation is that it allows us to distinguish between effects which come from the electronegativity differences of the components, others which have their origin in the spatial polarization of the subsystem, when they are actually brought into contact in a given geometry,^{54,60} and, finally, those related to the particular method we employ to adjust the charging state.

As shown in Fig. 5(a), the results from the EN prediction and the Bader analysis of the composite systems depending on

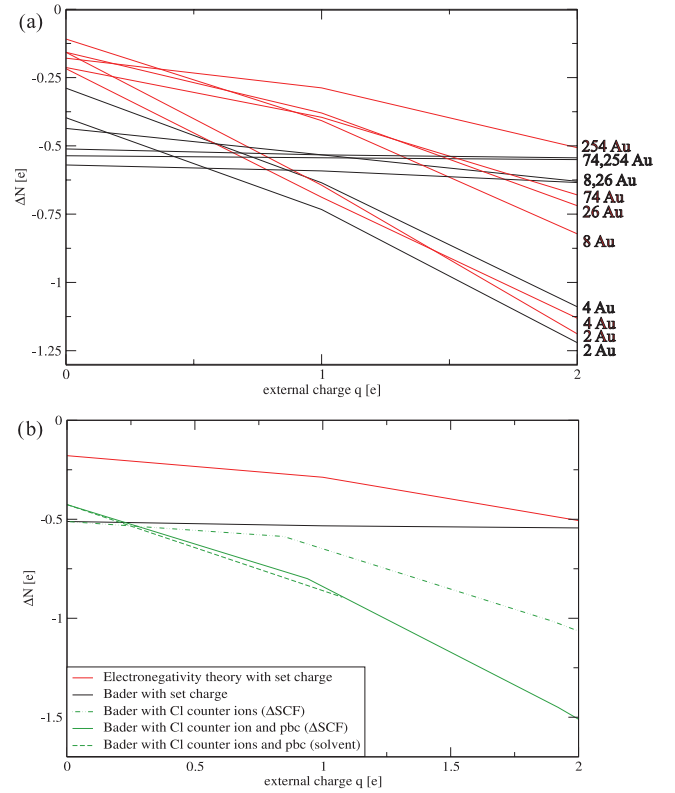


FIG. 5. (Color online) Electron loss on the complex when brought into contact with Au clusters of varying size and an external charge of up to $+2|e|$ is applied. (a) The values predicted from electronegativity theory (red) and from calculations where the complex is coupled to gold clusters in a composite system and the charge distribution is analyzed with the Bader analysis (black). (b) The ΔN values from these two sets of model calculations are compared with calculations of the device region, where the external charge was imposed as a countercharge localized on Cl ions with and without periodic boundary conditions (pbc), which are shown as solid and dashed green lines.

the Au cluster size differ. In this comparison when we apply EN theory, the charge transfer is slightly underestimated for an external charge $q = 0|e|$. Raising q to finite values leads to an overestimation of ΔN with respect to the Bader analysis for the composite system. The deviation at high external charges is small for fewer than four gold atoms on both junction sides but increases with the Au cluster size.

Figure 5(b) puts a different perspective on these qualitative differences when we compare the charge distributions obtained from both EN theory and the Bader analysis of the cluster calculations with the results for the periodic device region (see also Table II). While in the latter case the charge on the molecule increases almost linearly with the countercharge, the two models do not predict this behavior for a cluster of 254 gold atoms. The reason can be found in the details of the charging-state definition, where for the model calculations an external charge is imposed, which is distributed homogeneously, and for the subsystem the introduced charge delocalizes over all the atoms in the cluster, leading to just a minor increase in its electronegativity with increasing q . This is a consequence of the hardness, as the derivative of the electronegativity [see

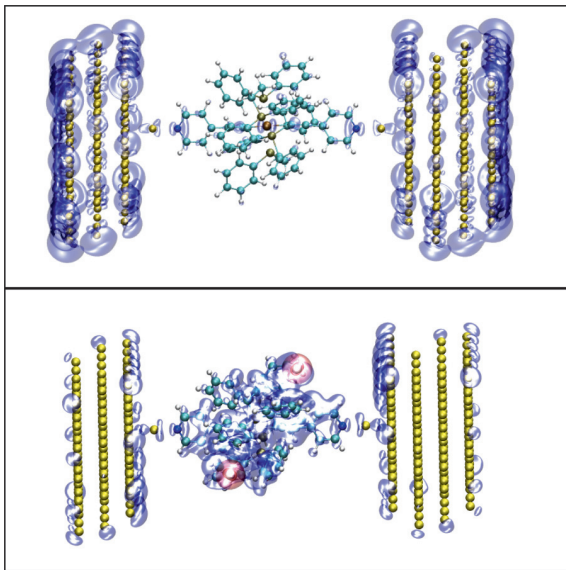


FIG. 6. (Color online) Electron density difference between the Ru complex in charging states +2 and 0, where the charge was put on the cluster by an external charge (top panel) or Cl ions, with the negative countercharge localized by Δ SCF (bottom panel). In both cases we show results from cluster calculations with an isovalue threshold of $2 \times 10^{-4}e$, where a loss of electronic charge is depicted in blue and a gain is red.

Eqs. (1) and (2)] becomes smaller with cluster size. On the other hand, the energy needed to extract an electron from the much smaller Ru complex increases strongly with its charging state compared to gold. As a consequence, the external charge is mostly absorbed by the Au cluster, leading to rather modest charging of the molecule with an increasing external charge in the cluster models.

If, on the other hand, we adjust the charging state also in the composite cluster calculations in the same way we did for the periodic cells, namely, by localizing the countercharge on a chlorine ion, the situation changes, as can be seen from the dashed green curve in Fig. 5(b). Instead of a globally defined external charge we now have one or two point charges of opposite sign situated around the cluster. As a consequence, a local Coulomb attraction term makes a localization of the positive charge on the Ru complex and the Au surface rather than the bulk regions more favorable. Figure 6 shows the charge-density difference between the +2 state and the neutral junction for the charging state defined by an external charge (top panel) and by chlorine atoms with charge localization enforced by Δ SCF (bottom panel). Without counterions the introduced positive charge is localized mostly on the gold atoms in the leads. Due to the nonperiodic setup of the cell

fractional positive charges propagate to the outward-pointing surfaces of the gold cluster because of their mutual repulsion. If the charging state is defined by chlorine counterions, on the other hand, the introduced positive charge is mostly localized on the Ru complex and the lead surface because it is attracted by the counterions. Fractions of positive charge are, however, still localized on the outer parts of the gold bulk since they are not hindered by the presence of a neighboring cell in a nonperiodic setup, and Fig. 5(b) shows that therefore periodic boundary conditions even increase the positive charge on the Ru-complex region.

V. SUMMARY

The aim of this paper was the description of coherent electron transport through a single-molecule junction containing a redox-active center with an emphasis on its charging. The correct description of the charge distribution within DFT is essential in this context, and we applied two independent methods for correcting the self-interaction error, namely, solvent screening and Δ SCF, where in both cases the countercharge is localized on a Cl ion, where this setup is meant to mimic the effect of a gate in an electrochemical STM setup. We found that the actual charge on the Ru complex in a charging state of +1 (i.e., corresponding to the formal oxidation state of +III of the Ru atom) is smaller than 1 when it is coupled to a gold surface, which might indeed be realistic since some of the charge can be absorbed by the leads. In order to investigate this issue we made predictions for model systems of varying size of the gold component within electronegativity theory, which we supplemented with cluster calculations. This analysis led us to the conclusion that some part of the charge should indeed be absorbed by the leads, but most of it remains on the complex due to Coulomb attraction, where the vicinity of the localized charge on the counterion has a stabilizing effect. Therefore, we assume that the charge distributions we find in our calculations for the device region are realistic in physical terms.

ACKNOWLEDGMENTS

G.K. and R.S. are currently supported by the Austrian Science Fund FWF, Project No. P22548. We are deeply indebted to the Vienna Scientific Cluster (VSC), whose computing facilities were used to perform all calculations presented in this paper (Project No. 70174) and where we were provided with extensive installation and mathematical library support by Markus Stöhr and Jan Zabloudil in particular. We gratefully acknowledge helpful discussions with Elvar Ö. Jónsson, Paweł Zawadzki, Marcin Dulak, Karsten W. Jacobsen, Kristian S. Thygesen, Victor Geskin, and Tim Albrecht.

*robert.stadler@univie.ac.at

¹Y. Meir and N. S. Wingreen, *Phys. Rev. Lett.* **68**, 2512 (1992).

²M. Brandbyge, J. L. Mozos, P. Ordejon, J. Taylor, and K. Stokbro, *Phys. Rev. B* **65**, 165401 (2002).

³Y. Xue, S. Datta, and M. A. Ratner, *Chem. Phys.* **281**, 151 (2002).

⁴A. R. Rocha, V. M. Garcia-Suarez, S. W. Baily, C. J. Lambert, J. Ferrer, and S. Sanvito, *Nat. Mater.* **4**, 335 (2005).

- ⁵K. S. Thygesen and K. W. Jacobsen, *Chem. Phys.* **319**, 111 (2005).
- ⁶C. Joachim, J. K. Gimzewski, R. R. Schlittler, and C. Chavy, *Phys. Rev. Lett.* **74**, 2102 (1995).
- ⁷M. A. Reed, C. Zhou, C. J. Muller, T. P. Burgin, and J. M. Tour, *Science* **278**, 252 (1997).
- ⁸J. Reichert, R. Ochs, D. Beckman, H. B. Weber, M. Mayor, and H. v. Löhneysen, *Phys. Rev. Lett.* **88**, 176804 (2002).
- ⁹R. H. M. Smit, Y. Noat, C. Untiedt, N. D. Lang, M. C. van Hemert, and J. M. van Ruitenbeek, *Nature (London)* **419**, 906 (2002).
- ¹⁰T. Albrecht, K. Moth-Poulsen, J. B. Christensen, A. Guckian, T. Bjø, J. G. Vos, and J. Ulstrup, *Faraday Discuss.* **131**, 265 (2006).
- ¹¹T. Albrecht, A. Guckian, J. Ulstrup, and J. G. Vos, *Nano Lett.* **5**, 1451 (2005).
- ¹²W. Haiss, H. van Zalinge, S. J. Higgins, D. Bethell, H. Höbenreich, D. J. Schiffrin, and R. J. Nichols, *J. Am. Chem. Soc.* **125**, 15294 (2003).
- ¹³A. M. Ricci, E. J. Calvo, S. Martin, and R. J. Nichols, *J. Am. Chem. Soc.* **132**, 2494 (2010).
- ¹⁴J. P. Perdew and A. Zunger, *Phys. Rev. B* **23**, 5048 (1981).
- ¹⁵J. Gräfenstein, E. Kraka, and D. Cremer, *Phys. Chem. Chem. Phys.* **6**, 1096 (2004).
- ¹⁶C. Toher, A. Filippetti, S. Sanvito, and K. Burke, *Phys. Rev. Lett.* **95**, 146402 (2005).
- ¹⁷R. Stadler, J. Cornil, and V. Geskin, *J. Chem. Phys.* **137**, 074110 (2012).
- ¹⁸M. Lundberg and P. E. M. Siegbahn, *J. Chem. Phys.* **122**, 224103 (2005).
- ¹⁹E. Ö. Jónsson, K. S. Thygesen, J. Ulstrup, and K. W. Jacobsen, *J. Phys. Chem. B* **115**, 9410 (2011).
- ²⁰J. Gavnholt, T. Olsen, M. Engelund, and J. Schiøtz, *Phys. Rev. B* **78**, 075441 (2008).
- ²¹T. Olsen, J. Gavnholt, and J. Schiøtz, *Phys. Rev. B* **79**, 035403 (2009).
- ²²B. Kim, J. M. Beebe, C. Olivier, S. Rigaut, D. Touchard, J. G. Kushmerick, X.-Y. Zhu, and C. D. Frisbie, *J. Phys. Chem. C* **111**, 7521 (2007).
- ²³K. Liu, X. Wang, and F. Wang, *ACS Nano* **2**, 2315 (2008).
- ²⁴S. Flores-Torres, G. R. Hutchinson, L. J. Soltzberg, and H. D. Abruña, *J. Am. Chem. Soc.* **128**, 1513 (2006).
- ²⁵J. E. McGrady, T. Lovell, R. Stranger, and M. G. Humphrey, *Organometallics* **16**, 4004 (1997).
- ²⁶S. Rigaut, C. Olivier, K. Costuas, S. Choua, O. Fadhel, J. Massue, P. Turek, J.-Y. Saillard, P. H. Dixneuf, and D. Touchard, *J. Am. Chem. Soc.* **128**, 5859 (2006).
- ²⁷S. Rigaut, J. Perruchon, S. Guesmi, C. Fave, D. Touchard, and P. H. Dixneuf, *Eur. J. Inorg. Chem.* **2005**, 447 (2005).
- ²⁸C. E. Powell, M. P. Cifuentes, J. P. Morral, R. Stranger, M. G. Humphrey, M. Samoc, B. Luther-Davies, and G. A. Heath, *J. Am. Chem. Soc.* **125**, 602 (2003).
- ²⁹S. Rigaut, K. Costuas, D. Touchard, J.-Y. Saillard, S. Golhen, and P. H. Dixneuf, *J. Am. Chem. Soc.* **126**, 4072 (2004).
- ³⁰G.-L. Xu, M. C. DeRosa, R. J. Crutchley, and T. Ren, *J. Am. Chem. Soc.* **126**, 3728 (2004).
- ³¹S. Rigaut, J. Perruchon, L. Le Pichon, D. Touchard, and P. H. Dixneuf, *J. Organomet. Chem.* **670**, 37 (2003).
- ³²S. Rigaut, L. Le Pichon, J.-C. Daran, D. Touchard, and P. H. Dixneuf, *Chem. Commun.* 1206 (2001).
- ³³S. Rigaut, D. Touchard, and P. H. Dixneuf, *Organometallics* **22**, 3980 (2003).
- ³⁴R. Stadler, K. S. Thygesen, and K. W. Jacobsen, *Nanotechnology* **16**, S155 (2005).
- ³⁵R. Stadler, K. S. Thygesen, and K. W. Jacobsen, *Phys. Rev. B* **72**, 241401(R) (2005).
- ³⁶R. Stadler, *Phys. Rev. B* **80**, 125401 (2009).
- ³⁷C. Li, A. Mishchenko, Z. Li, I. Pobelov, Th. Wandlowski, X. Q. Li, F. Würthner, A. Bagrets, and F. Evers, *J. Phys. Condens. Matter* **20**, 374122 (2008).
- ³⁸M. Ruben, A. Landa, E. Lörtscher, H. Riel, M. Mayor, H. Görls, H. B. Weber, A. Arnold, and F. Evers, *Small* **4**, 2229 (2008).
- ³⁹H. Cao, J. Jiang, J. Ma, and Y. Luo, *J. Am. Chem. Soc.* **130**, 6674 (2008).
- ⁴⁰E. Leary, H. Höbenreich, S. J. Higgins, H. van Zalinge, W. Haiss, R. J. Nichols, C. M. Finch, I. Grace, C. J. Lambert, R. McGrath, and J. Smerdon, *Phys. Rev. Lett.* **102**, 086801 (2009).
- ⁴¹A. Tawara, T. Tada, and S. Watanabe, *Phys. Rev. B* **80**, 073409 (2009).
- ⁴²I. Rungger, X. Chen, U. Schwingenschlögl, and S. Sanvito, *Phys. Rev. B* **81**, 235407 (2010).
- ⁴³R. G. Parr and R. G. Pearson, *J. Am. Chem. Soc.* **105**, 7512 (1983).
- ⁴⁴J. J. Mortensen, L. B. Hansen, and K. W. Jacobsen, *Phys. Rev. B* **71**, 035109 (2005).
- ⁴⁵J. Enkovaara *et al.*, *J. Phys. Condens. Matter* **22**, 253202 (2010).
- ⁴⁶J. P. Perdew, K. Burke, and M. Ernzerhof, *Phys. Rev. Lett.* **77**, 3865 (1996).
- ⁴⁷A. Nitzan, *Annu. Rev. Phys. Chem.* **52**, 681 (2001).
- ⁴⁸J. Taylor, M. Brandbyge, and K. Stokbro, *Phys. Rev. Lett.* **89**, 138301 (2002).
- ⁴⁹K. Stokbro, J. Taylor, and M. Brandbyge, *J. Am. Chem. Soc.* **125**, 3674 (2003).
- ⁵⁰P. Zawadzki, K. W. Jacobsen, and J. Rossmeisl, *Chem. Phys. Lett.* **506**, 42 (2011).
- ⁵¹P. Zawadzki, J. Rossmeisl, and K. W. Jacobsen, *Phys. Rev. B* **84**, 121203(R) (2011).
- ⁵²GHEMICAL, <http://www.bioinformatics.org/ghemical/ghemical/index.html>.
- ⁵³R. Stadler and K. W. Jacobsen, *Phys. Rev. B* **74**, 161405(R) (2006).
- ⁵⁴R. Stadler, *J. Phys. Conf. Ser.* **61**, 1097 (2007).
- ⁵⁵R. Stadler, *Phys. Rev. B* **81**, 165429 (2010).
- ⁵⁶W. Tang, E. Sanville, and G. Henkelman, *J. Phys. Condens. Matter* **21**, 084204 (2009).
- ⁵⁷G. Henkelman, A. Arnaldsson, and H. Jónsson, *Comput. Mater. Sci.* **36**, 254 (2006).
- ⁵⁸R. S. Mulliken, *J. Chem. Phys.* **2**, 782 (1934).
- ⁵⁹L. C. Balbas, E. Las Heras, and J. A. Alonso, *Z. Phys. A* **305**, 31 (1982).
- ⁶⁰R. F. Nalewajski, *J. Am. Chem. Soc.* **106**, 944 (1984).

PAPER II

High-Conductive Organometallic Molecular Wires with
Delocalized Electron Systems Strongly Coupled to Metal
Electrodes

High-Conductive Organometallic Molecular Wires with Delocalized Electron Systems Strongly Coupled to Metal Electrodes

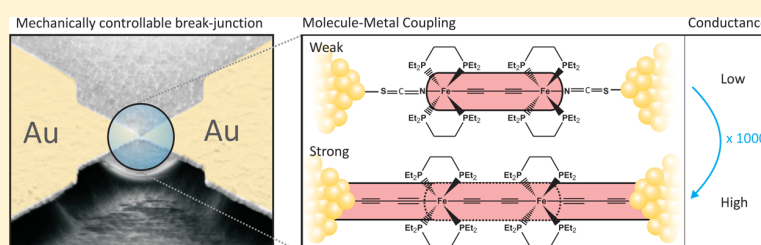
Florian Schwarz,[†] Georg Kastlunger,[‡] Franziska Lissel,[§] Heike Riel,[†] Koushik Venkatesan,^{*,§} Heinz Berke,^{*,§} Robert Stadler,^{*,‡} and Emanuel Lörtscher^{*,†}

[†]IBM Research—Zurich, Säumerstrasse 4, CH-8803 Rüschlikon, Switzerland

[‡]Department of Physical Chemistry, University of Vienna, Sensengasse 8/7, A-1090 Vienna, Austria

[§]Department of Chemistry, University of Zürich Winterthurerstrasse 190, CH-8057 Zürich, Switzerland

S Supporting Information



ABSTRACT: Besides active, functional molecular building blocks such as diodes or switches, passive components, for example, molecular wires, are required to realize molecular-scale electronics. Incorporating metal centers in the molecular backbone enables the molecular energy levels to be tuned in respect to the Fermi energy of the electrodes. Furthermore, by using more than one metal center and sp-bridging ligands, a strongly delocalized electron system is formed between these metallic “dopants”, facilitating transport along the molecular backbone. Here, we study the influence of molecule–metal coupling on charge transport of dinuclear $X(PP)_2FeC_4Fe(PP)_2X$ molecular wires ($PP = Et_2PCH_2CH_2PEt_2$); $X = CN$ (1), NCS (2), NCS_e (3), C_4SnMe_3 (4), and C_2SnMe_3 (5) under ultrahigh vacuum and variable temperature conditions. In contrast to 1, which showed unstable junctions at very low conductance ($8.1 \times 10^{-7} G_0$), 4 formed a $Au-C_4FeC_4FeC_4-Au$ junction 4' after $SnMe_3$ extrusion, which revealed a conductance of $8.9 \times 10^{-3} G_0$, 3 orders of magnitude higher than for 2 ($7.9 \times 10^{-6} G_0$) and 2 orders of magnitude higher than for 3 ($3.8 \times 10^{-4} G_0$). Density functional theory (DFT) confirmed the experimental trend in the conductance for the various anchoring motifs. The strong hybridization of molecular and metal states found in the C–Au coupling case enables the delocalized electronic system of the organometallic Fe_2 backbone to be extended over the molecule–metal interfaces to the metal electrodes to establish high-conductive molecular wires.

KEYWORDS: Molecular Wire, Single-Molecule Junctions, Electronic Transport, Break-Junctions, Organometallic Compounds, Density Functional Theory

Molecular electronics aims at employing single molecules as functional building blocks in electronic circuits. Besides such active components which provide, for example, current rectifying or switching properties, also passive components such as molecular wires are required for the realization of molecular-scale electronics. Generally, an ideal wire has lowest resistance with almost linear (ohmic) and length-independent (ballistic) transport properties. For molecular wires, the required high conductance can in principle be achieved if low injection barriers for charge-carriers are present at the molecule–metal interfaces, if molecular orbitals (MOs) are available close to the Fermi energy of the electrodes, and if a large degree of electronic conjugation across the backbone is present. Already the first task seems to be difficult to achieve as the most frequently used thiol anchoring^{1,2} suffers from an electronically weak molecule–metal coupling. Additionally, multiple bonding sites available on the Au surface for the

thiol bond give rise to alternating energy barriers for charge-carrier injection and result in large fluctuations in the transport properties. Therefore, other anchoring schemes such as nitriles,³ isocyanides,⁴ amines,⁵ and pyridines⁶ were investigated. Dithiocarbamates⁷ were demonstrated to increase the molecule–metal coupling compared to previously used single-bond anchors by at least 1 order of magnitude and to simultaneously reduce fluctuations. The use of fullerenes as anchors^{8–10} seems promising, because of the larger molecule–metal interface and the affinity of fullerenes for precious metals.¹¹ However, it turned out that the transport-limiting barriers shifted from the molecule–metal interfaces onto the molecular backbone, independently of the specific connection

Received: July 29, 2014

Revised: September 5, 2014

Published: September 18, 2014

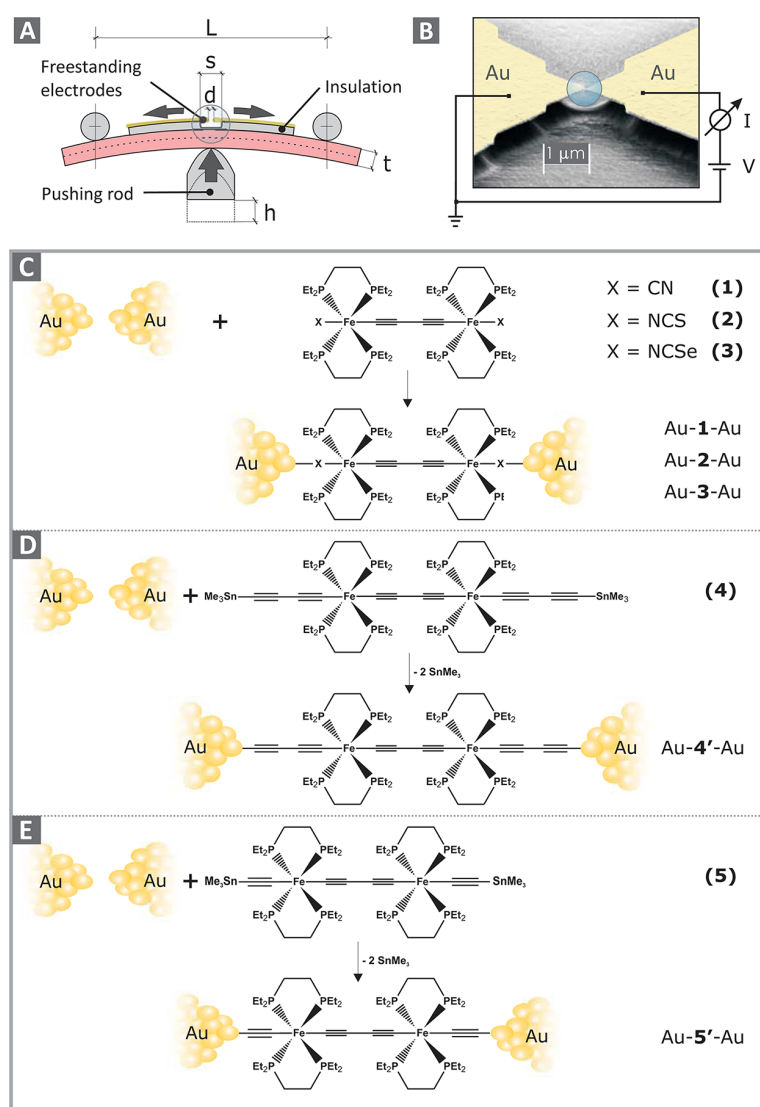


Figure 1. (A) Operation principle of a mechanically controllable break-junction. (B) Scanning electron microscope (SEM) image of a microstructured sample. (C) Compounds 1–3 with corresponding reaction schemes upon coupling to Au electrodes. In contrast to compounds 1–3, the SnMe_3 end groups of 4 and 5 cleave off and direct C–Au bonds are formed yielding the Au-4'–Au (D) and the Au-5'–Au junction (E), respectively.

scheme to the fullerene.¹² In contrast to fullerenes with many, but weak, sp^2 “bonds”, the direct C–Au bond showed unprecedented high conductances for oligophenyls up to $0.9\ G_0$,¹³ (for one phenyl ring) close to the theoretical maximum of $1\ G_0$ (with $G_0 = 2e^2/h \simeq 77\ \mu\text{S}$ the conductance quantum). The C–Au bond can be established either by extrusion of a trimethyltin moiety¹³ or post deprotection of a trimethylsilyl moiety.¹⁴ Currently, the direct C–electrode bond seems to be the most promising coupling scheme also for graphene electrodes^{15,16} if polymerization via the free termini can be prevented.

Oligo(phenylene ethynylene)s (OPEs) were considered as one class of molecular wires as their conjugated backbone enables electron transport. In that respect, C–Au coupled OPEs are currently the highest conductive molecular wires^{13,14} with an exponential conductance decay due to tunneling of approximately 1 order of magnitude per phenyl ring. Organometallic molecules¹⁷ with incorporated metal centers form

delocalized electron systems between two or more metal centers if appropriate ligand connections over unsaturated C bridges are chosen.¹⁸ Furthermore, the MO levels can be tuned by the metal centers to better align with the Fermi energy of the leads. Motivated by this seminal idea, we have devised dinuclear Fe complexes¹⁹ $\text{X}(\text{PP})_2\text{FeC}_4\text{Fe}(\text{PP})_2\text{X}$ consisting of a $[\text{FeC}_4\text{Fe}]$ backbone with highly delocalized electronic systems.²⁰ To investigate the effect of molecule–metal coupling on transport across the $[\text{FeC}_4\text{Fe}]$ backbone and its influence on the delocalized electronic system, we varied only the end groups coordinatively or covalently bonded to the $[\text{FeC}_4\text{Fe}]$ unit. All compounds can be considered as rigid-rod like structures with reduced conformational degrees of freedom. Figure 1 C shows compounds 1–3 bound coordinatively via terminal CN, NCS, and NCSe end-groups to Au, whereas the SnMe_3 end-capped compounds 4 and 5 (Figure 1D and 1E) allow for different covalent bonding motifs (see Supporting Information), for example, to form a direct covalent C–Au σ

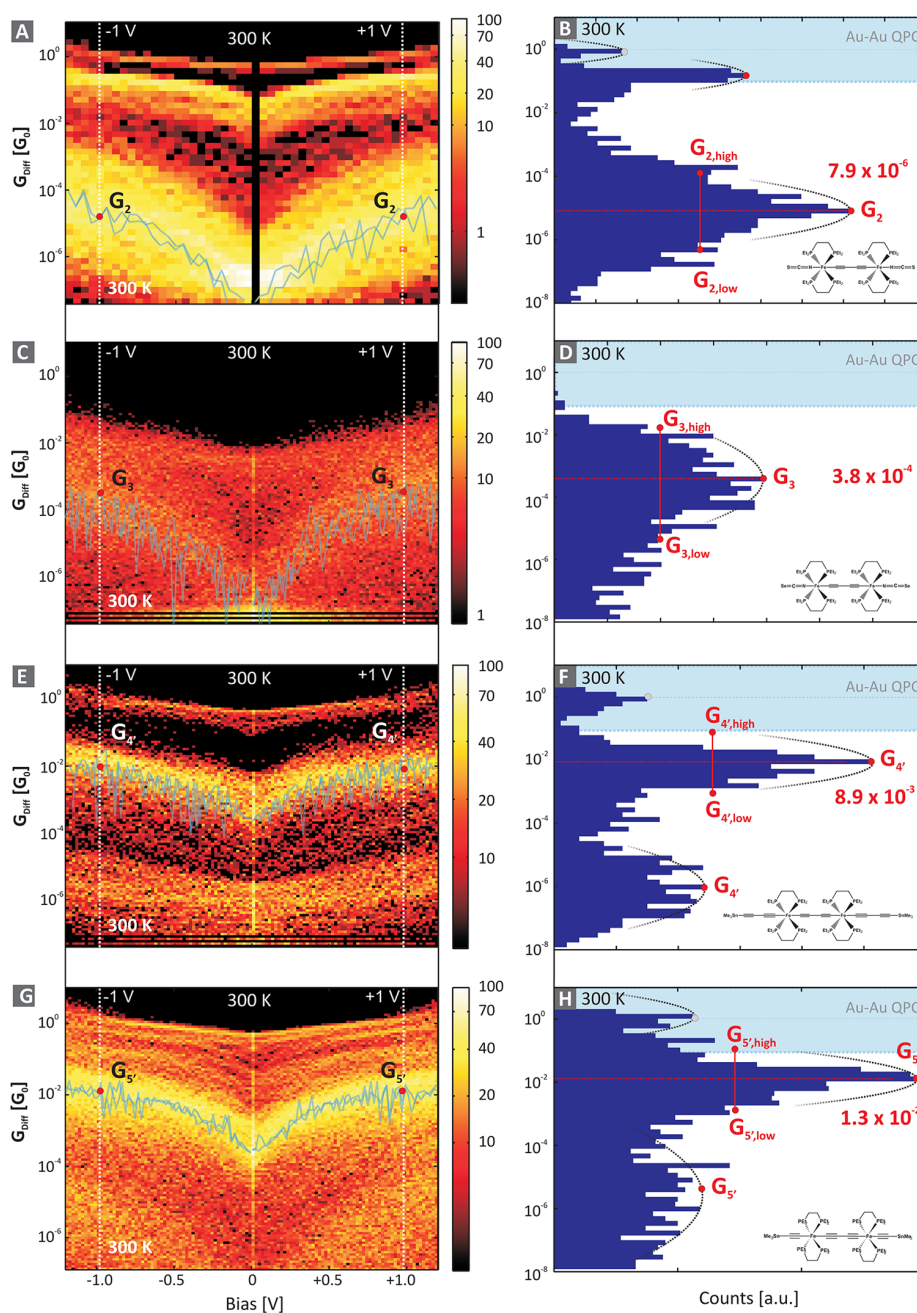


Figure 2. Density plots of the differential conductance vs voltage, $G_{\text{Diff}}-V$, characteristics acquired upon repeated opening of the junction at 300 K for compounds **2** (A), **3** (C), **4'** (E), and **5'** (G) upon opening of the junction at 300 K. Individual $G_{\text{Diff}}-V$ curves (raw data) are plotted in transparent blue to display the functional behavior of an individual curve. Corresponding conductance histograms extracted at ± 1.0 V are displayed for **2** (B), **3** (D), **4'** (F), and **5'** (H). The blue area signals the smallest electrode separations that can either lead to a direct Au–Au contact (and hence a QPC) or multimolecule junctions. The maximum conductance accumulation is labeled in red with a fwhm estimation for the peak width.

bond after extrusion of the SnMe_3 groups. The loss of the $-\text{SnMe}_3$ capping leads to a reduction in length of the anchoring groups and hence a shorter electrode–electrode distance for the resulting Au–molecule–Au system. The junction's length, however, determines also the direct electron-tunneling contribution between the electrodes, a non-negligible electron path parallel to the molecular-mediated one.²¹ Accordingly, we couple C_4-SnMe_3 end groups to the Fe centers to achieve a length of 2.322 nm (distance between binding Au atoms) for the Au–**4'**–Au junction that is comparable to the one of the

Au–**2**–Au (2.257 nm) and Au–**3**–Au (2.328 nm) junctions. In order to investigate length-effects on the molecule–electrode coupling, we have designed additionally compound **5** with shorter C_2-SnMe_3 end groups, which forms the Au–**5'**–Au system with an electrode separation comparable to Au–**1**–Au. All $[\text{FeC}_4\text{Fe}]$ compounds exhibit a high charge-delocalization between the two metal centers and can be oxidized or reduced reversibly in solution with up to three oxidation states at relatively low potentials (<1.0 V).^{19,20} (see Supporting Information).

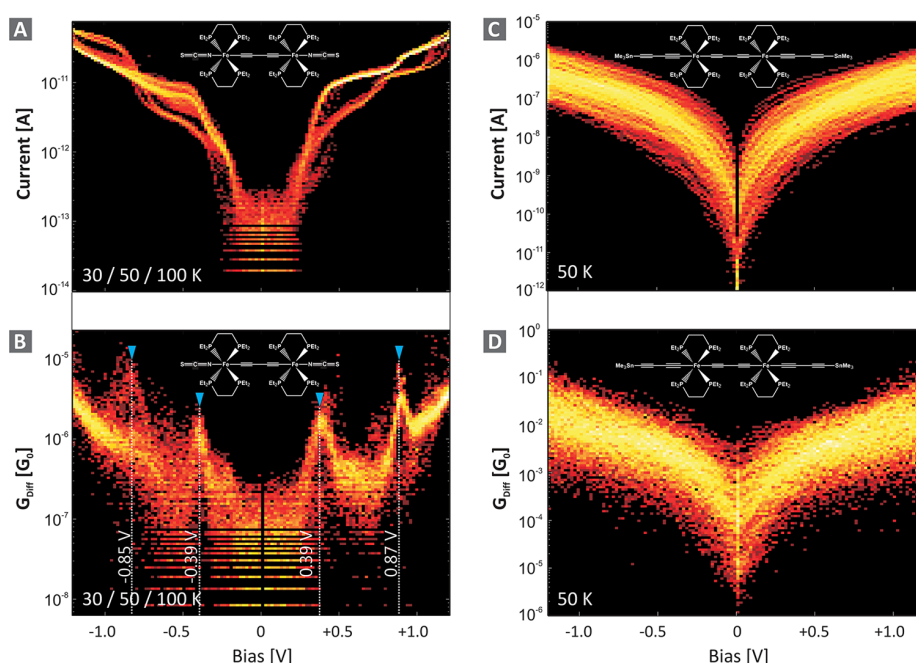


Figure 3. I – V and G_{Diff} – V characteristics taken at low temperatures upon repeated opening the junction for **2** in (A) and (B), and for **4'** in (C) and (D), respectively. For **2**, resonant transport through molecular orbitals gives rise to conductance peaks at specific voltages that are symmetric in respect to bias. In contrast, **4'** reveals exclusively monotonic curves without the appearance of discrete MOs. Furthermore, current levels are 3 orders of magnitude higher for the high-bias regime of **4'**, and 4 orders of magnitude higher for the low-bias regime due to the appearance of a conductance gap of approximately 0.8 V for **2**.

To perform transport measurements, we use electron-beam-structured break-junctions (Figure 1 B) that are mechanically actuated in a three-point bending mechanism (Figure 1 A) operated in an ultrahigh vacuum environment (UHV; pressure $p < 2 \times 10^{-9}$ mbar) and at variable temperature ($10 \text{ K} < T < 300 \text{ K}$)²² (see Supporting Information for details). Statistical data acquisition is performed by taking several hundred I – V characteristics curves in subsequent junction forming and breaking cycles.²² Due to microscopic surface reconfigurations under the applied high fields and at elevated temperatures, only the opening data is considered. We first report on the transport properties of the compounds **1**–**5** taken at room-temperature (300 K). The measurement of compound **1** upon initial junction closing and subsequent opening and closing cycles under a fixed bias of 50 mV resulted in histograms that showed less distinct molecular signatures with a small conductance accumulation located at around $8.1 \times 10^{-7} G_0$ (see Supporting Information). I – V data acquisition was not possible due to highly unstable junctions. In contrast, compounds **2**, **3**, **4**, and **5** (transformed into **4'**, and **5'** respectively, upon attachment to the Au electrodes) gave reproducible I – V data upon repeated opening of the junction. The I – V data gathered was then mathematically derived to obtain (differential) conductance vs voltage, G_{Diff} – V , curves. The entity of all these opening curves is displayed as a “density plot” in the left column of Figure 2 with the color code representing the grade of accumulation. The data contains 1033 I – V characteristics taken for **2** (with a junction forming probability of 70%), 812 for **3** (70%), 636 **4** (98%), and 1929 for **5** (70%) as acquired during the identical measurement protocols of comparable cycle numbers. On the basis of the most probable accumulations, we have selected individual G_{Diff} – V characteristics (transparent blue curves) to display the functional behavior of individual curves. In addition,

conductance histograms were constructed by taking the conductance data at $\pm 1.0 \text{ V}$ from the opening curves (see Supporting Information for histograms extracted at other voltages and in absence of molecules). According to our measurement approach, the electrodes are brought in very close contact (approximately 0.1 nm) during every cycle, which results either in the formation of a direct Au–Au contact or multimolecular junctions, depending primarily on the diffusion of surface Au atoms under the applied high field. Hence, the close-contact or high-conductance regime of $(0.08\text{--}5.0) G_0$, therefore, is considered as not appropriately controlled at room temperature and henceforth indicated by a blue shaded background in the right column of Figure 2.

Figure 2A shows one broad and two narrow accumulations of G_{Diff} – V data for **2**. The corresponding conductance peaks in the histogram are located at $0.95 G_0$, $1.5 \times 10^{-1} G_0$, and $7.9 \times 10^{-6} G_0$ as displayed in Figure 2B. The first distribution represents Au–Au QPCs that are formed repeatedly during the measurement process. The most dominant and, hence, most probable distribution at $7.9 \times 10^{-6} G_0$ is attributed to the formation of a Au–**2**–Au junction. In contrast, transport measurements of compound **3** reveal no clear accumulation in the G – V data (Figure 2 C). Instead, a spread in the G_{Diff} – V data from $10^{-5} G_0$ to $10^{-2} G_0$ is found. The conductance histogram confirms this finding by a broad peak located at $3.8 \times 10^{-4} G_0$. Much more distinct are the results for compound **4**, where three peaks are found at $0.86 G_0$, $8.9 \times 10^{-3} G_0$, and $9.6 \times 10^{-7} G_0$ (Figure 2 F), as could also be presumed from the G – V distribution (Figure 2 E). Here, the first peak again originates from Au–Au metal junctions, whereas the second and third one are due to the formation of a Au–**4'**–Au junction. From the peak height, that is, the relative occurrence, we preliminarily conclude that the most probable conductance

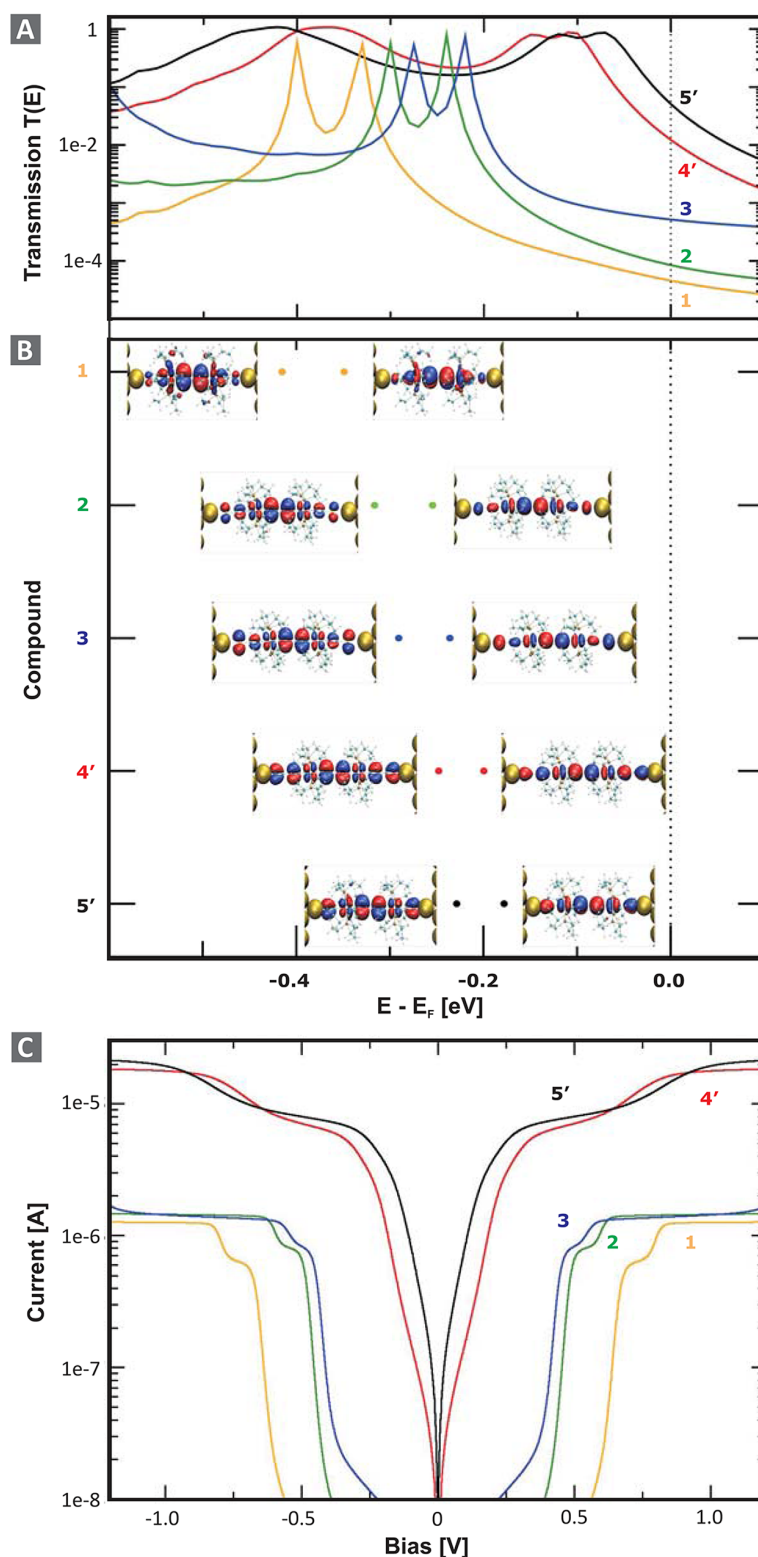


Figure 4. (A) Transmission functions for compounds 1 to 5' as calculated by DFT (color coding according to (B)). (B) Energetic positions of the HOMO and HOMO-1 of compounds 1 to 5' represented as dots with different colors for the different systems with respect to the Fermi energy of the electrodes. Also given are the respective spatial distributions of these HOMO and HOMO-1. The slight shift of the transmission peaks toward the electrode Fermi Level results from the hybridization of the MOs with the gold bands, which is removed by the subdiagonalization process used to obtain the molecular states in the composite system. (C) Calculated $I-V$ curves obtained from the transmission functions $T(E)$ in a rigid band approximation where the bias dependence of $T(E)$ is disregarded.

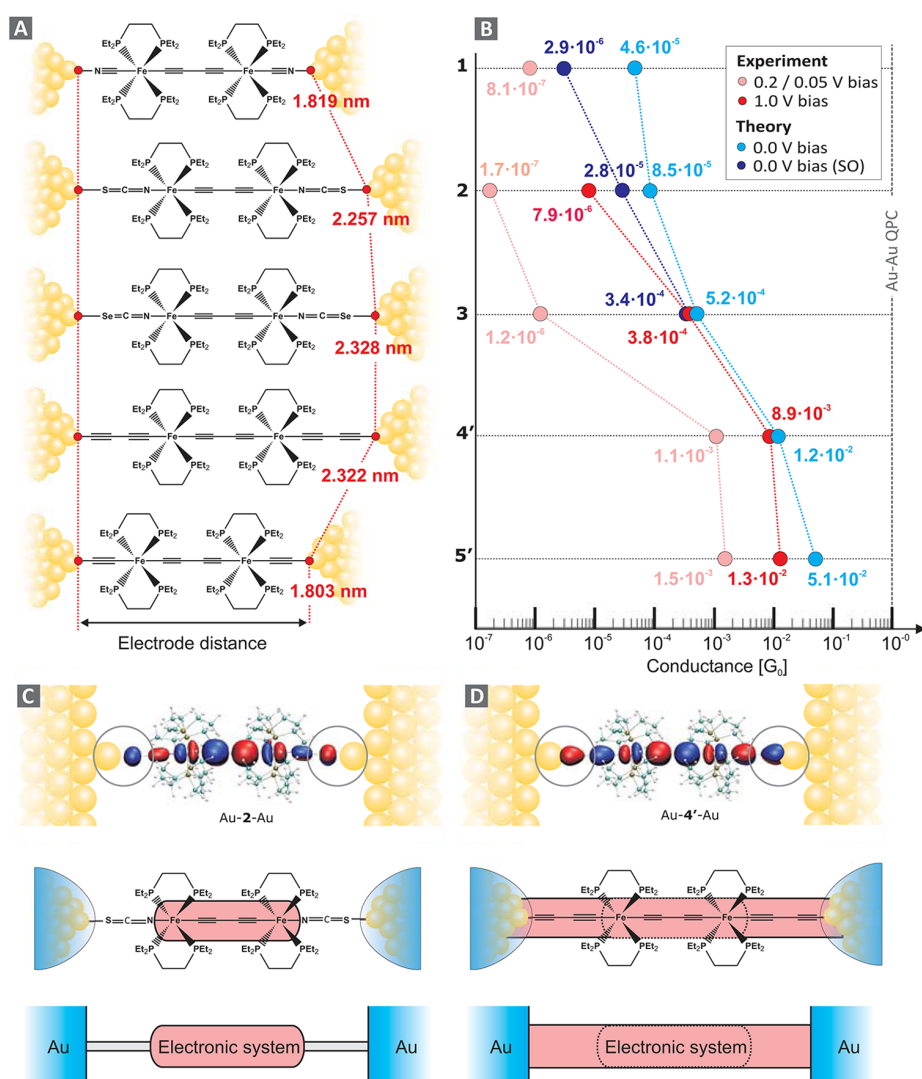


Figure 5. (A) Calculated Au–Au distances of the resulting molecular junctions for compounds **1** to **5'**. (B) Comparison of conductances for all compounds determined by experiment (300 K; 200 mV, 1.0 V) and DFT (0 K, zero bias, with and without scissor operator (SO) corrections). The experimental data point for **1** was achieved by low-bias measurements (50 mV). Schematic representation of the Au–**2**–Au (C) and the Au–**4'**–Au (D). The strong hybridization of metal and molecular states in the case of Au–**4'**–Au as evidenced by the difference in the HOMO's amplitude on the bonding site as obtained from DFT (gray circles), leads to the formation of a strong molecule–metal bond and enables to extend the delocalized electronic system between the two Fe centers over the molecule–electrode interfaces, in contrast to the weakly bonded Au–**2**–Au system.

is $7.9 \times 10^{-6} G_0$ for **2**, $3.8 \times 10^{-4} G_0$ for **3**, and $8.9 \times 10^{-3} G_0$ for **4'** (all taken at 1 V). Besides the difference in the conductance maxima, also the spread in conductance differs clearly for the three different anchor groups being studied. For NCS and NCSe anchoring, the widths of the conductance histograms are approximately 3–4 orders of magnitude (e.g., $G_{3,\text{high}}/G_{3,\text{low}} = 4 \times 10^3$, estimated from the full width at half max (fwhm) of a Gaussian-like peak), and much less for direct C–Au anchoring, approximately 1–2 orders of magnitude ($G_{4,\text{high}}/G_{4,\text{low}} = 2.5 \times 10$). This smaller conductance variation is also found for the second C–Au coupled and shorter Au–**5'**–Au system as displayed in Figure 2G and H, which show an even higher conductance of $1.3 \times 10^{-2} G_0$.

At room temperature, the MOs energy level are usually broadened and the Fermi energy of Au is broadened too, leading to rather monotonic and continuous I – V characteristics

as displayed in Figure 2 for all compounds. In contrast, the MOs usually become apparent in G – V characteristics at low temperatures, typically at less than 100 K, because of the reduced thermal broadening. Therefore, we investigated the transport properties exemplarily for **2** and **4'** at low temperatures (Figure 3). The data exhibits a symmetric conductance gap of approximately 0.8 V for **2**, independent of the temperature (the data contains 120 I – V characteristics, 40 taken at 30 K, 50 and 100 K each). In the low-voltage range up to ± 0.25 V, no MOs are available for electrons to tunnel through. At higher bias, however, the current starts to increase as frontier MOs (according to DFT the HOMO, see below) get into resonance. As can be seen best in the G – V representation, where the resonant MOs are represented by peaks, they are located at -0.85 V, -0.39 , 0.39 , and 0.87 V. They are spaced symmetrically with respect to bias polarity, as it is expected for

symmetric molecules and symmetric coupling. In addition to the conductance gap and the appearance of discrete MO resonances in **2**, many I - V characteristics with the appearance of hysteretic conductance switching are found (see Supporting Information). All these findings differ strongly to those for compound **4'**, where only monotonous curves without a conductance gap were recorded at low temperatures. Figure 3 shows 100 I - V (C), and G_{Diff} - V (D) characteristics of **4'**, taken at 50 K (similar data for 30 and 100 K); besides the absence of discrete MO peaks, the transport properties are more linear and the current levels are 3 to 4 orders of magnitude higher.

To study the MO alignment and landscape, we performed density functional theory (DFT) calculations with a PBE XC-functional within a NEGF-DFT framework^{23–25} using the GPAWcode^{26,27} to compute transmission probabilities, $T(E)$. In order to account for self-interaction errors and image charge effects present in DFT with local XC-functionals we applied a scissor operator (SO), according to Quek et al.,⁵ to the weaker coupled molecules **1** to **3** (see Supporting Information). All DFT calculations were carried out without treating spin polarization as a degree of freedom because previous tests on Fe complexes with the same ligand field revealed the low spin configuration to be the ground state. The results of the DFT calculations for the transmission functions $T(E)$ and eigenenergies of the respective orbitals HOMO and HOMO-1 relative to E_F are presented in Figure 4A and B for the compounds **1** to **5'**. Figure 4C displays calculated I - V curves that were obtained from the transmission functions $T(E)$ in a rigid band approximation where the bias dependence of $T(E)$ is disregarded, as $I = (2e/h) \int_{-\infty}^{+\infty} T(E) [f_1(E) - f_2(E)] dE$ with $f_{1,2}$ as the respective Fermi functions for the two electrodes at 50 K and their chemical potentials shifted by $\pm eV/2$. The figure illustrates the relation between the energetic position of those two MOs and the characteristic double peaks in the transmission. Furthermore, it shows the spatial distribution of these two MOs. Both the eigenvalues and the shape of the relevant MOs are similar for all systems, consisting of π -orbitals delocalized over the entire molecular backbone and containing equal amounts of both Fe d states. For each system, the HOMO and HOMO-1 differ only in the sense that they are rotated by 90° to each other, which might indicate an energetic degeneracy of the two states. However, the rotational symmetry is slightly disturbed by the (PP)₂ ligands on the Fe centers explaining the small energetic splitting and therefore the appearance of a double-peak structure in the transmission function. The conductance at zero bias, which is given in Figure 5 B) and compared to experimental findings, is mainly influenced by the tails of the HOMO and HOMO-1 peaks, leading to quite different values among the compounds investigated. Although the metal-molecule coupling is quite high for all anchor groups, the two C-Au end groups surpass the others with rather strong covalent bonding, which leads not only to broad peaks in the transmission function but also to a more distinct energy shift of the peaks toward E_F caused by hybridization of the MOs and the lead bands. It can be seen that the aligned MO eigenenergies for the different anchor schemes are rather similar to the exception of compound **1**, thereby ruling out structural variations in the charge transfer^{28–30} as a possible source for the differences in the transmission peak energies for compound **2**–**5'**, and leaving only variations in the hybridization strengths as explanation. As a consequence, even the rather long C₄ anchors of **4'** lead to a

higher conductance than the coordinatively bonding end groups CN, NCS, and NCSe, although the rate of coherent tunneling decreases rapidly with the Au-Au distance in a molecular junction. Similar to the arguments for the superior conductance provided by the C-metal end groups, also the conductance ordering for the thiol and selenium anchors can be rationalized by the fact that the electronic coupling strength of Se-Au exceeds that of S-Au^{31,32} due to a larger overlap of the wave functions. We start the discussion of experimental and theoretical findings with compound **1**. The presence of only weak and rather unlikely molecular signatures (of $8.1 \times 10^{-7} G_0$ at 50 mV bias) in the low-bias transport data of compound **1**, can have several reasons: first, the conductance of compound **1** is either below our experimental resolution ($\ll 1.0 \times 10^{-8} G_0$); second, the CN binding to Au is weak and the resulting Au-**1**-Au junction is not stable under high bias; or third, the bulky ligands prevent the terminals to bind to the Au electrodes due to the short distance to the Fe center. For compounds **2**, **3**, **4'**, and **5'**, the room-temperature experiments worked reproducibly and the conductance data displayed in Figure 2 shows values that range from slightly larger than $1 G_0$ down to $10^{-8} G_0$. Hence, it is ensured that all possible configurations during the junction forming and breaking procedure, from fully open Au contacts to Au-molecule-Au junctions and direct Au-Au QPCs were probed. The QPC peak at $1 G_0$ confirms that the electrodes completely touched (at least in some of the cycles) in the required gentle way, that is, not fusing the contact entirely. The data gathered, noticeably, represents conductances of all possible electrode distances. In case of **2**, a broad peak with a maximum at $7.9 \times 10^{-6} G_0$ is formed. The fluctuations giving rise to this broad peak are typically generated by variations in the S-Au bond as multiple bonding sites (top, hollow, bridge, etc.) are available on the Au surface. An even wider peak is found for the Se-Au bond of compound **3**, indicating multiple bonding sites with fast binding kinetics and low transition states for site exchange that do not necessarily need thermodynamic activation for the weaker Se-Au (binding energy of 0.516 eV compared to 0.669 eV for S-Au) bond. For both C-Au coupled compounds **4'** and **5'**, much narrower conductance accumulations are found. In the DFT calculations, the top position was identified to be the energetically most stable configuration. As a consequence, the C-Au anchors of compounds **4'** and **5'** are supposed to be in their equilibrium bonding-site configuration even under mechanical manipulation of the junction, which results in narrow conductance histogram peaks. In the transport data of compound **4'** (and weaker also in case of **5'**), a second, broader but smaller peak compared to the main peak at $8.9 \times 10^{-3} G_0$ is found at $9.6 \times 10^{-7} G_0$. The appearance of a second peak at a lower average conductance for **4'** (and similar also for **5'**) is presumed to originate from the various bonding scenarios of the C end group: incomplete cleavage of the SnMe₃ capping, formation of chemically reasonable alkynyl vinylidene trimethyltin species $[(-C\equiv C)(\text{SnMe}_3)C\equiv C]$ upon binding to the gold electrode resulting in the formation of a carbene type bond to the Au electrode $[Au-C_4FeC_4Fe-C\equiv C(\text{SnMe}_3)-C\equiv C-Au] = Au-4''-Au$ (see Supporting Information), transport through one of the bis(diethylphosphino)ethane ligands (as one or two arms of the phosphine ligands could lift-off to form $Fe-PCH_2-CH_2-P \rightarrow Au$) and noncleaved end groups cappings. Alternatively in our understanding, also reductive C-C coupling forming a dimerized $Au-C_4FeC_4FeC_8FeC_4FeC_4-Au$ ($Au-4'-4'-Au$) junctions

(similarly for 5') can occur. As such details of the junction configuration are experimentally not directly accessible, the conductances of the Au–4'–4'–Au and Au–5'–5'–Au dimer junctions and the vinylidene-coupling case were exemplarily calculated (see Supporting Information). A conductance of $1.05 \times 10^{-5} G_0$ was found for the dimer junction Au–4'–4'–Au. In the transmission function of the dimer, the slope at the Fermi level is relatively high, which means that a small energy shift of 0.1 eV would result in a lower calculated conductance. This notion is in agreement with the experimental finding as such a small shift in energy could also be argued to arise from deficiencies of DFT such as gap underestimation. Due to the good agreement between DFT and experiments for both the “monomer” and the “dimer” compounds, we conclude that spontaneous dimerization is most likely the origin for the low-conductance peaks of compounds 4 (and also 5), in agreement with the observation of dimerization in SnMe₃-capped oligophenyls with C–Au anchors.¹³ A dimerization explains further why the contacting traces for molecular signatures are 5–7 times longer for the low-conductance *I*–*V*s compared to the high-conductance *I*–*V*s (see Supporting Information).

When comparing the main peaks in the conductance data at high bias (1.0 V) or low bias (0.2 V, see Supporting Information) of 2, 3, 4' and 5' measured at 300 K, a good qualitative agreement with DFT at zero-bias is found as directly compared in Figure 5 B). The zero-bias conductance according to DFT and the low-bias current in the experiments are both much higher for 4' or 5' than for 2 and 3, which indicates that the LDOS is much higher for the C–Au coupled systems than that of the others. The orbital distribution indicates that a strong hybridization of MOs and metal states takes place at the molecule–metal interfaces in the C–Au coupled system as evidenced by the difference in the HOMO's amplitude on the bonding site as obtained from DFT data highlighted by circles in Figure 5 D. This hybridization shifts HOMO and HOMO-1 closer to *E_F*, leading to an earlier onset in electron transport as evidenced by the low-temperature transport properties where the conductance gap has even vanished (Figure 3). Injection barriers estimated from minima in the transition-voltage-spectroscopy representation ($\ln(I/V^2) - (1/V)$; see Supporting Information) reveal a similar barrier height of $(1.75 \pm 0.3) 1/V$ for 4' and $(1.85 \pm 0.3) 1/V$ for 5' in contrast to $(4.2 \pm 1.5) 1/V$ for 3, and $(5.5 \pm 1.5) 1/V$ for 2 at 300 K. The strong hybridization of metal and molecular states established by the C–Au coupling might further be the reason why the hysteretic switching behavior found at low temperatures for the weakly coupled compound 2 (see Supporting Information) was not revealed in the strong C–Au coupled compound 4' as the MOs are more pinned and intrinsic functionality might be prohibited. The energetic positions of the frontier MOs found for compound 2 at around ± 0.4 V at low temperatures are in quantitative agreement with the energetic difference between HOMO and *E_F* calculated by DFT to be around 0.25–0.30 eV as illustrated in Figure 4B. These values are around 100 meV smaller than the MO energies in Figure 3B, which is due to the mean field character of DFT with semilocal exchange correlation functionals that do not capture many body effects.^{33,34}

Compared with trimethylsilyl¹⁴ or trimethyltin-capped oligophenyls with a direct Au–benzene attachment,³⁵ the conductance of compound 4' is more than 10-fold higher if similar wire lengths, *l*, (approximately 2 nm) are taken into

account. When comparing with organometallic ruthenium(II) bis(σ -arylacetylide) complexes with SCN–Au coupling,^{36,37} the conductance of 4' is more than 1 order of magnitude higher. For trimethyltin-capped polyphenyls with additional carbon atoms in the Au–C–benzene bonds,¹³ a conductance of $1.4 \times 10^{-2} G_0$ was found for four phenyl units, similarly high as the one of compound 4'. When taking the dimer system Au–4'–4'–Au into account, we can create a preliminary length-dependence for the conductance decrease with wire length ($G \propto e^{-\beta/l}$) of the Fe-based organometallic wires to compare with state-of-the-art molecular wires (see Supporting Information). The decay constants of $\beta = 4.4 \text{ nm}^{-1}$ (determined by experimental values at 200 mV or 1.0 V) and $\beta = 3.5 \text{ nm}^{-1}$ (DFT at zero bias) are both higher than for the organometallic ruthenium(II) bis(σ -arylacetylide) complexes^{36,37} ($\beta = 1.02$ – 1.64 nm^{-1}) or purely organic oligothiophenes³⁸ ($\beta = 1.0 \text{ nm}^{-1}$) with lowest decay constants reported so far. The values estimated and calculated are closer to decay constants for phenyls coupled via C–Au¹³ ($\beta = 4.0$ – 6.0 nm^{-1}). A full experimental study of oligomeric organometallic molecules with one to four repeating Fe units, however, has to confirm this preliminary estimation.

In summary, we have theoretically and experimentally investigated the influence of molecule–metal coupling on the electron transport properties of dinuclear Fe complexes. We varied the molecule–metal coupling systematically by using different anchoring schemes, such as CN, NCS, NCSe, C₂SnMe₃, and C₄SnMe₃ with the latter two end groups leading to a direct C–Au bond after SnMe₃ extrusion. Whereas the CN termination did not result in stable junctions, all other end groups yielded reproducible transport junctions that enabled the determination of the room-temperature coupling strengths, which follow the order $\Gamma_{\text{NCS–Au}} < \Gamma_{\text{NCSe–Au}} < \Gamma_{\text{C}_4\text{–Au}} < \Gamma_{\text{C}_2\text{–Au}}$ in qualitative agreement with DFT calculations. Moreover, the reproducible binding of the C–Au motif upon extrusion or migration of the SnMe₃ end-group was demonstrated to occur also at low temperatures (50 K), leading to the formation of high-conductive molecular wires. Overall, the class of organometallic compounds with delocalized electron systems between two and more metal centers is a promising concept to achieve long and highly conductive wires due to an extension of the electronic system of the [FeC₄Fe] unit over the molecule–metal interfaces to the electrodes by strong hybridization. Beyond that, organometallic compounds are an attractive framework for the integration of intrinsic functionality for future applications such as redox activity for conductance switching and memory application.

■ ASSOCIATED CONTENT

Supporting Information

Supporting Information on the synthesis of the compounds, the experimental setup, control measurements, histograms at other voltages, and additional DFT calculations. This material is available free of charge via the Internet at <http://pubs.acs.org>.

■ AUTHOR INFORMATION

Corresponding Authors

*E-mail: hberke@chem.uzh.ch. (H.B.)

*E-mail: venkatesan.koushik@chem.uzh.ch. (K.V.)

*E-mail: robert.stadler@univie.ac.at. (R.S.)

*E-mail: eml@zurich.ibm.com. (E.L.)

Notes

The authors declare no competing financial interest.

ACKNOWLEDGMENTS

We are grateful to B. Gotsmann, V. Schmidt, and W. Riess for scientific discussions and to M. Tschudy, U. Drechsler, and Ch. Rettner for technical assistance. Funding from the National Research Programme “Smart Materials” (NRP 62, grant 406240-126142) of the Swiss National Science Foundation (SNSF) and the University of Zürich is gratefully acknowledged. G.K. and R.S. are currently supported by the Austrian Science Fund FWF, project Nr. P22548 and are deeply indebted to the Vienna Scientific Cluster VSC, on whose computing facilities all DFT calculations have been performed (project Nr. 70174).

REFERENCES

- (1) Bumm, L. A.; Arnold, J. J.; Cygan, M. T.; Dunbar, T. D.; Burgin, T. P.; Jones, L. II; Allara, D. L.; Tour, J. M.; Weiss, P. S. *Science* **1996**, *271*, 1705–1707.
- (2) Reed, M. A.; Zhou, C.; Muller, C. J.; Burgin, T. P.; Tour, J. M. *Science* **1997**, *278*, 252–254.
- (3) Metzger, R. M.; Chen, B.; Höpfner, U.; Lakshmikantham, M. V.; Vuillaume, D.; Kawai, T.; Wu, X.; Tachibana, H.; Hughes, T. V.; Sakurai, H.; Baldwin, J. W.; Hosch, C.; Cava, M. P.; Brehmer, L.; Ashwell, G. J. *J. Am. Chem. Soc.* **1997**, *119*, 10455–10466.
- (4) Chen, J.; Calvet, L. C.; Reed, M. A.; Carr, D. W.; Grubisha, D. S.; Bennett, D. W. *Chem. Phys. Lett.* **1999**, *313*, 741–748.
- (5) Quek, S. Y.; Neaton, J. B.; Hybertsen, M. S.; Venkataraman, L.; Choi, C. H.; Louie, S. G. *Nano Lett.* **2007**, *7*, 3477–3482.
- (6) Kamenetska, M.; Su, Y. Q.; Whalley, A. C.; Steigerwald, M. L.; Choi, H. J.; Louie, S. G.; Nuckolls, C.; Hybertsen, M. S.; Neaton, J. B.; Venkataraman, L. *J. Am. Chem. Soc.* **2010**, *132*, 6817–6821.
- (7) von Wrochem, F.; Gao, D.; Scholz, F.; Nothofer, H.-G.; Nelles, G.; Wessels, J. M. *Nat. Nanotechnol.* **2010**, *5*, 618–623.
- (8) Martin, C. A.; Ding, D.; Sørensen, J. K.; Bjørnholm, T.; van Ruitenbeek, J. M.; van der Zant, H. S. J. *J. Am. Chem. Soc.* **2008**, *130*, 13198–13199.
- (9) Fock, J.; Sørensen, J. K.; Lörtscher, E.; Vosch, T.; Martin, C. A.; Riel, H.; Kilså, K.; Bjørnholm, T.; van der Zant, H. *Phys. Chem. Chem. Phys.* **2011**, *13*, 14325–14332.
- (10) Lörtscher, E.; Geskin, V.; Gotsmann, B.; Fock, J.; Sørensen, J. K.; Bjørnholm, T.; Cornil, J.; van der Zant, H. S. J.; Riel, H. *Small* **2013**, *9*, 209–214.
- (11) Joachim, C.; Gimzewski, J. K.; Schlittler, R.; Chavy, C. *Phys. Rev. Lett.* **1995**, *74*, 2102–2105.
- (12) Leary, E.; Gonzalez, T. M.; van der Pol, C.; Bryce, M. R.; Filippone, S.; Martin, N.; Rubio Bollinger, G.; Agraï, N. *Nano Lett.* **2011**, *11*, 2236–2241.
- (13) Chen, W.; Widawsky, J. R.; Vazquez, H.; Schneebeli, S. T.; Hybertsen, M. S.; Breslow, R.; Venkataraman, L. *J. Am. Chem. Soc.* **2011**, *133*, 17160–17163.
- (14) Hong, W.; Li, H.; Liu, S.-H.; Fu, Y.; Li, J.; Kaliginedi, V.; Decurtins, S.; Wandlowski, T. *J. Am. Chem. Soc.* **2012**, *134*, 19425–19431.
- (15) Cao, Y.; Dong, S.; Liu, S.; Liu, Z.; Guo, X. *Angew. Chem., Int. Ed.* **2013**, *52*, 3906–3910.
- (16) Lörtscher, E. *Nat. Nanotechnol.* **2013**, *8*, 381–384.
- (17) Ceccon, A.; Santi, S.; Orian, L.; Bisello, A. *Coord. Chem. Rev.* **2004**, *248*, 683–724.
- (18) Pevny, F.; Di Piazza, E.; Norel, L.; Drescher, M.; Winter, R. F.; Rigaut, S. *Organometallics* **2010**, *29*, 5912.
- (19) Lissel, F.; Schwarz, F.; Blaque, O.; Riel, H.; Lörtscher, E.; Venkatesan, K.; Berke, H. *J. Am. Chem. Soc.* **2014**, DOI: 10.1021/ja507672g.
- (20) Lissel, F.; Fox, T.; Blaque, O.; Polit, W.; Winter, R. F.; Venkatesan, K.; Berke, H. *J. Am. Chem. Soc.* **2013**, *135*, 4051–4060.
- (21) Gotsmann, B.; Riel, H.; Lörtscher, E. *Phys. Rev. B* **2011**, *84*, 205408.
- (22) Lörtscher, E.; Weber, H. B.; Riel, H. *Phys. Rev. Lett.* **2007**, *98*, 176807.
- (23) Brandbyge, M.; Mozos, J.-L.; Taylor, J.; Stokbro, K. *Phys. Rev. B* **2002**, *65*, 165401.
- (24) Xue, Y.; Datta, S.; Ratner, M. A. *Chem. Phys.* **2002**, *281*, 151.
- (25) Rocha, A. R.; Garcia-Suarez, V. M.; Bailey, S. W.; Lambert, C. J.; Ferrer, J.; Sanvito, S. *Nat. Mater.* **2005**, *4*, 335.
- (26) Mortensen, J. J.; Hansen, L. B.; Jacobsen, K. W. *Phys. Rev. B* **2005**, *71*, 035109.
- (27) Enkovaara, J.; Rostgaard, C.; Mortensen, J. J.; Chen, J.; Dulak, M.; Ferrighi, L.; Gavnholt, J.; Glinzvad, C.; Haikola, V.; Hansen, H. A.; Kistoffersen, H.; Kuisma, M.; Larsen, A. H.; Lehtovaara, L. *J. Phys.: Conf. Ser.* **2010**, *22*, 253202.
- (28) Stadler, R.; Jacobsen, K. W. *Phys. Rev. B* **2006**, *74*, 161405.
- (29) Stadler, R. *J. Phys.: Conf. Ser.* **2006**, *61*, 1097–1101.
- (30) Stadler, R. *Phys. Rev. B* **2010**, *81*, 16429.
- (31) Patrone, L.; Palacin, S.; Bourgoin, J.-P.; Lagoute, J.; Zambelli, T.; Gauthier, S. *Chem. Phys.* **2002**, *281*, 325–332.
- (32) Yaliraki, S. N.; Kemp, M.; Ratner, M. A. *J. Am. Chem. Soc.* **1999**, *121*, 3428–3434.
- (33) Geskin, V.; Stalder, R.; Cornil, J. *Phys. Rev. B* **2009**, *80*, 085411.
- (34) Stadler, R.; Cornil, J.; Geskin, V. *J. Chem. Phys.* **2012**, *137*, 074110.
- (35) Chen, Z. L.; Skouta, R.; Vazquez, H.; Widawsky, J. R.; Schneebeli, S.; Chen, W.; Hybertsen, M. S.; Breslow, R.; Venkataraman, L. *Nat. Nanotechnol.* **2011**, *6*, 353–357.
- (36) Kim, B.; Beebe, J. M.; Olivier, C.; Rigaut, S.; Touchard, D.; Kushmerick, J. G.; Zhu, X.-Y.; Frisbie, C. D. *J. Phys. Chem. C* **2007**, *111*, 7521–7526.
- (37) Luo, L.; Benamer, A.; Brignou, P.; Choi, S. H.; Rigaut, S.; Frisbie, C. D. *J. Phys. Chem. C* **2011**, *115*, 19955–19961.
- (38) Yamada, R.; Kumazawa, H.; Noutoshi, T.; Tanaka, S.; Tada, H. *Nano Lett.* **2008**, *8*, 1237–1240.

PAPER III

Density functional theory based calculations of the transfer
integral in a redox-active single-molecule junction

Density functional theory based calculations of the transfer integral in a redox-active single-molecule junction

Georg Kastlunger and Robert Stadler*

Department of Physical Chemistry, University of Vienna, Sensengasse 8/7, A-1090 Vienna, Austria

(Received 19 December 2013; published 12 March 2014)

There are various quantum chemical approaches for an *ab initio* description of transfer integrals within the framework of Marcus theory in the context of electron transfer reactions. In our paper, we aim to calculate transfer integrals in redox-active single molecule junctions, where we focus on the coherent tunneling limit with the metal leads taking the position of donor and acceptor and the molecule acting as a transport mediating bridge. This setup allows us to derive a conductance, which can be directly compared with recent results from a nonequilibrium Green's function approach. Compared with purely molecular systems we face additional challenges due to the metallic nature of the leads, which rules out some of the common techniques, and due to their periodicity, which requires \mathbf{k} -space integration. We present three different methods, all based on density functional theory, for calculating the transfer integral under these constraints, which we benchmark on molecular test systems from the relevant literature. We also discuss many-body effects and apply all three techniques to a junction with a Ruthenium complex in different oxidation states.

DOI: [10.1103/PhysRevB.89.115412](https://doi.org/10.1103/PhysRevB.89.115412)

PACS number(s): 73.63.Rt, 73.20.Hb, 73.40.Gk

I. INTRODUCTION

In ultrahigh vacuum and at very low temperatures, the electron transport problem in single-molecule junctions is nowadays straightforwardly accessible to a computational treatment with a nonequilibrium Green's function (NEGF) approach [1] in combination with a density functional theory (DFT) based description of the electronic structure of the separate and combined components of the junction, namely the leads and the scattering region [2–5]. The theoretical modeling of experiments with an electrochemical scanning tunneling microscope (STM) [6–9] is more challenging, because here depending on the setup as well as structural details of the system, two competing electron transport mechanisms have to be considered, namely, electron hopping, which is a thermally induced multiple step process and coherent tunneling, which is the standard one-step phenomenon known from benchmark molecules relatively strongly coupled to metallic electrodes at temperatures close to 0 K. In both cases, an atomistic description of the process under electrochemical conditions provides a formidable challenge for a DFT based theory. For the former, the difficulty lies in a simplified and compact but nevertheless sufficiently accurate description of the nuclear vibrations of the molecule and solvent which drive the electron flow. For the latter, it becomes necessary to adjust the oxidation state of the redox active center in the scattering region and therefore deal with the issue of charge localization in a multicomponent system, which we addressed in a recent publication [10] where we also established a connection to our earlier work on electronegativity theory, Fermi level alignment, and partial charge distributions within a single-molecule junction [11–13].

In our current paper, we focus on calculating the transfer integral [14] in a single molecule junction, which is a key ingredient in the semiclassical Marcus theory often used for the description of electron hopping in purely molecular systems.

This is a first step in treating hopping and coherent tunneling on the same theoretical level, which enables a direct comparison of the coherent tunneling conductance calculated from Marcus theory with that obtained from a NEGF approach and lays the ground for a description of electron hopping in our future work, where the reorganization energy and driving force will also have to be considered. For the quantum chemical description of the transfer integral, there are two types of commonly used frameworks: (1) those that look for the minimum adiabatic state splitting, which is estimated either through Koopman's theorem [15] or by tuning energy differences with external perturbations [14], and (2) those that depend on defining the diabatic states, such as the Mulliken-Hush method [16] and its generalization [17], the block diagonalization method [18], and the fragment charge difference method [19]. Because Slater determinant based techniques are rather unsuitable for the description of metallic systems (this holds also for parametrized approaches, which are very popular for the description of electron transfer processes in organic solids [20]), methods for both (i) and (ii) have also been developed within the framework of DFT more recently.

We use three of these methods in our article. Within category 1, we employ an energy gap approach [14,21], where we define the splitting of adiabatic states in a single particle version as the energy difference between suitably selected Kohn-Sham (KS) orbitals of our system and in a many body version, where we use the generalized Δ SCF technique [22–25] for localizing a charge in particular orbitals, thereby including also electronic relaxation effects in our estimation of the energy splitting of adiabatic states at the transition point. For exploiting category 2, namely, the derivation of transfer integrals via the definition of diabatic states, we use two fundamentally different approaches. One is based on calculating explicitly the coefficients for the expansion of adiabatic into diabatic states [26–28], where we introduce again a single particle and a many-body version. The other is Larsson's formula for the estimation of an effective coupling [19,29], which is a multistate approach, where the contributions of all bridging molecular orbitals (MOs) are summed up. This last

*robert.stadler@univie.ac.at

approach we use only with KS orbitals, because we could not find a meaningful many body implementation within DFT.

The paper is organized as follows. In the next section, we introduce the three different methods for calculating the transfer integral in our article by applying them to a 3×3 tight-binding (TB) Hamiltonian, which was also previously used by others for demonstration purposes [30]. In Sec. III, we describe how we combine the three techniques with DFT calculations, which we perform by using the GPAW code [31,32] and benchmark our approaches by comparing our results for molecular systems previously studied by other groups, namely, for intermolecular hole transport in a diethylene dimer [33] and for intra-molecular electron transport in a tetrathiafulvalene-diquinone anion (Q-TTF-Q⁻) [34]. In Sec. IV, we employ all techniques for the evaluation of the transfer integral in a single molecule junction with two gold electrodes connected by a Ru-complex with transport mediating MOs around the Fermi level. Here, we study the influence of the representation of the leads, starting with four-atom gold clusters and ending up with a periodic slab description of the surface, where k point integration becomes an important issue [35]. By using Nitzan's equations [36,37], we relate the conductance to the transfer integral in Marcus theory, where for the coherent tunneling limit at low bias the reorganization energy and driving force can be disregarded, and we get reasonable quantitative agreement with our previous results, where we used a NEGF-DFT technique to calculate transmission functions for the same system [10].

II. THREE METHODS FOR THE EVALUATION OF THE TRANSFER INTEGRAL

In this section, we introduce all three methods used in this article for calculating transfer integrals by applying them to the diabatic Hamiltonian \mathbf{H} of order 3×3 ,

$$\mathbf{H} = \begin{pmatrix} \varepsilon_D & V_{DB} & V_{DA} \\ V_{DB} & \varepsilon_B & V_{BA} \\ V_{DA} & V_{BA} & \varepsilon_A \end{pmatrix}, \quad (1)$$

where ε_D , ε_B , and ε_A are the onsite energies of a donor, a bridge and an acceptor state, respectively, and V_{DB} , V_{DA} , and V_{BA} the respective electronic couplings between them. When we now specify the parameters in this Hamiltonian with $\varepsilon_A = \varepsilon_D = 0$, $\varepsilon_B = 1$, $V_{DB} = V_{BA} = -0.1$ and $V_{DA} = -0.01$, which is representative for typical molecular donor/bridge/acceptor systems and identical with the setup studied in Ref. [30] a diagonalization of \mathbf{H} results in the adiabatic states,

$$\begin{aligned} \psi_1 &= 0.701\phi_D + 0.136\phi_B + 0.701\phi_A, & \varepsilon_1 &= -0.029, \\ \psi_2 &= 0.701\phi_D - 0.701\phi_A, & \varepsilon_2 &= 0.010, \\ \psi_3 &= 0.096\phi_D - 0.991\phi_B + 0.096\phi_A, & \varepsilon_3 &= 1.019. \end{aligned} \quad (2)$$

If we use the energy gap method [14,21] for evaluating the transfer integral, we obtain the expression

$$H_{DA}^{\text{gap}} = (\varepsilon_2 - \varepsilon_1)/2, \quad (3)$$

where it is important to note that the eigenenergies of the adiabatic states ψ_1 and ψ_2 have been selected in this definition because of their high amplitudes on the donor and acceptor states, while the third adiabatic state ψ_3 , which is mostly

localized on the bridge state can be disregarded. In praxis, as we will also discuss in the following sections, there are always two distinct adiabatic states which can be used for forming the energy difference in Eq. (3) even for larger Hamiltonians as long as the donor and the acceptor are characterized by a single state on each side [21].

Another definition of the transfer integral can be obtained by Larsson's formula for the derivation of an effective coupling [19,29]

$$H_{DA}^{\text{effect}} = V_{DA} - \sum_{i=1}^N \frac{V_{Di}V_{iA}}{\varepsilon_{A,D} - \varepsilon_i}, \quad (4)$$

where the direct coupling between donor and acceptor V_{DA} as well as the contributions from all N bridge states in an arbitrary system are added up explicitly and $N = 1$ for the 3×3 Hamiltonian in Eq. (1).

For the third technique, we employ for calculating the transfer integral, we follow the work of Migliore [26–28] and use the amplitudes on the donor and acceptor sites, i.e., the expansion coefficients $a_{D,1}$ and $a_{A,1}$, respectively, of the wave function for the adiabatic state with the lowest energy (the ground state ψ_1) in Eq. (1) to formulate

$$H_{DA}^{\text{coeff}} = \frac{a_{D,1}a_{A,1}}{a_{D,1}^2 - a_{A,1}^2}(\varepsilon_A - \varepsilon_D). \quad (5)$$

Since the diabatic states in Eq. (1) are orthogonal to each other by definition, we do not need to apply the orthogonalization procedure detailed in Refs. [26–28] at this point, but we applied it to the DFT calculations, which we will present in the next section. In contrast to the energy gap and effective coupling techniques, where $\varepsilon_A = \varepsilon_D$ has been assumed because the energies of the initial and final state need to be equal at the transition point where the transfer integral is defined in dependence on the reaction coordinate q , for the expansion coefficient method Eq. (5) has a discontinuity at this point, as is illustrated in the concrete example of Eq. (2), which gives $a_{A,1} = a_{D,1} = 0.701$. As it has been shown in the appendixes of Refs. [26] and [27], this discontinuity can be eliminated leading to the expected correct result at the transition state coordinate but the closer the transition state is approached the higher the demands on the computational accuracy become. This leads to a trade off, where Eq. (5) is used close to but not at the transition point and for the model Hamiltonian in Eq. (1), q can be varied by varying $\varepsilon_D - \varepsilon_A$.

It is illustrative to compare the values obtained for H_{DA} from the three methods described in this section numerically for the Hamiltonian defined in Eq. (1) for the set of parameters which result in the adiabatic wave functions in Eq. (2). This is done in Table I, where it can be seen that H_{DA}^{coeff} converges towards 0.02 for small values of $\varepsilon_D - \varepsilon_A$, while $H_{DA}^{\text{gap}} = 0.0195$ and $H_{DA}^{\text{effect}} = 0.02$. As discussed in Ref. [21], the applicability of the effective coupling method depends on $|\varepsilon_B - \varepsilon_{A,D}|$ being reasonably large and all couplings being reasonably small. In order to be more quantitative with this statement, we use the Hamiltonian in Eq. (1) with $\varepsilon_A = \varepsilon_D = V_{DA} = 0.0$ and $V_{DB} = V_{BA}$ to derive $H_{DA}^{\text{effect}} = -V_{DB}^2/\varepsilon_B$ and $H_{DA}^{\text{gap}} = 0.5(0.5\varepsilon_B - \sqrt{2V_{DB}^2 + 0.25\varepsilon_B^2})$ for this special case, which we both plot in dependence on V_{DB} and ε_B in Fig. 1. It can be seen that the agreement between both methods is

TABLE I. Transfer integral H_{DA}^{coeff} as calculated with the expansion coefficient method [26–28] in Eq. (5) for the Hamiltonian in Eq. (1) with the parameters $\varepsilon_B = 1$, $V_{DB} = V_{BA} = -0.1$, and $V_{DA} = -0.01$. For the same parameters one can derive $H_{DA}^{\text{gap}} = 0.0195$ from Eq. (3) and $H_{DA}^{\text{effect}} = 0.02$ from Eq. (4) with $\varepsilon_A = \varepsilon_D = 0$.

ε_D	ε_A	$\varepsilon_D - \varepsilon_A$	$a_{A,1}$	$a_{D,1}$	H_{DA}^{coeff}
0.0	0.0	0.0	0.701	0.701	divergent
-0.01	0.01	0.02	0.845	0.518	0.0197
-0.1	0.1	0.2	0.991	0.093	0.0189
-0.5	0.5	1.0	0.998	0.017	0.0167

ideal for $|\varepsilon_B - \varepsilon_{A,D}|$ above 0.2 eV and $|V_{DB}|$ below 0.1 eV. Most systems we investigate in this article have Hamiltonians broadly within this range, but from Fig. 1 it can be also seen that the results from the two methods move away from each other only gradually for larger couplings or smaller on-site energy differences.

III. DFT CALCULATIONS OF THE TRANSFER INTEGRAL FOR MOLECULAR BENCHMARK SYSTEMS

We now want to benchmark the three methods for evaluating H_{DA} , which we have introduced in the last section on real molecular systems instead of just TB matrices, where we choose two systems for which H_{DA} has been studied extensively in the literature. The first is an ethylene dimer, where inter molecular hole transport occurs between the local highest occupied MOs (HOMOs) of two ethylene molecules [33], which represent the diabatic initial and final state of the process, respectively, and form the two adiabatic bonding and antibonding states through their hybridization as we illustrate in Fig. 2. The second test system is a Q-TTF-Q⁻ anion, where intra molecular electron transfer between two quinone rings is mediated by a bridge [34] and the lower lying adiabatic state is shown in Fig. 3. This latter case is more challenging to describe correctly, since (i) it is not obvious whether the sulfur atoms should be seen as part of the initial/final state or as part of the bridge and (ii) due to the direct covalent connection between the donor/acceptor states and the bridge

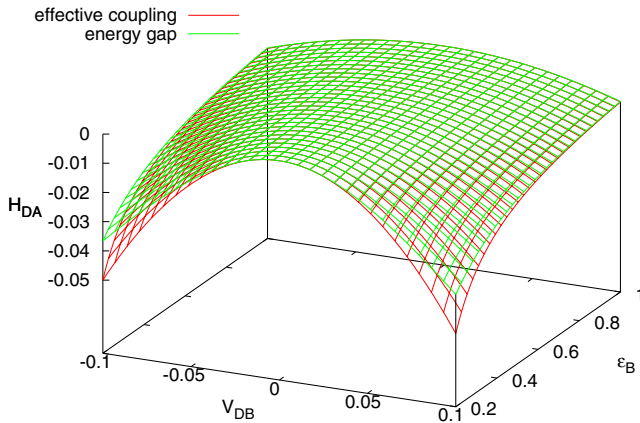


FIG. 1. (Color online) H_{DA}^{effect} and H_{DA}^{gap} for the Hamiltonian in Eq. (1) with $\varepsilon_A = \varepsilon_D = V_{DA} = 0.0$ and $V_{DB} = V_{BA}$.

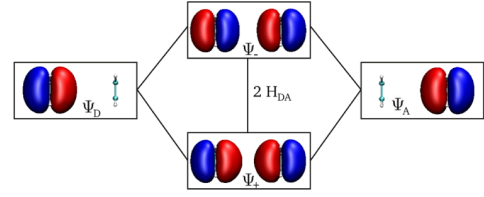


FIG. 2. (Color online) Molecular orbitals for a dimer of ethylene molecules as studied in Ref. [33], where the initial state ψ_D for hole transport is the HOMO of the left molecule, and the final state ψ_A the HOMO on the right one, and these orbitals form the adiabatic bonding and antibonding states, ψ_+ and ψ_- , respectively, through their hybridization.

states the self interaction (SI) problem of DFT, which results in an artificial tendency towards charge delocalization, becomes an issue [38–41].

All DFT calculations in this article were performed with the GPAW code [31,32], where the core electrons are described with the projector augmented wave (PAW) method and the basis set for the KS wave functions can be optionally chosen to be either a real space grid or a linear combination of atomic orbitals (LCAO), and we used both for the benchmarking calculations in the following, where the LCAO basis set has been applied on a double ζ level with polarization functions (DZP). The sampling of the potential energy term in the Hamiltonian is always done on a real space grid when using GPAW, where we chose 0.18 Å for its spacing and the same value when the grid also defines the basis set. For the XC functional we use the semilocal Perdew-Burke-Ernzerhof (PBE) [42] parametrization but we compare it with the hybrid functional B3LYP [43] for the cases where we find an indication for an artificial delocalization of electronic states. A tool of GPAW we also use extensively in the following is the generalized Δ SCF method, where the spatial expansion of an orbital enforced to contain a charge can be defined as an arbitrary linear combination of Bloch states [22,23]. By extracting or adding one electron from the system and inserting the corresponding charge into a predefined orbital in the beginning of every iteration step, the self-consistency cycle progresses as usual but with the charge density of this particular orbital as a contribution to the external potential.

For the evaluation of the transfer integral with the energy gap method for the hole transport in the ethylene dimer, one can, in principle, just obtain the two adiabatic states as the HOMO and HOMO-1 from a standard DFT calculation and insert their respective KS eigenenergies into Eq. (3). We refer

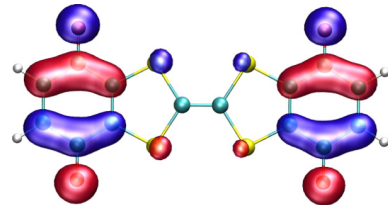


FIG. 3. (Color online) The SOMO of Q-TTF-Q⁻, which is the energetically lower lying adiabatic state for intra-molecular electron transfer in this system.

TABLE II. Transfer integral H_{DA} for the ethylene dimer in Fig. 2 calculated with three different techniques, which are applied in single particle (SP) and many-body (MB) variants, where the results are compared with those from Ref. [33] and are given in eV.

basis set	H_{DA}^{gap}		H_{DA}^{effect}		H_{DA}^{coeff}		H_{DA} (Lit.)
	SP	MB	SP	MB	SP	MB	
LCAO	0.030	0.026	0.033	0.033	0.043	0.043	0.046
grid	0.050	0.043	–	–	0.068	0.068	(Ref. [33])

to this as a single-particle (SP) approach in the following. Alternatively, one can use the Δ SCF method in two separate calculations where an electron has been removed from either one or the other of these two orbitals in order to obtain total energies values whose insertion into Eq. (3) should ensure that H_{DA}^{gap} calculated this way also contains contributions from the relaxation of all other electrons in reaction to this charge [44,45]. This is what we call the many-body (MB) approach in the remainder of this article. In Table II, we compare SP and MB values of H_{DA}^{gap} for the ethylene dimer, where we calculated both with a LCAO as well as a grid basis set.

For the definition of H_{DA}^{effect} a subdiagonalization procedure [46,47] is required, where a Hamiltonian is obtained that contains a block with the on-site energies of orbitals localized on the left ethylene molecule and another block of states belonging to the right one with the couplings between left and right as nondiagonal elements. Since the ethylene dimer does not contain bridge states, only the direct coupling element between initial and final state, i.e., the first term on the right side of Eq. (4) is needed to obtain H_{DA}^{effect} for this system. For this method, we only define a SP mode, and consider MB calculations to be impractical.

While H_{DA}^{gap} and H_{DA}^{effect} have to be calculated at the ground state of the system with respect to the coordinates of the nuclei which corresponds to a reaction coordinate $q = 0$, H_{DA}^{coeff} diverges at this point as illustrated in the last section in the discussion of Table I. In order to define a suitable q in terms of nuclear coordinates, we followed the procedure in Ref. [34], where the ground-state coordinates \mathbf{R}_0 for the positively charged dimer are supplemented by relaxations for the charged initial and final states (with the charge localized through Δ SCF on the left or right molecule, respectively) resulting in the sets of coordinates \mathbf{R}_{-1} and \mathbf{R}_1 for $q = -1$ and 1 , respectively, and the interpolation formula $\mathbf{R}_q = 0.5q(q+1)\mathbf{R}_1 - (q-1)(q+1)\mathbf{R}_0 + 0.5q(q-1)\mathbf{R}_{-1}$ can be applied to obtain the coordinates for an arbitrary value of q . In the following, we show results from calculations for $q = 0.2$ wherever it is not stated otherwise. For calculating H_{DA}^{coeff} in a SP mode, we make use of the same block diagonalization of KS states already mentioned in connection with H_{DA}^{effect} in the paragraph above, where the local HOMOs of the separate ethylene molecules in the dimer now have different energies due to the asymmetry of the system at $q = 0.2$ and a finite energy difference can be obtained for Eq. (5). By forming and diagonalizing a 2×2 Hamiltonian from these two local HOMOs and the direct coupling between them, the expansion coefficients $a_{A,1}$ and $a_{D,1}$ can also be straightforwardly derived. In MB mode ϵ_A and ϵ_D are the total energies of the initial and final states, respectively, and

therefore Δ SCF calculations constraining the positive charge on the left ethylene molecule at $q = -1$ and at the right one at $q = 1$ have to be performed. The expansion coefficients $a_{A,1}$ and $a_{D,1}$ on the other hand are again quantities related to the transition point, and we use the wave-function overlap within the projector augmented wave (PAW) formalism [32] to obtain them at $q = 0.2$, where the coefficients of the expansion of adiabatic into diabatic states are equivalent to those for the expansion of constrained diabatic states into KS states if normalized correctly. We also tested the orthogonalization procedures for the energy gap and the expansion coefficient methods suggested in Refs. [26–28,33], respectively, and found them to have no numerical effect for any system studied in this paper, where all states in the definitions we chose were orthogonal already.

From Table II, it can be seen that for the ethylene dimer all three methods agree perfectly with each other in SP mode, where only the energy gap technique can be applied also with a grid basis set, while for the other two approaches the LCAO basis is needed for the subdiagonalization procedure of KS states [46,47]. There is a bit more fluctuation of results in MB mode but overall the deviations are moderate, where more accuracy tends to deliver slightly higher values assuming that the grid basis is better converged than the LCAO basis and that MB in general gives an improvement over SP. We also show the number obtained by Bredas and co-workers for the same system in Ref. [33], which matches perfectly with our MB values of H_{DA}^{coeff} with a LCAO and H_{DA}^{gap} with a grid basis. One might wonder why the MB values do not differ more when compared with their SP counterparts given that electronic relaxation provides a factor of two when, e.g., comparing the addition energy of a H_2 molecule in a junction with the molecules KS-HOMO/LUMO gap [44]. This discrepancy is best understood by focusing on Eq. (3) for the calculation of H_{DA}^{gap} from two separate total energy calculations with a positive charge in first the energetically lower and than the higher of the two adiabatic states in Fig. 2, which are the global HOMO and HOMO-1 of the dimer. Contrarily to the bonding HOMO and antibonding LUMO of H_2 , which differ considerably in their respective spatial distribution, the HOMO and HOMO-1 of the ethylene dimer mostly differ in their phase, i.e., their minima and maxima are at exchanged positions for the second ethylene molecule. This is, however, irrelevant for the electron density that is formed from these orbitals where the minima and maxima both give local peaks and the effect of the relaxation of the other electrons in the system should be similar for both states, thereby almost canceling out when the difference in Eq. (3) is formed. In general, such a good agreement between the SP and MB mode of the energy gap method can always be expected because transfer integrals are usually below 0.1 eV in value, which corresponds to a rather low level of hybridization between the donor and acceptor states and therefore to rather similar spatial distributions of the bonding and antibonding adiabatic states.

It has to be stressed that the ethylene dimer is a rather unchallenging system in the sense that the initial and final states are not connected to each other by covalent bonds and therefore no bridge states exist. The difficulties that can arise in the presence of a bridge are illustrated for the Q-TTF- Q^- anion in Table III, where H_{DA} has been calculated in

TABLE III. Transfer integral H_{DA} for the Q-TTF-Q⁻ anion in Fig. 3 calculated with all three techniques in SP mode, where the Sulfur atoms are taken as part of the initial and final states in the first row, and as part of the bridge states in the second row. All numbers in this table have been calculated with a LCAO basis set and are given in eV.

	H_{DA}^{gap} (MO)	H_{DA}^{gap} (diag.)	H_{DA}^{effect}	H_{DA}^{coeff}
S on donor/acceptor	0.031	0.023	0.023	0.023
S on bridge	0.031	0.042	0.064	0.057

SP mode with all three methods. Although like in the dimer case, also for the anion the energy difference of the SOMO and LUMO from the standard DFT calculation can be used directly for determining H_{DA}^{gap} for electron transfer, there is an ambiguity here because the initial and the final state have not been explicitly defined and, in principle, several diabatic states localized on the two quinone rings could contribute to what we take as the adiabatic states. This ambiguity can be overcome by block-diagonalizing the KS Hamiltonian over the donor, bridge and acceptor areas, selecting one state in the donor area as initial and one in the acceptor area as final state, keeping all N bridge states, and then diagonalizing the resulting $(N + 2) \times (N + 2)$ Hamiltonian, where the two adiabatic states for forming the energy difference can be chosen by the criterion of a high amplitude at the initial and final state as discussed in the previous section. We distinguish between these two ways of deriving H_{DA}^{gap} in SP mode just described by referring to them as H_{DA}^{gap} (MO) and H_{DA}^{gap} (diag.). The latter becomes especially important in the next section, where we have the Bloch states of the gold leads as initial and final states and their selection becomes a crucial issue for the transfer integral. The same $(N + 2) \times (N + 2)$ Hamiltonian is also relevant for the derivation of H_{DA}^{effect} , where now the first term in Eq. (4) gives only a negligible contribution and the N bridge states are all entering into the sum. Also H_{DA}^{coeff} we obtain by diagonalizing a $(N + 2) \times (N + 2)$ Hamiltonian for the expansion coefficients but this one now represents the electronic structure for the nuclear coordinates corresponding to $q = 0.2$.

The most important question if a molecular bridge exists between the donor and acceptor states is the decision which atoms are still part of the initial/final state and which atoms should be assigned to the bridge. Although this decision is in principle arbitrary if all parts of the system are connected by covalent bonds, for some systems there are natural choices as we discuss in the next section where the initial and final states are on the gold leads and the molecule is the bridge. For the Q-TTF-Q⁻ anion, there is no *a priori* way to make a superior assignment for the sulfur atoms and we compare the results for both possibilities in Table III. For H_{DA}^{gap} (MO), there is no difference because we do not describe our initial and final states explicitly as stated above and therefore do not specify where their location starts and ends. For all other methods, the values for the transfer integral vary between the two choices of what is the bridge as they should. The correct value of H_{DA} has to depend on the exact definition of A and D or in other words the transfer integral for two quinone rings with sulfur ends connected by an ethylene bridge is different from the

TABLE IV. Transfer integral for the Q-TTF-Q⁻ anion (at $q = 0$ and 0.2 for H_{DA}^{gap} and H_{DA}^{coeff} , respectively) calculated with PBE and B3LYP functionals in MB mode. All results in this table have been obtained with a grid basis set and are given in eV. The result of Ref. [34] for this system is also shown for comparison.

	H_{DA}^{gap}	H_{DA}^{coeff}	H_{DA} (Lit.)
PBE	0.026	0.117 (0.157)	0.130
B3LYP	0.036	0.053 (0.035)	(Ref. [34])

one for two quinone rings connected by an ethylene tetrathiol bridge. More interestingly, while all three methods give the same result with the S atoms as part of donor and acceptor, they exhibit quite a spread of results if these atoms are part of the bridge. This finding can be explained by coming back to the discussion around Fig. 1 where it has been shown that the methods only give the same results for reasonably small couplings and reasonably large energy differences. If the S atoms are considered to be part of the bridge, the couplings reach values of up to 0.8 eV and therefore the methods slightly diverge for this case.

In Table IV, we show H_{DA} for the Q-TTF-Q⁻ anion calculated with the energy gap and expansion coefficient techniques in MB mode. The main numbers for H_{DA}^{coeff} have been calculated with the sulfur atoms as part of the initial and final state, while a definition with the S atoms being part of the bridge has been used for the numbers in parentheses. All results we presented so far have been produced with a PBE [42] parametrization of the XC functional, while in Table IV we also compare with data using the hybrid functional B3LYP [43] instead. It can be seen that the PBE version of H_{DA}^{coeff} deviates from all the other values we have calculated for the transfer integral in the Q-TTF-Q⁻ anion by an order of magnitude but interestingly is almost equal to the value found in Ref. [34]. The explanation of this deviation can be found in the SI problem, which makes the expansion coefficients $a_{D,1}$ and $a_{A,1}$ almost equal even if asymmetry is induced by setting $q = 0.2$. This artefact can be even more highlighted by calculating the expansion coefficients at $q = -1$, where one of them should be close to 0 and the other one close to 1, which is indeed the case for B3LYP ($a_{D,1} = 0.95$, $a_{A,1} = 0.001$) but not for PBE ($a_{D,1} = 0.77$, $a_{A,1} = 0.64$). This problem does not occur for the PBE calculations of H_{DA}^{coeff} for the ethylene dimer presented in Table II where $a_{D,1} = 0.99$ and $a_{A,1} = 0.10$, because in this case there is no bridge linking the donor and acceptor [41]. Since in the expansion method the diabatic states are defined as a linear combination of the adiabatic states, the SI error cannot lead to an artificial overdelocalization where the charges are already maximally delocalized over donor and acceptor (as is the case for the ethylene dimer) but it has an effect on the Q-TTF-Q⁻ anion where the charge can spill onto the bridge.

In summary, we can conclude from this section that all three methods agree with each other quite well for the chosen benchmark systems and that results from single particle and many body calculations are of the same order of magnitude. We therefore restrict our study to the SP mode in the remainder of this article.

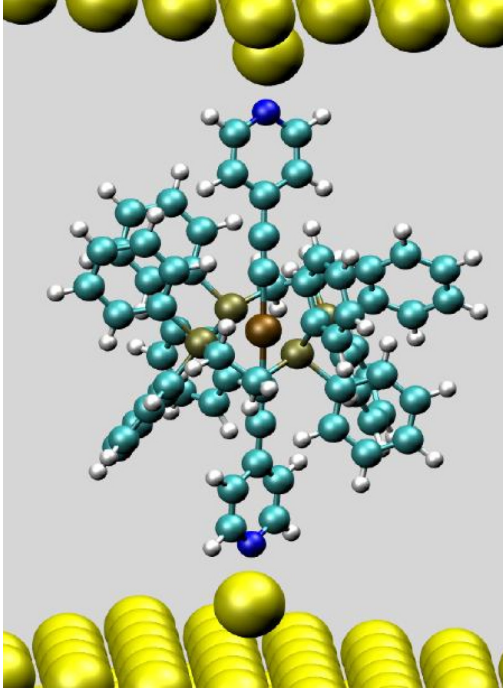


FIG. 4. (Color online) Geometry of the $\text{Ru}(\text{PPh}_2)_4(\text{C}_2\text{H}_4)_2$ bis(pyridylacetylide) complex bonded to ad-atoms on Au fcc (111) surfaces, where the conductance has been studied within the framework of NEGF for the neutral and oxidized complex in Ref. [10].

IV. CALCULATION OF THE TRANSFER INTEGRAL FOR A REDOX ACTIVE SINGLE MOLECULE JUNCTION

In a recent paper, we studied the coherent electron transport through the $\text{Ru}(\text{PPh}_2)_4(\text{C}_2\text{H}_4)_2$ bis(pyridylacetylide) complex in Fig. 4 by using a NEGF formalism for the conductance, and where we switched the oxidation state of the redox active ruthenium atom between +II and +III corresponding to an overall charge of 0 and +1 on the molecular complex, respectively [10]. The +1 charge on the complex we achieved by fixing the charge on a Cl counter ion with the ΔSCF technique [22,23] and ensuring overall charge neutrality in the unit cell of our device region, so that the negative charge on the chlorine anion resulted in a compensating positive charge on the complex. In Ref. [10], we also tested a second method for charge localization, which made use of solvent screening and was computationally more expensive but in the current article no water molecules were added to our cell, because the more efficient approach based on ΔSCF achieved equivalent or even better results. We chose this particular Ru-complex because it was used in previous conductance measurements [48,49] as a monomer of chains, where depending on the chain length either coherent transport or electron hopping was observed [48], and because this molecular species is in general considered to be a good starting point for the investigation of chains with multiple redox active centers [50]. In contrast to Ref. [48], we use pyridyl groups as anchors to the leads because they provide peaks in the transmission function, which are narrow enough to assume that a charge on the complex has an impact on the conductance but broad enough to avoid the Coulomb blockade regime [51–53].

In the present article we relate the conductance G of the molecular junction in Fig. 4 to the transfer integral, where the electrodes play the role of the initial and the final state in a one-step electron transfer reaction and the redox-active molecule acts as a mediating bridge. The relation between H_{DA} and G was explicitly described by Nitzan [36,37], where adopted to our definition of H_{DA} the conductance was expressed as

$$G(E_F) = \frac{H_{DA}^2 \Gamma_A \Gamma_D G_0}{[(E_F - E_D)^2 + \Gamma_D^2/4][(E_F - E_A)^2 + \Gamma_A^2/4]}, \quad (6)$$

with G_0 being the conductance quantum, and Γ_D and Γ_A the widths of the donor and acceptor levels due to their couplings to the left and right metal leads, respectively. In such a setup, only metallic surface states close to E_F are relevant for the conductance through the junction and if only such bands are considered as the initial and final states of the corresponding electron transfer reaction the energy differences $E_F - E_D$ and $E_F - E_A$ vanish in Eq. (6), which can now be simplified to

$$G(E_F) = H_{DA}^2 \frac{16}{\Gamma_D \Gamma_A} G_0. \quad (7)$$

By using this expression and setting $\Gamma_D = \Gamma_A = 0.5 \text{ eV}$, which is reasonable for the coupling width of gold leads [54], the transfer integral can be obtained from the conductance as $H_{DA}^G \approx \sqrt{G(E_F)}/8$, where in Table V, we list the values we derive in this way from the conductances in Ref. [10] as a benchmark for the three methods introduced in the current article.

In order for Eq. (7) to be valid, only metal bands, which contribute to the density of states (DOS) at the Fermi level, can be considered as donor and acceptor states. Therefore we calculated $H_{DA,\mathbf{k}}$ for all relevant donor-acceptor pairs weighted with a \mathbf{k} -point-resolved DOS,

$$H_{DA,\mathbf{k}} = \frac{\sum_{i=1}^N H_{DA,i,\mathbf{k}} * \rho(E_F)_{i,\mathbf{k}}}{\sum_{i=1}^N \rho(E_F)_{i,\mathbf{k}}}, \quad (8)$$

where ρ is the density and finally integrated $H_{DA,\mathbf{k}}$ over \mathbf{k} space following the procedure of Marcus and co-workers [35]. Another aspect that has to be considered for the proper choice of initial and final states is their localization on the gold adatoms, which couple directly to the molecular bridge, since only those can contribute significantly to the electron transfer reaction. Bulk bands, that are close to the Fermi level but have no connection to the molecule would lower H_{DA} in Eq. (8) artificially, where the statistical weight is only defined by the DOS. Therefore we introduced the exclusion criterion that the metallic states entering Eq. (8) have a coupling with one of the two most relevant MOs (the HOMO-1 and the LUMO), which is larger than 10^{-3} .

In theory, the initial and the final states in our calculations should have the same energy for each donor/acceptor pair, because the junction in Fig. 4 has a high symmetry and the transfer integral has to be defined at the transition point of the corresponding reaction. In practice, however, small asymmetries introduced by the torsional degrees of freedom in the molecular bridge can lead to differences in diabatic energies in the range of 10^{-3} eV . Since the H_{DA} values in this section are in the order of 10^{-4} eV , we corrected Eq. (3)

TABLE V. Transfer integrals for the junction in Fig. 4 calculated with energy gap, effective coupling and expansion coefficient methods in SP mode. The gold leads are small clusters of four atoms on each side in the Au pyramid columns and the periodic surfaces from Ref. [10] everywhere else, where Γ point only calculations are also compared with the average over 8 \mathbf{k} points in the irreducible Brillouin zone. H_{DA}^G has been defined as $\sqrt{G(E_F)}/8$, where the values of $G(E_F)$ have been taken from Ref. [10]. All results are given in eV.

Charge	Au pyramid			Γ point only			H_{DA}^G	8 \mathbf{k} points			
	H_{DA}^{gap}	H_{DA}^{effect}	H_{DA}^{coeff}	H_{DA}^{gap}	H_{DA}^{effect}	H_{DA}^{coeff}		H_{DA}^{gap}	H_{DA}^{effect}	H_{DA}^{coeff}	H_{DA}^G
0	3.57×10^{-3}	3.63×10^{-3}	3.65×10^{-3}	2.95×10^{-4}	3.05×10^{-4}	3.05×10^{-4}	4.41×10^{-4}	1.06×10^{-3}	1.02×10^{-3}	1.02×10^{-3}	4.96×10^{-4}
+1	3.16×10^{-3}	3.26×10^{-3}	3.18×10^{-3}	4.28×10^{-4}	4.72×10^{-4}	4.69×10^{-4}	1.00×10^{-3}	1.95×10^{-3}	1.65×10^{-3}	1.25×10^{-3}	1.37×10^{-3}

to account for these asymmetries following the procedure of Bredas and co-workers [33], where the differences of the diabatic energies are explicitly subtracted,

$$H_{DA}^{\text{gap}} = \frac{\sqrt{(\varepsilon_1 - \varepsilon_2)^2 - (\epsilon_A - \epsilon_D)^2}}{2}. \quad (9)$$

For the application of the expansion coefficient method, it is an advantage that small energy differences between donor and acceptor states exist, because here we can interpret them as finite values of q , since this technique cannot be applied at the transition point as discussed in detail in the previous two sections. The effective coupling method can be corrected by replacing the denominator $\varepsilon_{A,D} - \varepsilon_i$ of the second term in Eq. (4) with $(\varepsilon_D + \varepsilon_A)/2 - \varepsilon_i$ [21]. Another consequence of the asymmetry in the junction are artificial deviations between the couplings of each MO to the two gold surfaces, which we corrected for by using a mean value for the coupling to both surfaces for all three techniques.

In Table V, we present H_{DA} values for the junction in Fig. 4 for a neutral (0) and charged (+1) complex calculated with all three methods at only the Γ point as well as averaged over the eight \mathbf{k} points in the irreducible Brillouin zone obtained from a $4 \times 4 \times 1$ grid. The values H_{DA}^G are obtained from the conductances in Ref. [10] for the same system and also given for comparison. While all the remaining numbers refer to the periodic junction also used in Ref. [10], for the first three columns (Au pyramid), small clusters of four gold atoms on each side in a tetrahedral configuration have been used as electrodes in order to assess the effect of a proper description of the gold leads on the numbers. The overall agreement of the three methods for calculating H_{DA} amongst themselves is excellent, which is not surprising because all relevant couplings between the MOs of the bridge and the surface states are in the range 10^{-3} – 10^{-2} and the molecular eigenenergies have at least a distance of 0.2 eV from E_F . When compared with H_{DA}^G the important aims are fulfilled, namely the order of magnitude is the same, and the transfer integral for the neutral state is always considerably smaller than that for the charged one. A better agreement could not

have been expected given that the values for H_{DA} are rather small and the approximative nature of the assumptions we made in deriving H_{DA}^G from $G(E_F)$. This is in particular true for the underestimation of the \mathbf{k} point dependence of H_{DA}^G in Table V, which stems from the fact that Γ_D and Γ_A in Eq. (7) depend on the density of states of the lead and should therefore be different for each \mathbf{k} point, which is not considered in our treatment, where we set both to 0.5 eV globally throughout the reciprocal space of the system. Only the results we obtained for the transfer integral with small clusters as gold leads are wrong, both in their order of magnitude and in the ranking with regard to 0 and +1 charge, where both can be easily explained. The small cluster size is responsible for a larger amplitude of the initial/final state on the Au adatom, thereby enhancing the coupling to all MOs [54] and resulting in artificially high values of H_{DA} . The charged complex does not have higher transfer integrals than the neutral one because for nonperiodic leads the charge introduced by the chlorine ion is mostly localized on the Au clusters as we investigated in detail in Ref. [10].

An important finding from the comparison of conductances of the two charging states of the Ru-complex in Ref. [10] was that for the neutral molecule it was determined by the molecular LUMO and LUMO + 1, with the contribution from the LUMO being distinctly larger. In the charged case, the molecular HOMO and HOMO-1 are shifted close to the Fermi energy of the metal leads, which makes them primarily responsible for the molecular conductance. The effective coupling method provides a good way to analyze whether the same holds true for the respective transfer integrals because the contributions from the MOs are additive in Eq. (4). In Table VI, we list the terms in the sum coming from the four MOs closest to E_F , where indeed it can be seen that the LUMO

TABLE VI. Individual contributions of the MOs in Fig. 5 to H_{DA}^{effect} . All values are given in eV.

Charge	HOMO-1	HOMO	LUMO	LUMO + 1
0	3.4×10^{-4}	3.3×10^{-5}	1.1×10^{-3}	-5.8×10^{-4}
+1	1.4×10^{-3}	4.4×10^{-5}	6.2×10^{-4}	-4.7×10^{-4}

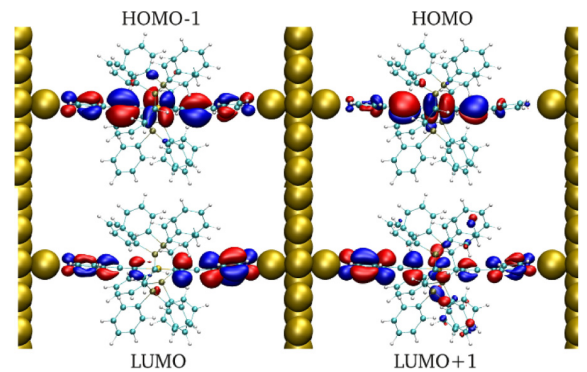


FIG. 5. (Color online) Molecular orbitals close to E_F for the junction in Fig. 4.

dominates for charge 0 and the HOMO-1 for charge +1. The HOMO adds only an amount which is two orders of magnitude smaller for both oxidation states, because it is mostly localized in the center of the molecule and only to a much lesser extent on the anchor groups as can be seen from Fig. 5. This results in rather low coupling of this orbital to the metal leads, which we also found from the NEGF calculations for the transmission functions in Ref. [10]. The contribution from the LUMO + 1 is also independent of the charging state but of larger magnitude than that of the HOMO, and for both systems its sign is different from that of the other MOs indicating destructive interference.

V. SUMMARY

The aim of this article was to identify suitable methods for calculating the transfer integral—which is a crucial quantity in Marcus theory—within a DFT framework for a setup where metallic leads act as donor and acceptor and a molecule in between them mediates electron or hole transport as a bridge. We found three techniques fit for that purpose, namely, (i) the energy gap method where H_{DA} is derived from the total energy difference of adiabatic states, (ii) Larsson’s formula which adds up the contributions from each MO of the molecular bridge, and (iii) a expansion coefficient approach where the amplitudes of the adiabatic states in a diabatic basis are used explicitly. For this assessment, we proceeded in three steps. First, we compared the three methods on an abstract level by applying them to 3×3 tight-binding matrices, where we

found good agreement between all of them for small couplings between the bridge and the donor/acceptor states and large respective on-site energy differences. In a second step, we benchmarked our DFT implementation of the three techniques for purely molecular systems with and without a bridge, which have been studied by other groups, where we also established that a many body approach gives only negligible corrections compared to single particle descriptions. Finally, we calculated H_{DA} for a single molecule junction where a Ru complex is coupled to two gold surfaces by pyridyl anchor groups using all three methods and assuming that surface states of the two leads act as donor and acceptor states, thereby describing coherent tunneling. Our results for H_{DA} were in excellent agreement with those derived from the conductance computed with a NEGF formalism for the same system in two different oxidation states.

ACKNOWLEDGMENTS

G.K. and R.S. are currently supported by the Austrian Science Fund FWF, Project No. P22548. We are deeply indebted to the Vienna Scientific Cluster VSC, on whose computing facilities all calculations presented in this paper have been performed (Project No. 70174) and where we were provided with extensive installation and mathematical library support by Markus Stöhr and Jan Zabloudil, in particular. We are deeply indebted to Pawel Zawadzki for sharing his expert knowledge in applying the generalized Δ SCF technique as implemented in the GPAW code with us, and gratefully acknowledge helpful discussions with Tim Albrecht.

-
- [1] Y. Meir and N. S. Wingreen, *Phys. Rev. Lett.* **68**, 2512 (1992).
 - [2] M. Brandbyge, J. L. Mozos, P. Ordejón, J. Taylor, and K. Stokbro, *Phys. Rev. B* **65**, 165401 (2002).
 - [3] Y. Xue, S. Datta, and M. A. Ratner, *Chem. Phys.* **281**, 151 (2002).
 - [4] A. R. Rocha, V. M. Garcia-Suarez, S. W. Baily, C. J. Lambert, J. Ferrer, and S. Sanvito, *Nat. Mater.* **4**, 335 (2005).
 - [5] K. S. Thygesen and K. W. Jacobsen, *Chem. Phys.* **319**, 111 (2005).
 - [6] T. Albrecht, K. Moth-Poulsen, J. B. Christensen, A. Guckian, T. Bjør, J. G. Vos, and J. Ulstrup, *Faraday Discuss.* **131**, 265 (2006).
 - [7] T. Albrecht, A. Guckian, J. Ulstrup, and J. G. Vos, *Nano Lett.* **5**, 1451 (2005).
 - [8] W. Haiss, H. van Zalinge, S. J. Higgins, D. Bethell, H. Höbenreich, D. J. Schiffrin, and R. J. Nichols, *J. Am. Chem. Soc.* **125**, 15294 (2003).
 - [9] A. M. Ricci, E. J. Calvo, S. Martin, and R. J. Nichols, *J. Am. Chem. Soc.* **132**, 2494 (2010).
 - [10] G. Kastlunger and R. Stadler, *Phys. Rev. B* **88**, 035418 (2013).
 - [11] R. Stadler and K. W. Jacobsen, *Phys. Rev. B* **74**, 161405(R) (2006).
 - [12] R. Stadler, *J. Phys.: Conf. Ser.* **61**, 1097 (2007).
 - [13] R. Stadler, *Phys. Rev. B* **81**, 165429 (2010).
 - [14] M. D. Newton, *Chem. Rev.* **91**, 767 (1991).
 - [15] K. D. Jordan and M. N. Paddon-Row, *Chem. Rev.* **92**, 395 (1992).
 - [16] N. S. Hush, *Prog. Inorg. Chem.* **8**, 391 (2007).
 - [17] R. J. Cave and M. D. Newton, *Chem. Phys. Lett.* **249**, 15 (1996).
 - [18] R. J. Cave and M. D. Newton, *J. Chem. Phys.* **106**, 9213 (1997).
 - [19] A. A. Voityuk and N. Rösch, *J. Chem. Phys.* **117**, 5607 (2002).
 - [20] G. Pourtois, D. Beljonne, J. Cornil, M. A. Ratner, and J. L. Bredas, *J. Am. Chem. Soc.* **124**, 4436 (2002).
 - [21] A. A. Voityuk, *Phys. Chem. Chem. Phys.* **14**, 13789 (2012).
 - [22] J. Gavnholt, T. Olsen, M. Englund, and J. Schiøtz, *Phys. Rev. B* **78**, 075441 (2008).
 - [23] T. Olsen, J. Gavnholt, and J. Schiøtz, *Phys. Rev. B* **79**, 035403 (2009).
 - [24] P. Zawadzki, K. W. Jacobsen, and J. Rossmeisl, *Chem. Phys. Lett.* **506**, 42 (2011).
 - [25] P. Zawadzki, J. Rossmeisl, and K. W. Jacobsen, *Phys. Rev. B* **84**, 121203(R) (2011).
 - [26] A. Migliore, S. Corni, R. Di Felice, and E. Molinari, *J. Chem. Phys.* **124**, 064501 (2006).
 - [27] A. Migliore, *J. Chem. Phys.* **131**, 114113 (2009).
 - [28] A. Migliore, *J. Chem. Theory Comput.* **7**, 1712 (2011).
 - [29] S. Larsson, *J. Am. Chem. Soc.* **103**, 4034 (1981).
 - [30] A. A. Voityuk, *Chem. Phys. Lett.* **451**, 153 (2008).

- [31] J. J. Mortensen, L. B. Hansen, and K. W. Jacobsen, *Phys. Rev. B* **71**, 035109 (2005).
- [32] J. Enkovaara, C. Rostgaard, J. J. Mortensen, J. Chen, M. Dulak, L. Ferrighi, J. Gavnholt, C. Glinsvad, V. Haikola, H. A. Hansen, H. H. Krisoffersen, M. Kuisma, A. H. Larsen, L. Lehtovaara, M. Ljungberg, O. Lopez-Acevedo, P. G. Moses, J. Ojanen, T. Olsen, V. Petzold, N. A. Romero, J. Stausholm-Møller, M. Strange, G. A. Tritsarlis, M. Vanin, M. Walter, B. Hammer, H. Häkkinen, G. K. H. Madsen, R. M. Nieminen, J. K. Nørskov, M. Puska, T. T. Rantala, J. Schiøtz, K. S. Thygesen, and K. W. Jacobsen, *J. Phys.: Condens. Matter* **22**, 253202 (2010).
- [33] E. F. Valeev, V. Coropceanu, D. A. da Silva Filho, S. Salman, and J.-L. Bredas, *J. Am. Chem. Soc.* **128**, 9882 (2006).
- [34] Q. Wu and T. Van Voorhis, *J. Chem. Phys.* **125**, 164105 (2006).
- [35] S. Gosavi and R. A. Marcus, *J. Phys. Chem. B* **104**, 2067 (2000).
- [36] A. Nitzan, *J. Phys. Chem. A* **105**, 2677 (2001).
- [37] A. Nitzan, *Annu. Rev. Phys. Chem.* **52**, 681 (2001).
- [38] J. P. Perdew and A. Zunger, *Phys. Rev. B* **23**, 5048 (1981).
- [39] J. Gräfenstein, E. Kraka, and D. Cremer, *Phys. Chem. Chem. Phys.* **6**, 1096 (2004).
- [40] C. Toher, A. Filippetti, S. Sanvito, and K. Burke, *Phys. Rev. Lett.* **95**, 146402 (2005).
- [41] R. Stadler, J. Cornil, and V. Geskin, *J. Chem. Phys.* **137**, 074110 (2012).
- [42] J. P. Perdew, K. Burke, and M. Ernzerhof, *Phys. Rev. Lett.* **77**, 3865 (1996).
- [43] A. D. Becke, *J. Chem. Phys.* **98**, 5648 (1993).
- [44] R. Stadler, V. Geskin, and J. Cornil, *Phys. Rev. B* **78**, 113402 (2008).
- [45] R. Stadler, V. Geskin, and J. Cornil, *Phys. Rev. B* **79**, 113408 (2009).
- [46] R. Stadler, V. Geskin, and J. Cornil, *Adv. Funct. Mat.* **18**, 1119 (2008).
- [47] R. Stadler, V. Geskin, and J. Cornil, *J. Phys.: Condens. Matter* **20**, 374105 (2008).
- [48] B. Kim, J. M. Beebe, C. Olivier, S. Rigaut, D. Touchard, J. G. Kushmerick, X.-Y. Zhu, and C. D. Frisbie, *J. Phys. Chem. C* **111**, 7521 (2007).
- [49] K. Liu, X. Wang, and F. Wang, *ACS Nano* **2**, 2315 (2008).
- [50] S. Rigaut, J. Perruchon, S. Guesmi, C. Fave, D. Touchard, and P. H. Dixneuf, *Eur. J. Inorg. Chem.* **2005**, 447 (2005).
- [51] R. Stadler, K. S. Thygesen, and K. W. Jacobsen, *Nanotechnology* **16**, S155 (2005).
- [52] R. Stadler, K. S. Thygesen, and K. W. Jacobsen, *Phys. Rev. B* **72**, 241401(R) (2005).
- [53] R. Stadler, *Phys. Rev. B* **80**, 125401 (2009).
- [54] R. Stadler and T. Markussen, *J. Chem. Phys.* **135**, 154109 (2011).

PAPER IV

Density functional theory based direct comparison of
coherent tunneling and electron hopping in redox-active
single-molecule junctions

Density functional theory based direct comparison of coherent tunneling and electron hopping in redox-active single-molecule junctions

Georg Kastlunger and Robert Stadler*

Department of Physical Chemistry, University of Vienna, Sensengasse 8/7, A-1090 Vienna, Austria
 and Institute for Theoretical Physics, Vienna University of Technology, Wiedner Hauptstrasse 8-10, A-1040 Vienna, Austria
 (Received 22 September 2014; revised manuscript received 17 December 2014; published 9 March 2015)

To define the conductance of single-molecule junctions with a redox functionality in an electrochemical cell, two conceptually different electron transport mechanisms, namely, coherent tunneling and vibrationally induced hopping, compete with each other, where implicit parameters of the setup such as the length of the molecule and the applied gate voltage decide which mechanism is the dominant one. Although coherent tunneling is most efficiently described within Landauer theory and the common theoretical treatment of electron hopping is based on Marcus theory, both theories are adequate for the processes they describe without introducing accuracy-limiting approximations. For a direct comparison, however, it has to be ensured that the crucial quantities obtained from electronic structure calculations, i.e., the transmission function $T(E)$ in Landauer theory and the transfer integral V , the reorganization energy λ , and the driving force ΔG^0 in Marcus theory, are derived from similar grounds, as pointed out by Nitzan and coworkers in a series of publications. In this paper our framework is a single-particle picture, for which we perform density functional theory calculations for the conductance corresponding to both transport mechanisms for junctions with the central molecule containing one, two, or three Ruthenium centers, from which we extrapolate our results in order to define the critical length of the transition point of the two regimes which we identify at 5.76 nm for this type of molecular wire. We also discuss trends in the dependence on an electrochemically induced gate potential.

DOI: [10.1103/PhysRevB.91.125410](https://doi.org/10.1103/PhysRevB.91.125410)

PACS number(s): 73.63.Rt, 73.20.Hb, 73.40.Gk

I. INTRODUCTION

Electron transport through single-molecule junctions in ultrahigh vacuum (UHV) and at very low temperatures is commonly described with a nonequilibrium Green's function (NEGF) approach [1] in combination with a density functional theory (DFT) based description of the electronic structure of the leads and the scattering region of the junction [2–5]. The modeling of the conductance and current/voltage (I/V) characteristics of single molecules at ambient conditions, at which an electrochemical scanning tunneling microscope (STM) [6–10] operates and which are necessary for the practicability of devices, is more challenging, because here two competing electron transport mechanisms have to be considered, namely, electron hopping and coherent tunneling. It depends on the adjustment of an electrochemical gate voltage as well as on structural details of the system which of these two mechanisms dominates the accumulated transfer rate of electrons. The distinction between the two is important for the design of molecular wires, where coherent tunneling prevails at short lengths regardless of the chemical structure but decays exponentially and then at some structure-dependent crossover point in molecular length gives way to the Ohmic behavior of electron hopping, which is crucial for making a wire of any use in real life [11]. The application of a gate potential for, e.g., implementing transistor properties [12] or optimizing the conductance properties of a wire is also easier to achieve in an electrochemical setup where no third electrode has to be placed close to the leads for source and drain and no strong local electric fields are required [13].

There have been a variety of experiments aimed at direct detection of the crossover length in molecular wires where

coherent tunneling is replaced by hopping. In a pioneering series of papers Ratner, Wasielewski, and coworkers [12–15] investigated the intramolecular electron transfer from a donor to an acceptor moiety via a bridge which consisted of oligo(phenylene vinylene) (OPV) molecules of increasing length, where optical absorption spectra allowed the derivation of charge separation and recombination rates and a switch in the transfer mechanism was detected when the bridge consisted of more than two monomers. More recently, Choi *et al.* measured the conductance of monolayers of oligophenyleneimine (OPI) thioliates adsorbed on a gold substrate with their length varying between 1.5 and 7 nm by using a STM and found the transition point at ~ 4 nm [16], while single-molecule measurements on the corresponding dithiolates in a break junction setup placed this crossover point in the range of 5.2–7.3 nm [17]. Lu *et al.* studied monolayers of oligo(phenylene ethynylene) (OPE) wires, where a transition from tunneling to hopping was observed at a molecular length of ~ 2.75 nm [18], while a transition length of about 3 nm was found for a series of oligo(arylene ethynylene) (OAE) derivatives in single-molecule measurements by Wandlowski and coworkers [19].

All theoretical attempts to identify and characterize the length of the transition between tunneling and hopping so far [20–24], to the best of our knowledge, suffer from two severe limitations which are also related to each other: (i) Hopping is characterized by model or tight-binding Hamiltonians in which crucial parameters such as on-site energies of monomer sites or the coupling between them are just set to some reasonable values and not derived from *ab initio* or any other type of electronic structure calculations, which would reflect their dependence on any details of the molecular structure under investigation. (ii) As a consequence, only N -step hopping could be investigated, in which it is assumed that the electron hops from one monomer to the other until it

*robert.stadler@tuwien.ac.at

reaches the final N th one. This is a reasonable assumption for simulations on DNA wires, on which, indeed, the theoretical articles quoted above focused, but the assumption is not justified at all for the highly conjugated OPV, OPI, OPE, and OAE wires, which have been in the experimental spotlight recently due to their higher conductance, and or for the wires with redox-active centers, which we describe further below. For conjugated systems in general one expects two-step hopping [15], in which an electron hops from the donor (or left lead) to the bridge (or central molecule) in the first step and then on to the acceptor (or right lead) in the second one.

While coherent tunneling is now routinely described within the single-particle framework of NEGF-DFT [2–5], with which we have recently shown that the oxidation state of the redox-active center in the scattering region can also be adjusted in two different ways [25], no *ab initio* procedure for the description of electron hopping in single-molecule junctions has so far been proposed. Our understanding of the hopping process in general relies on Marcus's theory of electron transfer reactions [26–28], which are the rate-limiting step in many redox reactions and for which the activation can be achieved thermally, photochemically, or by applying an external potential. The key parameters in this theory, namely, the transfer integral V , the reorganization energy λ , and the driving force ΔG^0 , are usually derived from quantum-chemical techniques for intramolecular [29] and intermolecular electron transfer [30], but defining and deriving them in the context of a single-molecule junction causes various technical and more fundamental issues to arise, and addressing these issues is one of the main achievements of this paper.

We carried out DFT calculations for both electron transport regimes, namely, coherent tunneling and hopping, for the three single-molecule junctions depicted in Fig. 1. We chose these particular types of molecules due to their high all-through conjugation and therefore high conductivity, as well as the presence of redox-active Ru centers which allow for efficient electrochemical gating. They also offer the possibility to alter their local redox state independently, which would require some structural modifications, but that is not the topic of this paper. Because of these benign properties of the displayed Ru complexes, conductance measurements and optical absorption experiments have been carried out on them in which thiol [31] and cyano anchors [32] have been used instead of the pyridyl

linkers in this work, which we prefer because of their stability under ambient conditions and their high junction-formation probability and because they do not require protecting groups during the adsorption process on the electrodes [19].

This paper is organized as follows: In the next section we give a detailed account of our theoretical framework for the two different electron transport regimes with an emphasis on how to obtain crucial parameters and quantities from DFT. In the following sections we use these methods to derive the crossover point in the molecular length dependence of the conductance for the systems in Fig. 1 from first principles and also discuss the effect of an electrochemical gate potential. In the last section we provide a summary of our results.

II. THEORETICAL FRAMEWORK AND COMPUTATIONAL DETAILS

Up to now the theoretical understanding of electron hopping in single-molecule junctions has been driven by the phenomenological models of Kuznetsov and Ulstrup [33–36] and some earlier work by Schmickler [37], while more recently, Nitzan addressed the relation between the conductance as the quantity calculated by the NEGF-DFT formalism for coherent tunneling and the transfer rate in Marcus's theory of electron hopping from a formal perspective [38,39]. Migliore *et al.* also developed a single-particle framework for two-step hopping [40], which is distinct from the usual picture based on enthalpies and total energies and therefore allows for an orbital interpretation. We make use of this framework heavily in our work, as discussed further below, but while in Ref. [40] general formal relationships are established and some typical values of V , λ , and ΔG^0 are used as a means of illustration without referring to a particular molecular system, the aim in our work is to derive these quantities for the junctions in Fig. 1 from first principles. In Marcus's theory the electron transfer process is described as a chemical reaction, whereas in our specific case it is an oxidation of the ground state of the molecules which in a quantum-chemical picture corresponds to the removal of an electron from the highest occupied molecular orbital (HOMO).

In our modeling of electron hopping we assumed a two-step process, in which a positive charge jumps from the left lead to the HOMO of the molecule, which we know to be conjugated throughout the whole molecule from our previous

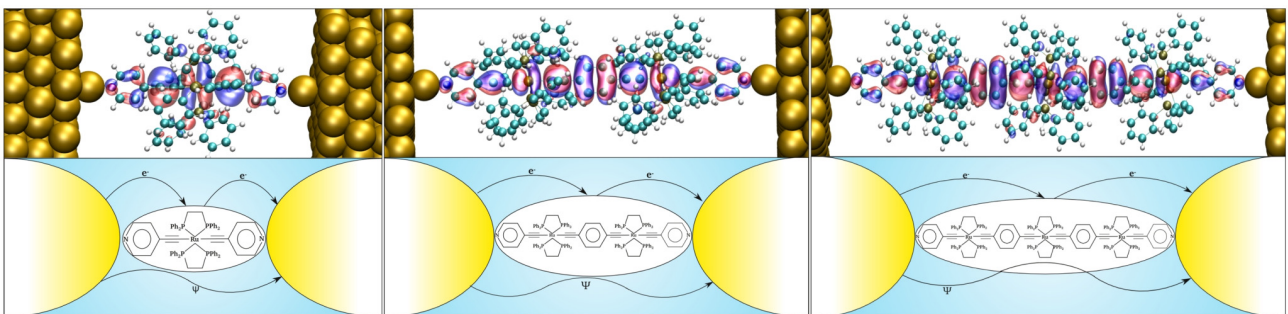


FIG. 1. (Color online) (top) Atomic structures and (bottom) chemical formulas of ruthenium bis(pyridylacetylide) complexes with one, two, and three $\text{Ru}(\text{PPh}_2)_4(\text{C}_2\text{H}_4)_2$ centers, which are coupled to gold leads via pyridyl-anchor groups. For all junctions in this figure NEGF-DFT calculations for coherent tunneling (as indicated by the wiggly line below the formulas) as well as DFT calculations of the two-step electron-hopping process following the recipe given in the main text (the two arrows above the formulas) have been carried out. In the top panels, the respective HOMOs for all structures, which are crucial in both transport regimes, are also shown on top of the molecular structures.

work [25,41], and then from there on to the right lead in the second step. Ratner and coworkers have pointed out that the situation might get more complicated even in conjugated wires due to torsional degrees of freedom, and electron transfer rates might be affected by their thermal activation [15,42]. While the phenyl groups separating two adjacent Ru centers in the structures shown in Fig. 1 are quite efficiently trapped by steric repulsion to the bulky substituents on ruthenium, the pyridyl anchors have, indeed, some flexibility which could break the conjugation ranging otherwise from the left lead to the right one. We performed DFT-based total-energy calculations, which showed that the energy barriers are 274 and 90 meV for rotating the phenyl ring in the middle and the pyridyl groups at the ends of the molecule, respectively. Since room temperature corresponds to only 25 meV, we can still assume that the conjugation is more or less undisturbed at ambient conditions if present from the beginning, i.e., if conformers have been successfully separated after chemical synthesis.

We calculated G_{hop} for room temperature and G_{coh} for 0 K. This might seem counterintuitive since G_{hop} depends considerably on the temperature because this type of electron transport is thermally activated, or, in other words, at 0 K there is no conductance due to hopping. By contrast, G_{coh} does not depend on the temperature in a first-order approximation and is affected by electron-phonon coupling only as a second-order effect. So our assumption was that we should model room-temperature behavior, which we treat explicitly for the hopping, but we neglect thermal effects for coherent tunneling.

A. Electronic structure calculations

All electronic structure calculations in this paper were performed with the GPAW code [43,44], in which the core electrons are described with the projector augmented wave (PAW) method and the basis set for the Kohn-Sham wave functions has been chosen to be a linear combination of atomic orbitals (LCAO) on a double-zeta level with polarization functions (DZP) for all electronic structure calculations. The sampling of the potential energy term in the Hamiltonian is done on a real-space grid when using GPAW, for which we chose 0.18 Å for its spacing and a Perdew-Burke-Ernzerhof (PBE) [45] parametrization for the exchange-correlation (XC) functional throughout this paper.

B. Coherent tunneling

Within NEGF-DFT [2–5] the transmission function $T(E)$ for coherent tunneling is defined by $T(E) = \text{Tr}(G_d \Gamma_L G_d^\dagger \Gamma_R)$, where $G_d = (E - H_d - \Sigma_L - \Sigma_R)^{-1}$ represents the Green's function of the device containing the self-energy matrices $\Sigma_{L/R}$ due to the left/right lead, $\Gamma_{L/R} = i(\Sigma_{L/R} - \Sigma_{L/R}^\dagger)$, and H_d is the Hamiltonian matrix for the device region, which contains not only the Ru complex but also three to four layers of the aligned Au surface on each side. Due to the rather large size of the central molecules, we had to use gold slabs with a 6×6 unit cell in the surface plane in order to ensure that neighboring molecules did not interact. For the same reason we used a $2 \times 2 \times 1$ \mathbf{k} -point grid corresponding to only two k points in the irreducible Brillouin zone for all transmission functions discussed in this paper.

C. Electron hopping

In order to describe electron hopping in single-molecule junctions, the famous Marcus-Hush formula [27,46,47] for the transfer rate in intra- or intermolecular electron transfer reactions needs to be modified because the initial and final states have to be replaced by the manifold of all occupied and unoccupied surface states in the lead with the right symmetry. This was first recognized by Chidsey [48], who modified the Marcus-Hush formula by introducing an integral over all metal states. In the present case we are dealing with a two-step reaction, in which in the first step we oxidize the molecule by charging it with a hole which is supposed to come from the left lead and in the second step we decharge the molecule again, i.e., reduce it, where the corresponding hole moves onto the right electrode. The overall conduction process is then described by the transfer rates of the corresponding two separate electron transfer reactions:

$$k_{\text{ox}} = \frac{2\pi}{\hbar} V^2 \frac{1}{\sqrt{4\pi\lambda k_b T}} \int e^{-\frac{(\lambda + \Delta G^0 + \epsilon)^2}{4\lambda k_b T}} [1 - f(\epsilon)] d\epsilon, \quad (1)$$

$$k_{\text{red}} = \frac{2\pi}{\hbar} V^2 \frac{1}{\sqrt{4\pi\lambda k_b T}} \int e^{-\frac{(\lambda - \Delta G^0 + \epsilon)^2}{4\lambda k_b T}} f(\epsilon) d\epsilon, \quad (2)$$

where $f(\epsilon) = 1/(e^{\epsilon/(k_b T)} + 1)$ is the Fermi function, which is part of both equations because in the oxidation reaction only the unoccupied states of the left lead can provide a positive charge (hole) and only the occupied states of the right lead can absorb it in the reduction of the molecule, where the thermal broadening of the Fermi levels of the leads at finite temperatures is also built into $f(\epsilon)$.

To calculate the overall conductance of the junction in the hopping regime, Migliore *et al.* derived an expression containing both k_{ox} and k_{red} to include the effect of both steps of the process [40], which in our symmetric case with the same electrode material and surface orientation as well as the same anchor group on both sides of the junction becomes

$$G_{\text{hop}} = \frac{e^2}{2k_b T} \frac{k_{\text{ox}} k_{\text{red}}}{k_{\text{ox}} + k_{\text{red}}}, \quad (3)$$

where the quantities V , λ , and ΔG^0 need to be defined on a single-particle level in order for us to be able to make a direct comparison with the conductance for coherent tunneling G_{coh} , which can be simply obtained by taking the value of the transmission function $T(E)$ as computed with NEGF-DFT at the Fermi energy. We note that Eq. (3) applies only in the limit of zero bias, i.e., for an infinitesimally low potential difference between the source and drain electrodes. It is, however, fully applicable for finite electrochemical gate voltages, where the respective potential is just added to the value of ΔG^0 in Eqs. (1) and (2).

1. Transfer integral

In a recent article we showed that the transfer integral $V_{\text{Au-Au}}$ between the metal electrodes bridged by the molecule can also be used to determine the conductance for coherent tunneling [41]. In the context of electron hopping, however, the conductance is defined by two consecutive reactions, where for both another transfer integral $V_{\text{Au-Mol}}$ is needed which describes the electronic coupling between the molecule and

one of the leads. In contrast to $V_{\text{Au-Au}}$, which we calculated only at the Fermi energy E_F in order to define G_{coh} , for electron hopping we need $V_{\text{Au-Mol}}$ to be integrated over all energies. This information can be neatly retrieved from the peak in $T(E)$ corresponding to the HOMO as calculated with NEGF-DFT for coherent tunneling because the width of this peak and $V_{\text{Au-Mol}}$ are directly related on a single-particle level. In practice, we cut the couplings to all other molecular orbitals and generate a transmission function containing only the contribution of the HOMO and then use $T_{\text{HOMO}}(E) = 4V^2/[(E - \epsilon_{\text{HOMO}})^2 + 4V^2]$ [49], where we obtain $T_{\text{HOMO}}(E)$ and ϵ_{HOMO} as direct results from NEGF-DFT and derive the transfer integral V from a numerical fit.

2. Driving force

In principle the driving force ΔG^0 in the electron transfer reaction we describe (where the respective Ru complex is neutral in the initial state and has a positive charge in the final state, while the corresponding counter charge on the leads is assumed to be taken from the Fermi level of a metal surface with macroscopic dimensions) could be formulated by relating the ionization potential (IP) of the complex as calculated from total-energy differences of the charged and uncharged free molecules to the work function (WF) of the gold surfaces [40]. Such a definition, however, would neglect the effect of the adsorption of the molecule on the metal, i.e., Fermi level alignment and charge equilibration [50–52], since both the metallic WF and the molecular IP would be computed for the leads and molecule separately. Therefore we use the HOMO's position relative to the Fermi level of the surface in the composite system [25] as a definition of ΔG^0 instead, where the level alignment is accounted for correctly. As an additional benefit we can make a direct comparison between I/V curves for electron hopping calculated in this way and the transmission function for coherent tunneling, where both are derived on a single-particle level and a gate potential can be applied in a rigid-band approximation.

3. Reorganization energy

The total reorganization energy used in the Eqs. (1) and (2) is defined as the sum of inner and outer contributions,

$$\lambda_{\text{tot}} = \lambda_{\text{in}} + \lambda_{\text{out}} = \lambda_{\text{in}} + \lambda_{\text{Born}} + \lambda_{\text{image}}, \quad (4)$$

where the latter can be further divided into a Born term accounting for the interaction of the charged molecule with the solvent and an image contribution, which describes the screening of the charge due to the vicinity of the metallic leads [53]. The inner reorganization energy λ_{in} , i.e., the energy gain due to the relaxation of the nuclear positions of the molecule as a consequence of charging, can be calculated either as the respective total-energy difference of the charged complex in its own equilibrium configuration minus a charged complex in the equilibrium configuration of the neutral molecule or, alternatively, as the total-energy difference from two calculations in which no charge is put on the two different equilibrium geometries. In practice, we take the average of these two possibilities.

For λ_{Born} , we employ a solvent continuum model as already suggested by Marcus [26–28], who used the Born

approximation to calculate the solvation energy of spherical ions [54]. For the Ru complexes in our paper, we need to extend this to the generalized Born approximation (GBA) [55],

$$\lambda_{\text{Born}} = \left(\frac{1}{\epsilon_{\infty}} - \frac{1}{\epsilon_s} \right) \sum_{i,j}^N \frac{\Delta q_i \Delta q_j}{f_{GB}}, \quad (5)$$

where ϵ_{∞} and ϵ_s are the optical and static permittivities of the solvent, respectively, and $\Delta q_{i,j}$ are the partial charge differences between the neutral and the oxidized states of the free molecule in vacuum, which were calculated as Mulliken charges from DFT, and where the van der Waals radii entering f_{GB} according to Ref. [55] have been taken from Ref. [56].

4. Screening by the leads

Within an image charge model, the contribution of the screening of the charge on the molecule between two planar metal surfaces to the reorganization energy can be described by an infinite sum of Coulomb interactions between the partial charges on the molecule and their infinite number of image charges in the electrodes [53,57,58],

$$\begin{aligned} \lambda_{\text{image}} = & -\frac{1}{2} \left(\frac{1}{\epsilon_{\infty}} - \frac{1}{\epsilon_s} \right) \sum_{i,j}^N \Delta q_i \Delta q_j \\ & \times \sum_{n=1}^{\infty} \left[\frac{1}{\sqrt{(z_i + z_j - 2nL)^2 + R_{ij}^2}} \right. \\ & - \frac{2}{\sqrt{(z_i - z_j + 2nL)^2 + R_{ij}^2}} \\ & \left. + \frac{1}{\sqrt{(z_i + z_j + 2(n+1)L)^2 + R_{ij}^2}} \right], \quad (6) \end{aligned}$$

where $R_{ij}^2 = (x_i - x_j)^2 + (y_i - y_j)^2$ and $x_{i,j}$, $y_{i,j}$, $z_{i,j}$ are the positions of the atoms of the molecule, with the z direction being the transport direction.

III. RESULTS AND DISCUSSION

A. Direct comparison of the conductance from coherent tunneling and electron hopping

In Table I we show all the results we derived for the structures in Fig. 1 directly from DFT calculations, i.e., the conductances G_{coh} and G_{hop} for coherent tunneling and electron hopping for zero bias and zero gate voltage, respectively, as well as the values for $k_{\text{ox}}/k_{\text{red}}$, V , ΔG^0 , and λ , which define G_{hop} through Eqs. (1)–(3). While G_{coh} decays exponentially with the length of the molecule as expected, G_{hop} shows an increase with molecular length at least for the three molecules under investigation. The transfer integral V decreases as the amplitude of the HOMO at the anchor group diminishes with a rise in molecular size. The reorganization energy also decreases with the size of the molecule because both the relaxations of internal degrees of nuclear freedom and the polarization of the solvent become energetically easier for a larger molecular volume. Finally, the driving force ΔG^0 also decreases with the molecular length because the

TABLE I. All quantities directly calculated from DFT for the three systems in Fig. 1, where G_{coh} and G_{hop} are given in units of G_0 , $k_{\text{ox}}/k_{\text{red}}$ is in units of s^{-1} , and V , ΔG^0 , and all contributions to λ are presented in eV.

	G_{coh}	G_{hop}	$k_{\text{ox}}/k_{\text{red}}$	V	ΔG^0	λ_{in}	$\lambda_{\text{out}} (\lambda_{\text{Born}}/\lambda_{\text{img}})$	λ_{tot}
Ru1	2.0×10^{-5}	1.2×10^{-25}	$3.1 \times 10^{-12}/2.4 \times 10^9$	1.35×10^{-3}	1.250	0.177	0.421 (0.661/−0.240)	0.597
Ru2	8.0×10^{-7}	1.4×10^{-17}	$3.5 \times 10^{-4}/2.4 \times 10^8$	4.50×10^{-4}	0.707	0.083	0.322 (0.495/−0.172)	0.407
Ru3	1.6×10^{-8}	5.4×10^{-16}	$1.3 \times 10^{-2}/6.5 \times 10^7$	8.03×10^{-5}	0.576	0.059	0.315 (0.446/−0.131)	0.374

HOMO-LUMO gap becomes smaller with the length of a semiconducting wire and therefore the HOMO moves closer to E_F .

The transfer rates k_{ox} and k_{red} in Table I are completely defined by the parameters V , λ , and ΔG^0 through Eqs. (1) and (2) and because of their dependence on the gate voltage behave like error functions, where k_{red} increases when k_{ox} decreases with a crossing point at ΔG^0 . Therefore a product of the transfer rates as in Eq. (3) results in a peak around ΔG^0 since one of the two factors is always minimal at larger energetic distances from ΔG^0 . A reduction of ΔG^0 with the length of the molecule leads to a shift of this peak towards the Fermi level, resulting in an increase of G_{hop} at zero gate voltage. An increase in the reorganization energy λ on the other side results in a widening and lowering of this peak because it leads to a shift of k_{ox} and k_{red} in opposite directions because of the difference in their respective dependence on the gate voltage.

In Fig. 2 we directly compare the transmission function $T(E)$ for coherent tunneling as obtained from NEGF-DFT with the hopping conductance as a function of gate voltage or an overpotential. While for the former it is assumed that V_{gate} is equal to the kinetic energy of incoming electrons E , for the latter, a zero gate voltage means that $\Delta G^0 = -\epsilon_{\text{HOMO}}$, as obtained by a subdiagonalization procedure from the transport Hamiltonian of the composite junction, where for a finite

voltage the applied potential is just added to ΔG^0 in Eqs. (1) and (2) as a scalar. Both assumptions are just implementations of a rigid-band approximation within a single-particle picture. While for $T(E)$ the transmission peak corresponding to the HOMO (red dotted line) that is slightly offset due to hybridization effects moves ever closer to E_F as the length of the molecule increases, it also becomes narrower since V is decreasing at the same time, where the accumulated effect is the exponential decay of G_{coh} . The blue peak illustrating the gate-voltage dependence of G_{hop} is also moving towards the Fermi level with an increase in molecular size, where its maximum is always at the energetic position of $\epsilon_{\text{HOMO}} = \Delta G^0$, representing zero overpotential. Its width and height, on the other hand, are defined by λ and V , and a continuous rise in the zero bias and zero gate G_{hop} is found when moving from Ru1 to Ru3.

B. Dependence of the conductance on molecular length and crossover point between the two transport regimes

In Table I it can also be seen that, although the values of G_{coh} and G_{hop} approach each other when going from Ru1 to Ru3, no crossover point between the two regimes can be reached within the scope of these three molecules. Since the junction with the Ru3 complex in Fig. 1 defines the limit of what can still be calculated with DFT in terms of the computational costs, we used exponential fits for G_{coh} and ΔG^0 as well as power-law fits for V and λ for an extrapolation of G_{coh} , G_{hop} , and $G_{\text{coh}} + G_{\text{hop}}$, where the results for a wire length ranging up to 10 nm are shown in Fig. 3.

The exponential decay for G_{coh} is a well-known property of coherent tunneling, where we evaluated a decay constant β of 2.7 nm^{-1} , which matches what is usually found in experiments for conjugated molecular wires well [19]. For the length dependence of G_{hop} we find an increase up to six Ru centers, but the roughly linear decay expected for Ohmic transport sets in for molecular wires longer than that.

We chose the particular functions we used for to fit V , λ , and ΔG^0 because they gave the best representation of our data, but their overall behavior has an intuitive physical explanation. At very small molecular lengths (the first two points in Fig. 3) both ΔG^0 and λ are rather large, and since they enter the exponents in Eqs. (1) and (2) with a negative sign, this results in small values of k_{ox} , k_{red} , and G_{hop} . The larger the molecular length is, the smaller λ and ΔG^0 become, and therefore the larger G_{hop} becomes. The reason for the drastic increase in G_{hop} and its subsequent stabilization is that we define ΔG^0 as the distance from the HOMO to the Fermi level, which becomes smaller with the molecular length (as can be seen from the peak shift in Fig. 2) and then converges to zero asymptotically. The behavior of λ points in the same direction,

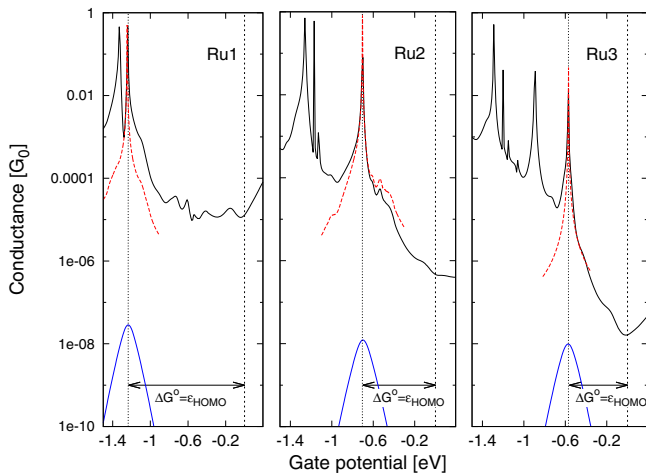


FIG. 2. (Color online) The transmission functions $T(E)$ for coherent tunneling for the three structures in Fig. 1 (black lines) are directly compared with the voltage dependent behavior of G_{hop} (blue lines), where for the description of the effect of an electrochemical gate the respective voltage is simply added to ΔG^0 in Eqs. (1) and (2) as an overpotential. The dotted red line shows $T(E)$ for electrons mediated only by the HOMO as described in detail in the main text.

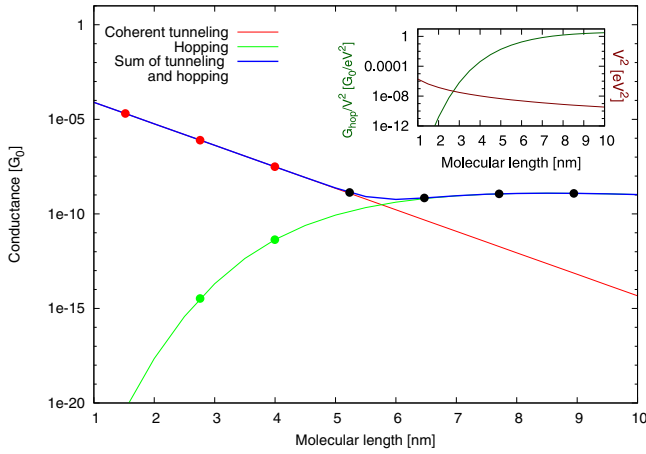


FIG. 3. (Color online) Extrapolation of the molecular length dependence of G_{coh} (red line) with an exponential fit and the length dependence of V , λ , and ΔG^0 , where the first two quantities were fitted with power laws and the third one was fitted with an exponential function, for the definition of G_{hop} (green line). The blue line represents the sum $G_{\text{coh}} + G_{\text{hop}}$, which corresponds to the conductance accessible to experiments for this type of molecular wire. The colored dots on each line refer to the values directly calculated from DFT for Ru1, Ru2, and Ru3, respectively, while at all higher lengths the extrapolations have been taken and marked with black dots. The inset shows the respective length-dependent evolutions of the contributions to G_{hop} from V^2 (red line) and the remaining factor (green line), which is exclusively defined by ΔG^0 and λ and is obtained by dividing G_{hop} by V^2 .

where the screening by the solvent decreases if a charge of one electron is spread out over larger molecular volumes, and this effect also has an asymptotic limit. At some point the

continuous decrease of V^2 in Eqs. (1) and (2) determines the further length dependence of G_{hop} . In the inset of Fig. 3 we show the two factors which determine G_{hop} in Eqs. (1) and (2) separately, where V^2 decays with the inverse of the length (red line) and the exponential containing ΔG^0 and λ (green line) rises sharply for small lengths but then approaches 1 at 8–10 nm.

From Fig. 3 we can identify the crossover or transition point from coherent transport to electron hopping where $G_{\text{coh}} = G_{\text{hop}}$ and find it at a molecular length of 5.76 nm. This is in the same range as the 5.6–6.8 nm for polythiophenes [59] and 5.2–7.3 nm for oligofluorene-based molecular wires [17] found in recent experiments but is somewhat higher than the ~ 3 nm for pyridyl-terminated OAEs [19], the ~ 2.75 nm for a series of amine-terminated OPEs [18], and the ~ 4 nm for thiol-anchored oligophenyleneimines [16], which were also recently measured.

C. Application of an electrochemical gate potential

Finally, we discuss the dependence of G_{coh} , G_{hop} , and $G_{\text{coh}} + G_{\text{hop}}$ on an electrochemically applied gate potential as depicted in Figs. 4(a), 4(b), and 4(c), respectively, where we chose a relatively small range of potentials because we use a rigid-band approximation for both transport regimes which assumes that the electronic structure is undisturbed by the applied voltage. In Ref. [60] it was found experimentally that increasing the gate voltage in one direction leads to a rapid increase in the conductance, while a voltage with the opposite sign had no effect. This was interpreted as a reduction of the complex with a negative potential, but in terms of our Fig. 2 it can also be seen as a climbing up of the peak related to the HOMO in both transport regimes. As pointed out earlier, there is a marked difference between the two regimes,

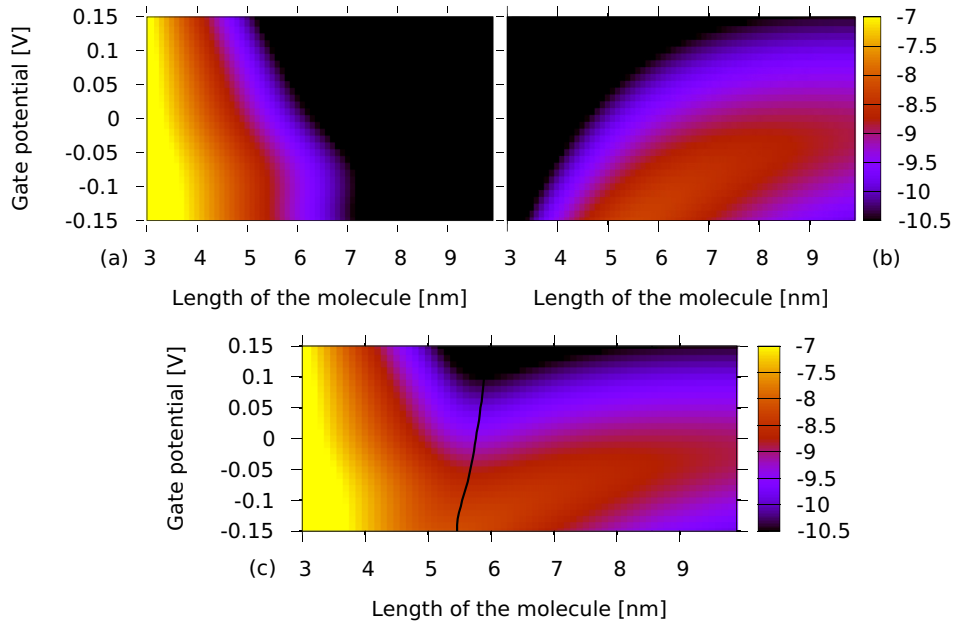


FIG. 4. (Color online) Color contours for the two-dimensional dependence of (a) G_{coh} , (b) G_{hop} , and (c) $G_{\text{coh}} + G_{\text{hop}}$ on the molecular length and on an electrochemical gate potential, where the color code is given on the side of the panels with the numbers referring to x in 10^x . In (c) a black dashed line is drawn where $G_{\text{coh}} = G_{\text{hop}}$.

where the peak is rather narrow for coherent transport and the range of voltages we chose is not sufficient for generating any clear trends in Fig. 4(a) but a negative voltage distinctly increases G_{hop} in Fig. 4(b), which reflects the broader peak for hopping found in Fig. 2. In Fig. 4(c) we also draw a black line where $G_{\text{coh}} = G_{\text{hop}}$ and find that the transition point between coherent tunneling and hopping is moving to smaller wire lengths for negative potentials in this two-dimensional picture. This finding provides additional means for experiments to shift the length range of Ohmic behavior towards smaller molecules. In many cases this could make the transition point accessible for experimental studies when longer wires are hard to synthesize or difficult to handle in measurements.

IV. SUMMARY

We performed DFT calculations for the conductance of a series of single-molecule junctions with redox-active molecular wires containing one, two, and three Ru atoms, where we treated both coherent tunneling and electron hopping within the same single-particle framework, which allowed for a direct quantitative comparison of the two electron transport regimes. An extrapolation of our *ab initio* results made it possible to identify a molecular length for a transition point between them at 5.76 nm, which is rather close to the values reported

from measurements on similar wires. We also investigated the dependence of this transition length on an electrochemically applied gate voltage, and we found that it can be shifted by an external potential, which provides experimentalists with another tool to study the crossover between transport regimes. This is also of technological relevance because only hopping has the Ohmic length dependence required for wire applications, and according to our finding, a gate voltage can move its onset towards shorter wires.

ACKNOWLEDGMENTS

G.K. and R.S. are currently supported by the Austrian Science Fund FWF, Project No. P22548 and P27272. We are deeply indebted to the Vienna Scientific Cluster VSC, in whose computing facilities all calculations presented in this paper have been performed (Project No. 70174 and 70671) and where we were provided with extensive installation and mathematical library support by M. Stöhr and J. Zablouil in particular. In addition G.K. is gratefully receiving the grant “Stipendium der Monatshefte für Chemie 2014” co-sponsored by the Austrian Academy of Science ÖAW, the Springer Verlag and the Austrian Chemical Society GÖCH. We gratefully acknowledge helpful discussions with T. Albrecht, M. Inkpen, and T. Wandlowski.

-
- [1] Y. Meir and N. S. Wingreen, *Phys. Rev. Lett.* **68**, 2512 (1992).
 - [2] M. Brandbyge, J. L. Mozos, P. Ordejón, J. Taylor, and K. Stokbro, *Phys. Rev. B* **65**, 165401 (2002).
 - [3] Y. Xue, S. Datta, and M. A. Ratner, *Chem. Phys.* **281**, 151 (2002).
 - [4] A. R. Rocha, V. M. Garcia-Suarez, S. W. Baily, C. J. Lambert, J. Ferrer, and S. Sanvito, *Nat. Mater.* **4**, 335 (2005).
 - [5] K. S. Thygesen and K. W. Jacobsen, *Chem. Phys.* **319**, 111 (2005).
 - [6] T. Albrecht, K. Moth-Poulsen, J. B. Christensen, A. Guckian, T. Bjørnholm, J. G. Vos, and J. Ulstrup, *Faraday Discuss.* **131**, 265 (2006).
 - [7] T. Albrecht, A. Guckian, J. Ulstrup, and J. G. Vos, *Nano Lett.* **5**, 1451 (2005).
 - [8] W. Haiss, H. van Zalinge, S. J. Higgins, D. Bethell, H. Höbenreich, D. J. Schiffrin, and R. J. Nichols, *J. Am. Chem. Soc.* **125**, 15294 (2003).
 - [9] A. M. Ricci, E. J. Calvo, S. Martin, and R. J. Nichols, *J. Am. Chem. Soc.* **132**, 2494 (2010).
 - [10] C. Li, A. Mishchenko, Z. Li, I. Pobelov, T. Wandlowski, X. Q. Li, F. Wrthner, A. Bagrets, and F. Evers, *J. Phys.: Condens. Matter* **20**, 374122 (2008).
 - [11] W. B. Davis, M. A. Ratner, and M. R. Wasielewski, *J. Am. Chem. Soc.* **123**, 7877 (2001).
 - [12] T. Albrecht, A. Guckian, J. Ulstrup, and J. G. Vos, *IEEE Trans. Nanotechnol.* **4**, 430 (2005).
 - [13] J. D. Zhang, A. M. Kuznetsov, I. G. Medvedev, Q. J. Chi, T. Albrecht, P. S. Jensen, and J. Ulstrup, *Chem. Rev.* **108**, 2737 (2008).
 - [14] E. A. Weiss, M. J. Ahrens, L. E. Sinks, A. V. Gusev, M. A. Ratner, and M. R. Wasielewski, *J. Am. Chem. Soc.* **126**, 5577 (2004).
 - [15] W. B. Davis, W. A. Svec, M. A. Ratner, and M. R. Wasielewski, *Nature (London)* **396**, 60 (1998).
 - [16] S. H. Choi, B. Kim, and C. D. Frisbie, *Science* **320**, 1482 (2008).
 - [17] T. Hines, L. Diez-Perez, J. Hihath, H. Liu, Z.-S. Wang, J. Zhao, G. Zhou, K. Müllen, and N. Tao, *J. Am. Chem. Soc.* **132**, 11658 (2010).
 - [18] Q. Lu, K. Liu, H. Zhang, Z. Du, X. Wang, and F. Wang, *ACS Nano* **3**, 3861 (2009).
 - [19] X. Zhao, C. Huang, M. Gulcur, A. S. Batsanov, M. Baghernejad, W. Hong, M. R. Bryce, and T. Wandlowski, *Chem. Mater.* **25**, 4340 (2013).
 - [20] Y. A. Berlin, A. L. Burin, and M. A. Ratner, *Chem. Phys.* **275**, 61 (2002).
 - [21] E. G. Petrov, Y. V. Shevchenko, and V. May, *Chem. Phys.* **288**, 269 (2003).
 - [22] W. B. Davis, M. R. Wasielewski, M. A. Ratner, V. Mujica, and A. Nitzan, *J. Phys. Chem. A* **101**, 6158 (1997).
 - [23] D. Segal, A. Nitzan, M. A. Ratner, and W. B. Davis, *J. Phys. Chem. B* **104**, 2790 (2000).
 - [24] D. Segal, A. Nitzan, W. B. Davis, M. R. Wasielewski, and M. A. Ratner, *J. Phys. Chem. B* **104**, 3817 (2000).
 - [25] G. Kastlunger and R. Stadler, *Phys. Rev. B* **88**, 035418 (2013).
 - [26] R. A. Marcus, *J. Chem. Phys.* **24**, 966 (1956).
 - [27] R. A. Marcus, *J. Chem. Phys.* **43**, 679 (1965).
 - [28] R. A. Marcus, *J. Electroanal. Chem.* **483**, 2 (2000).
 - [29] G. Pourtois, D. Beljonne, J. Cornil, M. A. Ratner, and J. L. Bredas, *J. Am. Chem. Soc.* **124**, 4436 (2002).
 - [30] J. Cornil, D. Beljonne, J. P. Calbert, and J. L. Bredas, *Adv. Mater.* **13**, 1053 (2001).
 - [31] K. Liu, X. Wang, and F. Wang, *ACS Nano* **2**, 2315 (2008).

- [32] B. Kim, J. M. Beebe, C. Olivier, S. Rigaut, D. Touchard, J. G. Kushmerick, X.-Y. Zhu, and C. D. Frisbie, *J. Phys. Chem. C* **111**, 7521 (2007).
- [33] J. E. T. Andersen, A. A. Kornyshev, A. M. Kuznetsov, L. L. Madsen, P. Møller, and J. Ulstrup, *Electrochim. Acta* **42**, 819 (1996).
- [34] A. M. Kuznetsov and J. Ulstrup, *Electrochim. Acta* **45**, 2339 (2000).
- [35] A. M. Kuznetsov and J. Ulstrup, *J. Phys. Chem. A* **104**, 11531 (2000).
- [36] J. Zhang, Q. Chi, T. Albrecht, A. M. Kuznetsov, M. Grubb, A. G. Hansen, H. Wackerbarth, A. C. Welinder, and J. Ulstrup, *Electrochim. Acta* **50**, 3143 (2005).
- [37] W. Schmickler, *J. Electroanal. Chem.* **204**, 31 (1986).
- [38] A. Nitzan, *J. Phys. Chem. A* **105**, 2677 (2001).
- [39] A. Nitzan, *Isr. J. Chem.* **42**, 163 (2002).
- [40] A. Migliore, P. Schiff, and A. Nitzan, *Phys. Chem. Chem. Phys.* **14**, 13746 (2012).
- [41] G. Kastlunger and R. Stadler, *Phys. Rev. B* **89**, 115412 (2014).
- [42] E. A. Weiss, M. J. Tauber, R. F. Kelley, M. J. Ahrens, and M. R. Wasielewski, *J. Am. Chem. Soc.* **127**, 11842 (2005).
- [43] J. J. Mortensen, L. B. Hansen, and K. W. Jacobsen, *Phys. Rev. B* **71**, 035109 (2005).
- [44] J. Enkovaara *et al.*, *J. Phys.: Condens. Matter* **22**, 253202 (2010).
- [45] J. P. Perdew, K. Burke, and M. Ernzerhof, *Phys. Rev. Lett.* **77**, 3865 (1996).
- [46] N. S. Hush, *J. Chem. Phys.* **28**, 962 (1958).
- [47] A. Van Vooren, V. Lemaire, A. Ye, D. Beljonne, and J. Cornil, *Chem. Phys. Chem.* **8**, 1240 (2007).
- [48] C. E. D. Chidsey, *Science* **251**, 919 (1991).
- [49] R. Stadler and T. Markussen, *J. Chem. Phys.* **135**, 154109 (2011).
- [50] R. Stadler and K. W. Jacobsen, *Phys. Rev. B* **74**, 161405(R) (2006).
- [51] R. Stadler, *J. Phys.: Conf. Ser.* **61**, 1097 (2007).
- [52] R. Stadler, *Phys. Rev. B* **81**, 165429 (2010).
- [53] E. P. Friis, Y. I. Kharkats, A. M. Kuznetsov, and J. Ulstrup, *J. Phys. Chem.* **102**, 7851 (1998).
- [54] M. Born, *Z. Phys.* **1**, 45 (1920).
- [55] D. Qiu, P. S. Shenkin, F. P. Hollinger, and W. C. Still, *J. Phys. Chem. A* **101**, 3005 (1997).
- [56] W. L. Jorgensen and J. Tirado-Rives, *J. Am. Chem. Soc.* **110**, 1657 (1998).
- [57] D. J. Mowbray, G. Jones, and K. S. Thygesen, *J. Chem. Phys.* **128**, 111103 (2008).
- [58] R. Stadler, V. Geskin, and J. Cornil, *Phys. Rev. B* **79**, 113408 (2009).
- [59] R. Yamada, H. Kumazawa, S. Tanaka, and H. Tada, *Appl. Phys. Express* **2**, 025002 (2009).
- [60] C. Li, V. Stepanenko, M.-J. Lin, W. Hong, F. Würthner, and T. Wandlowski, *Phys. Status Solidi B* **250**, 2458 (2013).

PAPER V

Field-induced conductance switching by charge-state
alternation in organometallic single-molecule junctions

Field-induced conductance switching by charge-state alternation in organometallic single-molecule junctions

Florian Schwarz^{1†}, Georg Kastlunger^{2,3†}, Franziska Lissel⁴, Carolina Egler-Lucas⁴, Sergey N. Semenov⁴, Koushik Venkatesan⁴, Heinz Berke⁴, Robert Stadler^{2,3} and Emanuel Lörtscher^{1*}

Charge transport through single molecules can be influenced by the charge and spin states of redox-active metal centres placed in the transport pathway. These intrinsic properties are usually manipulated by varying the molecule's electrochemical and magnetic environment, a procedure that requires complex setups with multiple terminals. Here we show that oxidation and reduction of organometallic compounds containing either Fe, Ru or Mo centres can solely be triggered by the electric field applied to a two-terminal molecular junction. Whereas all compounds exhibit bias-dependent hysteresis, the Mo-containing compound additionally shows an abrupt voltage-induced conductance switching, yielding high-to-low current ratios exceeding 1,000 at bias voltages of less than 1.0 V. Density functional theory calculations identify a localized, redox-active molecular orbital that is weakly coupled to the electrodes and closely aligned with the Fermi energy of the leads because of the spin-polarized ground state unique to the Mo centre. This situation provides an additional slow and incoherent hopping channel for transport, triggering a transient charging effect in the entire molecule with a strong hysteresis and large high-to-low current ratios.

Switching an electric signal from a low- to a high-current state is one of the key elements in an electric circuit with applications in signal processing, logic data manipulation or storage. In current Si-based technologies with device dimensions approaching the sub-5 nm range, it becomes increasingly difficult to maintain large high-to-low current ratios mainly because of leakage currents. Therefore alternative switching mechanisms are needed. In single-molecule electronics, a variety of intrinsic conductance-switching mechanisms¹ exists: gating of the molecular orbitals (MOs) by electrostatic² or electrochemical means³, which requires a third electrode, or modifying specific photoactive molecular structures, for example by optically irradiating the molecule to form or break bonds^{4–7}. Mechanically induced changes in the molecule–metal coupling⁸ can also lead to conductance alternations. Another trigger is the electric field inherently present in a molecular transport junction: conformational changes due to interactions between the electric field and molecular dipoles were demonstrated to alternate the conductance of single-molecule junctions^{9–11} by up to a factor of 70.

Mechanisms that have the potential to be more powerful exploit intrinsic molecular quantum phenomena related to spin and charge states. An early example of addressing the spin state of a single molecule^{12–14} revealed Kondo resonances using cobalt (Co) metal centres¹⁵. More recently, a spin cross-over was induced by an electric field in iron (Fe)-based molecular nanoclusters¹⁶ (with high-to-low ratios of ~2), and in a coupled spin pair of two Co atoms¹⁷ (with high-to-low ratios of 2–3). Regarding intrinsic charge states, Coulomb blockade peaks were reported in ruthenium (Ru)-containing wires¹⁸, but not confirmed in self-assembled monolayers¹⁹. On the single-molecule level, Ru-based molecules showed conformation-induced changes

in the conductance²⁰ rather than changes due to intrinsic redox mechanisms. Two Ru metal centres in a photochromatic compound demonstrated reversible light-induced conductance switching in ensemble junctions^{21,22}. In another study, the importance of the copper (Cu) coordination on the conductance was demonstrated²³.

Placing individual metal centres in the transport pathway

Earlier we studied dinuclear organometallic Fe compounds with various anchoring schemes^{24,25} and discovered indications of field-induced conductance switching in the case of weak molecule–metal coupling. Motivated by these findings, we have developed mononuclear organometallic compounds of the type $(\text{MeCOSc}_6\text{H}_4\text{-C}\equiv\text{C})_2\text{M}(\text{P}\text{r}\text{P})_2$ ($\text{M} = \text{Fe}$; $\text{P}\text{r}\text{P} = 1,2\text{-bis}(\text{diethylphosphino})\text{ethane}$: (1); $\text{M} = \text{Ru}$, Mo (Molybdenum); $\text{P}\text{r}\text{P} = 1,2\text{-bis}(\text{diphenylphosphino})\text{ethane}$: (2), (3)) using weak thiol coupling^{26,27} to preserve molecule-internal spin and charge degrees of freedom for the solid-state molecular junctions. Fe, Ru and Mo were chosen as metal centres. The synthetic strategy aims to place the metal centres within the transport pathway (Fig. 1a,b) to achieve an optimal influence on transport and maximum interaction with the electric field. We used identical acetylenic backbones to constrain the variable parameters to the metal centres and their ligand fields. To prevent dimerization, the sulphur end groups were acetyl-protected, with the protection groups being hydrolysed *in situ*, forming the metal–molecule–metal junctions Au-1'-Au , Au-2'-Au , and Au-3'-Au (Fig. 1c). For the Fe metal centre, we used the bidentate phosphine ligand *depe* (*depe* = 1,2-bis(diethylphosphino)ethane) and for the Ru²⁸ and Mo centres, *dppe* (*dppe* = 1,2-bis(diphenylphosphino)ethane) chelate ligands. To extend the molecular length to 2.5 nm (S–S distance), we chose phenylene

¹IBM Research - Zurich, Säumerstrasse 4, Rüschlikon 8803, Switzerland. ²Department of Physical Chemistry, University of Vienna, Sensengasse 8/7, Vienna 1090, Austria. ³Institute for Theoretical Physics, TU Wien - Vienna University of Technology, Wiedner Hauptstrasse 8-10, Vienna 1040, Austria.

⁴Department of Chemistry, University of Zürich, Winterthurerstrasse 190, Zürich 8057, Switzerland. [†]These authors contributed equally to this work.

*e-mail: eml@zurich.ibm.com

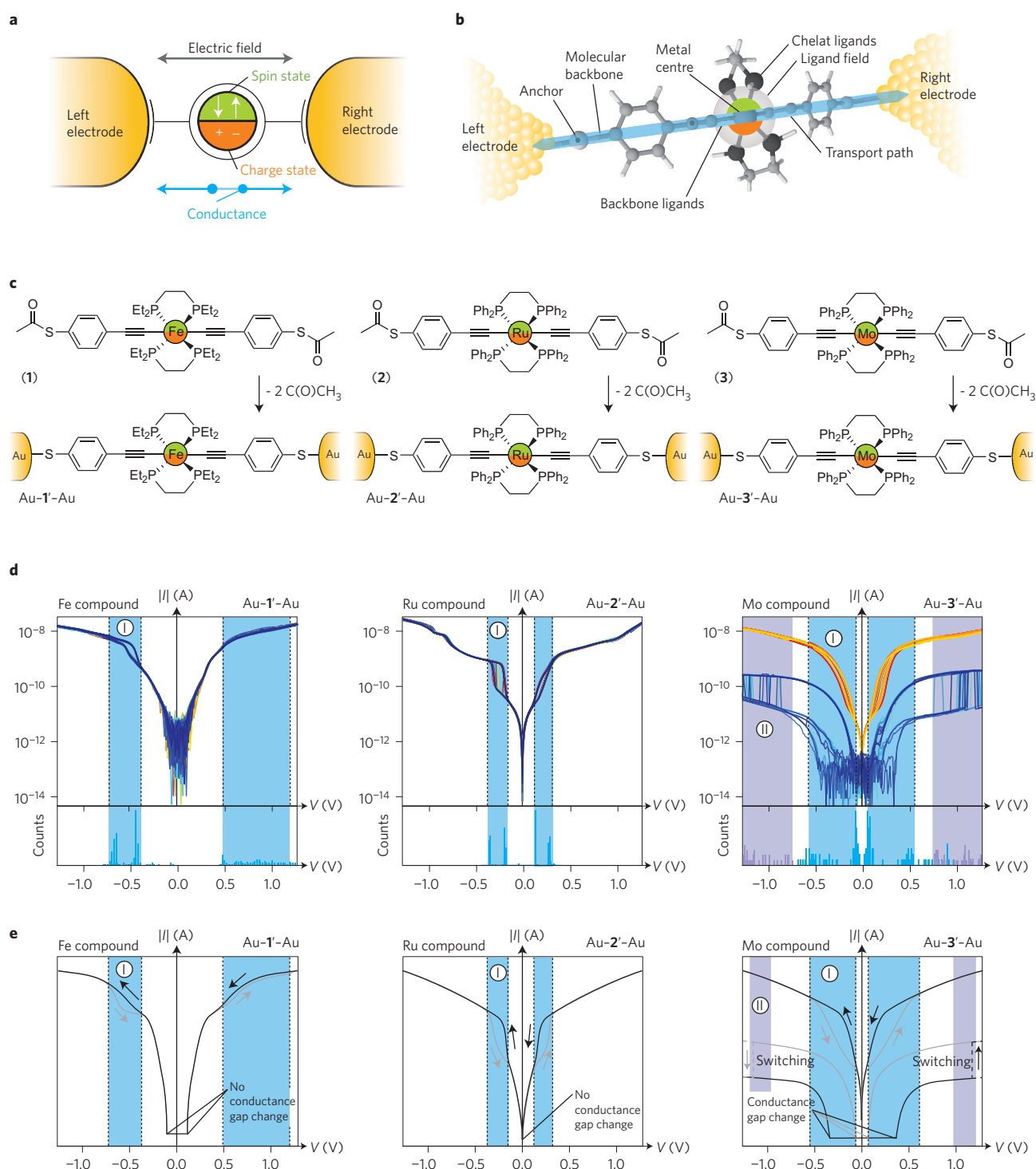


Figure 1 | Organometallic single-molecule junctions bearing Ru, Fe and Mo metal centres to provide charge and spin degrees of freedom. **a**, Addressing spin (green) and charge (orange) states of a molecular junction through manipulating the electric field present by means of the bias applied in a two-terminal geometry. **b**, Anatomy of the organometallic molecular junction with one metal centre placed directly in the charge-transport pathway. **c**, Mononuclear compounds of type *trans*-(MeCOSC₆H₄-C≡C-)₂M(PnP)₂ (M = Fe; PnP = 1,2-bis(diethylphosphino)ethane: (1); M = Ru, Mo; PnP = 1,2-bis(diphenylphosphino)ethane: (2), (3)). The representative transport junctions Au-1'-Au, Au-2'-Au and Au-3'-Au are also shown. **d**, 50 representative *I-V* characteristics taken at 50 K. The Fe 1 and Ru 2 compounds both show a continuous splitting of the *I-V* curves, providing a hysteresis region (blue background). Here, no change in the conductance gap or in the high-bias conductance is found. The same type of curve (labelled I) is found also for the Mo compound 3 (blue curves) with a slightly larger hysteresis regime. In addition, there is a second type of curve (labelled II; orange curves) that reveals an abrupt switching accompanied by a large change in the conductance gap (violet background). Type II curves are acquired just before breaking the Au-3'-Au junction (upon gradually increasing the electrode distance). **e**, Schematic representation of the two types of hysteresis (blue shading) with continuous type I (Fe, Ru and Mo compounds 1, 2 and 3) and abrupt switching type II (Mo compound 3 only).

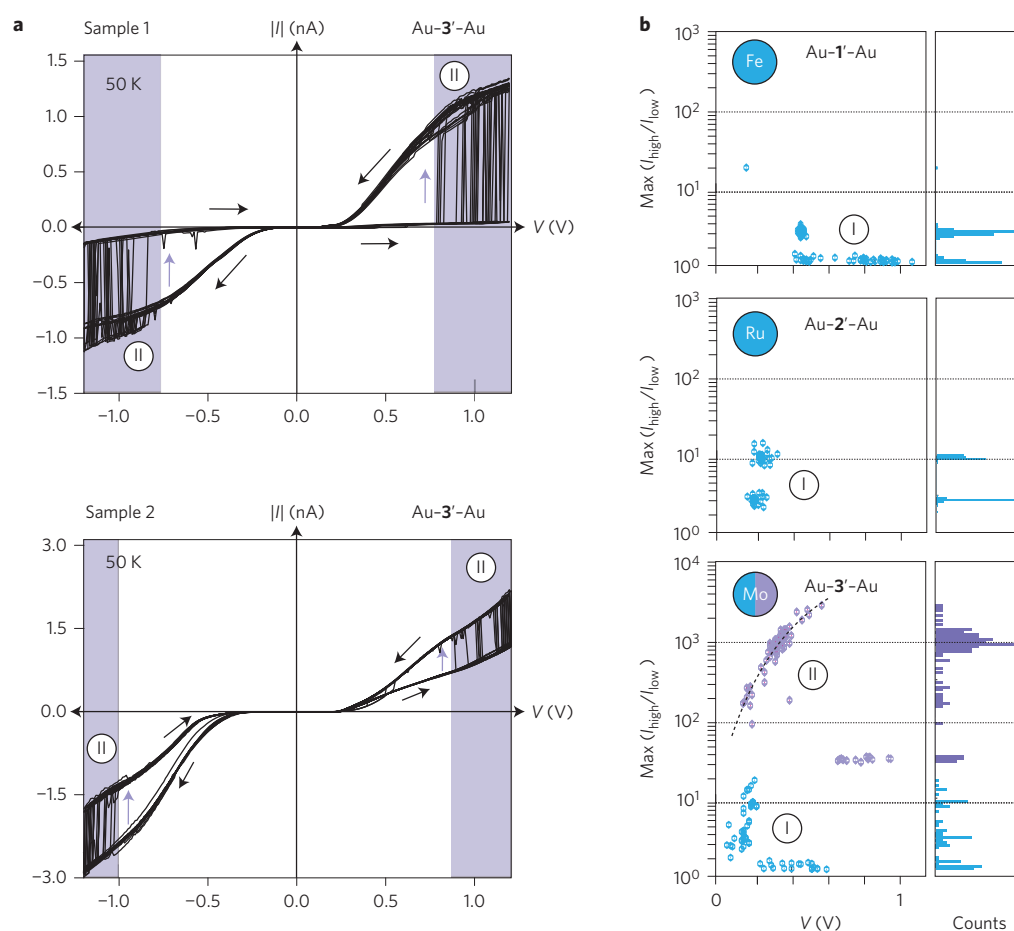


Figure 2 | High-to-low current ratios for type I and type II curves. **a**, Type II hysteretic curves are plotted on a linear current scale found for the Mo junction Au-3'-Au, revealing an abrupt switching from a low- to a high-conductance regime (50 K). Two datasets measured on fully independent samples are plotted, with typical differences for single-molecule experiments regarding the current amplitude and switching voltages. **b**, Statistics on maximum high-to-low current ratios extracted in the hysteresis regime for type I and type II curves for all compounds. Whereas type I ratios vary from 1.5 (Fe compound **1**) to 20 (Mo compound **3**), the type II switching found only for compound **3** attains 2,500 at a bias of less than 0.6 V. The ratio seems to follow a voltage dependence as indicated by the black dotted line.

spacers as conducting backbones. The synthesis of **2** was reproduced using a previously reported procedure^{28,29}, whereas new synthetic protocols were established for **1** and **3** (see Supplementary Information for details).

Conductance switching in single-molecule junctions

First, we perform current-voltage I - V data acquisition by repeatedly forming and breaking the junction³⁰ (see Supplementary Information). In the entire dataset, we find a substantial number of curves (~90%) that all exhibit distinct features differing from conventional non-linear molecular transport, namely, curves with hysteretic behaviour. Here, the curves acquired for sweeps from negative to positive bias are separated in a given voltage range from those acquired in the opposite direction. For the Au-1'-Au junction, around 85% of the curves show hysteresis, for Au-2'-Au 80%, and for Au-3'-Au 95%. Figure 1d shows 50 representative I - V curves taken at 50 K (see Supplementary Information Sections 10, 16–18 for statistics, sampling rate and temperature dependence). The hysteretic behaviour of the three compounds differs in the voltage range and the transition between the two envelopes. Accordingly, we categorized the I - V curves into two types. Type I curves are found for all compounds and are characterized by a small hysteresis that affects only a particular section of the voltage (blue backgrounds in Fig. 1d), whereas the curves for the

low- and high-bias regimes are nominally identical. The conductance gap (as defined by the onset in transport) is not altered, and the transition between the curves is continuous. Type II curves are only found for the Mo compound and differ from type I curves by an approximately 100× lower current and an abrupt switching between two distinct curves, accompanied by a hysteresis. Here, the conductance gaps change substantially (from 0.15 to 0.85 V, for example). Figure 1e summarizes the experiments schematically, further providing the sweep directions. When analysing the occurrences of type I and type II curves, we find that they depend on the junction configuration: type II curves are found just before breaking the molecular junction and show a switching between two distinct states (Fig. 2a). When extracting the maximum high-to-low ratio in the hysteresis region and plotting it versus the corresponding voltage (Fig. 2b), we find that type I curves display a narrow energy distribution, whereas type II curves seem to depend non-linearly on energy, with an increasing ratio for increasing bias. The high-to-low current ratios are 1.5 to 20 for type I switching consistently for all compounds, and exceed 1,000 for type II switching.

Coherent tunneling and decoherent hopping transport

In principle, several possible explanations exist for the hysteretic curves at smaller junction distances (type I) and the abrupt

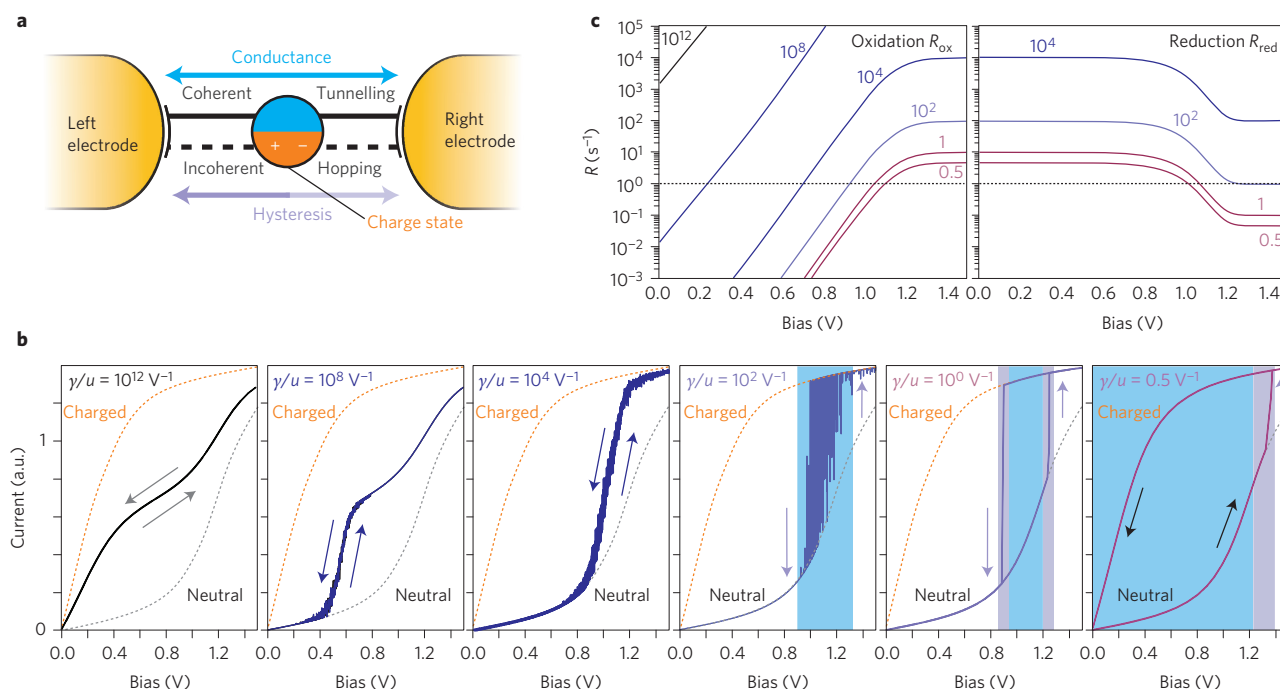


Figure 3 | Two-channel transport mechanism in single-molecule junctions and its influence on current switching and hysteresis. **a**, Model for a two-channel transport mechanism through a molecular junction with a fast coherent tunnelling path (cyan) responsible for the conductance, and a slow, incoherent hopping path (violet) causing hysteresis, by charging, for example. **b**, Calculated I - V curves from a two-state tight-binding model, with one strongly and one weakly coupled MO. The parameters used in this model are $\Delta E_{\text{ox/red}} = 0.1$ eV for the localized MO, a reorganization energy of 0.1 eV and a bias sweep rate of 1 V s^{-1} ; the onsite energies for the delocalized MO in the neutral and the charged system are set to -0.6 eV and -0.1 eV, respectively. The driving force ΔG^0 of the reaction depends on both $\Delta E_{\text{ox/red}}$ and the average bridge population in the fast channel³³. In our calculations, the bias sweeping rate determines the integration time, Δt , between two voltages, whereas the hopping rate for both oxidation and reduction is defined by the square of the same MO-metal-coupling, Γ , or the super exchange rates, $\gamma = (2\pi/\hbar) \Gamma^2$ which thereby determines the number of hopping processes (from the reduced to the oxidized state and vice versa) that occur within Δt . The current follows a monotonous trace between the neutral (grey dotted line) and charged (orange dotted line) states for $\gamma/u \geq 10^4 \text{ V}^{-1}$, but the I - V characteristics reveals a bistable range for decreasing rates that finally leads to hysteresis (blue background) and an abrupt switching around 1 (violet background indicates abrupt switching regimes). **c**, Corresponding reaction rates for oxidation, R_{ox} , and reduction, R_{red} , as a function of bias and different ratios of the coupling strength, γ , and the bias sweeping rate, u .

switching at larger junction distances (type II). As the ground state of the Mo compound **3** and some of the excited states of the Fe compound **1** and the Ru compound **2** are magnetic, a high-spin/low-spin (HS/LS) crossover is suggested, given the observed switching in similar systems^{16,17}. There, the HS/LS crossover caused a drastic change in the electronic structure across the entire electron wavelength spectrum that accompanied the switching between two distinct electronic states. In our experimental data, however, we do not find such drastic changes, for example there is no change in the conductance gap for type I curves and almost identical curves for certain voltage regimes for both types. Moreover, the nuclei of the molecules would adapt to that and thereby preclude hysteresis simply because there is nothing that could cause a time delay. In contrast, an oxidation or reduction of the transition metal compounds would enable a potential observation of hysteresis, as proposed theoretically^{31–33}. Those authors argued that if the charging rate is similar to the bias sweeping rate, a time delay required for a memory effect could occur, making the charging visible in the I - V curves. Here, the conductance is governed by a coherent tunnelling channel mediated by a delocalized molecular orbital (MO) ('fast channel'), whereas hysteresis is related to charging of a localized MO in an electron-hopping channel ('slow channel') (Fig. 3a). The probability that the localized MO is occupied determines the respective conductance contributions from the two charging states at every bias increase.

To simulate transport through single molecules, these charging probabilities were implemented in a stochastic approach. For

calculating I - V curves, we combine proposed algorithms³³ with data from density functional theory (DFT) calculations for the transmission (defining coherent tunnelling) and the transfer integral, reorganization energy and driving force (describing electron hopping^{34–36}). First, we demonstrate that by varying the ratio between the bias sweeping rate and the charging/hopping rate, the abrupt switching shown in Fig. 1c can be qualitatively reproduced for a simple two-MO tight-binding model. In Fig. 3b, we show I - V curves simulated for forward and reverse bias sweeps for various coupling strengths, γ , and fixed voltage sweeping rates, u . For the strongest coupling, $\gamma/u = 10^{12} \text{ V}^{-1}$, a statistical average of multiple switching events is observed, and as a consequence, the forward and backward sweeps fall together with the average of the two limiting I - V curves obtained from the integration of the transmission functions of the reduced and the oxidized systems (shown as orange and gray dotted lines in Fig. 3b, respectively). When lowering the coupling to $\gamma/u = 10^4 \text{ V}^{-1}$, averaging covers a smaller number of redox processes per integration time, Δt , resulting in fringes. For $\gamma/u = 100 \text{ V}^{-1}$, there is roughly one jump in each integration interval, and for the weakest coupling, $\gamma/u = 0.5 \text{ V}^{-1}$, only a single jump happens during a full sweep. Going from the strongest to the weakest coupling step by step (Fig. 3b), the voltage range where both sweeps follow the lower curve for low bias and the upper one for high bias becomes larger because ever higher voltages are needed to increase the likelihood of jumps. In the wide range of couplings from $\gamma/u = 10^{12}$ to 100 V^{-1} , however, the forward and backward I - V curves still follow the same path, although our

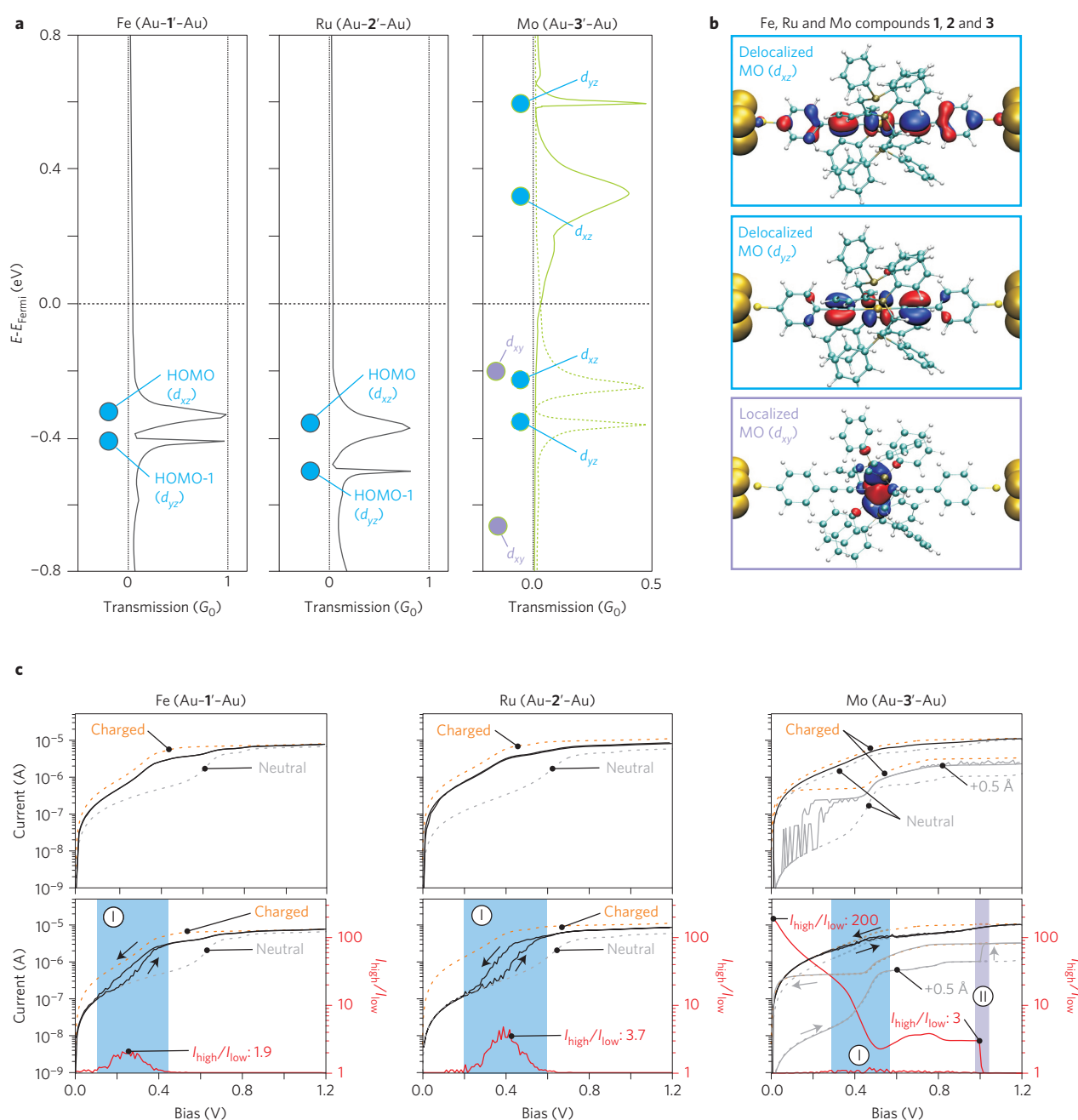


Figure 4 | DFT-derived transmission and molecular orbitals as well as transport characteristics calculated under finite bias. a, Total transmission functions (grey and green curves) and selected MO eigenenergies (dots) with respect to $E_{\text{Fermi,Au}}$ obtained from a subdiagonalization of the transport Hamiltonian, and the respective transmission functions calculated with NEGF-DFT; the two are plotted separately for spin-up and spin-down electrons for Mo compound **3** because of the latter's spin-polarized ground state (green lines). **b**, Spatial distributions of the MOs with the delocalized HOMO and HOMO-1 and a localized MO (with d_{xy} symmetry) found only for the Mo compound to lie in the relevant energy window. **c**, I - V curves calculated by a NEGF-DFT approach combined with a hopping description for the charging of the slow channel³⁶ by using the hysteresis formalism³³. The top row shows uncorrected I - V curves using the parameters given in Table 1, whereas for the calculations in the lower panels, the transfer integral is scaled down by a factor of 100 for reasons given in the main text. For Mo compound **3** a weaker coupling results in the abrupt switching curves. The red curves provide the ratio between high and low currents for the two types of hysteresis. All I - V curves were simulated from 100 bias steps in each direction with integration times of 0.01 s for the forward and 0.1 s for the backward sweeps.

stochastic approach creates uncertainties or line-thickening for ratios of γ/u smaller than 10^8 V^{-1} . Only when γ/u is as low as 1 V^{-1} does an irreversible switching or a 'lock-in' process take place, where the forward sweep follows the lower limiting curve for the reduced state and the backward sweep the upper one for the oxidized state; a scenario that qualitatively explains the type II

curves for the Mo junction. Figure 3c displays the hopping rates for oxidation (R_{ox}) and reduction (R_{red}), showing that the lower the ratio, the later R_{ox} and R_{red} cross the horizontal line defining the sweeping rate. R_{ox} determines the probability of charging the compounds, whereas the stability of this oxidized state depends inversely on R_{red} . Therefore, as can be seen from the left-hand

Table 1 | Parameters for electron hopping calculated from DFT for the three compounds at equilibrium geometry and for Mo compound 3 with the S-Au bond elongated by 0.5 Å on each side.

	ΔG^0	λ_{in}	λ_{img}	λ_{tot}	V
Fe (Au-1'-Au)	0.408	0.079	-0.021	0.057	2.6×10^{-3}
Ru (Au-2'-Au)	0.499	0.094	-0.022	0.072	2.3×10^{-3}
Mo (Au-3'-Au)	0.203	0.075	-0.017	0.058	1.2×10^{-5}
Mo (+0.5 Å)	0.269	0.075	-0.013	0.062	1.3×10^{-6}

All values are given in eV. The definitions used within our DFT calculations for the driving force ΔG^0 , the two contributions summing up to the reorganization energy λ_{tot} , namely its inner part λ_{in} and screening by the electrodes (λ_{img}), and the transfer integral V are described in detail in ref. 36.

panel of Fig. 3c, the bias necessary for reaching the charged state is inversely proportional to the coupling strength. R_{red} , in contrast, decreases with the coupling strength, which makes a reduction even at lower biases less likely, finally enabling the occurrence of a lock-in process during bias sweeps.

Let us now look at the electronic structures of the transport junctions as obtained from DFT calculations (Fig. 4). Energetic positions of the MOs and their spatial distributions, as well as the corresponding transmission functions, are computed by a nonequilibrium Green's function (NEGF) DFT formalism^{37–39} with the GPAW code^{40,41}. Because Mo compound 3 is the only compound among the three with a spin-polarized ground state, we show its MO eigenenergies and transmission functions for spin-up and spin-down separately (green curves in Fig. 4a). The magnetic property of the Mo system is the reason why a very localized MO with d_{xy} symmetry on the metal atoms (where z is the transport direction) moves close to the Fermi level for one spin orientation (violet dots). In contrast, this MO lies far outside of any reasonable bias window for Fe compound 1 and Ru compound 2. As a high degree of localization of a MO results in a very weak coupling to the electrodes, this MO can be considered the slow channel for the Mo compound, while for the Fe and Ru compounds the HOMO-1 (d_{yz}) plays this role. For all three systems, the fast channel is provided by the delocalized HOMO d_{xz} (Fig. 4b).

To calculate the hopping rates for the oxidation/reduction that govern the switching between neutral and charged compounds, we follow an approach developed earlier³⁶. Table 1 lists all relevant parameters for both charging states for all three systems at the equilibrium distance. For the Mo compound, it also gives those values at an elongation of the bonding distance between the anchor group and the electrodes by 0.5 Å on both sides according to the experimental findings that type II curves are found for elongated junctions just before rupture. The driving force ΔG^0 , which is defined by the energy difference of the slow-channel MO and the Fermi energy (E_{Fermi}), is lower for Mo than for Fe and Ru by a factor of 2–3. Its transfer integral is two orders of magnitude smaller and even three orders of magnitude smaller at the elongated distance. Because of the self-interaction problem of DFT, which becomes more severe for localized states, the calculations overestimate the spatial extension of the respective orbital and thereby also the transfer integral. Additionally, we have to account for the fact that the binding of the molecule to the metal surfaces is idealized in our DFT calculations, where we use perfectly planar Au(111) surfaces and symmetric bonding of the compounds at equilibrium distances. To account for these aspects, all calculated transfer integrals are consistently scaled down by a factor of 100 for the calculated I - V curves in the lower panels of Fig. 4c. In all panels, different sweeping rates are used for the forward and backward sweep, in agreement with the experimental situation (see Supplementary Information). Whereas for the Au-1'-Au and the Au-2'-Au junctions, an elongated configuration reveals only a minor influence on the hysteresis and the functional behaviour,

the Au-3'-Au junction shows an abrupt transition at the weaker coupling conditions induced by elongation. This situation perfectly reproduces the experimental findings in terms of switching energy, relative current levels, type of hysteresis and drastic change in the conductance gap. Furthermore, DFT calculations can also reproduce the high-to-low current ratios, which are around 1.5–4.5 for type I hysteresis and around 200 for type II hysteresis with abrupt switching (Fig. 4c).

Conclusions

In summary, we have experimentally and theoretically investigated the transport properties of organometallic molecules containing Fe, Ru and Mo metal centres in their transport pathway. We find hysteretic transport properties with continuous transitions for all three transport junctions, and additionally an abrupt switching for the Mo compound. Comprehensive DFT modelling, taking into account bias-driven charging, indicates an oxidation/reduction mechanism mediated by a weakly coupled, localized MO that is unique to the Mo compound because of its spin-polarized ground state. This MO gives rise to abrupt switching with high-to-low current ratios of greater than 1,000, outperforming all previously explored molecular-intrinsic conductance-switching mechanisms, for example magnetoresistance⁴². DFT combined with a two-channel transport model qualitatively agrees with experiments regarding the functional behaviour of the hysteresis. We therefore conclude that intrinsic redox functionality is maintained in weakly coupled solid-state organometallic junctions, remains accessible at feasible electric fields in a two-terminal geometry, and can be controlled by tuning the voltage sweeping rate in respect to the intrinsic oxidation and reduction rates. Moreover, by bias-induced charge-state alternations, a conductance switching with technologically relevant high-to-low current ratios exceeding 1,000 at voltages of 1.0 V could be achieved in a single-molecule building block. Although technological parameters such as fatigue, switching speed, non-volatility and so on remain to be determined in real device geometries, such small-scale building blocks could in principle fulfill future requirements for memory by providing reasonably low operational fields, speed, and large high-to-low current ratios.

Methods

Methods and any associated references are available in the [online version of the paper](#).

Received 11 February 2015; accepted 5 October 2015;
published online 16 November 2015

References

1. Van der Molen, S. J. & Liljeroth, P. Charge transport through molecular switches. *J. Phys.* **22**, 133001 (2010).
2. Song, H. *et al.* Observation of molecular orbital gating. *Nature* **462**, 1039–1043 (2009).
3. Liao, J. *et al.* Cyclic conductance switching in networks of redox-active molecular junctions. *Nano Lett.* **10**, 759–764 (2010).
4. Irie, M. Diarylethenes for memories and switches. *Chem. Rev.* **100**, 1685–1716 (2000).
5. Dulic, D. *et al.* One-way optoelectronic switching of photochromic molecules on gold. *Phys. Rev. Lett.* **91**, 207402 (2003).
6. Kronemeijer, A. J. *et al.* Reversible conductance switching in molecular devices. *Adv. Mat.* **20**, 1467–1473 (2008).
7. Van der Molen, S. J. *et al.* Light-controlled conductance switching of ordered metal-molecule-metal devices. *Nano Lett.* **9**, 76–80 (2009).
8. Quek, S. Y. *et al.* Mechanically controlled binary conductance switching of a single-molecule junction. *Nature Nanotech.* **4**, 230–234 (2009).
9. Blum, A. S. *et al.* Molecularly inherent voltage-controlled conductance switching. *Nature Mater.* **4**, 167–172 (2005).
10. Lörtscher, E., Cizek, J. W., Tour, J. M. & Riel, H. Reversible and controllable switching of a single-molecule junction. *Small* **2**, 973–977 (2006).
11. Meded, V., Bagrets, A., Arnold, A. & Evers, F. Molecular switch controlled by pulsed bias voltages. *Small* **5**, 2218–2223 (2009).

12. Kahn, O. & Martinez, C. J. Spin-transition polymers: From molecular materials toward memory devices. *Science* **279**, 44–48 (1998).
13. Sato, O., Tao, J. & Zhand, Y.-Z. Control of magnetic properties through external stimuli. *Angew. Chem. Int. Ed.* **46**, 2152–2187 (2007).
14. Baadjji, N. *et al.* Electrostatic spin crossover effect in polar magnetic molecules. *Nature Mater.* **8**, 813–817 (2009).
15. Park, J. *et al.* Coulomb blockade and the Kondo effect in single-atom transistors. *Nature* **417**, 722–725 (2002).
16. Prins, F., Morabal-Capilla, M., Osorio, E. A., Coronado, E. & van der Zant, H. S. J. Room-temperature electrical addressing of a bistable spin-crossover molecular system. *Adv. Mater.* **23**, 1545–1549 (2011).
17. Wagner, S. *et al.* Switching of a coupled spin pair in a single-molecule junction. *Nature Nanotech.* **8**, 575–579 (2013).
18. Kim, B. *et al.* Temperature and length dependence of charge transport in redox-active molecular wires incorporating Ruthenium(II) bis(σ -arylacetylide) complexes. *J. Phys. Chem. C* **111**, 7521–7526 (2007).
19. Luo, L. *et al.* Length and temperature dependent conduction of Ruthenium-containing redox-active molecular wires. *J. Phys. Chem. C* **115**, 19955–19961 (2011).
20. Ruben, M. *et al.* Charge transport through a cardan-joint molecule. *Small* **4**, 2229–2235 (2008).
21. Meng, F. *et al.* Photo-modulable molecular transport junctions based on organometallic molecular wires. *Chem. Sci.* **3**, 3113–3118 (2012).
22. Meng, F. *et al.* Orthogonally modulated molecular transport junctions for resettable electronic logic gates. *Nature Commun.* **5**, 3023 (2014).
23. Ponce, J. *et al.* Effect of metal complexation on the conductance of single-molecular wires measured at room temperature. *J. Am. Chem. Soc.* **136**, 8314–8322 (2014).
24. Schwarz, F. *et al.* High-conductive organometallic molecular wires with delocalized electron systems strongly coupled to metal electrodes. *Nano Lett.* **14**, 5932–5940 (2014).
25. Lissel, F. *et al.* Organometallic single-molecule electronics: Tuning electron transport through (diphosphine)₂FeC₄Fe(diphosphine)₂ building blocks by varying the molecule–metal anchoring scheme from coordinative to covalent. *J. Am. Chem. Soc.* **136**, 14560–14569 (2014).
26. Reed, M. A., Zhou, C., Muller, C. J., Burgin, T. P. & Tour, J. M. Conductance of a molecular junction. *Science* **278**, 252–254 (1997).
27. Zotti, L. A. *et al.* Revealing the role of anchoring groups in the electrical conduction through single-molecule junctions. *Small* **6**, 1529–1535 (2010).
28. Wuttke, E. *et al.* Divinylphenylene- and ethynylvinylphenylene-bridged mono-, di-, and triruthenium complexes for covalent binding to gold electrodes. *Organometallics* **33**, 4672–4686 (2014).
29. Touchard, D. *et al.* Vinylidene-, Alkynyl-, and *trans*-bis(alkynyl)ruthenium complexes. Crystal structure of *trans*-[Ru(NH₃)(C≡C-Ph)(Ph₂PCH₂CH₂PPh₂)₂]PF₆. *Organometallics* **16**, 3640–3648 (1997).
30. Lörtscher, E., Weber, H. B. & Riel, H. Statistical approach to investigating transport through single molecules. *Phys. Rev. Lett.* **98**, 176807 (2007).
31. Galperin, M., Ratner, M. & Nitzan, A. Hysteresis, switching, and negative differential resistance in molecular junctions: A polaron model. *Nano Lett.* **5**, 125–130 (2005).
32. Kuznetsov, A. M. Negative differential resistance and switching behavior of redox-mediated tunnel contact. *J. Chem. Phys.* **127**, 084710 (2007).
33. Migliore, A. & Nitzan, A. Irreversibility and hysteresis in redox molecular conduction junctions. *J. Am. Chem. Soc.* **135**, 9420–9432 (2013).
34. Kastlunger, G. & Stadler, R. Charge localization on a redox-active single-molecule junction and its influence on coherent electron transport. *Phys. Rev. B* **88**, 035418 (2013).
35. Kastlunger, G. & Stadler, R. Density functional theory based calculations of the transfer integral in a redox-active single-molecule junction. *Phys. Rev. B* **89**, 115412 (2014).
36. Kastlunger, G. & Stadler, R. A density functional theory based direct comparison of coherent tunnelling and electron hopping in redox-active single molecule junctions. *Phys. Rev. B* **91**, 125410 (2015).
37. Brandbyge, M., Mozos, J.-L., Taylor, J. & Stokbro, K. Density-functional method for nonequilibrium electron transport. *Phys. Rev. B* **65**, 165401 (2002).
38. Xue, Y., Datta, S. & Ratner, M. A. First-principles based matrix Green's function approach to molecular electronic devices: General formalism. *Chem. Phys.* **281**, 151–170 (2002).
39. Rocha, A. R. *et al.* Towards molecular spintronics. *Nature Mater.* **4**, 335–339 (2005).
40. Mortensen, J. J., Hansen, L. B. & Jacobsen, K. W. Real-space grid implementation of the projector augmented wave method. *Phys. Rev. B* **71**, 035109 (2005).
41. Enkovaara, J. *et al.* Electronic structure calculations with GPAW: A real-space implementation of the projector augmented-wave method. *J. Phys.* **22**, 253202 (2010).
42. Schmaus, S. *et al.* Giant magnetoresistance through a single molecule. *Nature Nanotech.* **6**, 185–189 (2011).

Acknowledgements

We are grateful to M. Koch for support with the synthesis of the end groups and to O. Blacque for single-crystal X-ray diffraction. We also acknowledge G. Puebla-Hellmann, V. Schmidt, and F. Evers for scientific discussions, and M. Tschudy, U. Drechsler and Ch. Rettner for technical assistance. We thank W. Riess and B. Michel for continuous support. Funding from the National Research Program “Smart Materials” (NRP 62, grant 406240-126142) of the Swiss National Science Foundation (SNSF) and the University of Zürich is gratefully acknowledged. G.K. and R.S. are currently supported by the Austrian Science Fund FWF, project Nos. P22548 and P27272, and are deeply indebted to the Vienna Scientific Cluster VSC, on whose computing facilities all DFT calculations were performed (project No. 70174). In addition, G.K. receives a grant co-sponsored by the Austrian Academy of Science ÖAW, Springer and the Austrian Chemical Society GÖCH.

Author contributions

F.L., C.E.-L., S.N.S., K.V., and H.B. designed and synthesized the compounds. F.S., and E.L. set up and performed the experiments and the data analysis. G.K. and R.S. carried out the calculations. F.S., G.K., K.V., H.B., R.S. and E.L. wrote the paper. All authors discussed the results and commented on the manuscript.

Additional information

Supplementary information is available in the [online version](#) of the paper. Reprints and permissions information is available online at www.nature.com/reprints. Correspondence and requests for materials should be addressed to: hberke@chem.uzh.ch (H.B.), venkatesan.koushik@chem.uzh.ch (K.V.) for chemistry, robert.stadler@tuwien.ac.at (R.S.) for DFT calculations, and eml@zurich.ibm.com (E.L.) for experimental work.

Competing financial interests

The authors declare no competing financial interests.

Methods

Chemical synthesis. The synthetic steps and full characterization of all compounds can be found in the Supplementary Information.

Transport measurements. Electron-beam-structured break junctions are mechanically actuated in a three-point bending mechanism operated under ultra-high-vacuum conditions (UHV; pressure $p < 2 \times 10^{-9}$ mbar) at 50 K³⁰. Molecules are deposited from a highly diluted solution in dry tetrahydrofuran (THF; 4×10^{-5} m/L). Electrical characterization is carried out with a Hewlett-Packard Semiconductor Parameter Analyzer HP4156B on repeated opening and closing of the molecular junction (more details can be found in the Supplementary Information).

Computational details. All calculations of transmission probabilities $T(E)$ and I - V curves were performed within a NEGF-DFT framework^{37–39} with the GPAW code^{40,41}. We chose a linear combination of atomic orbitals (LCAO) on a double zeta level with polarization functions (DZP) for the basis set and a Perdew–Burke–Ernzerhof (PBE) parameterization for the exchange–correlation (XC) functional.

The MO eigenenergies were calculated by decoupling the basis functions localized on the molecule from those of the surface states via a subdiagonalization of the transport Hamiltonian³⁴.

For the redox process, we combine a recent formalism³³ with a coherent tunnelling description based on NEGF-DFT for the calculation of the I - V characteristics of the reduced and oxidized states and a hopping description of the redox reaction based on Marcus theory³⁶. By calculating the bias-dependent reaction rates of oxidation and reduction, a probability P can be determined that describes the probability of the system being in one of the respective charge states after a given integration time Δt . To simulate single I - V sweeps, we apply a stochastic approach, in which we trap the system into one distinct charge state in every step. By calculating the change of probability dP , defined by either $dP = R_{\text{ox}} dt$ or $dP = R_{\text{red}} dt$, between two time steps t and $t + dt$, where $dt \ll \Delta t$, and comparing dP defined in this way with a random number between 0 and 1, we create a criterion for the switching between the two states. The overall current is then calculated from a mean value $I(V) = (1/n) \sum_{i=1}^n I(V, i)$, averaging over all n current values, with $\Delta t = ndt$. More details can be found in the Supplementary Information.

Curriculum vitae



Professional address: Vienna University of Technology, Karlsplatz 13, A-1040 Vienna, Austria.

Email: Georg.Kastlunger@tuwien.ac.at

Telephone number: +43-1-58801-13651

Main research topics: Single molecule electronics, Electron transport theory, Density functional theory

Personal Data: Born on 12 November 1985 in Meran(o), Italy.

Nationality: Italian.

Professional Experience:

- Nov 15 - present: Employment at the department of theoretical physics at the Vienna University of Technology (TU Wien) in the FWF-project P27272 "Electrochemical interference" in the group of Robert Stadler.
- Nov 14 – Oct 15: Employment at the department of theoretical physics at the Vienna University of Technology (TU Wien) funded by the research grant "Stipendium der Monatshefte für Chemie" cofunded by the Austrian Academy of Sciences (ÖAW), the Society of Austrian Chemists (GÖCH) and Springer Science+Business Media.
- Jul 14 – Sep 14: Employment at IBM Research - Zurich (Rüschlikon, CH) as a research assistant in the group of Emanuel Lörtscher.
- Mar 12 – Jun 14: Employment at the Department of Physical Chemistry at the University of Vienna as Project member for the work on the FWF- project P22548 "Electrochemical charge transport" with Robert Stadler as the project leader.
- Oct 11 – Feb 12: Research scholarship, funded by the "Provinz Bozen", South Tyrol, Italy, in the FWF-project P22548 "Electrochemical charge transport" with Robert Stadler as the project leader.
- Mar 10 – Aug 11: Research scholarship with Prof. R. Podloucky at the Institute of Physical Chemistry at the University of Vienna, for the work on the diploma thesis

Education and academic qualification:

- 2011: Graduation with distinction, 08.08.2011
- 2010-2011: Diploma thesis in the group of Prof. R. Podlucky, Institute of Physical Chemistry, University of Vienna
- 2004-2011: Study of Chemistry at the University of Vienna, with main focus on physical chemistry
- 1999-2004: Grammar school in Meran(o), Italy

Main international collaborators:

IBM Research - Zürich: Emanuel Lörtscher, Florian Schwarz

University of Zürich: Koushik Venkatesan, Franziska Lissel, Heinz Berke

Teaching activities:

- Winter term 2012/2013, 2013/2014 and summer term 2015: Tutor in the undergraduate lecture course *270161 Mathematik für LA Chemie*.
- Winter term 2012/2013: Cosupervision in the undergraduate practical course *270105 Wahlfachpraktikum C (Bachelormodul) - Physikalische Chemie / Materialchemie in the winter term 2012/2013*.
- Summer term 2012: Cosupervision in the undergraduate practical course *270165 Forschungsbeispiel aus theoretischer und komputativer Materialchemie und Polymerchemie*
- Summer term 2012: Cosupervision in the undergraduate practical course *Computer in der Materialchemie - UNIX (LINUX), Graphik, Textverarbeitung LATEX, Homepage-Erstellung mit HTML*.

Publication list

Publications in peer-reviewed journals:

1. G. Kastlunger and R. Stadler, *Charge localization on a redox-active single-molecule junction and its influence on coherent electron transport*, Phys. Rev. B **88**, 035418 (2013).
2. G. Kastlunger and R. Stadler, *Density functional theory based calculations of the transfer integral in a redox-active single molecule junction*, Phys. Rev. B **89**, 115412 (2014)
3. F. Schwarz, G. Kastlunger, F. Lissel, H. Riel, K. Venkatesan, H. Berke, R. Stadler, and E. Loertscher, *High-Conductive Organometallic Molecular Wires with Delocalized Electron Systems Strongly Coupled to Metal Electrodes*, Nano Letters **14**, 5932-5940 (2014)
4. G. Kastlunger and R. Stadler, *Density functional theory based direct comparison of coherent tunneling and electron hopping in redox-active single-molecule junctions*, Phys. Rev. B **91**, 125410 (2015)
5. Florian Schwarz, Georg Kastlunger, Franziska Lissel, Carolina Egler-Lucas, Sergey N. Semenov, Koushik Venkatesan, Heinz Berke, Robert Stadler and Emanuel Lörtcher, *Field-induced conductance switching by charge-state alternation in organometallic single-molecule junctions*, Nature Nanotechnology, in press, published online: 16 November 2015 (DOI: 10.1038/NNANO.2015.255)
6. Florian Schwarz, Michael Koch, Georg Kastlunger, Heinz Berke, Robert Stadler, Koushik Venkatesan, Emanuel Lörtcher, *Charge Transport and Conductance Switching in Rationally Designed Redox-active Azulene Derivatives*, submitted (2015)

Publications for the general public and other publications:

1. Diploma thesis with the title “First-principles study of the Fe-rich $\text{Fe}_x\text{Ni}_y\text{Al}_{1-x-y}$ alloy system”. Published on the E-thesis platform of the University of Vienna (<http://othes.univie.ac.at/15335/>)

Requested conference contributions:

1. G. Kastlunger, F. Schwarz, E. Lörtcher and R. Stadler, *Charge Transport in redox-based molecular switches*, ECME 2015, Strasbourg, France (2015)
2. X. Zhao, G. Kastlunger and R. Stadler, *Coherent tunneling and electron hopping in linear and branched molecules with multiple redox centers*, ECME 2015, Strasbourg, France (2015)

3. G. Kastlunger and R. Stadler, *Theory of charge transport through single redox-active transition metal complexes*, ECSSC 2015, Vienna, Austria (2015)
4. Puebla-Hellmann, G.; Bachmann, M.; Schwarz, F.; Kastlunger, G.; Riel, H. E.; Venkatesan, K.; Berke, H.; Stadler, R.; Loertscher, E., *Nanopores: A room-temperature stable and scalable platform for molecular electronics*, IEEE Nano 2015, Rome (Italy) (2015)
5. G. Kastlunger and R. Stadler, *Theory of charge transport through single redox active transition metal complexes*, VSS 2015, Vienna, Austria (2015)
6. G. Kastlunger and R. Stadler, *Coherent electron transport in single molecule junctions under electrochemical conditions*, "Modeling Single Molecule Junctions: Novel Spectroscopies and Control", Berlin, Germany (2013)
7. G. Kastlunger and R. Stadler, *Coherent electron transport in single molecule junctions under electrochemical conditions*, ECME 2013, London, England (2013)
8. R. Stadler and G. Kastlunger, *Electron hopping transport in single molecule junctions under electrochemical conditions*, ECME 2013, London, England (2013)
9. G. Kastlunger and R. Stadler, *Electron hopping transport in single molecule junctions under electrochemical conditions*, ElecMol12 - 6th International Meeting on Molecular Electronics, Grenoble, France (2012).
10. R. Stadler and G. Kastlunger, *Coherent electron transport in single molecule junctions under electrochemical conditions*, ElecMol12 - 6th International Meeting on Molecular Electronics, Grenoble, France (2012).
11. G. Kastlunger and R. Stadler, *Towards a theoretical description of electrochemical charge transport*, CECAM workshop on Quantum Transport in Molecular Nanostructures, Dublin, Ireland (2012).
12. G. Kastlunger, M. Leitner, D. Reith, and R. Podlucky, *First-principles Study of the $Fe_xNi_yAl_{1-x-y}$ Alloy System by the Cluster Expansion*, ViCom Workshop, Vienna, Austria (2011)
13. G. Kastlunger, M. Stoeck, D. Reith, and R. Podlucky, *Cluster Expansion study of $Fe_xNi_yAl_{1-x-y}$ alloys*, DPG- Fruehjahrstagung, Dresden, Germany (2011).

Invited seminar talks:

1. February 25th 2013, *Coherent electron transport in single molecule junctions under electrochemical conditions*, presented at the Center for Atomic-Scale Materials Design (CAMD) at the Technical University of Denmark, Denmark.
2. October 17th 2011, *Towards a theoretical description of electrochemical charge transport*, presented at the Center for Atomic-Scale Materials Design (CAMD) at the Technical University of Denmark, Denmark.